

**Experimental Basis for an Orthotropic Failure Model for Application in Crash
Simulation**

zur Erlangung des akademischen Grades eines
DOKTORS DER INGENIEURWISSENSCHAFTEN (Dr.-Ing.)
der Fakultät für Maschinenbau
der Universität Paderborn

vorgelegte
DISSERTATION

von
M.Sc. Marc Patrick Stolzenburg
aus Dillenburg

1. Gutachten : Prof. Dr. rer. nat. Thomas Tröster
2. Gutachten : Prof. Dr. rer. nat. Robert Brandt

Tag der mündlichen Prüfung : 02.05.2018

Zusammenfassung

Um das Verhalten von Strukturen frühzeitig im Entwicklungsprozess mittels numerischer Simulationen vorhersagen zu können, ist eine genaue Beschreibung der Materialeigenschaften notwendig. Diese Arbeit fokussiert sich auf das orthotrope Versagen von hoch- und ultrahochfesten Stahlblechen. Das Materialverhalten wurde u.a. mittels optischer Dehnungsmessung untersucht und zeigte eine Abhängigkeit von dem Belastungszustand und der Probenorientierung. Zudem wurde für einen ausgewählten hochfesten Stahl der Einfluss der Materialdicke auf das Materialverhalten bestimmt.

Auf Basis der lokalen Dehnungen wurde die plastische Instabilität, definiert als Beginn der makroskopischen Schädigung, experimentell bestimmt. Mittels der lokalen Dehnungen und eines Plastizitätsmodells wurden die Lastpfade der untersuchten Proben ermittelt, die Belastungszustände bei Versagen bestimmt und die Versagenskurven des Materialmodells definiert.

Anhand der experimentellen Ergebnisse wurden die Materialien orthotrop charakterisiert. Um den Einfluss der Orthotropie zu bestimmen, wurde eine Robustheitsanalyse durchgeführt. Mittels der Materialmodelle konnte das Verhalten der Proben vorhergesagt werden. Allerdings zeigte das orthotrope Materialmodell einen nur geringen Einfluss auf das untersuchte Bauteil der Robustheitsanalyse.

Summary

To predict the behaviour of structures at early stages of the development process by numerical simulations sufficiently, a proper description of material properties, e.g. rolling induced orthotropy of sheet metals, is necessary. This work focuses on the orthotropic failure of high and ultrahigh strength steel sheet metals. Material behaviour was investigated by applying various measurement methods, e.g. digital image correlation, revealing a dependency on the loading and the specimen orientations. Moreover, the influence of the material thickness was examined for selected high strength steels.

The plastic instability, which defines the onset of damage of the continuum, was specified experimentally based on the local strain fields. These were also utilised to describe the load paths incorporating the applied plasticity model. On basis of these load paths the failure points as well as the failure curves of the material model were established.

Based on the experimental results, all materials were characterised including their orthotropic properties. To distinguish the effect of orthotropy, a robustness analysis was conducted. Even though the material model was able to represent the different specimens, only minor effects were observed for the virtually investigated component.

List of Publications

No publications were made during this thesis.

Acknowledgements

There are many people who contributed to this thesis and also supported me over the last three years.

First of all I want to thank Professor Dr. Thomas Tröster of the institute *Leichtbau im Automobil* at the University of Paderborn for the fruitful and inspiring discussions as well as his guidance and support during the last three years. Moreover, I am thankful for the remarks of Professor Dr. Robert Brandt of the institute *Werkstoffsysteme für den Fahrzeugleichtbau* at the University of Siegen.

Furthermore, I am grateful for the discussions with Dr. Thorsten Marten and Mr. Holger Block from the institute *Leichtbau im Automobil* of the University of Paderborn.

I also want to thank my colleagues at Opel, especially Dr. Beate Lauterbach, Dr. Thorsten Michler, Mr. Daniel Riemensperger and Mr. Jan Morawski for the constructive comments as well as helpful and interesting discussions, deepening my understanding of mechanics and microstructure. Your guidance and support kept me on track. Moreover, I am grateful for the support of Mr. Moritz Hammacher and Mr. Dieter-Günter Mann during my experiments.

Special thanks go to my Ph.D.-colleagues Dr. Constantin Diez and Dr. Nikolai Sygusch who had their share in making the time of the thesis a pleasant and interesting journey. Moreover, I thank Mr. Alexander Kremer, Mr. Dirk Toewe and Mr. Philip Kunze.

I also want to thank Dr. David Forster for his review of the thesis.

Finally, I want to express my deepest thanks to my family, who always supported and motivated me not only over the last three years. Moreover, I want to thank you, Sarah Willim, my wife for your love, backing and our little daughter Mia, who only came into this world a few months ago, but has already become the biggest motivation for this thesis.

Index

Acknowledgements	v
Symbols	iii
Abbreviations	vi
1 Introduction	1
1.1 Background	1
1.2 Objective.....	1
1.3 Thesis Outline.....	2
2 Literature Review	4
2.1 Mechanical Framework	4
2.2 Modelling of Metals	7
2.2.1 Elasto-Plastic Material Behaviour	7
2.2.2 Material Hardening.....	11
2.2.3 Material Failure	11
2.3 Microstructural Researches.....	14
2.3.1 Strain Heterogeneities within the Microstructure	15
2.3.2 Texture Evolution	16
2.3.3 Damage and Failure Mechanisms.....	17
2.3.4 Bake-Hardening Effect.....	21
3 Experimental Investigation	22
3.1 Experimental Results of Quasi-Static Standard Testing	22
3.1.1 CR340LA PB 0.6 mm.....	23
3.1.2 CR340LA PB 1.1 mm.....	27
3.1.3 CR340LA PB 1.8 mm.....	33
3.1.4 Opposition of the Three Investigated CR340LA Sheets.....	38
3.1.5 MS1500 PB 1.0 mm.....	40
3.2 Formation of Lüders-bands	44
3.3 Microstructural Investigation.....	45
3.4 Distortional Hardening	48
3.5 Behaviour of Double-Shear Specimens	50
3.6 Strain Localisation and Failure	52
4 Plastic Instability.....	57
4.1 Experimental Procedure	57
4.2 3D-Extension of the Marciak-Kuczynski model	65
5 Experimental Determination of Load-Paths	68
6 Failure Characterisation	73
6.1 Orthotropic Fracture Model	73

6.2	Parameter Study	75
6.3	Parameter Identification	81
6.4	Orthotropic Hardening	81
6.5	Estimation of the Damage Parameters	83
7	Numerical Simulations	86
7.1	Bake-hardening Effect.....	86
7.2	Simulation Results	88
7.2.1	CR340LA 1.1 mm in Bake-hardening Condition (Shell)	88
7.2.2	MS1500 1.0 mm in Bake-hardening Condition (Shell)	93
7.3	Model Validation.....	97
7.3.1	Validation of CR340LA 1.1 mm-Material Model	97
7.3.2	Validation of MS1500-Material Model.....	99
7.4	Investigations of Virtual Components	101
7.4.1	Influence of Orthotropy on Hole Expansion Test.....	102
7.4.2	Robustness Analysis of Double-Hat Profile.....	103
7.4.3	Comparison of the CR340LA Fracture Properties.....	107
8	Summary and Discussion	108
9	Outlook.....	120
10	Appendix	121
10.1	Additional Experimental Results of MS1500.....	121
10.2	Microstructural Investigations.....	123
10.3	Additional Measurements to Determine the Plastic Instability Point.....	128
10.4	Weighting of non-proportional load paths	138
10.5	Characterised Material Models	139
10.5.1	Characterisation of CR340LA in 0.6 mm Sheet Thickness	139
10.5.2	Characterisation of CR340LA in 1.1 mm Sheet Thickness	140
10.5.3	Characterisation of CR340LA in 1.8 mm Sheet Thickness	142
10.5.4	Characterisation of MS1500 in 1.0 mm Sheet Thickness	143
10.6	Simulation Results CR340LA in 0.6 mm Sheet Thickness	145
10.6.1	CR340LA 0.6 mm: Force-Displacement & Local Strains	145
10.6.2	CR340LA 0.6 mm: Validation	148
10.7	Simulation Results CR340LA in 1.8 mm Sheet Thickness	149
10.7.1	CR340LA 1.8 mm: Force-Displacement & Local Strains	149
10.7.2	CR340LA 1.8 mm: Validation	153
10.8	Virtual Component-Test Geometries	154
10.8.1	Geometry of Hole Expansion Test.....	154
10.8.2	Geometry of Compression Test.....	155
11	Bibliography	156
	Curriculum Vitae	167

Symbols

The parameters within this work can be subdivided into Greek and Latin symbols. Tensorial components of 0th order (scalars) are not highlighted. Tensors of 1st order and higher are highlighted in bold, 2nd order tensors additional with single, 4th order tensors with double brackets.

Greek Symbols

Symbol	Unit	Description
$[\boldsymbol{\varepsilon}]$	-	Strain tensor
$[\boldsymbol{\sigma}]$	N/m ²	Stress tensor
$[\boldsymbol{\sigma}_{iso}]$	N/m ²	Untransformed (isotropic) stress tensor of failure model
$[\widehat{\boldsymbol{\sigma}}_{ortho}]$	N/m ²	Orthotropic transformed stress tensor of failure model
$[\boldsymbol{\sigma}_{dev.}]$	N/m ²	Deviatoric part of stress tensor
$[\boldsymbol{\sigma}_{hydro.}]$	N/m ²	Hydrostatic part of stress tensor
$[\widetilde{\boldsymbol{\sigma}}_{\alpha}]$	N/m ²	Transformed local stress tensor
α	N/m ²	Coefficient of additional bake-hardening flow potential term
β, γ	-	Coefficient of additional bake-hardening flow potential term
β	N/m ²	Cohesion coefficient of Hosford-Coulomb model
γ_1, γ_2	-	Distinct grain orientations within γ -fiber
Γ	-	Strain ratio of shear to loading direction (Γ -value)
Γ^*	-	Modified Γ -value
Δ	N/m ²	Error of numerical simulation and experimental stresses
ϵ	-	Equivalent plastic strain
ϵ_0	-	Initial plastic strain of Swift strain hardening law
ϵ_i $i \in [1,2,3]$	-	Principle strains
$\tilde{\epsilon}_p$	-	Actual plastic strain
$d\epsilon_p$	-	Equivalent plastic strain increment
ϵ_f	-	Failure strain
ϵ_f^{prop}	-	Failure strain of proportional load path
$d\epsilon_{ij}$ $i, j \in [x, y, z]$	-	Strain increment in material ij-direction
$d\epsilon_{material\ TD}$	-	Strain increment in material transverse direction
$d\epsilon_{Specimen\ TD}$	-	Strain increment in specimen transverse direction
$d\epsilon_{material\ IPS}$	-	In-plane shear strain increment in material coordinate system
$d\epsilon_{specimen\ loading}$	-	Strain increment in specimen loading direction
$d\epsilon_{thick}$	-	Strain increment in specimen thickness direction
$d\epsilon_{width}$	-	Strain increment in specimen width direction
$d\epsilon_{zB}, d\epsilon_{zA}$	-	Thickness strain increment of Marcinia-Kuczynski model
η	-	Stress triaxiality
θ	°	Lode Angle
$\bar{\theta}$	-	Lode Angle Parameter
κ	-	Distortion Coefficient
ν	-	Poisson-Number
ρ	kg/m ³	Mass density
$\bar{\sigma}$	N/m ²	Equivalent stress due to von Mises
$\hat{\sigma}$	N/m ²	Third invariant of the deviatoric stress tensor

$\tilde{\sigma}$	N/m ²	Averaged stress in simulation without stress fade out
σ_0	N/m ²	Yield Strength
σ_i $i \in [1,2,3]$	N/m ²	Principle Stresses
σ_{ij} $i, j \in [x, y, z]$	N/m ²	Stress components in local coordinate system
$\bar{\sigma}_{\text{Barlat91}}$	N/m ²	Equivalent stress of Barlat'91 yield model
σ_{EXP}	N/m ²	Averaged stress obtained experiment
$\bar{\sigma}_{\text{HF}}$	N/m ²	Equivalent yield strength due to Hosford
$\bar{\sigma}_i$ $i \in [1, n]$	N/m ²	Strain hardening function
σ_n	N/m ²	Normal stress of Mohr-Coulomb model
σ_m	N/m ²	Hydrostatic mean stress
$\hat{\sigma}_{\text{ortho I}}$	N/m ²	First principle stress of transformed stress tensor
$\hat{\sigma}_{\text{ortho III}}$	N/m ²	Third principle stress of transformed stress tensor
σ_{SIM}	N/m ²	Averaged stress in simulation
$\bar{\sigma}_{\text{Swift}}$	N/m ²	Equivalent yield strength of Swift hardening law
τ	N/m ²	Shear stress of Mohr-Coulomb model
$\varphi_1, \varphi_2, \Phi$	rad	Euler Angles
ϕ	N/m ²	Yield potential

Latin Symbols

Symbol	Unit	Description
$[[C]]$	N/m ²	Stiffness Tensor
$[I]$	-	Unity Tensor
$[Q]$	-	Rotation tensor
$[S]$	N/m ²	Deviatoric part of stress tensor
$[S_{\text{iso}}]$	N/m ²	Untransformed (isotropic) stress deviator of failure model
$[S_{\text{ortho}}]$	N/m ²	Orthotropic transformed stress deviator of failure model
a	-	Plastic exponent of Hershey-Hosford model
a, c, h, p, M	-	Parameters of Barlat'89 model
A, B, C, F, G, H, M	-	Parameters of Barlat'91 model
b_r	-	Burger's vector
c	-	Friction coefficient of Hosford-Coulomb model
c_d	-	Drag coefficient
c_{ijkl} $i, j, k, l \in [1,2,3,4]$	N/m ²	Components of 4 th order stiffness tensor
c_1	-	Friction-like coefficient of Mohr-Coulomb model
c_2	N/m ²	Shear resistance of Mohr-Coulomb model
D	-	Damage variable
\tilde{D}	-	Actual damage value
ΔD	-	Damage increment
D_{crit}	-	Damage at plastic instability
D_{exp}	-	Damage exponent of GISSMo
E	N/m ²	Youngs Modulus
F, G, H, L, M, N	-	Weighting coefficients of Hill'48 model
f	-	Sheet thickness ratio (MK model)
f_0	-	Initial sheet thickness ratio (MK model)
F_{exp}	-	Fading exponent of GISSMo
k	N/m ²	Initial yield strength of Swift strain hardening law
K_i $i \in [1,2]$	N/m ²	Transformed stress invariants of Barlat'89 model

n	-	Strain hardening exponent of Swift hardening lawn
n_{ortho}	-	Orthotropic Swift strain hardening exponent
n_{ij} $i, j \in [x, y, z]$	-	Swift strain hardening exponents in ij-material direction
R	-	Lankford-Coefficient
R^*	-	Modified Lankford-Coefficient
R_0	-	Lankford-Coefficient in 0° to RD
R_{45}	-	Lankford-Coefficient in 45° to RD
R_{90}	-	Lankford-Coefficient in 90° to RD
R_{av}	-	Averaged Lankford-Coefficient
R_b	-	Biaxial Lankford-Coefficient
R_{eH}	N/m^2	Upper yield strength of distinct yield point
R_{eL}	N/m^2	Lower yield strength of distinct yield point
R_{pl}	-	Plane Lankford-Coefficient
$R_{p0,2\%}$	N/m^2	Yield strength obtained at 0.2 % plastic strain
S_i $i \in [1,2,3]$	N/m^2	Principle deviatoric stresses
S_{ij} $i, j \in [x, y, z]$	N/m^2	Deviator components in local coordinate system
t	m	Sheet thickness
t_i $i \in [A, B]$	m	Sheet thickness within section A or B (MK model)
w_i $i \in [1, n]$	-	Weighting factor of flow curve mixture
Y	N/m^2	Yield strength
Y_{Si} $i \in [1,2]$	N/m^2	Strain hardening function in different directions

Abbreviations

Abbreviation	Description
1 st GEN	1 st Generation (of Advanced High Strength Steel)
2 nd GEN	2 nd Generation (of Advanced High Strength Steel)
3 rd GEN	3 rd Generation (of Advanced High Strength Steel)
A50	Tensile specimens with proportionality factor related to 50 mm gauge length
AHSS	Advanced High Strength Steel
BARL91	Barlat yield criterion, proposed in 1991
BAT	Biaxial Tension
BCC	Body-Centred Cubic
BH	Bake-hardening steel
CBB	Cell-block boundary
CP	Complex Phase steel
CR	Cold Rolled
DIC	Digital Image Correlation
DP	Dual Phase steel
EBSD	Electron Backscatter Diffraction
EMC	Extended Mohr-Coulomb model
EU	European Union
Euro NCAP	European New Car Assessment Programme
FB	Ferritic-Bainitic steel
FCC	Face-Centred Cubic
FEM	Finite Element Method
GISSMo	Generalized Incremental Stress-State dependent damage Model
GTN	Gurson-Tvergaard-Needleman model
HAGB	High Angle Grain Boundary
HC	Hosford-Coulomb model
HF	Hot Formed steel
HSLA	High Strength Low Alloy steel
IF	Interstitial Free steel
IF-HS	Interstitial Free-High Strength steel
LAGB	Low Angle Grain Boundary
LCE	Low Carbon Equivalent
LIAD	Load Induced Anisotropic Damage
MAGD	Model Add Generalised Damage (LS-DYNA failure model)
MC	Mohr-Coulomb model
MIAD	Material Induced Anisotropic Damage
MK	Marciniak-Kuczynski model
MS	Martensitic Steel
NR05	Specimen with notch radius of 5 mm
NR80	Specimen with notch radius of 80 mm
ND	Normal Direction
ODF	Orientation Distribution Function
OLM	Optical Light Microscopy
PB	Paint Bake condition
PST	Plane Strain Tension
RD	Rolling Direction

RVE	Representative Volume Element
SAGB	Small Angle Grain Boundary
SDR	Shear Double Radius
SE	Scanning Electron-detector
SEM	Scanning Electron Microscopy
SEP	Steel test specification (German: <i>Stahl-Eisen-Prüfblatt</i>)
TD	Transverse Direction
TRIP	Transformation Induced Plasticity steel
TWIP	TWinning Induced Plasticity steel
UAT	Uniaxial Tension
UHSS	Ultra High Strength Steel
USA	United States of America
UTS	Ultimate Tensile Strength
voest	voestalpine Stahl AG (German: Vereinigte Österreichische Eisen- und Stahlwerke Alpine Stahl AG)
YLD2000	Barlat yield criterion proposed in 2000
YS	Yield Strength

1 Introduction

1.1 Background

Over the past few years more stringent regulations in fuel consumption have been enacted, e.g. in the EU and the USA. Simultaneously, there has been an increase in requirements for crash-worthiness tests like the Euro NCAP. To satisfy the fuel consumption regulations, the energy efficiency of automobiles has to increase, which can be achieved by more effective aerodynamics (lowering the c_d -value), higher power train efficiency or a lower vehicle mass. This work focuses mainly on the option of lowering the vehicle mass, which leads to one of the most challenging tasks in automotive design: Lowering the vehicle mass and simultaneously rising the crashworthiness. To satisfy these requirements, it is common to use fibre reinforced plastics, aluminium or high strength steels. With respect to low costs, steel is still widely used due to a preferable combination of high strength and high ductility. Therefore, this work solely considers the characteristics of high strength steels and examines its behaviour in different tests.

The most widely used semi-manufactured products in automotive production are sheet metals, which are produced by rolling. They undergo different hot and cold rolling as well as additional annealing steps. The cold rolling process affects an alignment of the microstructure in rolling direction, which results in orientation dependent material properties. It can be observed that yield and ultimate tensile strength as well as fracture strain change with the specimen alignment to the rolling direction. This orientation dependency of properties is generally called anisotropy, which is strongly contingent on the production process beside material choice. Moreover, the properties of sheet metals comprise an inner symmetry, which can be expressed by three orthogonal mirror planes. This restrictive case of anisotropy is called orthotropy.

The vehicle-prototypes and their components undergo several physical tests during the development process, e.g. endurance tests, crash tests, aerodynamic tests etc. These tests are time-consuming and cost-intensive due to manufacturing time and quantity. To reduce the number of tests, an essential tool in modern vehicle development is the numerical simulation, replacing physical tests by simulations. This leads to more predictions early in the development process prior to (prototype-) manufacturing. The numerical simulation can also be used for various vehicle optimisations like weight, aerodynamic resistance or endurance. Several numerical methods exist which have specific advantages, e.g. in fluid- or structure simulations. For simulation of structures the Finite-Element-Method (FEM) is commonly utilised.

1.2 Objective

A wide range of different steel types exists, exhibiting a characteristic elongation and tensile strength, which can be expressed as the so-called “steel banana” and is depicted in Figure 1-1. Its banana shape results from the stress-strain behaviour of conventional steels as well as the so-called 1st generation of Advanced High Strength Steels (1st GEN AHSS) like martensitic or dual- and complex phase steels respectively (MS, DP and CP). The original banana shape was enlarged as a start by the development of the so-called 2nd GEN AHSS, the TRIP- and TWIP-

steels, which use alternative deformation mechanisms like strain induced phase transformation (TRIP-steel) and mechanical twinning (TWIP-steels). Recent developments have lead to 3rd GEN AHSS, which combine strengthening mechanisms of 1st GEN AHSS (e.g. martensitic and bainitic transformation, solid solution strengthening, grain refinement and precipitation hardening) and of 2nd GEN AHSS (twinning and phase transformation).

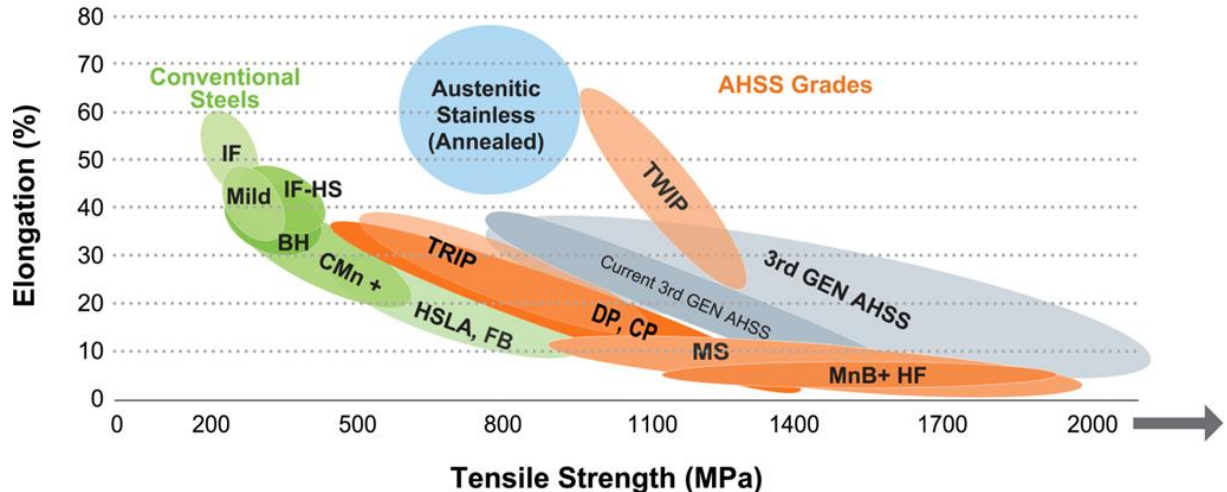


Figure 1-1: Elongation dependent on tensile strength of different steel types, resulting in the so-called “steel-banana” for conventional steels and AHSS-grades excluding TWIP-steels [Wor17]

It is common to utilise orientation independent (isotropic) material models for crash simulation, even though the manufacturing process can induce an orientation dependency (orthotropy). The prediction ability of numerical simulations depends, among other things, on the accurate description of material behaviour. Consequently, within this work, the orthotropic properties of different steel types are experimentally examined to identify characteristic properties of orthotropic material behaviour. This includes orientation dependent elasto-plastic material properties. Furthermore, the work focuses on orthotropic material failure like damage properties, the effect of damage on material behaviour and fracture strains. To classify the effect of orthotropic material modelling on the results of numerical simulations, different specimen types and orientations as well as virtual components are investigated.

1.3 Thesis Outline

In this work, the steel types CR340LA (High Strength Low Alloy - HSLA, Ultimate Tensile Strength (UTS) at 520 MPa) and MS1500 (Martensitic Steel - MS, UTS at 1500 MPa) are investigated. The investigation comprises different flat specimens to obtain material behaviour at stress states ranging from shear to biaxial tension. The experimental examination includes Digital Image Correlation (DIC)-measurements, Optical Light Microscopy (OLM) and Scanning Electron Microscopy (SEM) of specimens and fracture surfaces. Additionally, EBSD-measurements are conducted to investigate the microstructural evolution during straining.

Recent failure models define damage of the continuum and material failure by strain surfaces within the so-called mixed stress-strain space, in which the stress state is defined by the so-called stress triaxiality and the Lode Angle. To characterise the onset of plastic instability, which is defined as the onset of damage of the continuum, a method is proposed based on DIC measurements and collateralised by SEM measurements. To distinguish the failure strain surface, target points within the mixed stress strain space are estimated by combining DIC-measurements and the plastic properties. A new orthotropic failure criterion is developed, to obtain orthotropic failure surfaces based on these points.

Based on the experimental results, the orthotropic plastic behaviour as well as failure properties and stress state dependent failure strains are characterised. The failure properties are estimated by a proposed hybrid method based on experimental and numerical results. In order to classify the effect of plastic and fracture orthotropy, virtual component tests are carried out with different degrees of orthotropy.

2 Literature Review

In this chapter, current microstructural investigations and the theoretical framework will be summarised. The former focuses on the plastic orthotropy, strain heterogeneities and different failure mechanisms, which are determined by the microstructure. Furthermore, the review of the mechanical framework includes a description of orthotropic yield functions as well as recent failure models.

2.1 Mechanical Framework

To describe orthotropic behaviour, a material fixed coordinate system has to be utilised. It commonly refers to the manufacturing process for sheet metals. The rolling process occurs in the rolling direction (RD), whereas the transverse direction (TD) marks the perpendicular orientation within the sheet metal plane. Moreover, the normal direction (ND) is aligned in sheet thickness direction (Figure 2-1). These three directions are the basic vectors of the sheet metal coordinate system and span the three symmetry planes which define orthotropy.

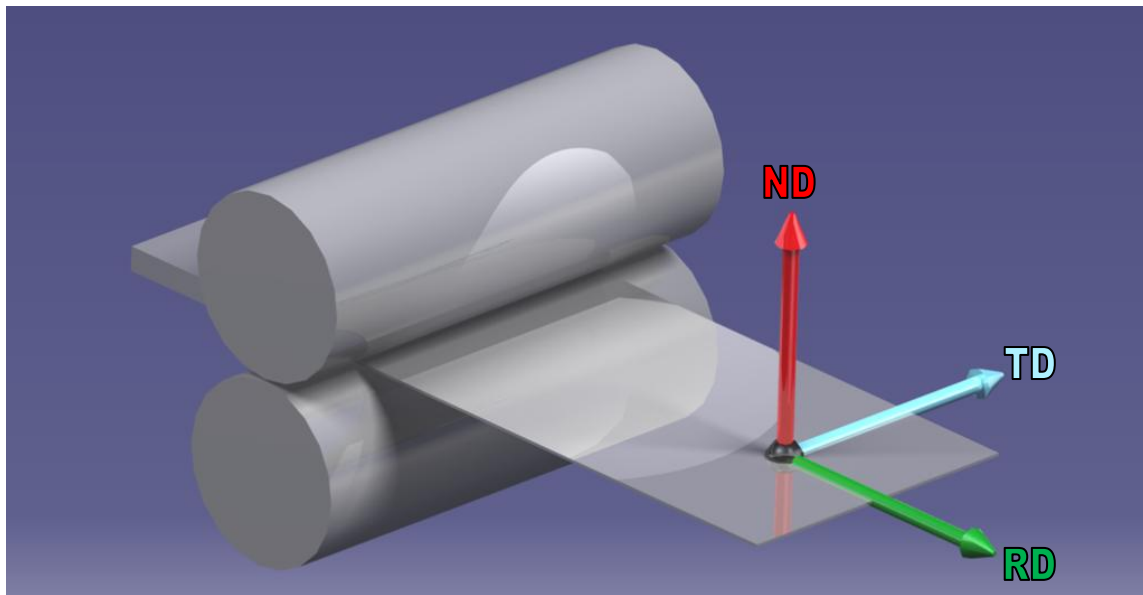


Figure 2-1: Sheet metal coordinate system aligned along the rolling direction (RD), transverse direction (TD) and sheet normal direction (ND)

The local material behaviour depends on the local stress state. It changes with material properties, specimen geometry or load case. The stress state is described by the symmetrical second order tensor $[\sigma]$, the so-called stress tensor. It is related to every infinitesimal volume element and represents normal and shear stresses for all directions. A graphical example is pictured in Figure 2-2. A tensor is always connected to a datum system, whose reorientation causes a change of the tensor components. The transformation of tensors in diagonal form leads to entries only along the diagonal, the principle values, as well as to the principle vectors, which define the axis of the transformed datum system. 1st order tensors are marked in bold further, 2nd order tensor in brackets additionally and 4th order tensors in double brackets.

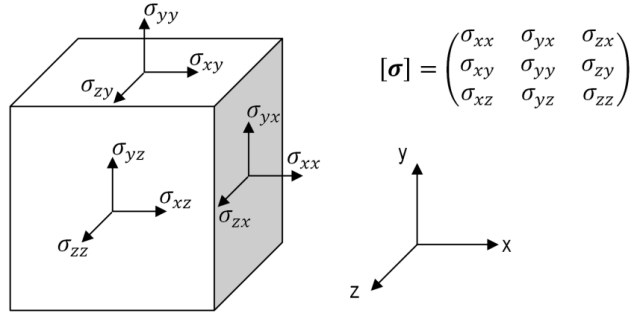


Figure 2-2: 6D-Stress tensor $[\sigma]$ at an infinitesimal volume element [Gro07]

The stress tensor $[\sigma]$ can be subdivided into a hydrostatic ($[\sigma_{\text{hydro.}}]$) and a deviatoric ($[\sigma_{\text{dev.}}]$) part (2-1), in which the hydrostatic mean stress σ_m is based on the first invariant of the stress tensor and $[\mathbf{I}]$ marks the unity tensor.

$$[\sigma] = [\sigma_{\text{hydro.}}] + [\sigma_{\text{dev.}}] = \left(\frac{1}{3} \sigma_m \cdot [\mathbf{I}] \right)_{\text{hydro.}} + \left([\sigma] - \frac{1}{3} \sigma_m \cdot [\mathbf{I}] \right)_{\text{dev.}} \quad (2-1)$$

The hydrostatic part only includes equal normal stresses in all three directions, leading to volume change only. In opposition, the deviatoric part affects pure isochoric shape change. In the context of metals, the deviatoric term corresponds to plastic deformation, whereas the hydrostatic part controls damage e.g. void nucleation or growth [Bri52]. To characterise each stress state the stress triaxiality η and the Lode Angle θ are introduced, which are based on the stress tensor. The stress triaxiality relates the stress proportions affecting volume change to those leading to shape changes. In contrast to η , the Lode Angle specifies the driving forces of the shape change e.g. mainly tension or pressure stresses. The stress triaxiality is calculated as ratio of σ_m and the equivalent stress $\bar{\sigma}$, which bases on the second invariant of the stress deviator $[\mathbf{S}]$. The operator $:$ describes the double dot product of two tensors, resulting in a scalar value by applying the summation convention.

$$\eta = \frac{\sigma_m}{\bar{\sigma}} \quad (2-2)$$

$$\sigma_m = \frac{1}{3} \text{Tr}([\sigma]) = \frac{1}{3} (\sigma_1 + \sigma_2 + \sigma_3) \quad (2-3)$$

$$[\mathbf{S}] = [\sigma_{\text{dev.}}] = [\sigma] - \sigma_m \cdot [\mathbf{I}] \quad (2-4)$$

$$\bar{\sigma} = \sqrt{\frac{3}{2} [\mathbf{S}] : [\mathbf{S}]} = \sqrt{\frac{1}{2} [(\sigma_1 - \sigma_2)^2 + (\sigma_1 - \sigma_3)^2 + (\sigma_2 - \sigma_3)^2]} \quad (2-5)$$

The range of the triaxiality is the space of real numbers. The norm of η is equal for tension ($\eta > 0$) or pressure ($\eta < 0$). Different stress states within the full stress triaxiality range are depicted in Figure 2-3. For hydrostatic tension, the stress triaxiality turns to infinity, where pure shear leads to $\eta = 0$. Uniaxial tension is characterized by $\eta = \frac{1}{3}$ biaxial tension by $\eta = \frac{2}{3}$.

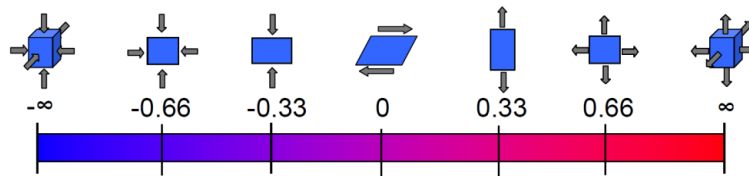


Figure 2-3: Stress triaxialities of different pressure and tension stress states [Feu13]

The Lode Angle θ defines the principle stress composition of the current shear stress state within the deviatoric plane. Metal plasticity is assumed to occur only under shear stress. As shown above the stress tensor can be divided into a hydrostatic and a deviatoric part. The first leads to the so-called hydrostatic axis, which corresponds to the vector $(1 \ 1 \ 1)^T$ within the principle stress space. The deviatoric part of the stress tensor defines a perpendicular plane to the hydrostatic axis. It is illustrated in Figure 2-4a in which the axes of the principle stress space are projected onto the deviatoric plane, resulting in an angle of 120° between the positive axes. Therefore, θ ranges from 0° to 60° in relation to the positive axes where 0° defines a tension and 60° a compression dominated shear stress state. A Lode Angle of 30° defines pure shear stress states. This behaviour is pictured in Figure 2-4a based on the σ_1 -direction.

With $\hat{\sigma}$, defined by (2-6), the Lode Angle θ can be calculated by equation (2-7). Instead of θ the Lode Angle Parameter $\bar{\theta}$ is often utilised, which is defined according to equation (2-8) and ranges from -1 ($\bar{\theta} = 60^\circ$) to $+1$ ($\bar{\theta} = 0^\circ$).

$$\hat{\sigma} = \sqrt[3]{\frac{9}{2} [\mathbf{S}] \cdot [\mathbf{S}] \cdot [\mathbf{S}]} = \sqrt[3]{\frac{27}{2} (\sigma_1 - \sigma_m)(\sigma_2 - \sigma_m)(\sigma_3 - \sigma_m)} \quad (2-6)$$

$$\theta = \frac{1}{3} \arccos \left(\frac{\hat{\sigma}}{\sigma} \right) \quad (2-7)$$

$$\bar{\theta} = 1 - \frac{6\theta}{\pi} = 1 - \frac{2}{\pi} \arccos \left(\frac{\hat{\sigma}}{\sigma} \right) \quad (2-8)$$

To describe the current stress state three types of coordinate systems are commonly used: The Cartesian, the Cylindrical and the Spherical coordinate system, which are shown in Figure 2-4b. Each coordinate system has its own advantages and its choice relies on the specific problem formulation.

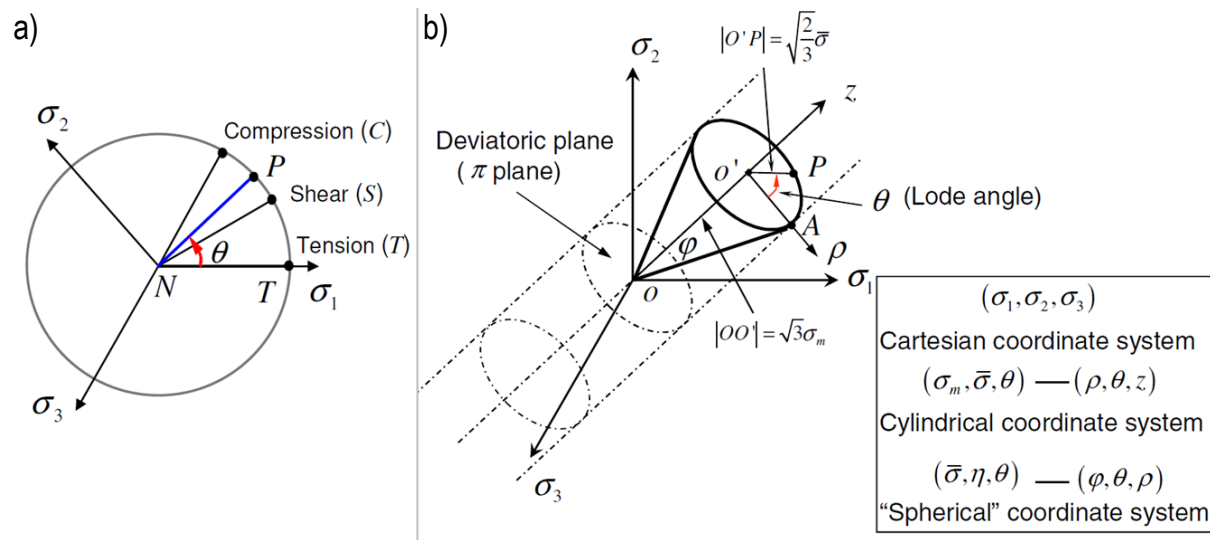


Figure 2-4: a) The Lode Angle based on σ_1 -direction in the deviatoric plane with von Mises yield surface, tension at $\theta=0^\circ$, shear at $\theta=30^\circ$ and compression at $\theta=60^\circ$ [Bas10], b) Description of the stress state by different coordinate systems [Wie10]

Cylindrical coordinate systems around the hydrostatic axis are commonly utilised to describe metal plasticity. Therefore, the hydrostatic pressure acts as height coordinate z . The deviatoric

plane is orthogonal to the hydrostatic axis and can be described by polar coordinates. The radial component is represented by $\bar{\sigma}$ and ρ respectively, whereas the Lode Angle θ indicates the angular component.

The formulation of the stress tensor takes place in the nine-dimensional stress space. Due to its symmetry it reduces to a six dimensional stress space with three normal and three shear stress components. The conversion into principle stress space $(\sigma_1, \sigma_2, \sigma_3)$ leads to three normal stresses only.

2.2 Modelling of Metals

Experimental material behaviour is a composition of different microscale effects. For modelling purposes, these effects are split into three parts: elasticity, plasticity and failure. They are captured by different model approaches. Combining the individual models leads to a mathematical description of the material behaviour.

Plastic strain behaviour is used to characterise orthotropy in sheet metal. The quotient of width to thickness plastic strains, presented in equation (2-9), is called the Lankford-Coefficient R .

$$R = \frac{d\epsilon_{\text{width}}}{d\epsilon_{\text{thick}}} \quad (2-9)$$

The Lankford-Coefficient is defined within the region of proportional elongation. It depends on the grain orientation of the microstructure [Huh05]. There are several definitions like R_α , which describes the Lankford-Coefficient at an angle of α with respect to the rolling direction. Commonly regarded directions are 0° , 45° and 90° to RD. The R -value can be understood as resistance to thinning [Tas09], [Bee10], [Kan13]. Higher Lankford-Coefficients result in higher plastic width strains compared to those in thickness direction [Tas09]. By taking the plastic incompressibility into account, the plastic width and thickness strain can be calculated by the plastic strain in loading direction and the R -value. An average of the three values R_0 , R_{45} and R_{90} is defined by R_{av} (2-10) [Wei07].

$$R_{\text{av}} = \frac{R_0 + 2 \cdot R_{45} + R_{90}}{4} \quad (2-10)$$

To describe the in-plane anisotropy, the planar anisotropy value R_{pl} is introduced, measuring the dependence of the R -value on the angle to rolling direction (2-11) [Wei07].

$$R_{\text{pl}} = \frac{R_0 - 2 \cdot R_{45} + R_{90}}{2} \quad (2-11)$$

In biaxial tension the biaxial Lankford-Coefficient R_b is elucidated similarly to uniaxial tension.

2.2.1 Elasto-Plastic Material Behaviour

Modelling of elastic material behaviour represents the dependency of stress on elastic strains. Elastic strains are fully reversible by load removal. In the general case of anisotropic elasticity the second stage stress tensor $[\sigma]$ depends on the fourth order elasticity tensor $[[C]]$ as well as the second stage strain tensor $[\epsilon]$ [Bec13], see equation (2-12).

$$[\boldsymbol{\sigma}] = [[\mathbf{C}]] : [\boldsymbol{\varepsilon}] \quad (2-12)$$

The fourth order tensor $[[\mathbf{C}]]$ exhibits 81 independent coefficients c_{ijkl} , which can be reduced due to symmetry conditions. For isotropic elasticity only two independent coefficients remain. It is sufficient to consider only small strains in which non-linearities can be neglected for many technical problems. The linear relation of stress and strain for 1D-deformations is described by Hooke's law [Wes30] (2-13).

$$\sigma = E \cdot \varepsilon \quad (2-13)$$

Here σ and ε describe the equivalent stress and strain. They are coupled by the Young's modulus E . Furthermore, the strain behaviour of elastic deformation is described by the Poisson-ratio ν which defines the negative ratio of elastic width to tensile strains. The Young's modulus can be determined from the uniaxial tension test up to the elastic limit, e.g. R_{eH} or $R_{p0,2\%}$, which describe the onset of plasticity. R_{eH} occurs in materials with distinct yield strength accompanied by Lüders-bands. For materials without distinct yield point the onset of plasticity is marked by $R_{p0,2\%}$ which is determined at 0.2 % of plastic strain.

To describe the onset and the evolution of plastic strains mathematically, a yield surface and the hardening behaviour have to be defined. In the general nine dimensional stress space the plastic potential Φ determines the onset of yielding (2-14) in which $\bar{\sigma}$ describes the equivalent stress and Y defines the yield strength in uniaxial tension.

$$\Phi(\bar{\sigma}, Y) = \bar{\sigma} - Y \leq 0 \quad (2-14)$$

For $\Phi < 0$ only elastic deformation has to be considered. $\Phi = 0$ indicates elasto-plastic material behaviour, whereas $\Phi > 0$ is not permitted. In addition, the plastic potential defines the plastic strain behaviour by the normal vector in the yield surface for each stress state. For associated plasticity, the onset of yielding as well as the plastic strain vector is defined by the same plastic potential. In contrast to that, two separate plastic potentials are specified to determine the onset of yielding and the plastic strain vector in non-associated plasticity. However, all further presented yield criteria assume associated plasticity.

One of the oldest yield criterion was proposed by Tresca in 1864 [Tre64] who observed plastic strains resulting from crystallographic gliding as a result of acting shear stresses. Plasticity arises from reaching a critical shear stress, where the acting shear stresses follow from the maximum of Mohr's circles. In the principle stress space the Tresca yield surface is represented by a hexagonal prism around the hydrostatic axis (2-15) [Ban10].

$$\max\{|\sigma_1 - \sigma_2|, |\sigma_1 - \sigma_3|, |\sigma_2 - \sigma_3|\} = Y \quad (2-15)$$

The Tresca yield criterion shows a good agreement with brittle materials but cannot represent ductile materials like metals adequately. For these materials, the Huber-Mises-Hencky-criterion is widely utilised with good results [Ban10]. It was proposed by Huber and von Mises in 1928 independently and later advanced by Hencky. It is based on the observations of the independence of hydrostatic pressure and yield behaviour. Each deformation can be subdivided into volumetric change and distortion. The former is affected by the hydrostatic pressure, the latter

only by deviatoric stresses. Therefore, the deformation energy, namely the elastic potential, can be subdivided into volumetric change energy and energy of distortion. Expressing and permuting the elastic potential and the volumetric change energy by principle stresses leads to the energy of distortion. The transition from elastic to plastic behaviour is assumed to occur at a critical value of the energy of distortion, leading to equation (2-16).

$$(\sigma_1 - \sigma_2)^2 + (\sigma_1 - \sigma_3)^2 + (\sigma_2 - \sigma_3)^2 = 2Y^2 \quad (2-16)$$

Independently, Hershey (1954) [Her54] and Hosford (1972) [Hos72] proposed a yield criterion. Therefore, it is called Hershey-Hosford criterion and is based, in contrast to the Huber-Mises-Hencky-criterion, on a non-quadratic formulation (2-17).

$$(\sigma_1 - \sigma_2)^a + (\sigma_1 - \sigma_3)^a + (\sigma_2 - \sigma_3)^a = 2Y^a \text{ with } a \in [1, \infty] \quad (2-17)$$

The plastic exponent a defines the shape of the yield surface. The criterion represents the Tresca criterion for $a = 1$ or $a = \infty$ and the von Mises criterion for $a = 2$ or $a = 4$. In all other cases, the yield surface forms between the Tresca and von Mises yield surface in which $a = 6$ is suggested for Body-Centred Cubic (BCC)- and $a = 8$ for Face-Centred Cubic (FCC)-materials [Ban10]. A generalisation in principle deviator stresses was postulated by Karafillis and Boyce in 1993 [Kar93].

The previously quoted yield criteria only describe the isotropic onset of plasticity. Regarding sheet metals or extrusion profiles, plastic orthotropy can play a major role. Different orthotropic yield criteria were proposed, which take specific material behaviour, like the lattice type, into account. All further presented phenomenological orthotropic yield criteria base on a transformation and accumulation within the stress space and relate yielding to the yield strength, commonly defined in uniaxial tension in 0° to RD.

To predict orthotropy in sheet metal forming Hill proposed a quadratic yield criterion in 1948 [Hil48], based on the Huber-Mises-Hencky-approach. Hill introduced the weighting factors F, G, H, L, M and N for the six terms of the von Mises yield criterion. Equation (2-18) represents the general formulation within the six-dimensional stress space.

$$F(\sigma_{yy} - \sigma_{zz})^2 + G(\sigma_{zz} - \sigma_{xx})^2 + H(\sigma_{xx} - \sigma_{yy})^2 + 2L\sigma_{xy}^2 + 2M\sigma_{xz}^2 + 2N\sigma_{yz}^2 = 2Y^2 \quad (2-18)$$

The six weighting factors depend on the six yield strengths X, Y, Z, R, S and T. The former three are the tensile yield strengths along rolling, transverse and sheet normal direction. The latter are the yield strengths under shear in RD/TD-, RD/ND- and TD/ND-direction. Plastic deformation leads to a distortion of the “principle axes of anisotropy”. Therefore, all six coefficients are only valid for the current state of anisotropy. In the isotropic case, all weighting factors are set to unity and hydrostatic pressure does not influence yielding. In contrast to that, hydrostatic pressure can affect shear in anisotropic materials. Moreover, investigations of the axis-symmetric deep drawing process show the formation of so-called “ears”. These ears form during the cup-cone test and result from orientation dependent differences in plastic flow, which de-

pend on the specific texture. The Hill'48 criterion is only suitable for materials forming four “ears” [Ban10], e.g. sheets of annealed aluminium, high strength steel [Kan87] or copper [Ant13].

In 1989 Frédéric Barlat et al. [Bar89] proposed an orthotropic extension of the isotropic Hershey-Hosford-yield criterion. Besides the assumption of orthotropy, Barlat assumes the plane stress state. The criterion is formulated by the two invariants K_1 and K_2 based on the stress tensor including normal and shear stresses. The tensor coordinate system is aligned to the “principle axes of anisotropy”, in which x corresponds to the rolling, y to the transverse and z to the sheet normal direction.

$$a|K_1+K_2|^M - a|K_1-K_2|^M + c|K_2|^M = 2Y^M \quad (2-19)$$

$$K_1 = \frac{\sigma_{xx} + h\sigma_{yy}}{2} \quad (2-20)$$

$$K_2 = \sqrt{\left(\frac{\sigma_{xx} + h\sigma_{yy}}{2}\right)^2 + p^2\sigma_{xy}^2} \quad (2-21)$$

The exponent M and the coefficients a, c, h and p describe the shape of the yield surface. The suggestion for the plastic exponent M is analogous to the Hershey-Hosford criterion.

Based on the previously presented proposal, the yield criterion was extended to the 6D-stress space by Barlat et al. [Bar91], see equation (2-22). In contrast to the Barlat'89 model [Bar89], basing on the two isotropic invariants K_1 and K_2 , plastic orthotropy is captured by a stress deviator transformation. The six coefficients A, B, C, F, G, H transform the components of the stress deviator, see equation (2-23), and define the yield surface shape in combination with the plastic exponent M.

$$|S_1 - S_2|^M + |S_2 - S_3|^M + |S_3 - S_1|^M = 2Y^M \quad (2-22)$$

with:

$$\begin{aligned} S_{xx} &= \frac{c(\sigma_{xx} - \sigma_{yy}) - B(\sigma_{zz} - \sigma_{xx})}{3} & ; & \quad S_{yz} = F \sigma_{yz} \\ S_{yy} &= \frac{A(\sigma_{yy} - \sigma_{zz}) - C(\sigma_{xx} - \sigma_{yy})}{3} & ; & \quad S_{zx} = G \sigma_{zx} \\ S_{zz} &= \frac{B(\sigma_{zz} - \sigma_{xx}) - A(\sigma_{yy} - \sigma_{zz})}{3} & ; & \quad S_{xy} = H \sigma_{xy} \end{aligned} \quad (2-23)$$

A further criterion to capture plastic orthotropy of the plane stress state was postulated by Barlat et al. in 2000 (YLD2000) [Bar03], subdividing the plastic potential into two sub-functions with separate stress tensor transformations. It incorporates the stress as well as the strain behaviour (Lankford-Coefficient) of uniaxial tension in three directions (0° , 45° and 90° to RD) including biaxial tension to define the yield surface shape.

Due to the extensive implementation of the Barlat'89 model in LS-DYNA, e.g. including orthotropic hardening or the temperature dependency, it is utilised for shell simulations later on. Furthermore, the framework of the Barlat model, proposed in 1991, is applied for solid simulations as well as to describe the orthotropic plasticity of different model extensions.

2.2.2 Material Hardening

The previously presented models describe the onset of plasticity. Further straining leads to the occurrence of plastic strains which can affect the yield surface. Three different mechanisms are pictured in Figure 2-5. Figure 2-5a presents the so-called isotropic hardening, which describes the uniform expansion of the yield surface in the stress space. The movement of the yield surface within stress space is called kinematic hardening and is pictured in Figure 2-5b. The movement results in a change of the yield strength during strain-reverse tests. The effect was first described by Johann Bauschinger in 1889 [Bau86] and is therefore called Bauschinger-Effect. A third hardening mechanism, the distortional hardening, is depicted in Figure 2-5c. It describes the yield surface deformation with plastic straining. This distortion can be evoked by e.g. orientation dependent expansion of the yield surface or the evolution of plastic properties with plastic straining.

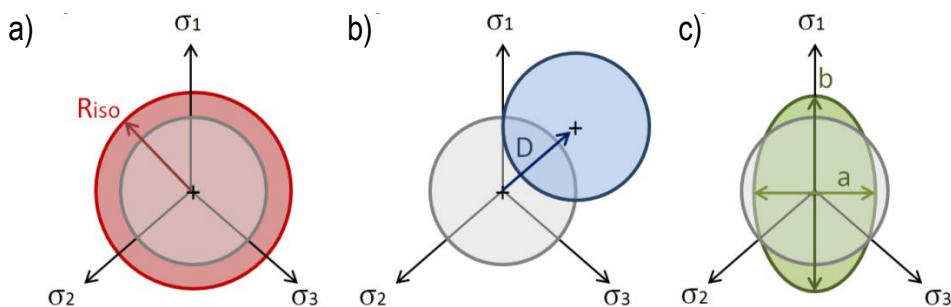


Figure 2-5: *Different strain hardening mechanisms, dividing into a): Isotropic hardening includes expanding of the yield surface, b): Kinematic hardening with movement of the yield surface in stress space and c): Distortional hardening with a change from a circular to an elliptical shaped yield surface with ellipsis axes a and b*

The utilised material models enable the definition of strain hardening by flow curves in addition to analytic hardening functions. The latter are exemplarily presented by the exponential strain hardening law postulated by Swift [Swi46], which is shown in equation (2-24). The equivalent stress $\bar{\sigma}_{\text{Swift}}$ is composed of the strength coefficient k , the hardening exponent n as well as the equivalent initial plastic strain ϵ_0 and equivalent plastic strain ϵ .

$$\bar{\sigma}_{\text{Swift}} = k(\epsilon_0 + \epsilon)^n \quad (2-24)$$

The Swift strain hardening law exhibits a good correlation to the investigated steels. Moreover, a huge number of further strain hardening laws exists, e.g. Voce [Voc45], Hollomon [Hol45] or El-Magd [EIM94], which describe the hardening-behaviour of various materials. The definition of flow curves can base on a single or a mixture of analytic hardening functions.

2.2.3 Material Failure

The suitable phenomenological description of material failure strongly depends on the specific material. Different approaches to predict material failure have been proposed. Simple criteria, like the principle stress, principle strain or maximum shear stress criterion predict failure by reaching one single critical value. These criteria do not accommodate to experimentally ob-

served failure behaviour of steels where a dependence on the stress state (stress triaxiality and Lode Angle) is observed. Based on the maximum shear stress criterion, the Mohr-Coulomb criterion [Cou76] (MC criterion) was proposed (2-25). It is capable of predicting brittle fracture of rocks or granular material, failing under pure elastic or small plastic strains. As unique feature the MC criterion forecasts the failure plane orientation due to its Lode Angle dependence. Fracture occurs along the most heavily loaded plane. The stress tensor is subdivided into a shear and a normal stress component (τ and σ_n). The two material constants c_1 and c_2 define material failure predicted by the MC criterion. Parameter c_1 can be understood as friction coefficient scaling the normal stress and c_2 defines the shear resistance. In general $c_1 \geq 0$ is applied where $c_1 = 0$ reduces the MC to the maximum shear stress criterion.

$$\tau + c_1 \sigma_n = c_2 \quad (2-25)$$

Besides its utilisation in geo-mechanics, the MC model is applied on isotropic ductile failure [Wil80], [Bai07], [Xue07], [Bar06a]. There are diverse extensions like the Modified Mohr-Coulomb (MMC model [Wie10]) or the Hosford-Coulomb model (HC model, [Mar15a]) as well as the application of a stress tensor transformation to meet anisotropy of ductile failure [Gu15].

Cockcroft and Latham [Coc68] developed a fracture criterion based on the plastic work done per unit volume at the fracture point. It incorporates the acting stress as well as the equivalent strain increment of the fracture point and predicts failure by reaching the so-called true ductility. Cockcroft and Latham [Coc68] define the true ductility as plastic work under pure uniaxial tensile load. The proposed model assumes tensile stresses to be necessary for material fracture, which never lead to failure under pressure load. The model was applied by Andrade [And17] and is able to foretell material failure for flat tensile specimens like standard tensile, notched or shear specimens. However, Andrade also showed that the failure criterion in the presented by Cockcroft and Latham [Coc68] overestimates the equi-biaxial test.

The previously discussed models do not include material softening due to damage. To contribute to failure of metals, material damage has to be considered. The microstructural mechanisms of damage and the resulting failure are discussed in detail in chapter 2.3.3. Damage can be defined on a microstructural basis by the occurrence of voids [Ben10], phase debonding [Tas09] or particle cracking [Tas09]. These mechanisms lead to microscale damage even at low macroscopic strains. On the basis of the macroscopic material behaviour, the damage of the microstructure is further classified into stable and unstable in this work. Stable microscale damage does not dominantly affect macroscopic material behaviour. In contrast to that, unstable microstructural damage is characterised by its dominant effect on a macro-scale, e.g. the onset of plastic instability.

Besides the microstructural description of isotropic damage, recent anisotropic damage models are proposed, which group into Load Induced Anisotropic Damage (LIAD) and Material Induced Anisotropic Damage (MIAD) models. Within the LIAD approach damage evolution is related to the principle loading direction. The isotropic damage parameters are not influenced by the distribution of second phase particles or the microstructure. In contrast to that, anisotropic damage

models following the MIAD-approach take the direction dependence of damage accumulation into account. [Nia12].

A recent approach for phenomenological modelling of material failure including damage behaviour is the GISSMo (Generalized Incremental Stress State dependent damage Model) [Bas11]. For general application, the model is defined within the mixed stress strain space $\bar{\varepsilon}_f - \eta - \theta$. It subdivides into four separate criteria: damage accumulation, plastic instability, stress fading and failure strains. Strains at plastic instability as well as failure strains have to be predefined by a surface within the mixed stress strain space. Damage evolution and stress fading, which describes the effect of damage on the local stress level, are exponential functions which have to be calibrated. In LS-DYNA, a generalisation of the GISSMo (called *MAT_Add_Generalized_-Damage or *MAT_MAGD) is implemented. It enables the separate definition of material damage and failure in up to three directions (0° , 45° and 90° to RD) based on GISSMo. For each direction, the onset of plastic instability, the failure strains, the accumulation of damage including a damage variable d_i ($d_1 (0^\circ)$, $d_2 (90^\circ)$ and $d_3 (45^\circ)$), and stress fading have to be defined. Furthermore, the damage type leading to element failure has to be defined, e.g., by reaching of unity of an equivalent (LIAD) or of a single (MIAD) damage variable. A more detailed model description for the standard GISSMo and its orthotropic extension can be found in [Liv16b], [DuB16], [Erh17]. DuBois et al. [DuB16] applied the standard GISSMo and the *MAT_MAGD to characterise failure behaviour of an aluminium extrusion, also including orthotropic plasticity, corresponding to LIAD. Only with the approach of orthotropic failure could the material behaviour be represented. Moreover, a fictitious application of *MAT_MAGD including anisotropic damage evolution can be found in [Erh17], representing MIAD.

Besides pure phenomenological models, a various number of approaches exist incorporating the microstructure in material damage up to failure. The investigations of McClintock [McC68] revealed failure of metals as a microscale process including nucleation, growth and coalescence of voids, leading to the macroscopic crack. These processes of damage evolution are comprised in the models of McClintock [McC71] as well as Rice and Tracey [Ric69]. The latter was extended by Rousselier [Rou87], adding work-hardening and a density evolution due to void nucleation and growth to Rice and Tracey's assumption of critical cavity growth ratio.

The previously described micro-structural processes are also included in the approach of the Gurson-Tvergaard-Needleman model (GTN model). It describes damage of ductile materials and its influence on the yielding behaviour. Gurson postulated a plastic potential due to yielding during void growth, in which void nucleation and growth are driven by hydrostatic stress within the model approach. Tvergaard and Needleman extended the Gurson model by introducing phenomenological coefficients and replacing the void volume fraction f by the damage function f^* . Experimental investigations have shown the suitability for tensile but not for shear loadings.

Due to its versatility as well as the ability of representing orthotropic failure, the *MAT_MAGD-approach is further utilised to model orthotropic failure in this work. Furthermore, the GISSMo is widely applied to model failure in crash simulation.

2.3 Microstructural Researches

Common material tests, like the uniaxial tension test, provide macroscopic material properties, which can be understood as the average of microscopic material behaviour. Microstructural effects can initiate fracture and have to be investigated, including the composite structure of multiphase steels as well as the texture evolution. Moreover, the mechanisms of void nucleation, growth and coalescence act at microscale at ductile failure. Because of focussing on steels for automotive application, the bake-hardening effect is important and will be discussed further.

Metal plasticity on microscale can only arise due to dislocation movement within the glide systems, defined by its glide planes, which results in pronounced anisotropic plastic behaviour of each single grain. Sheet metals, commonly used in automotive industry, exhibit a thickness considerably higher than the grain size. Therefore, despite the pronounced anisotropy of the single grains, isotropic material behaviour on macro-scale can be obtained by randomly distributed grain orientations. The orientation distribution can be described by the texture. Plastic deformation, e.g. from the cold rolling process during sheet metal manufacturing, leads to a reorientation of grains in preferred directions. Figure 2-6a visualises the change from an omnidirectional to a rolling texture. The orientation of each grain is defined by the three Euler Angles φ_1 , ϕ and φ_2 within the so-called Euler-space. The three angles define the coordinate axes of an Cartesian coordinate system ranging from 0° to 90° due to orthotropy. The Euler Angles can be obtained experimentally by utilising Electron BackScatter Diffraction measurement technique (EBSD). By applying EBSD on a representative microstructure, the determined statistical distribution of grain orientations, represented by the Orientation Distribution Function (ODF), is valid for each equal microstructural area of the material. A more detailed description of microstrucutral measurements of grain orientations and the connected ODFs can be found in [Suw14].

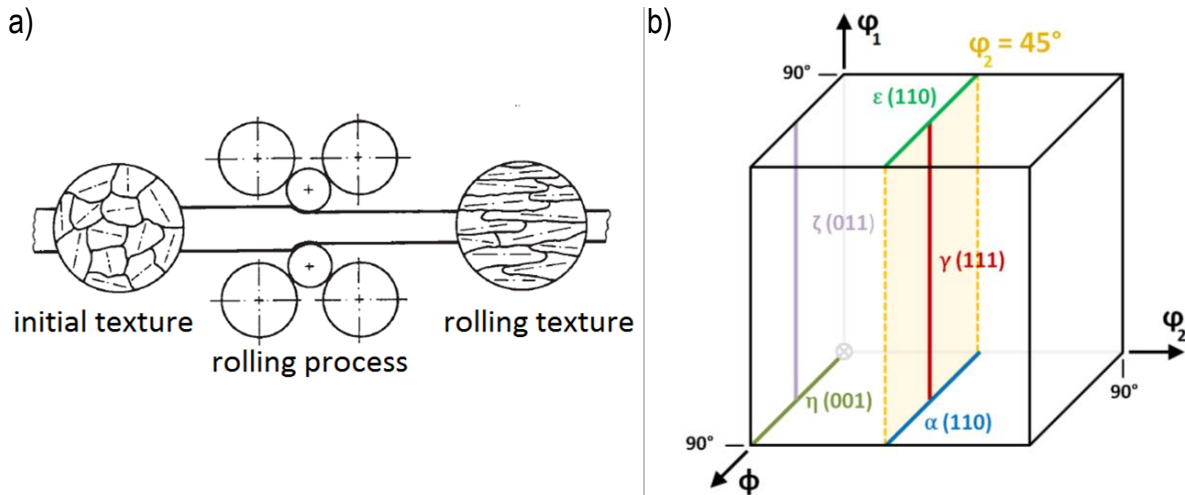


Figure 2-6: a) Realignment of crystallographic axis during rolling process [Wei07], b) fiber textures within the Euler-space, including the characteristic cold rolling fibers α and γ [Got13]

The Euler Angles describe the rotation of two coordinate systems, the crystal and the reference system, which, in general, coincides with the sheet metal reference system. Starting with

equally oriented crystal and reference system, φ_1 defines a rotation around the reference z-axis. Φ describes a further rotation around the x-axis of the crystal coordinate system, whereas φ_2 elucidates the last rotation around the z-axis of the crystal coordinate system. Dependent on the deformation process, preferred grain orientations arise, which can be represented as lines within the Euler Space, which are called “fibers”. The rolling process leads to the so-called α and γ fibers which are both defined by $\varphi_2 = 45^\circ$ and additionally by $\varphi_1 = 0^\circ$ for the α - and $\Phi = 45^\circ$ for the γ -fiber. Both of them as well as additional fibers and their orientations within the Euler-space are shown in Figure 2-6b.

2.3.1 Strain Heterogeneities within the Microstructure

Investigations of strain fields at micro-scale level have shown a highly heterogeneous strain distribution. Common dual phase steel generally consists of ferrite and martensite. Both phases differ in yield strength and ductility. Due to the same Young's moduli of ferrite and martensite, there is no stress transfer within the elastic region [Maz07]. Martensite features a higher yield strength whereas ferrite exhibits a higher ductility. Therefore, the ferrite controls yielding [Maz07], where martensite still remains elastic. As a result, a strain localisation at or near the phase interface takes place. The appearance of this non-uniform deformation leads to localised deformation bands within large and soft ferrite grains. In Figure 2-7 the strain localisation within ferrite grains near the interface to martensite is shown, leading to progressive damage formation within this area [Gha10]. Due to the very strong interface between both phases Ghadbeigi et al. [Gha10] observed strains up to 130 % in ferrite and 110 % in martensite grains, leading to void nucleation due to separation of martensite islands.

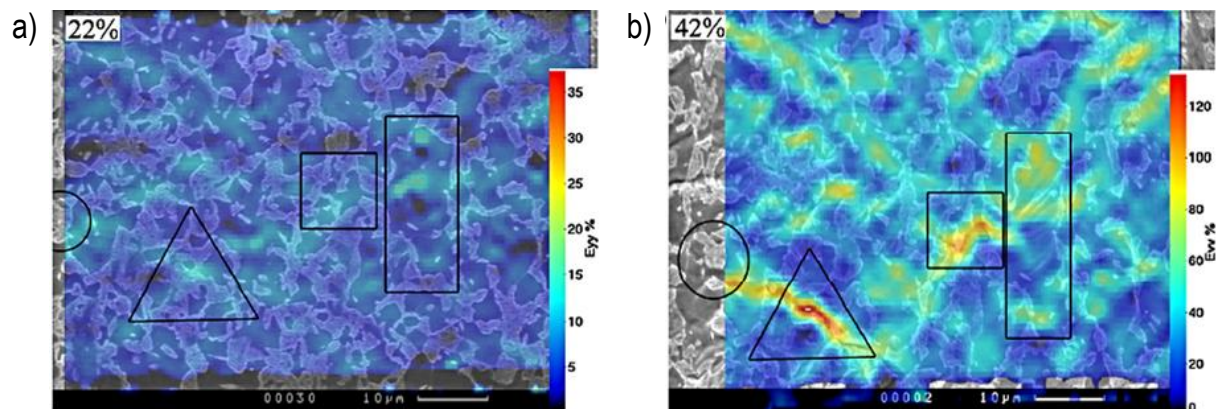


Figure 2-7: Local strain fields on microstructural scale depicting strain localisation at the interface of ferrite (light) and martensite (dark) in dual phase steel during uniaxial tension test at 22 % (l.) and 42 % (r.) tensile strain [Gha10]

Kang et al. [Kan07] reported high strain heterogeneities in ferritic areas constrained by martensite in comparison to pure ferrite or martensite. In this case, the ratio of ferrite grain size and surrounding martensite width influences the heterogeneity. Heat treatment like annealing also affects the strain distribution between both phases. It leads to diffusion of carbon in martensite and therefore increases the strains to initiate damage substantially, resulting in a greater ductility of the steel [Kan07].

The orientation of slip planes is coupled with the grain orientations and lattice structure. Texture analysis of sheet metal reveal orientation differences in directly neighbouring grains. Depending on the grain orientations, the grain boundaries can be subdivided into small ($<5^\circ$ SAGB), low ($<15^\circ$, LAGB) and high ($>15^\circ$, HAGB) angle grain boundaries. SAGB and LAGB only result in small changes of the Burger's vectors¹, leading to a direct slip transfer beyond the grain boundary. In contrast to that, HAGBs are accompanied by large changes of the Burger's vector, resulting in piled-up dislocations at the grain boundaries. Figure 2-8 visualises the compression strains at LAGB (Figure 2-8a) and HAGB (Figure 2-8b), as proposed by Patriarca et al. [Pat13]. The EBSD figures (left) show the sample position and grain orientation. The right side shows the different oriented slip planes and their impact on the resulting Burger's vector $|b_r|$. At LAGB a homogeneous strain distribution is measured. In contrast to that, the HAGB strain field is highly heterogeneous.

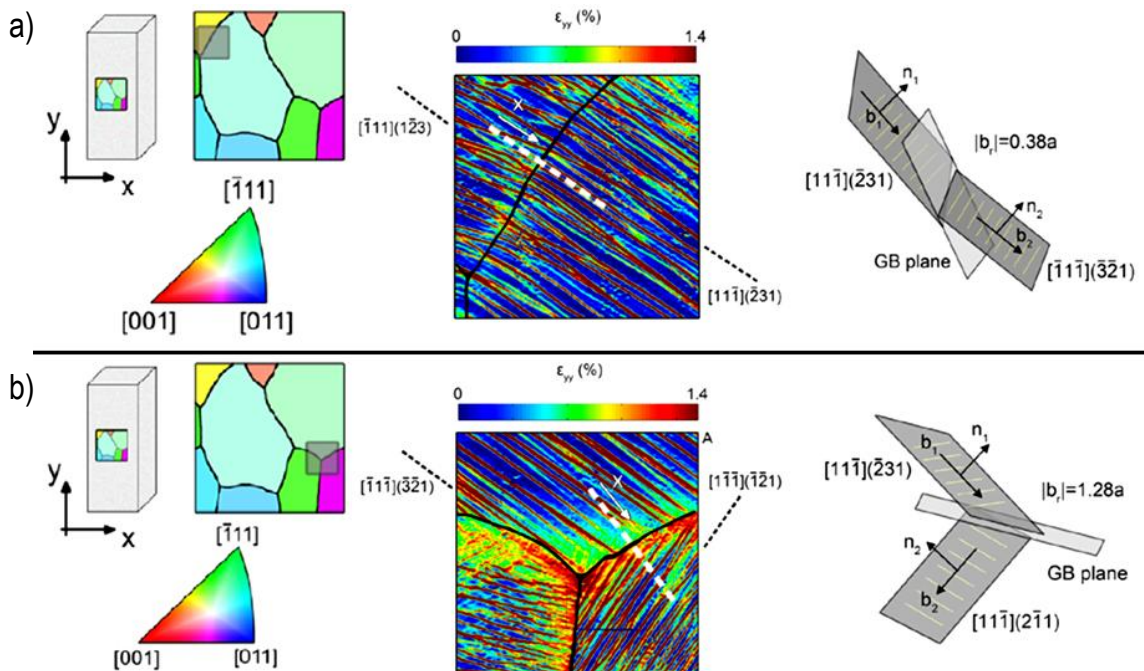


Figure 2-8: Strain transmission in dependence of grain orientation at a) low and b) high angle grain boundaries. The orientation of the investigated grains is pictured at the left, whereas the middle depicts the local strain field demonstrating the strain transmission of equal grain orientations and elevated strains at the grain boundary for misaligned grains. On the right the different Burger's vectors are pictured [Pat13]

2.3.2 Texture Evolution

Plastic deformation of metals occurs in slip planes. Their orientation and therefore the grain orientation with respect to the loading direction influences texture evolution. Several studies

¹The Burger's vector characterises the type of dislocation and describes the dislocation direction [Got13]

observed stable and unstable orientations depending on the loading [Ger15], [Nes01b], [Gar05]. For example, in uniaxial tension γ_2 ($\varphi_1 = 60^\circ$, $\phi = 55^\circ$, $\varphi_2 = 45^\circ$) is the most stable orientation, whereas in shear it is the most unstable one. Furthermore, the generation of one family of dislocation cell-block boundaries (CBB) in shear is observed, which is roughly parallel to macroscopic shear direction. Unstable grains tend to generate two very polarised families of CBBs parallel to most active slip planes but perpendicular to shearing direction [Nes01b], [Pee01b]. The polarisation leads to a subdivision into slightly misoriented lamellas. Unstable grains also tend to rotate into a stable position affected by slip plane orientation [Nes01b], [Gar05]. The rotation rate depends on the misorientation to a stable position [Gar05]. Therefore, straining leads to a disappearance of unstable grain orientations [Nes01b]. Something similar is observed for non-proportional load paths, which are a sequence of monotonic loadings leading to multiple texture evolutions. With increasing strain, the texture is dominated by the last load step. Initial dislocation walls tend to disappear and form new ones [Nes01b], [Gar05]. The results of polycrystal simulations performed by Nesterova et al. [Nes01b] are pictured in Figure 2-9a. It depicts the texture change of different grain orientations due to increasing monotonic shear stress, for which the γ_1 ($\varphi_1 = 30^\circ$, $\phi = 55^\circ$, $\varphi_2 = 45^\circ$) orientation is most stable; no reorientation is observed. In contrast to that, there is a big texture change for γ_2 orientation, which is the most unstable one for this type of loading. Figure 2-9b shows the simulation results of grain reorientation during a Bauschinger shear sequence. Moreover, Nesterova et al. [Nes01b] reported a good agreement between simulation and microstructural measurements.

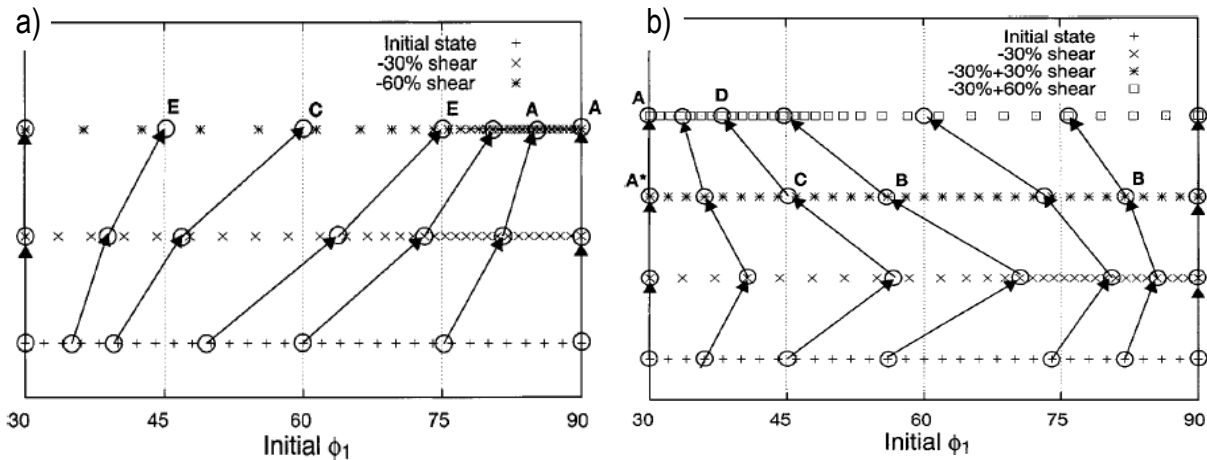


Figure 2-9: Simulation of evolution of different grain orientations under a) shear loadings (0 %, -30 %, -60 %), b) Bauschinger shear sequence (0 % shear, -30 % shear, 0 % shear, +30 % shear) [Nes01a]

2.3.3 Damage and Failure Mechanisms

Nucleation, growth and coalescence of voids are the three mechanisms of ductile failure [McC68]. The specific fracture mechanism depends on several factors like internal purity, the volume fraction, homogeneity or the appearance of other phases, e.g. martensite islands [Uth09], heat treatment [Zha14] or stress-strain conditions. Especially the hydrostatic pressure influences void nucleation and its growth rate [Ric69], [Moh09], [Ger15], [Ben10]. Gerstein et al. [Ger15] report symmetric fracture of sheet metals along their normal direction with their centre

layer as symmetric plane. While the central layer is dominated by equi-axed dimples and micro-void coalescence, the surface layers exhibit faces of cleavage and inclusion in dimples [Ger15]. Furthermore, based on numerical simulations Mohr et al. [Moh09] concluded sheet metal fracture to start at its centre layer due to the highest equivalent plastic strains.

The two main mechanisms of void nucleation are particle fracture and particle matrix debonding [Ben10], [Ste08]. Hancock et al. [Han76] assumed decohesion when radial stresses reach a critical value at the particle matrix interface. Decohesion occurs in steels at ferrite martensite phase boundaries but also at hard inclusions [Tas09], [Kan07], [Ben10], [Han76], [Las07]. Voids can also arise by particle fracture due to cracking of, for example MnS inclusions [Dun10], [Ben04a], [Sav10] or martensite islands [Maz07]. Figure 2-10 presents different void nucleation mechanisms arising at different stress states like uniaxial tension (UAT), plane strain tension (PST) and biaxial tension (BAT). Besides particle/matrix decohesion (a) particle cracking (c)/(d) and martensite fracture (e), phase decohesion at ferrite/martensite boundary is also visualised (f).

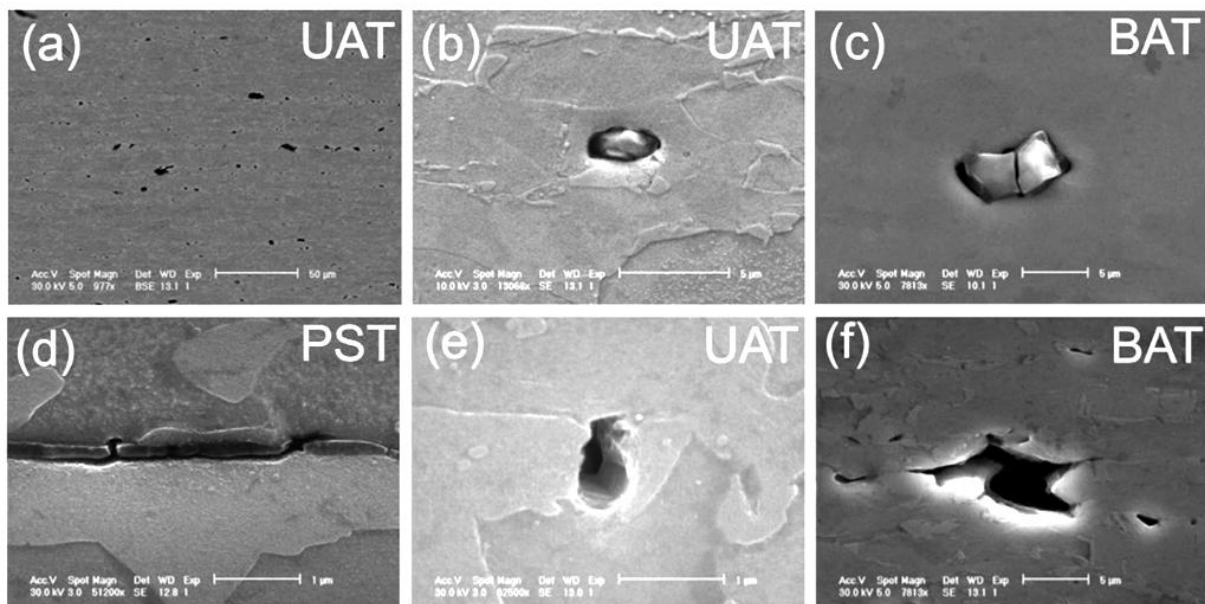


Figure 2-10: a) Damage evolution in DP-steel prior strain localisation: void nucleation and growth is observed through the mechanisms of (b)) particle-matrix decohesion, (c and d) particle cracking, (e) martensite fracture and (f) phase boundary decohesion [Tas09]

Benzerga et al. [Ben10] investigated different material properties and their influence on void nucleation. Table 2-1 depicts, e.g. the impact of matrix yield strength, particle stiffness or stress state on the void nucleation mechanism, which is influenced by the martensite volume fraction and its size [Maz07]. Furthermore, Maziani et al. [Maz07] reported a reduction of micro-void nucleation due to a co-deformation of martensite with the ferrite matrix in dual phase steels. A higher martensite volume fraction leads to favoured martensite plasticity and therefore to higher true fracture stresses and strains [Maz07]. A similar relationship was reported by Kang et al. [Kan07] for DP-steel with regard to ferrite and its surrounding martensite width. Besides the

material properties the particle orientation influences the void nucleation mechanism [Las07]. Figure 2-11 pictures the void nucleation mechanism (particle cracking or decohesion) dependent on particle orientation with respect to the loading direction. Particles which are aligned up to 45° to the loading direction lead to particle fracture. Particles which are aligned between 45° and 90° show a high probability of decohesion.

Table 2-1: Influencing factors on particle/matrix debonding and particle cracking [Ben10]

Parameter	Trend	
	Decohesion	Cracking
Matrix yield strength	↓	↗
Matrix hardening exponent	↓	↗
Particle elongation	↓	↗
Particle stiffness	↗	↗
Load orientation: axial	↓	↗
Load orientation: transversal	↗	↘
Load triaxiality	↗	↘

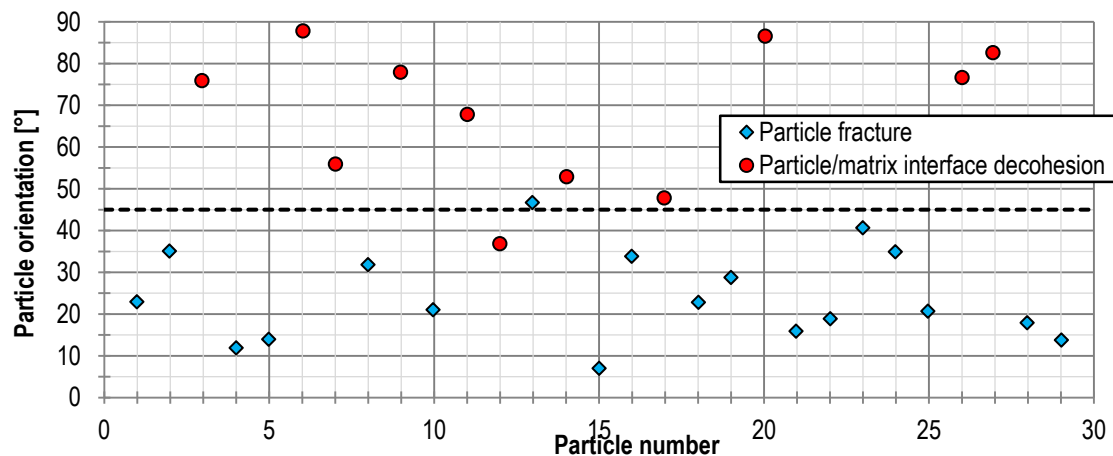


Figure 2-11: Impact of particle orientation to loading direction on void nucleation (interface decohesion/particle fracture) [Las07]

Prior localisation only limited void growth was observed for IF-steel. Kang et al. [Kan13] as well as Tasan et al. [Tas09] concluded an increased importance of damage beyond localisation. As contrasted to that, Tasan et al. [Tas09] also reported a significant damage accumulation prior to localisation in DP-steels. For different martensitic steel grades Savic et al. [Sav10] found different void sizes after fracture. They suggested the material ductility as a major factor for void sizes.

After void nucleation a further straining leads to an opening of nucleated voids due to plastic deformation of the surrounding matrix [Las07],[Sav10]. According to Hancock et al. [Han76], those deformations need high local strains for small-scale hole growth. Those strains result from the plastic instability [Han76] and the accompanied strain localisation. Pores can also emerge and grow at inclusions [Ger15]. The growth rate and void shape depend on the stress state. Tasan et al. [Tas09] reported less sharp tips at voids nucleated in uniaxial tension compared to biaxial tension. Where uniaxial tension leads to negative minor strains, they turn positive in biax-

ial tension [Tas09]. At stress triaxialities lower than $\frac{2}{3}$ inclusions can stop further void growth. This effect becomes important under predominantly deviatoric loadings [Ben10]. Macroscopic fracture arises due to material cracks which result from the coalescence of large voids. These are generated by the coalescence of smaller voids or their elongation. Thus, the isolated consideration of single void coalescence is insufficient but explains the principle mechanism behind crack initiation.

Void coalescence indicates the shift from a homogeneous to a highly localised deformation state [Ben10], [Ben02]. Figure 2-12 pictures the three different main modes of void coalescence [Ben10]. The most common mode is internal necking. Between neighbouring voids a flow localisation can arise [Han76], leading to thinning and fracturing of the matrix material, which results in void linkage. Coalescence in micro-shear bands is the second most common mode, which is also known as “void-sheet” coalescence [Ben10]. The coalescence depends on the relative positions of voids and micro-shear bands. Within the void-sheets, stable void growth is suddenly terminated, leading to decreasing local ductility, despite the voids being still apart [Ben10].

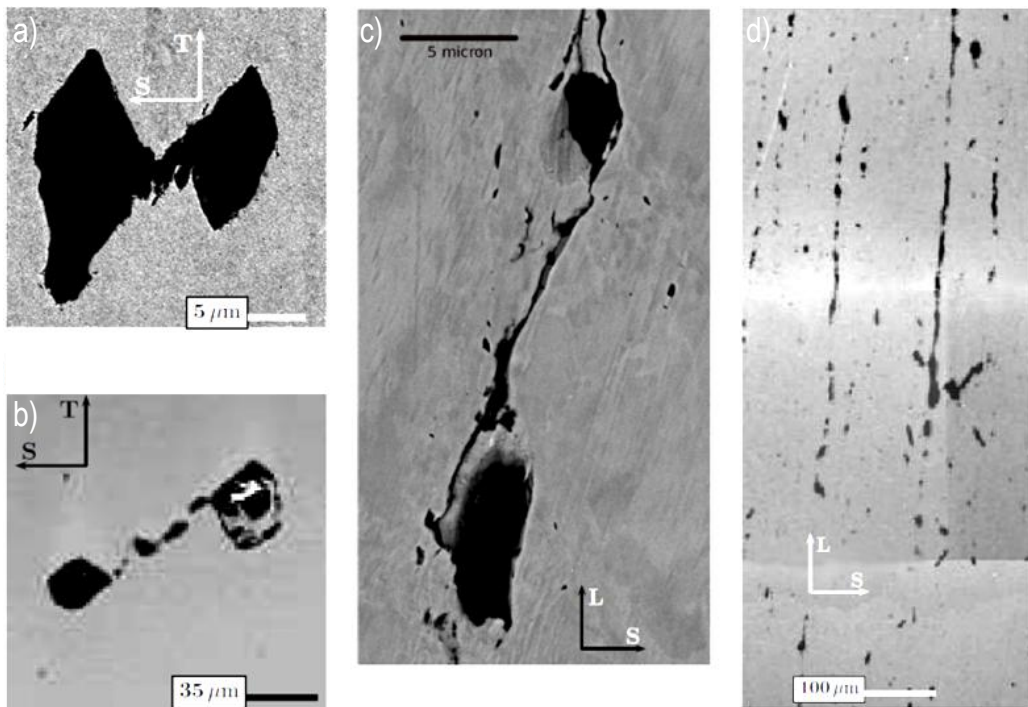


Figure 2-12: Modes of void coalescence within coordinate system aligned in longitudinal- (L), transverse- (T) and short transverse-/thickness-direction (S), a): Internal necking, b/c): coalescence in micro-shear band, d): coalescence in columns, in all pictures, load in vertical direction, a) to c): axisymmetric load, d) plane strain [Ben10]

The formation of voided columns marks the third mode of void coalescence. In steels containing elongated MnS inclusions, it is the most dominant mode. Only a small effect on macroscopic ductility but strong effect of voided columns on micro-delamination was observed by Benzerga et al. [Ben10]. Dunand et al. [Dun14] also described coinciding microcracks in loading direction with the position of Mn and Mo segregation bands.

There is also an interaction of larger and smaller voids. Hancock et al. [Han76] described a significant increase for hole growth-rate adjacent to large holes. This allows larger holes to grow by coalescence of smaller holes. This effect is found to be orientation dependent [Han76]. In comparison to that, larger neighbouring voids tend to link by micro-cracks instead of a complete coalescence.

2.3.4 Bake-Hardening Effect

The materials of the assembled car body undergo a heat treatment during the multi-step paint process. Temperatures of 150 to 200°C for 15 to 30min lead to a short range diffusion of interstitial atoms like carbon or nitrogen. The interstitials diffuse to the dislocation cores, pin the dislocations and hinder their movement. At a certain stress level, dislocations break free and yielding occurs. This effect leads to an increase in yield but not in ultimate tensile strength and is called “bake-hardening effect”. The rising ratio of yield strength to ultimate tensile strength raises the risk of brittle fracture and decreases the deformation capacity [Kan11] and can also generate so-called Lüders-bands [Bal09]. Within these bands a dislocation break free accompanied by local strain bands arises.

The characteristics of the bake-hardening effect depend on the material properties and the manufacturing process. The former include the chemical compositions, the grain size, the volumetric composition, the morphology and the configuration of the phases. The degree of work hardening, also e.g. the position of parts in the assembly, the temperature and the time window during manufacturing process are important manufacturing parameters influencing the bake-hardening effect [Kan11]. The bake-hardening behaviour can also result from the coating process during sheet metal manufacturing, e.g. from hot dip zinc coating. To include the bake-hardening effect into material testing, specimens can undergo a so-called bake-hardening simulation. According to SEP 1240 [SEP06] the specimens have to be exposed to 170°C for 20 minutes with an additional heating-up time less than 7 minutes.

In material testing, the specific material and its pre-straining are the key factors of the bake-hardening effect besides the heat treatment. In some materials there is a strong influence on material behavior, while in other cases, no effect is seen [Lin13]. For a DP600 steel Lindqvist [Lin13] reports a smooth yielding behaviour in all material tests. After pre-straining and baking, there is also no indication on deterioration of ductility [Lin13]. In contrast Kantereit [Kan11] reported on a significant influence of pre-strain and temperature on the mechanical properties of CR180 and DP800 but not of DP1000LCE.

The bake-hardening effect is dependent on the dislocation density, which is affected by plastic straining. To estimate the effect of plastic deformation on the bake-hardening behaviour the base-material with different pre-strains is commonly investigated. In this work “BH” identifies specimens which underwent the bake-hardening simulation to identify the material condition; an affiliated number specifies the pre-strain in percent. The uniaxial pre-strain is commonly applied prior bake-hardening simulation and specimen manufacturing.

3 Experimental Investigation

The focus of the experimental investigation is the orthotropic failure of steel. Three sheet thicknesses (0.6 mm, 1.1 mm and 1.8 mm, from the same manufacturer) of the cold rolled, micro-alloyed, ferritic steel CR340LA and one thickness (1.0 mm) of the full martensitic cold rolled MS1500 are investigated. A standard quasi-static testing procedure is performed for all four materials. For selected specimen types and materials Scanning Electron Microscopy-measurements (SEM) as well as Electron BackScatter Diffraction (EBSD) and Optical Light Microscopy (OLM) investigations are conducted to investigate the microstructure.

3.1 Experimental Results of Quasi-Static Standard Testing

To characterise stress state dependent orthotropic material behaviour, an extensive testing procedure, with initial triaxialities between 0.00 and 0.67, is performed. The testing includes standard tensile as well as notched, shear and biaxial-tension specimens. The geometry of the standard tensile specimens concurs with SEP 1240 [SEP06], exhibiting a gauge length of 50 mm (A50). Notched specimens with 80 mm and 5 mm notch radii (NR80 and NR05) respectively are examined. For shear testing of CR340LA the specimen geometry developed by the voestalpine [Til13] is utilised. Due to the material dependency of shear specimens, an adapted geometry is used for shear testing of MS1500, see [Dub15]. Material properties within biaxial tension are obtained from Bulge-tests. The different specimen geometries are pictured in Figure 3-1.

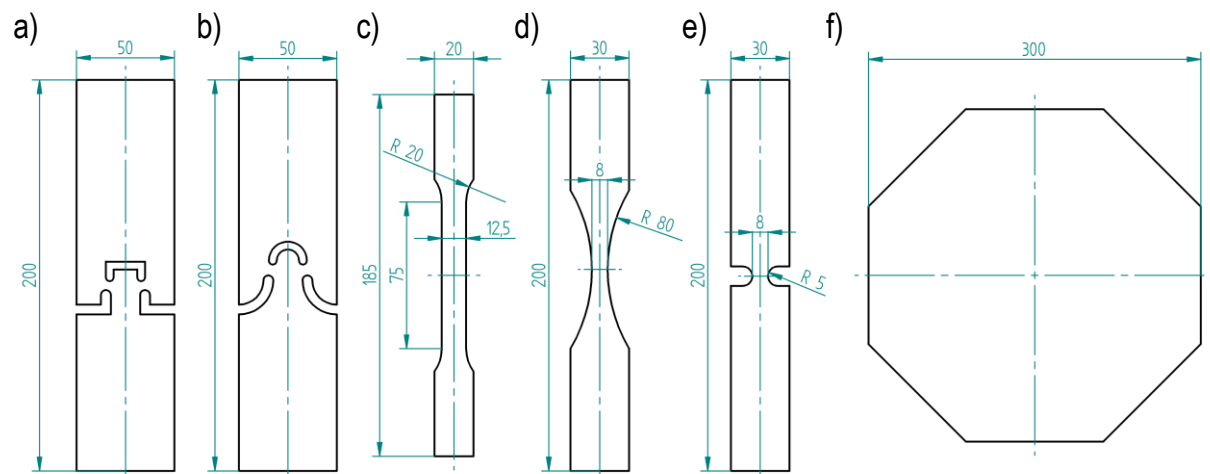


Figure 3-1: Listing of the investigated specimen geometries: a) Shear Double Radius (SDR) specimen [Dub15], b) VOEST-double-shear specimen [Til13], c) standard tension with a parallel length of 75 mm and a gauge length of 50 mm (A50), d) 80 mm notch radius (NR80), e) 5 mm notch radius (NR05), and f) Bulge-test

To receive material properties in a crash relevant material condition, all specimens undergo the so-called bake-hardening simulation. The heat treatment is performed according to SEP 1240 [SEP06] at 170°C for 20 minutes with additional 5 minutes heating-up time prior to specimen machining. All specimens (except for Bulge-testing) are manufactured by electro spark machin-

ing with a roughness of 6.3 μm of the cutting edges. Due to the insensitivity of the Bulge-test on the roughness of its cutting edges, no separate manufacturing steps of the Bulge-specimens are conducted.

Except for biaxial tension, all tests are executed at an Instron 5585 tensile testing machine. According to SEP 1240 [SEP06] the strain rate is set to 0.4 %/s in relation to the specimen gauge length. For the 50 mm gauge length of A50 tensile specimens, this results in a velocity of 0.2 mm/s and is adapted for shear and notched specimens. Biaxial tension is realised by Bulge-tests (100 mm diameter), which are performed at a “Profipress 160T” press. As medium a metal forming gel is used. Besides the pressure of the forming gel, surface strains as well as the surface displacements are measured. All surface strain measurements are processed with a sample frequency of 10Hz by the Digital-Image-Correlation-System (DIC-System) ARAMIS 4M from the GOM GmbH. To compute the local surface strains the ARAMIS V6.3.1 software is utilised, applying a facet size of 0.5 mm x 0.5 mm for all specimens.

To capture orthotropy experimentally the specimens are aligned in steps of 22.5° from 0° to 90° with respect to rolling direction except for shear and biaxial tension. For shear specimens the local loading direction differs from specimen orientation. In biaxial tension the investigation of different specimen orientations is obsolete. Besides material parameters, for example Young's Modulus or Poisson-Number, the force-displacement data and the local strain behaviour is investigated. The latter is obtained at failure point within the Cartesian specimen coordinate system. In it the y-direction is aligned in tensile direction; the x-direction marks the specimen transverse and the z-axis is aligned in specimen thickness direction. Furthermore, the characteristic results are coloured dependent on the specimen orientation in cyan (-45° to RD), purple (0° to RD), blue (22.5° to RD), green (45° to RD), orange (67.5° to RD) and red (90° to RD). Additionally, coloured beams mark the scattering of the displacements at material failure of specimens in 0°, 45° and 90° to RD.

3.1.1 CR340LA PB 0.6 mm

In this section, the experimental results of the investigated CR340LA with a sheet thickness of 0.6 mm in bake-hardening condition are displayed. In Table 3-1 the basic material parameters, obtained from standard tensile tests from 0° to 90° with respect to RD, are presented. Beside isotropic elasticity, only minor variations of the Lankford-Coefficient or UTS are observed. Only the yield strength varies from 0° (421 MPa) to 90° (442 MPa) considerably.

Table 3-1: Mechanical properties obtained from standard tensile tests of CR340LAPB 0.6 mm

Parameter	0°	22.5°	45°	67.5°	90°
Youngs Modulus [GPa]	202	210	208	211	208
Poisson-Number	0.29	0.30	0.29	0.29	0.31
Yield Strength [MPa]	421	425	435	439	442
UTS _{tech} [MPa]	462	466	467	465	464
Ratio YS / UTS _{tech}	0.91	0.91	0.93	0.94	0.95
UTS _{true} [MPa]	529	531	534	533	532
Lankford-Coefficient R	0.91	0.90	0.90	1.04	1.07

In Figure 3-2 the force-displacement behaviour of standard tensile specimen is presented in all five investigated directions. All tests reveal a distinct yield point followed by Lüders-strains. These strain-bands form at local technical strains of 4.5 % in 0° and 5.4 % in 90° to RD respectively measured by DIC. The different Lüders-strain levels lead to differing displacements during Lüders-band development. These displacements range from 2.2 mm in 0° to 2.7 mm in 90° direction. The distinct yield point, which marks the beginning of the Lüders-Effect, varies within 3.2 kN in 0° and 3.5 kN in 90° to RD. The force levels during Lüders-band development groups into about 3.0 kN (0° and 22.5° direction) and about 3.1 kN (45°, 67.5° and 90° orientation).

Disregarding the distinct yield point, all directions exhibit a maximum force of 3.3 kN. Dependent on the specimen orientation, it is reached at 6.5 mm ± 0.2 mm (90° to RD), 7.2 mm ± 0.2 mm (45° and 6.5° to RD) and 8 mm ± 0.1 mm (0° and 22.5° to RD). Besides the displacements at UTS, the fracture displacements deviate from the specimen orientation. The highest displacement is detected in 0° direction with 13.0 mm, whereas specimens in 22.5° direction fail at displacements of 12.7 mm. Lower displacements of around 12.0 mm are measured in 45° and 67.5° to RD. The lowest displacements of 11.5 mm arise in 90° orientation.

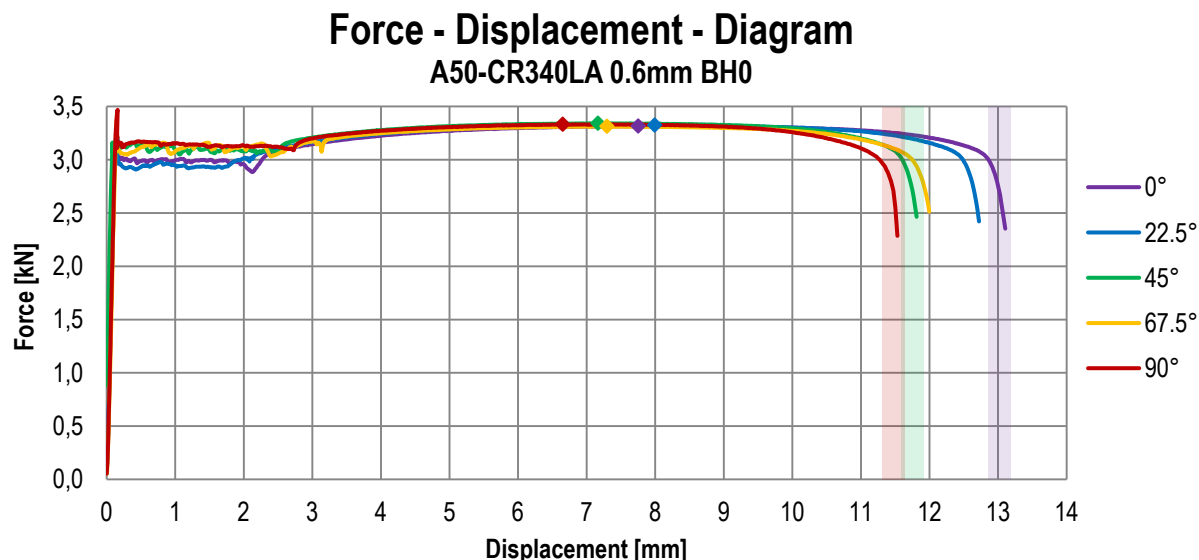


Figure 3-2: Force-Displacement diagram for A50 specimens of CR340LA in 0.6 mm sheet thickness in bake-hardening condition

The force displacement data of NR80 specimens are pictured in Figure 3-3. As seen for standard tensile specimen, the notched specimens also exhibit a distinct yield point with subsequent development of Lüders-strains. All investigated specimens demonstrate an equal maximum force of 2.3 kN, as previously seen for standard tensile specimens. Despite the equal force maximum, a clear orientation dependency in displacements at maximum force is observed within a range of 0.5 mm, with a maximum at 0° (2.5 mm ± 0.1 mm) and a minimum at 67.5° and 90° to RD (2.0 mm ± 0.1 mm). This clear orientation dependency is also monitored at material failure. Only specimens in 67.5° to RD show lower displacements. Moreover, all specimens fail at nearly 1.9 kN.

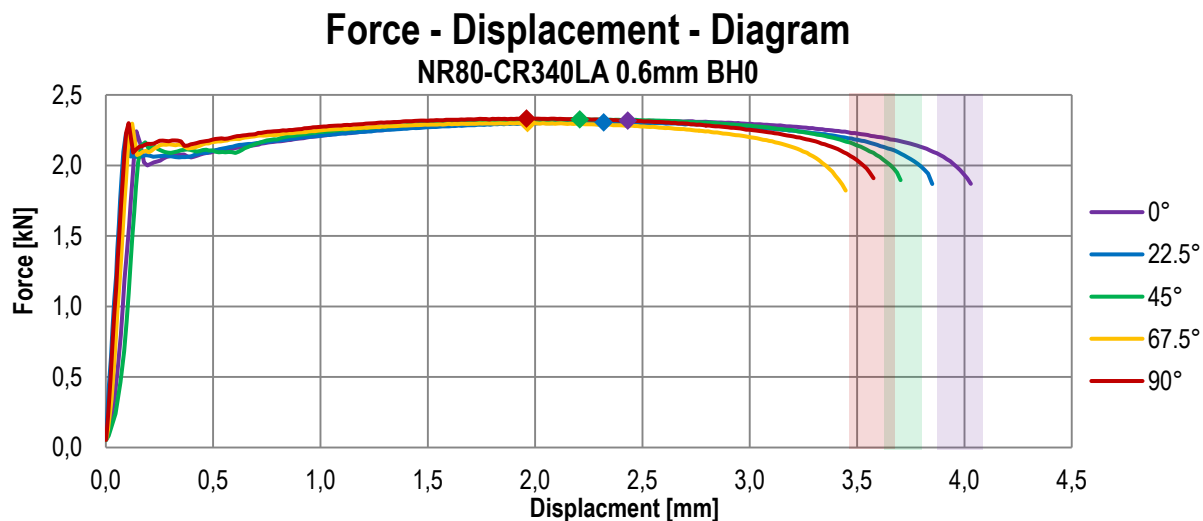


Figure 3-3: Force-Displacement diagram for NR80 specimens of CR340LA in 0.6 mm sheet thickness in bake-hardening condition

The force displacement diagrams of the NR05 specimens are displayed in Figure 3-4. All examined directions show a distinct yield point but only weakly developed. Due to the strain concentration in the notch, developing Lüders-bands were not observed if only at the arising distinct yield point. As previously witnessed for A50 and NR80 specimens an equal maximum force is measured yet at differing displacements. The force-maximum arises at 0.70 mm for all directions except in 0° in which 0.80 mm are measured. Moreover the displacements up to fracture range from 1.4 mm (0°) to 1.25 mm (90° to RD).

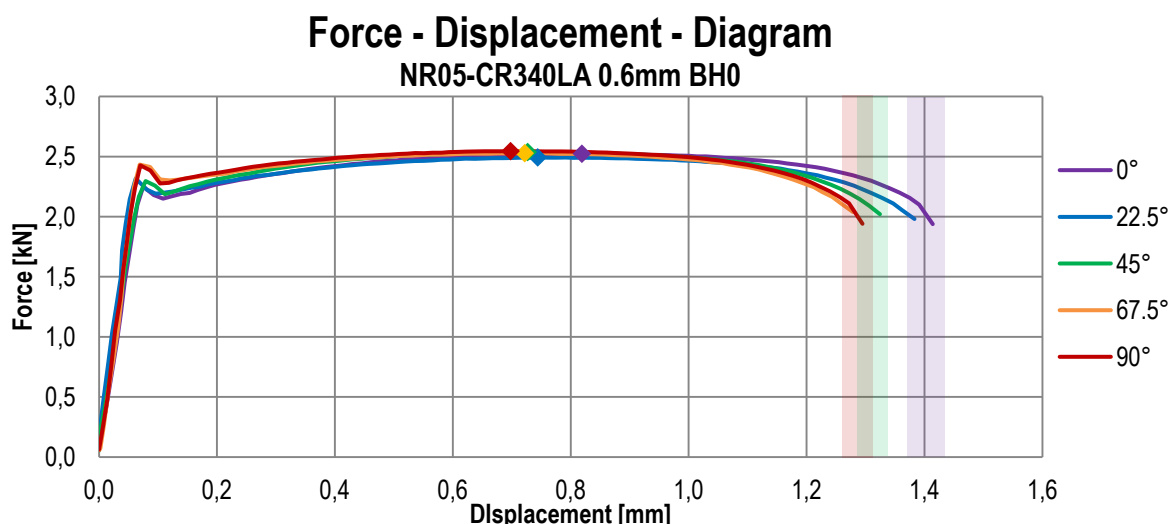


Figure 3-4: Force-Displacement diagram for NR05 specimens of CR340LA in 0.6 mm sheet thickness in bake-hardening condition

In Figure 3-5 the relative force-displacement behaviours beyond force-maximum of A50 in a), NR80 in b) and NR05 specimens in c) are depicted. The displacements as well as the force-level are related to the force maximum. Except for uniaxial tension, both notched specimen-types lead to similar relative force-displacement curves for all directions. Only uniaxial tension specimens in 0° to RD deviate from the behaviour in all other directions beyond UTS.

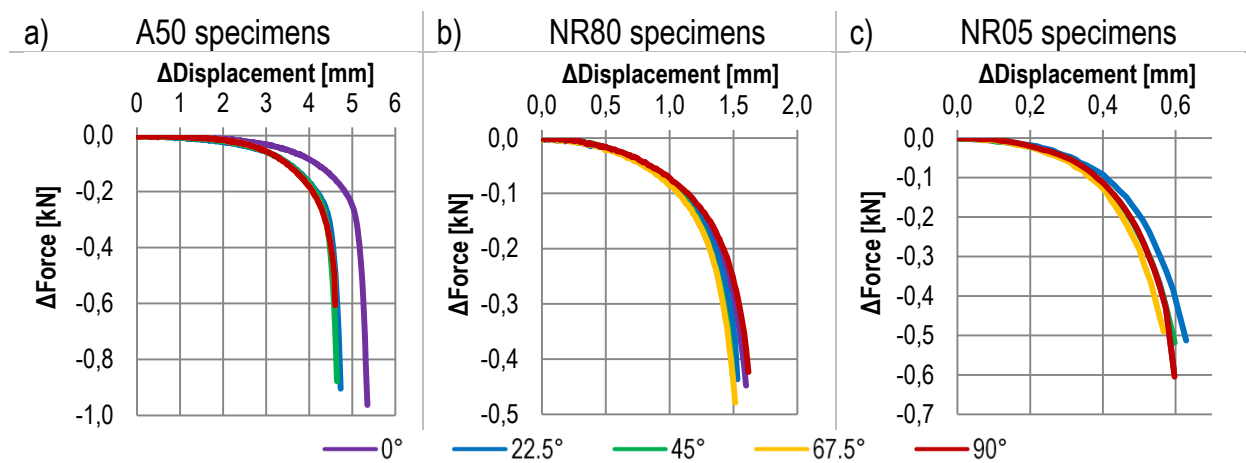


Figure 3-5: Post-UTS-behaviour obtained from CR340LA 0.6 mm obtained of a) A50, b) NR80 and c) NR05 specimens, represented as force- and displacement difference related to UTS

No valid shear tests could be performed for the CR340LA in 0.6 mm sheet metal thickness. Different shear specimen geometries were investigated but all buckled during loading. Buckling results from pressure stresses within the gauge area during shear loading in combination with a low geometrical moment of inertia due to low sheet thickness and high local strains. A specimen geometry that did not buckle could not be identified for this sheet thickness.

Finally, Figure 3-6 pictures the result of the Bulge-test for the 0.6 mm sheet thickness. Failure arises at dome displacements of 31 mm and a pressure of 8.0 MPa. In contrast to previously investigated flat tensile tests, no pronounced decrease in pressure indicates material failure.

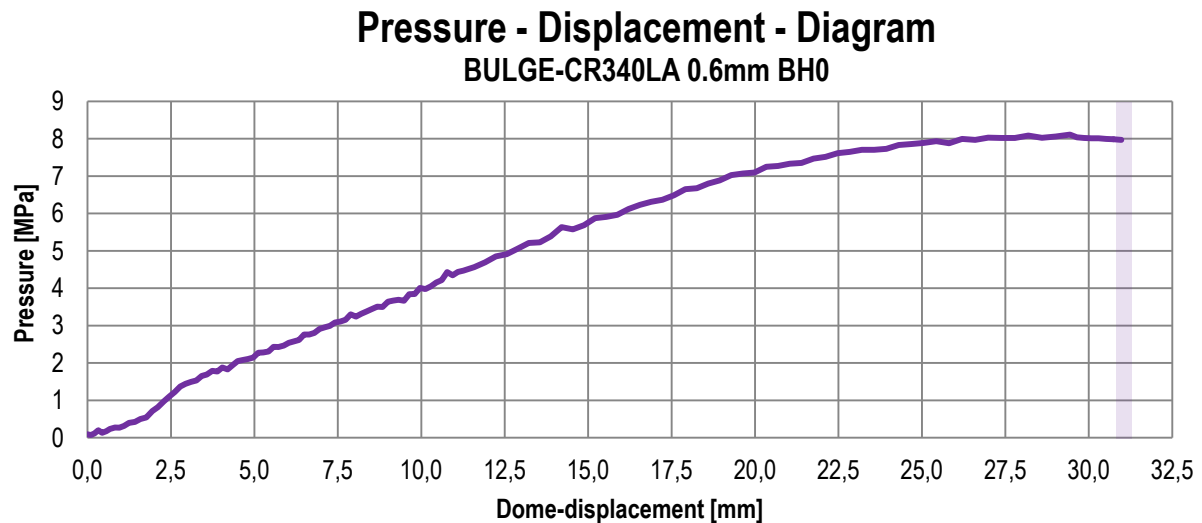


Figure 3-6: Pressure-Displacement-Diagram obtained from Bulge-test of CR340LA with a sheet thickness of 0.6 mm in bake-hardening condition

Table 3-2 presents the true equivalent strains at failure for all examined specimen types and orientations revealing only minor orthotropic effects. For standard tensile and NR80 specimens no orientation dependency is observed. Only specimens with 5 mm notch radius show orthotropy with a minimum in equivalent strains at failure in 0° with 0.41 and a maximum in 45°

with 0.55. Regarding biaxial testing, equivalent strains of 0.77 are received, which is similar to results obtained from standard tension specimens.

Table 3-2: True equivalent failure strains for the investigated specimen types for CR340LA PB 0.6 mm

Specimen	0°	22.5°	45°	67.5°	90°
A50	0.75	0.77	0.73	0.75	0.74
NR80	0.67	0.66	0.65	0.66	0.66
NR05	0.41	0.49	0.55	0.54	0.52
Bulge			0.77		

3.1.2 CR340LA PB 1.1 mm

The CR340LA with a sheet thickness of 1.1 mm is further investigated, including the bake-hardening condition BH0. Its mechanical properties, obtained from standard tensile tests, are presented in Table 3-3. The tests show a variation of the Lankford-Coefficient, the yield and the ultimate tensile strength. The Lankford-Coefficient varies within a range of 0.85 to 1.21; its maximum of 1.21 is observed in 45° direction. Hence, the plastic strains in width direction are dominant compared to thickness strains. The Lankford-Coefficients in 0° and 22.5° to RD are lower than 1. Consequently, the plastic strains in thickness direction are dominant. In 67.5° and 90° direction nearly isotropic plastic strain behaviour is monitored.

Table 3-3: Mechanical properties obtained from standard tensile tests of CR340LAPB 1.1 mm

Parameter	0°	22.5°	45°	67.5°	90°
Youngs Modulus [GPa]	208	211	214	207	210
Poisson-Number	0.30	0.300	0.30	0.30	0.30
Yield Strength [MPa]	389	406	412	414	416
UTS_{tech} [MPa]	457	455	448	460	466
Ratio YS / UTS_{tech}	0.85	0.89	0.92	0.90	0.89
UTS_{true} [MPa]	526	519	517	527	535
Lankford-Coefficient R	0.87	0.85	1.21	1.08	1.06

Figure 3-7 pictures the force-displacement data of standard tensile tests (A50). They reveal orthotropy of yield strength, UTS and displacements up to failure. The steels exhibit a distinct yield point followed by the development of Lüders-bands, which arise up to about 1.5 mm. The force-level remains constant during Lüders-band developement with the lowest level in 0° (about 5.2 kN) and the highest in 90° to RD with about 5.7 kN. The force at Lüders-strains is staggered from 0° to 90°, 5.4 kN occur at 45° specimens.

A nearly similar maximum in force, resulting in equivalent UTS, is obtained for specimens from 0° to 45°, which occurs at a displacement of about 8.0 mm ± 0.2 mm. Elevated UTS are measured in 67.5° and 90° with a more clear increase of the latter, comming along with a decrease in specimen elongations at UTS with 7.5 mm ± 0.2 mm in 67.5° and 7.2 mm ± 0.2 mm in 90°. The displacements up to fracture are spread from 13.0 mm to 14.1 mm with the lowest

displacements arising for specimens in 0° to RD. Despite the same displacement at UTS the 45° direction exhibits the highest displacements at fracture with 14.1 mm. In addition, A50 specimens in 90° to RD show an elongation of 13.7 mm at fracture.

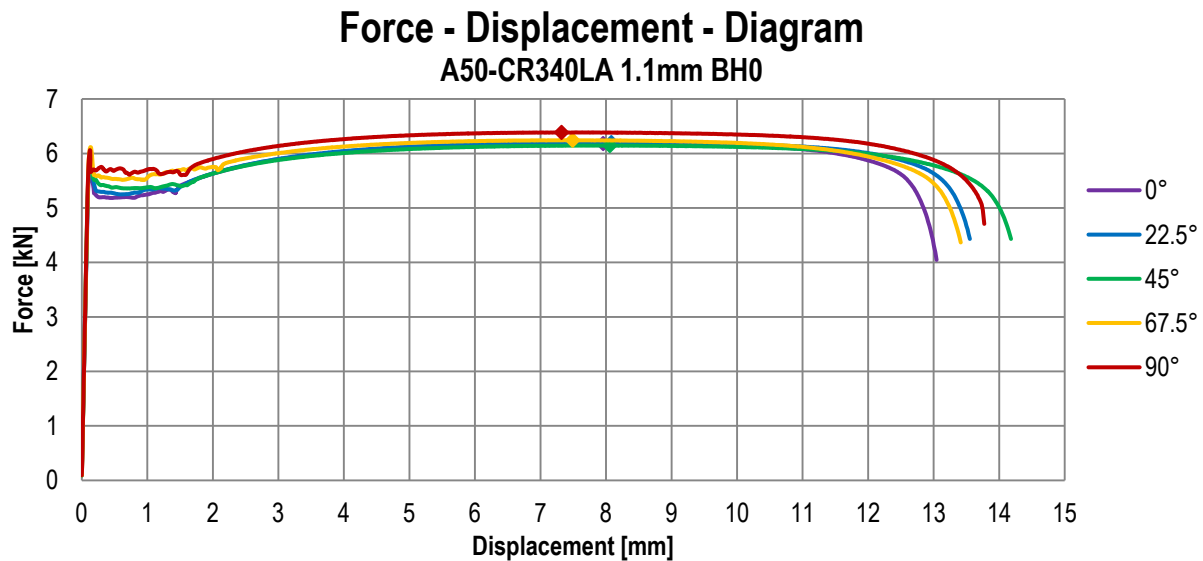


Figure 3-7: Force-Displacement diagram for A50 specimens of CR340LA in 1.1 mm sheet thickness in bake-hardening condition

Figure 3-8 depicts the force-displacement behaviour of flat tensile specimens with 80 mm notch radius. The tests reveal similar behaviour as seen by A50 tensile specimens. Moreover, all specimens exhibit an extremely pronounced distinct yield point which represents the maximum force in 45° to 90° to RD. For 0° and 22.5° direction the distinct yield point is only slightly lower than the maximum force. With disregard to the distinct yield point, the force-maximum is observed with 4.1 kN in 45° and 4.2 kN in 90° to RD. The maxima in 0° and 22.5° to RD arise at $2.4 \text{ mm} \pm 0.1 \text{ mm}$, for the other directions at $2.1 \text{ mm} \pm 0.1 \text{ mm}$.

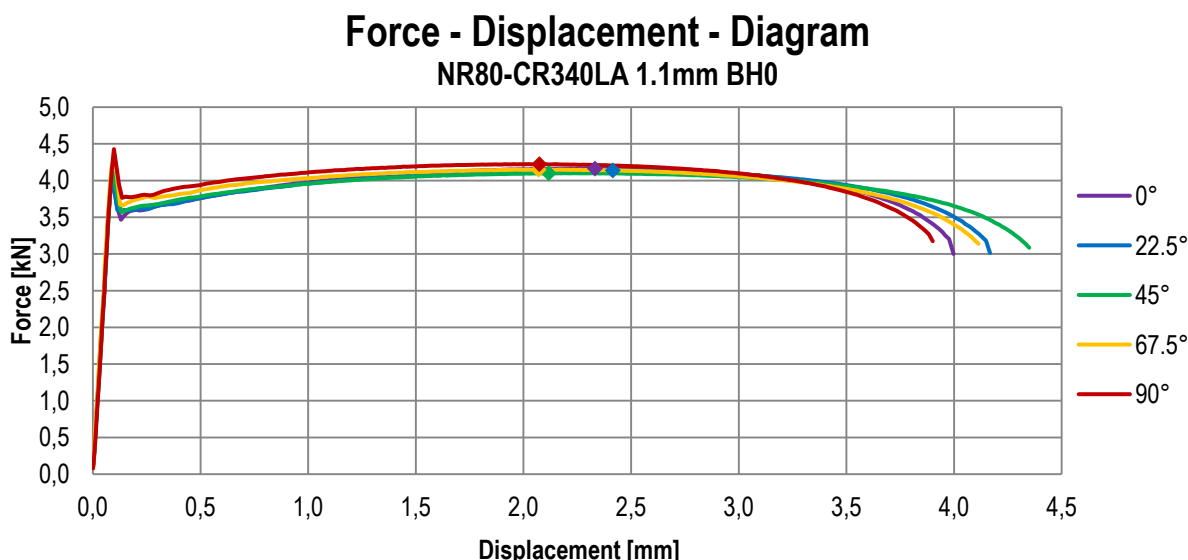


Figure 3-8: Force-Displacement diagram for NR80 specimens of CR340LA in 1.1 mm sheet thickness in bake-hardening condition

This shift towards lower displacements can be related to the distinct yield point overshooting the force-maximum. It limits the plastic deformation in combination with the specimen geometry to a narrower area in loading direction than in 0° or 22.5° to RD.

The displacements at failure range from 3.8 mm in 90° to 4.3 mm in 45° direction. No dependence of the displacements at failure and those at force maximum is witnessed. Opposing the results obtained in 0° and 90° to RD, similar displacements at failure are obtained despite varying deflections at maximum force. Moreover the 45° direction demonstrates the highest failure displacements as well as low ones at force maximum compared to specimens aligned in 0° to RD.

The force displacement behaviour of notched specimen with a radius of 5 mm is displayed in Figure 3-9. The tests reveal a distinct yield point but less pronounced as previously seen for NR80 specimens. NR05 specimens in 0° to 45° show the same maximum force and additionally the same specimen elongation. A slight increase in force maximum is observed in 67.5° and 90°, which goes along with decreasing displacements. All specimens exhibit nearly similar specimen elongations at failure with 1.70 mm. Only 90° specimens show slightly decreasing fracture displacements with 1.55 mm.

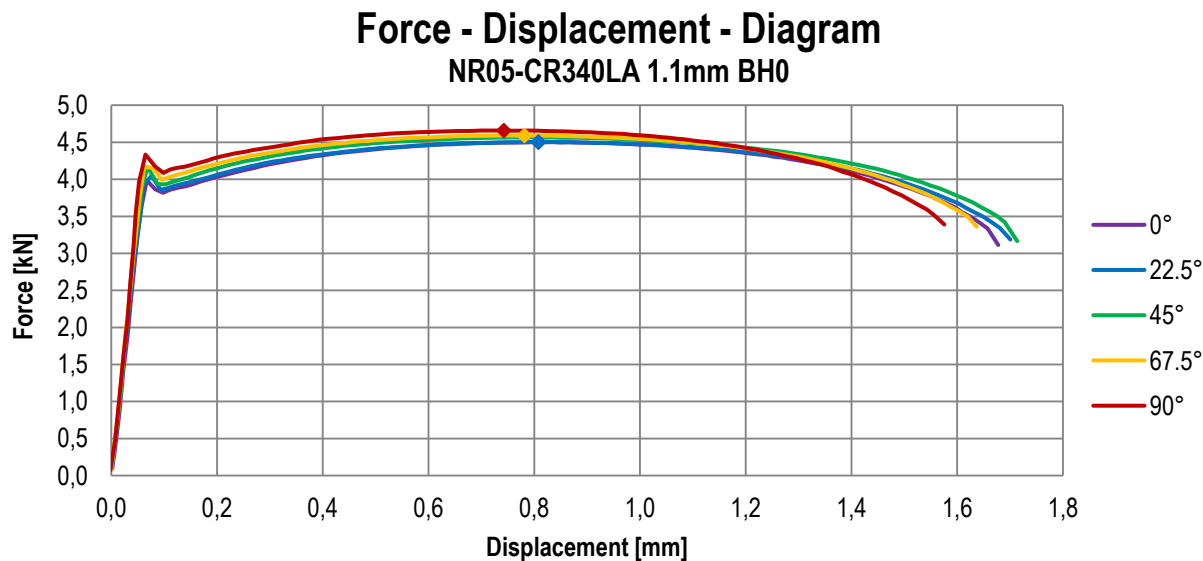


Figure 3-9: Force-Displacement diagram for NR05 specimens of CR340LA in 1.1 mm sheet thickness in bake-hardening condition

The post-force-maximum behaviour of standard tensile as well as the investigated notched specimens is presented in Figure 3-10. Regarding A50 specimens, a spread of 1.5 mm between 0° and 90° to RD is detected. In contrast to that, the force-displacement behaviour of NR80 specimens ranges from 1.6 mm to 2.2 mm, however, now between 0° and 45° direction. For specimens with a 5 mm notch radius nearly no orientation dependent deviations are measured.

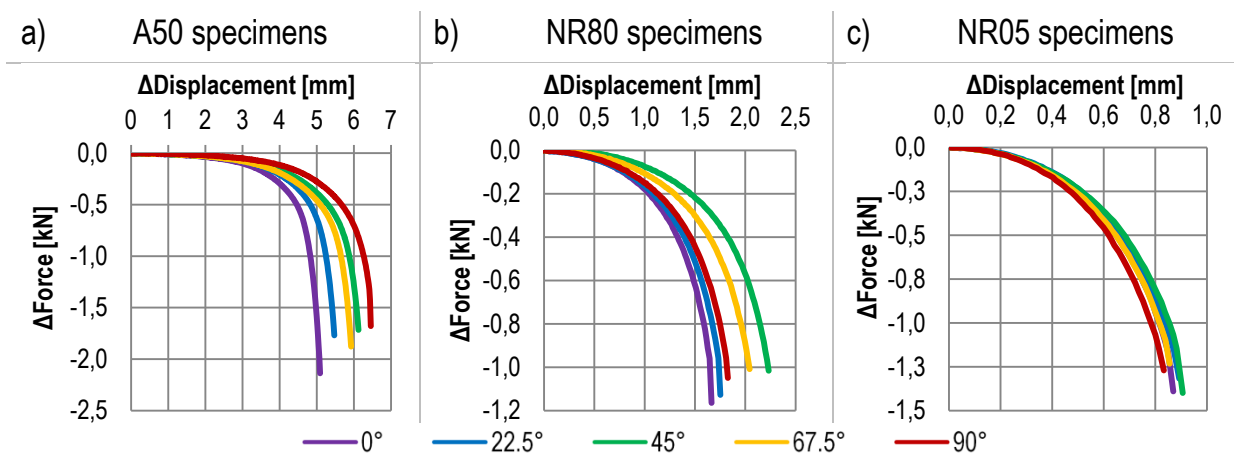


Figure 3-10: Post-UTS-behaviour obtained from CR340LA 1.1 mm obtained of a) A50, b) NR80 and c) NR05 specimens, represented as force- and displacement difference related to UTS

Figure 3-11 presents the force-displacement data of voest-shear specimens aligned in -45° to 90° with respect to RD. The displacements mirror the elongation between two points in the middle of the specimen, 25 mm below and above the shear sections. As previously seen, yielding is marked for all directions by a distinct yield point, but is observed to be less pronounced than for other investigated flat tensile specimens. Up to a displacement of 4.0 mm all directions show equal force-displacement behaviour. Beyond that, the force level of specimens in -45° as well as $+45^\circ$ to RD begins to decrease. Furthermore, the force-displacement curves of specimens aligned in 0° and 90° begin to deviate from each other at displacements of 4.2 mm. As a result, similar displacements (5.8 mm) at fracture are observed for specimens in $\pm 45^\circ$ direction as well as for specimens in 90° to RD. Contrasted to that, specimens in 0° direction show displacements of 6.4 mm up to fracture. A more detailed investigation based on the surface strain fields of the voest-shear specimens for CR340LA in 1.8 mm sheet thickness is conducted in chapter 3.5.

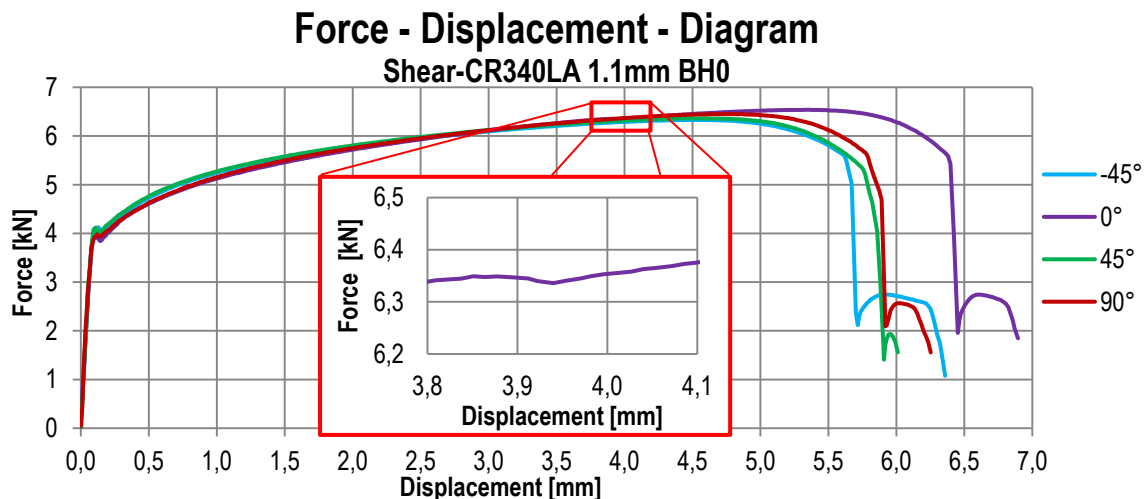


Figure 3-11: Force-displacement curves for shear specimens with voest geometry of CR340LA with 1.1 mm and in bake-hardening condition

Regarding the force-displacements in 0° direction, a kink can be found between 3.9 mm and 4.0 mm displacement. This peculiarity only arises for 0° specimens with a sheet thickness of 1.1 mm. The investigated shear specimens, aligned in 0° to RD, prove the highest displacements up to fracture but also the maximum force. Moreover, the lowest yield strength is obtained for uniaxial tension specimens in 0° to RD: The combination of elevated maximum force in 0° in comparison to the relatively low yield strength in 0° leads to plastic deformation of the tongue between both shear sections. As a result, a kink within the force-displacement diagram can be observed.

Figure 3-12 depicts the result of the conducted Bulge-test. It pictures the pressure of the Bulge-gel dependent on the dome displacement. The maximum pressure of 14.3 MPa is reached at dome displacements of 30 mm. At a displacement of 34.5 mm material failure is observed at a pressure of 13.7 MPa. It leads to a crack which does not start at the dome but is orientated in rolling direction. The crack orientation is investigated in detail in chapter 3.1.3.

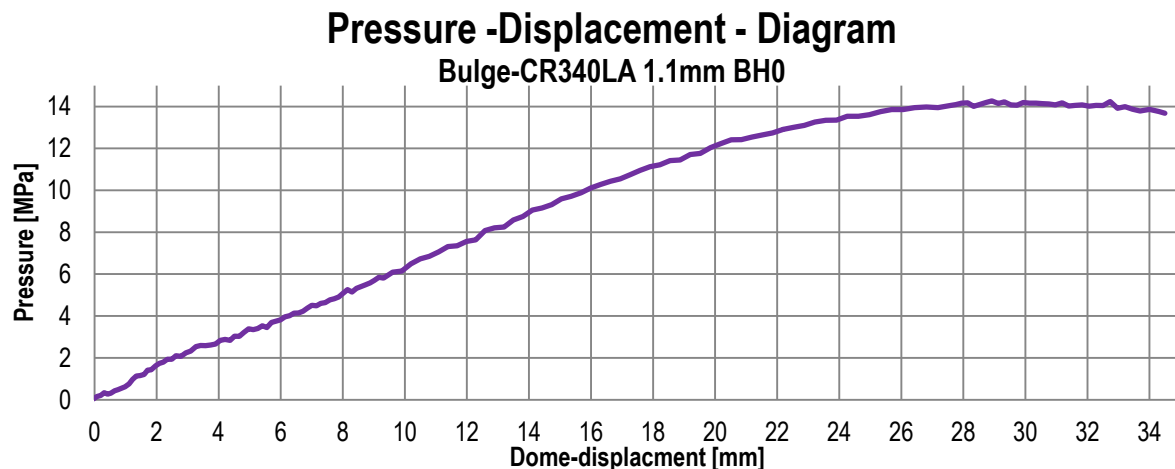


Figure 3-12: Pressure-Displacement-Diagram obtained from Bulge-test of CR340LA with a sheet thickness of 1.1 mm and in paint-bake condition

Figure 3-13 displays the local strain paths (major vs. minor strain) within the failure zone of all investigated specimen types. For a better overview only the specimens aligned in 0° to RD are shown. All specimens exhibit a linear strain path at the beginning of loading. Under subsequent loading all specimens tend to deviate from linear strain behaviour. For double shear specimens the strain paths of both shear sections are included. SHEAR 0° -1 names the cross section which fails first. The remaining cross section calls SHEAR 0° -2. Both cross sections SHEAR 0° -1 and SHEAR 0° -2 show deviating strain paths with the onset of loading with a more pronounced deviation from a linear strain path at SHEAR 0° -1. In contrast to that, both cross sections demonstrate similar major strains up to failure.

Additionally the strain paths of A50, NR80 and NR05 specimens are pictured, proving a clear trend towards the plane strain stress state ($\varepsilon_2 = 0$). The maximum principle strains portray their dependency on the stress triaxiality: the higher the triaxiality, the lower the failure strains. For biaxial tension, two strain paths have to be considered: one at failure point and one at the dome. The dome exhibits nearly biaxial tension with no deviation from linear strain behaviour. In

contrast to that, the onset of loading also leads to a biaxial strain path showing decreasing minor strains with subsequent loading.

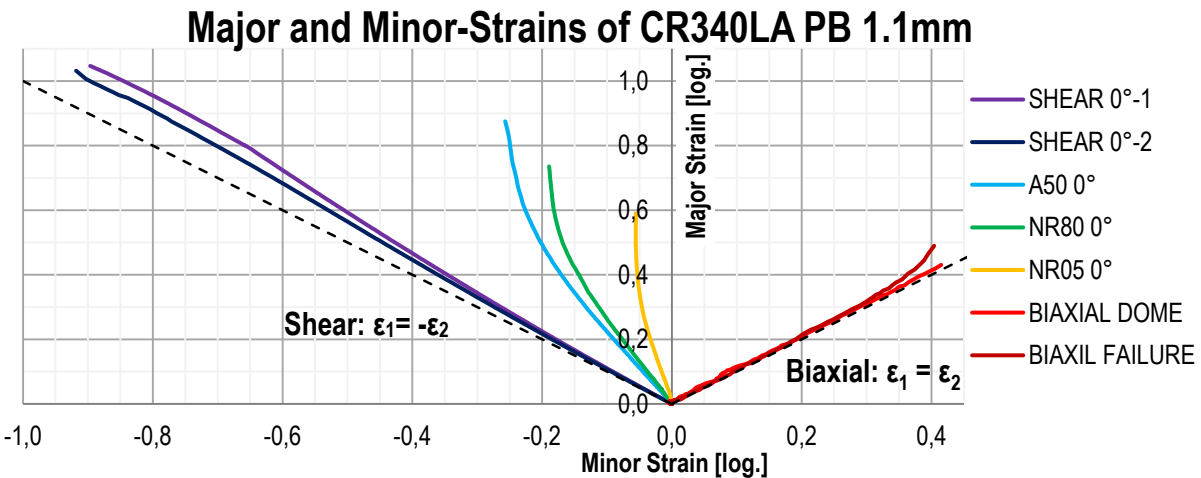


Figure 3-13: Local strain behaviour of all investigated specimen types with orientation of 0° to RD within the failure zone, SHEAR 0°-1 defines the cross section where failure of shear specimens begins. The local strains for Bulge-testing subdivide into behaviour at the dome (BIAXIAL-DOME) and failure point (BIAXIAL FAILURE). Additionally, the strain paths of A50, NR80 and NR05 specimens are displayed.

The local strain behaviour within the fracture zone of A50, NR80 and NR05 specimens in 0°, 45° and 90° to RD is presented in Figure 3-14, displaying the local strains in specimen transverse dependent on the strains in specimen longitudinal direction. For all specimen types the 45° direction shows the highest longitudinal as well as transverse strains.

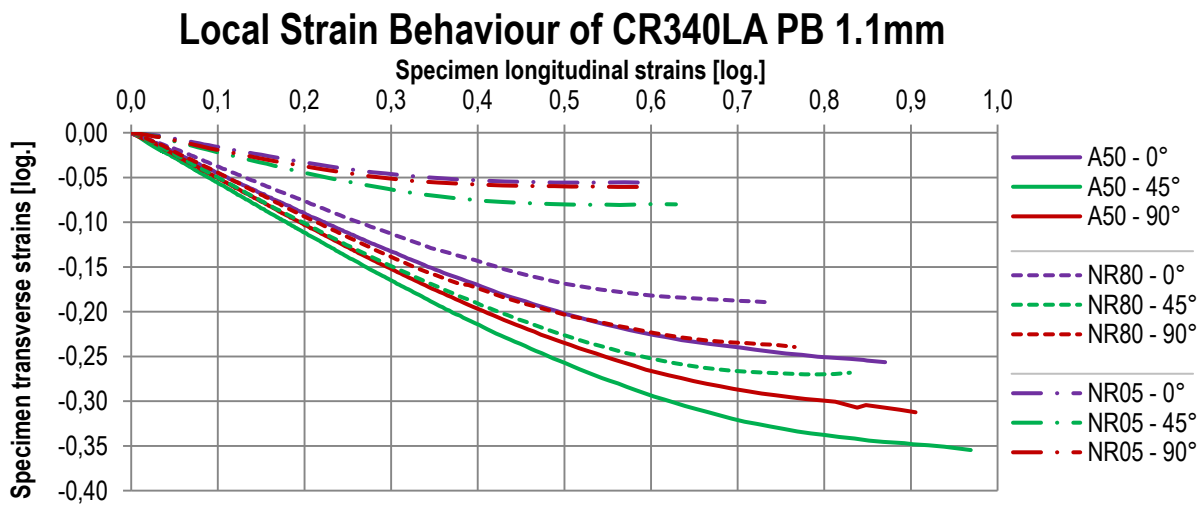


Figure 3-14: Comparison of local strain behaviour in specimen longitudinal and transverse direction of A50 (straight), NR80 (dashed) and NR05 (dash dotted) in 0°, 45° and 90° to RD

In comparison to that, the lowest strains in specimen transverse and longitudinal direction are measured in 0° direction. Specimens in 90° to RD exhibit a strain path in between both. With increasing initial stress triaxiality the strain behaviour equals within the fracture zone. All specimens show a linear strain path at the beginning of loading. Beyond force-maximum a deviation

from linear strain path with decreasing transverse strains is observed. It has to be mentioned that the force-maximum point does not mark the beginning of deviation. Complementary to the decrease of transverse strains, an increase of strains in specimen thickness direction is found.

The linear strain behaviour can also be expressed for standard tensile specimens by the Lankford-Coefficient, which can be understood as resistance to thinning [Tas09],[Bee10],[Kan13]. Regarding the different specimen types as well as the different directions, thinning is indicated as limiting factor for straining. This limit does not only vary with the material but also with the specimen direction.

The true equivalent strains at failure for CR340LA in 1.1 mm sheet thickness are presented in Table 3-4. For all shear specimens, comparable failure strains are obtained. Even though the investigated shear specimens in 0° to RD exhibit the maximum displacements, its failure strains are not elevated. Regarding A50, NR80 and NR05 specimens the 45° direction exhibits the highest equivalent failure strains, whereas 0° and 90° behave similarly. Moreover, the observed failure strains in biaxial tension (0.85) are alike to those obtained in uniaxial tension in 0° to RD (0.87).

Table 3-4: True equivalent strains for the investigated specimen types for CR340LA PB 1.1 mm

Specimen	0°	22.5°	45°	67.5°	90°
Shear	1.12	-	1.19	-	1.20
A50	0.87	1.03	1.05	1.03	0.91
NR80	0.80	0.90	0.89	0.88	0.81
NR05	0.69	0.67	0.70	0.67	0.67
Bulge			0.85		

3.1.3 CR340LA PB 1.8 mm

The results of CR340LA with a sheet thickness of 1.8 mm are presented in this section. Besides isotropic elastic properties, mild orthotropic plastic behaviour is detected. The maxima of the yield strength and the UTS are measured at specimens aligned in 90° direction. The lowest strengths are observed at 0° to RD. The calculated Lankford-Coefficients reveal the highest value of 1.18 in 90° to RD. Nearly similar *R*-values are obtained in 0° and 45° direction with 0.93 and 0.96. The ratio of yield and technical ultimate strength indicates the highest hardening potential in rolling (0°) whereas the lowest is observed in transverse direction (90°).

Table 3-5: Mechanical properties obtained from standard tensile tests of CR340LAPB 1.8 mm

Parameter	0°	22.5°	45°	67.5°	90°
Youngs Modulus [GPa]	207	210	206	210	211
Poisson-Number	0.30	0.30	0.31	0.29	0.31
Yield Strength [MPa]	368	375	406	415	420
UTS_{tech} [MPa]	453	460	474	471	463
Ratio YS / UTS_{tech}	0.81	0.82	0.86	0.88	0.91
UTS_{true} [MPa]	516	525	533	532	529
Lankford-Coefficient R	0.93	0.94	0.96	1.11	1.18

Figure 3-15 displays the experimental force-displacement curves of the standard tensile test. All specimens exhibit a distinct, but weakly pronounced, yield point. Furthermore, specimen behaviour up to maximum force groups into 0° to RD and 90° to RD equivalent behaviour. Whereas 0° and 22.5° specimens show Lüders-bands up to 0.8 mm all other directions demonstrate the development of Lüders-bands up to 1.3 mm. These bands develop for specimens in 45° to 90° orientation at forces of 8.7 kN in contrast to 8.0 kN in 0° and 22.5° direction. The force maxima behave similarly with 9.5 kN (0° to RD) and 10.0 kN (90° to RD) respectively. Regarding the displacements at UTS, they reveal related values of $7.5 \text{ mm} \pm 0.2 \text{ mm}$ for all specimens between 0° and 67.5° to RD. In contrast to that, the ultimate tensile strength arises at $7.0 \text{ mm} \pm 0.2 \text{ mm}$ for specimens aligned in 90° direction. Material failure occurs at displacements of 13.7 mm for all directions except for 90° direction: These specimens exhibit a significantly lower displacement at fracture with 12.5 mm.

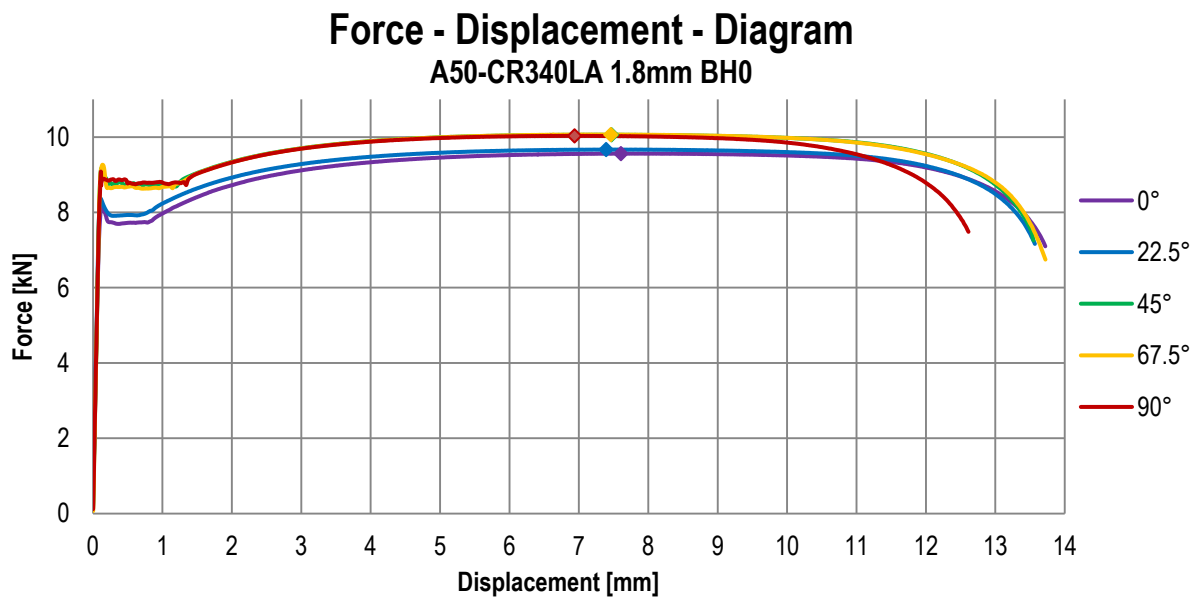


Figure 3-15: Force-Displacement diagram for A50 specimens of CR340LA in 1.8 mm sheet thickness in bake-hardening condition

The force-displacement results of NR80 specimens are pictured in Figure 3-16. All specimens prove a distinct yield point at force levels of 5.8 kN (0° to RD) up to 6.3 kN (90° to RD). The onset of yielding is not accompanied by the development of Lüders-bands at the specimen surface. Moreover, all specimens show a similar force maximum of 6.5 kN except in 90° with 6.7 kN. The force maxima are measured at displacements between $2.2 \text{ mm} \pm 0.1 \text{ mm}$ (45° to 90° to RD) and $2.4 \text{ mm} \pm 0.1 \text{ mm}$ (0° to RD). A nearly similar spread of displacements at failure is observed between 4.35 (67.5° to RD) and 4.55 mm (0° to RD).

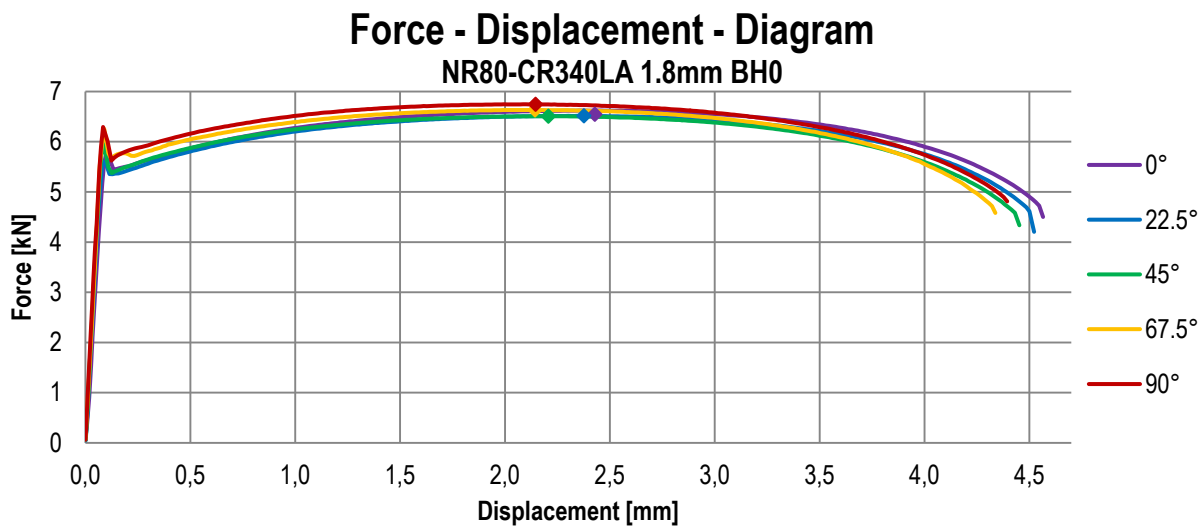


Figure 3-16: Force-Displacement diagram for NR80 specimens of CR340LA in 1.8 mm sheet thickness in bake-hardening condition

Figure 3-17 displays the force-displacement curves of the investigated NR05 specimens. Like in all previous tests, a peak at the force-displacement curves is measured at the transition from elastic to elasto-plastic behaviour. The maximum force of all directions is observed at 67.5° as well as 90° to RD with 7.6 kN. For other specimens 7.3 kN are scaled. The force maxima arise at displacements of 0.8 mm for all directions, except in 0° in which 0.9 mm are measured. Regarding the displacements at fracture, they reveal a maximum of 2.1 mm at 0° to RD with a transition to 1.9 mm in 90° direction.

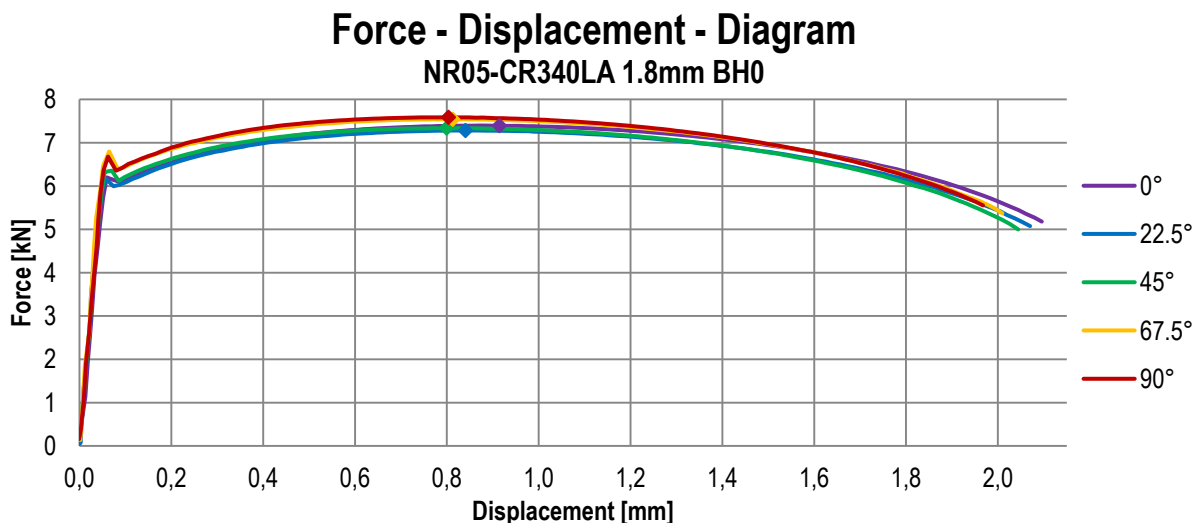


Figure 3-17: Force-Displacement diagram for NR05 specimens of CR340LA in 1.8 mm sheet thickness in bake-hardening condition

The relative force-displacement behaviour beyond force maximum for CR340LA in 1.8 mm sheet thickness is pictured in Figure 3-18. All regarded specimen types exhibit nearly no variation beyond force maximum. Only standard tensile specimens in 90° to RD show slightly earlier decrease.

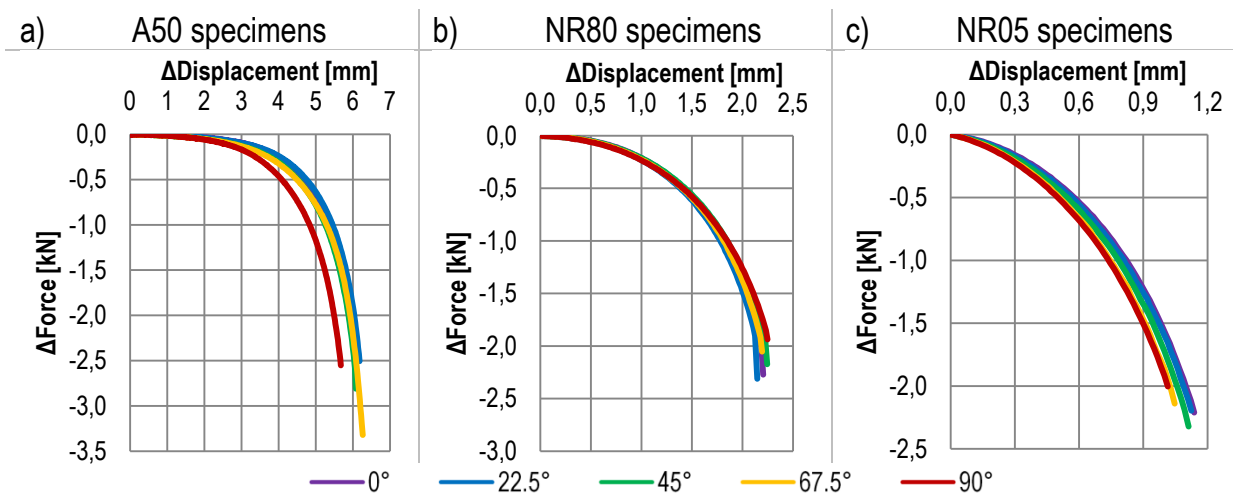


Figure 3-18: Post-UTS-behaviour obtained from CR340LA 1.8 mm obtained of a) A50, b) NR80 and c) NR05 specimens, represented as force- and displacement difference related to UTS

In Figure 3-19 the force-displacement curves of shear specimens in -45° , 0° , $+45^\circ$ and 90° orientation are depicted. Plasticity occurs at 6.0 kN where a small peak, caused by the Lüders-Effect, can be detected. Although the specimens in 0° direction exhibit a lower force-level, all directions show a similar hardening behaviour.

The displacements at force maxima are around 5.3 mm for all specimen directions except 0° orientation, where 6.0 mm are measured. The 0° direction also deviates from the other directions regarding displacements at failure. They show a displacement at failure of 6.5 mm for -45° and 90° and 6.7 mm for $+45^\circ$. At 0° average failure displacements of 7.2 mm are measured.

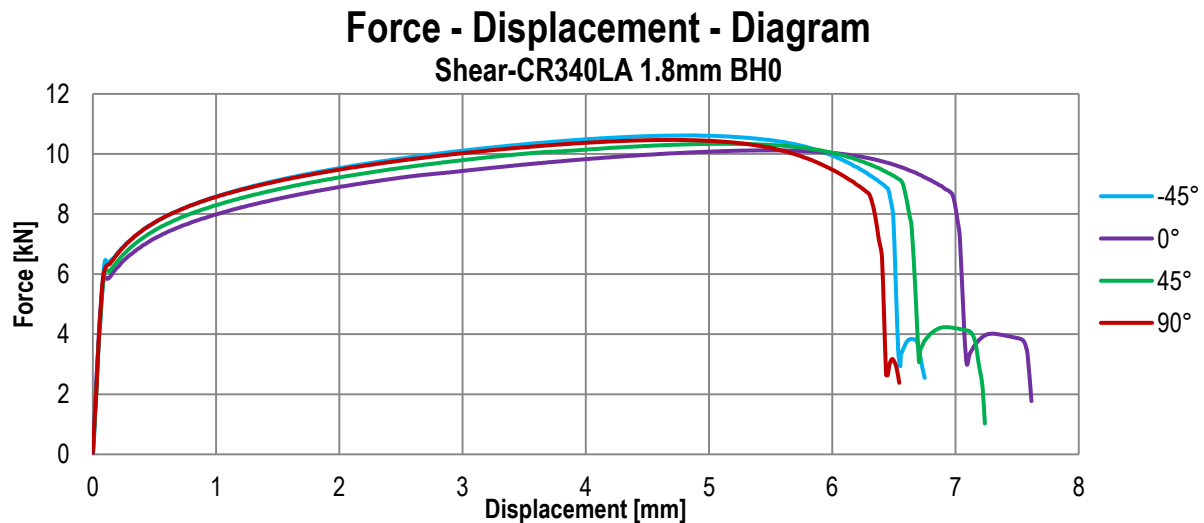


Figure 3-19: Force-displacement curves for shear specimens with voest geometry of CR340LA with 1.8 mm and in bake-hardening condition

The dome displacement-pressure data of the conducted Bulge-test of CR340LA in 1.8 mm sheet thickness are presented in Figure 3-20. The Bulge-test reveals a maximum pressure of 24.0 MPa at a dome displacement of 30.0 mm. Failure occurs at a dome height of 33.5 mm and pressure of 23.2 MPa.

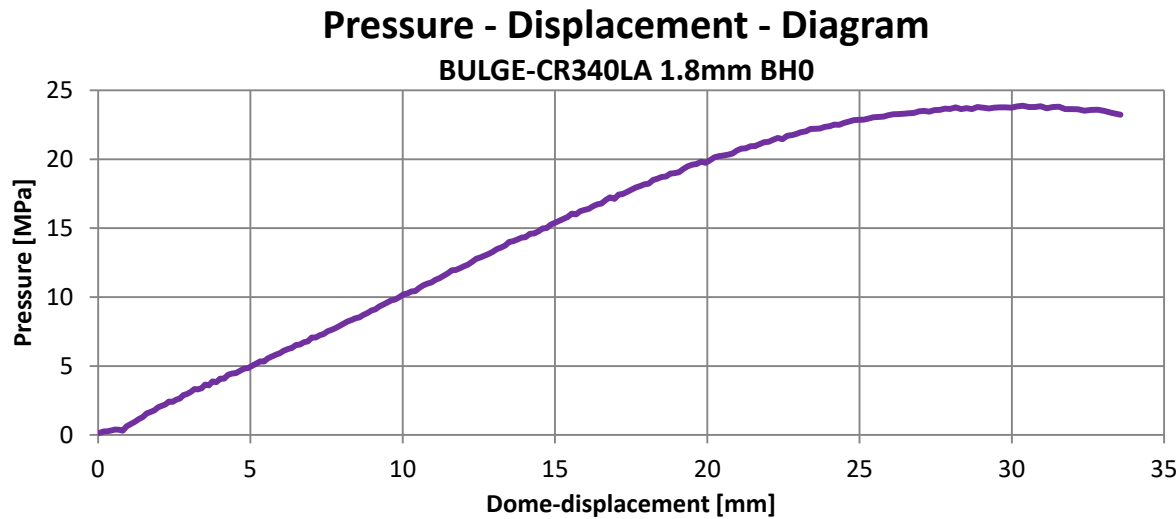


Figure 3-20: Pressure-Displacement-Diagram obtained from Bulge-test of CR340LA with a sheet thickness of 1.8 mm and in paint-bake condition

Figure 3-21 pictures the surface strain fields in rolling as well as in transverse direction, obtained from the bulge-test just before failure. Despite the biaxial stress state, both directions exhibit different strain behaviour indicating orientation dependent damage accumulation. In rolling direction a clear band of high strains develops along the path in which material failure arises. In contrast to that, only a very slight band of elevated strains evolves in transverse direction. Furthermore, the strain band in rolling direction does not develop at the dome.

Regarding local strain behaviour of the Bulge-dome as well as at a point within the localisation band, it reveals different strain histories. DIC-measurements indicate a biaxial strain state at the dome, which is also observed within the localisation zone at the beginning of loading. The onset of strain localisation leads to a strain path change from a biaxial- towards a plane strain path.

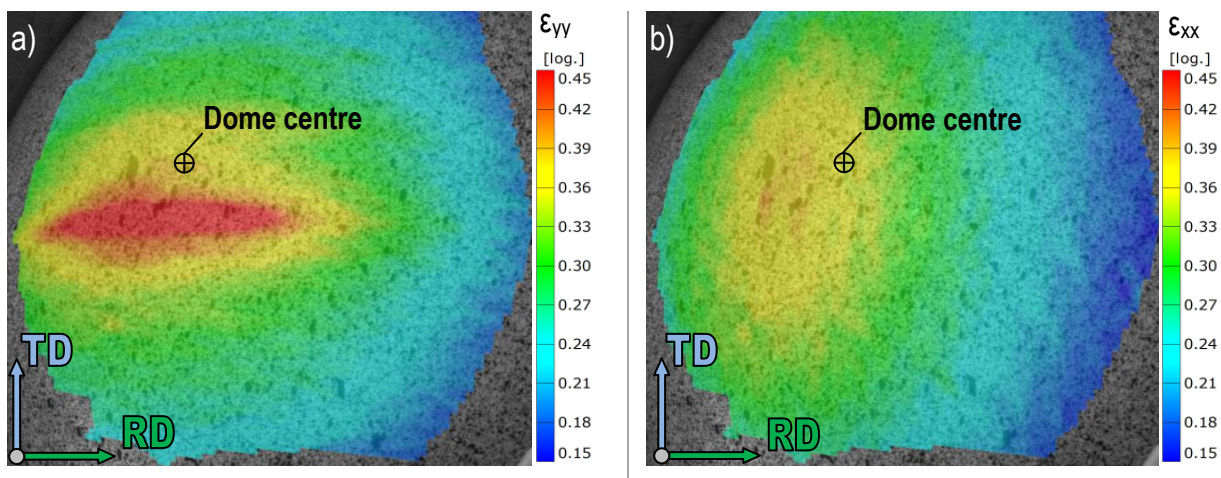


Figure 3-21: Surface strain fields in a) rolling direction and b) transverse direction obtained from the Bulge-test with marked Bulge-dome

The true equivalent failure strains, obtained by DIC-measurements, of all investigated specimens are presented in Table 3-6. While in shear no deviations are observed, standard tensile specimens exhibit an orientation dependency due to decreasing failure strains from 0° with 1.04

to 0.93 in 90°. A similar dependency, but vice versa is monitored: the minimum in failure strain occurs in 0° and increases from 0.84 to 0.98 in 90°. Therefore, higher failure strains for NR80 than for A50 specimens arise in 90°. Only small deviations in equivalent failure strains are measured for NR05 specimens, which results in no orthotropic behaviour in plane strain stress state.

Table 3-6: *True equivalent strains for the investigated specimen types for CR340LA PB 1.8 mm*

Specimen	0°	22.5°	45°	67.5°	90°
Shear	1.26	-	1.28	-	1.28
A50	1.04	1.03	1.01	0.97	0.93
NR80	0.84	0.89	0.91	0.91	0.98
NR05	0.74	0.77	0.78	0.75	0.74
Bulge			0.97		

3.1.4 Opposition of the Three Investigated CR340LA Sheets

The results of the comparison of all three sheet thicknesses of CR340LA are presented in Figure 3-22 to Figure 3-25. Instead of force-displacement data, the force-level is referred to the initial minimal cross section and is further called normalised stress.

Regarding the normalised stresses of A50 specimens, as presented in Figure 3-22, they reveal different stress levels at the development of Lüders-bands, followed by a similar strain hardening behaviour up to UTS for all directions. The normalised stresses at Lüders-bands increase with decreasing material thickness. The strain hardening behaviour up to UTS of all sheet thicknesses and directions agrees with the trend of the Swift hardening function. Therefore, the three material directions 0°, 45° and 90° to RD are approximated by the Swift hardening function. The length of the Lüders bands corresponds to the strain obtained by the calibrated Swift hardening function received at the stress within the Lüders bands. The relation fits for every direction. The normalised stress-displacement behaviour beyond UTS deviates dependent on the direction. Whereas in 0° direction nearly no deviation can be found, a pronounced divergence arises in 90° with highest displacements at 1.1 mm and lowest at 0.6 mm specimens. For the displacements at failure in 45° and 90° to RD no regularity is found.

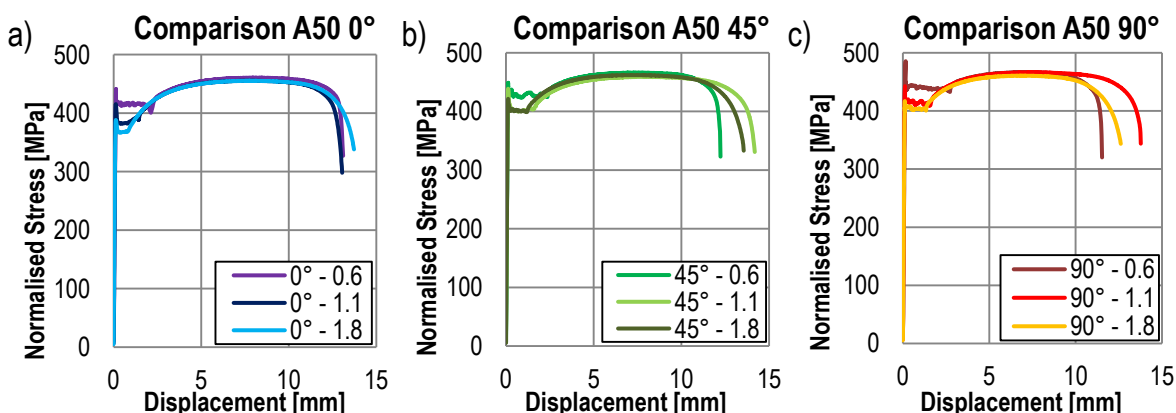


Figure 3-22: *Normalised force-displacement diagram for standard tensile specimens in a) 0° to RD, b) 45° to RD, c) 90° to RD*

The comparison of NR80 specimens can be found in Figure 3-23. The development of Lüders strains is not as pronounced as for A50 specimens but also shows a clear thickness dependency for all specimen directions. Only slight deviations arise in failure displacements of all directions, which show a thickness dependency. The highest displacements arise for the 1.8 mm, the lowest for the 0.6 mm sheet thickness.

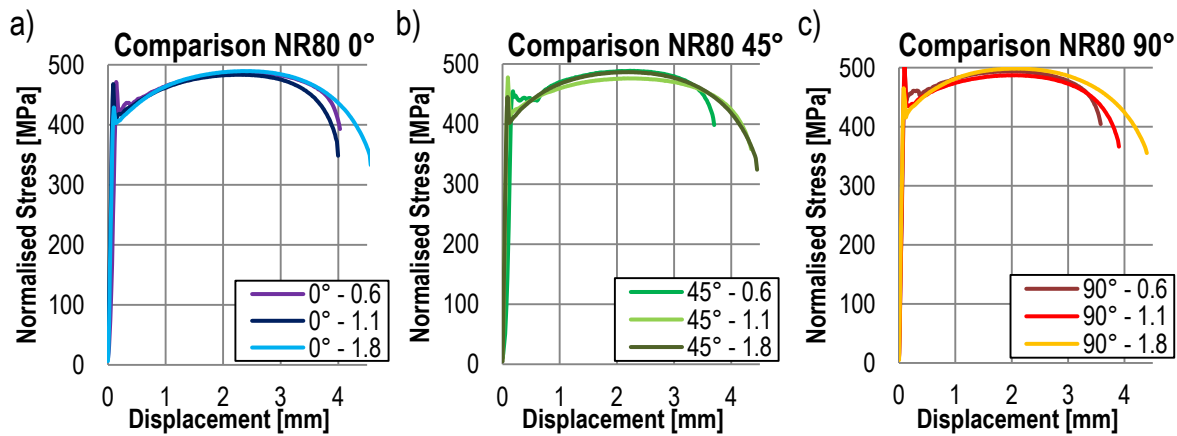


Figure 3-23: Normalised force-displacement diagram for NR80 specimens in a) 0° to RD, b) 45° to RD, c) 90° to RD

Also for NR05 specimens a similar plastic behaviour up to maximum normalised stress is observed and presented in Figure 3-24. No distinctive effect of Lüders-band development is found for all directions. Regarding the drop of normalised stress level beyond normalised stress maximum, a regular behaviour can be noticed. Again, the highest displacements are measured for specimen with 1.8 mm sheet thickness and the lowest displacement for the 0.6 mm sheets. The result concurs with the observation of increasing thickness strains and stresses of NR05 specimens and the growing resistance against thinning with increasing sheet thickness.

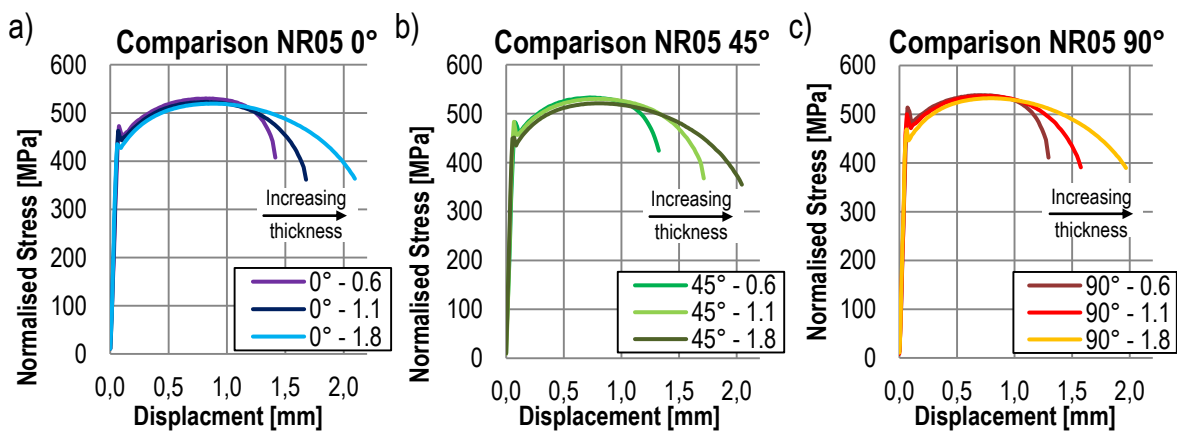


Figure 3-24: Normalised force-displacement diagram for NR05 specimens in a) 0° to RD, b) 45° to RD, c) 90° to RD

The results of shear specimens in 0° and 90° orientation of 1.1 mm and 1.8 mm thick sheets indicate different material behaviours (Figure 3-25). Besides thickness independent plastic behaviour, an increase in sheet thickness results in higher displacements up to failure. The characteristic behaviour, with highest displacements in 0° to RD, is found for both material thick-

nesses. Furthermore, the difference of displacements at failure for 0° and 90° specimens is thickness independent at 0.5 mm. The presented behaviour in 0° and 90° also mirrors the specimens in $\pm 45^\circ$ to RD. Regarding all three Bulge-tests, all normalised pressure-displacement curves are nearly identical. They exhibit the same slope and decrease during material damage and failure. Only slight deviations are found of the dome displacements at failure.

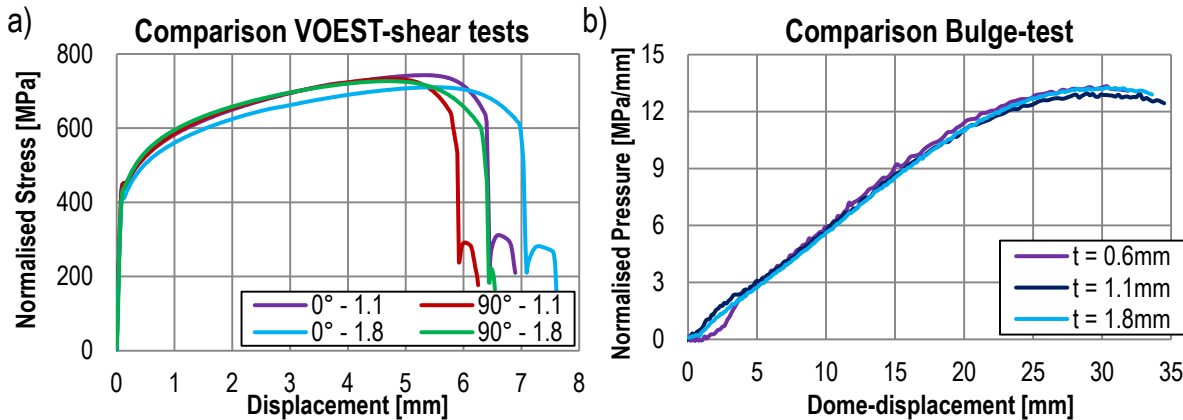


Figure 3-25: a) Normalised force-displacement diagram for voest shear specimens in 1.1mm and 1.8mm in 0° and 90° to RD, b) Normalised pressure-displacement diagram for Bulge-specimens

3.1.5 MS1500 PB 1.0 mm

The investigated MS1500 steel is delivered in 1.0 mm sheet thickness and in uncoated condition. The investigation of standard tensile specimens reveals a slightly lower Young's Modulus with 200 GPa in comparison to the previously investigated CR340LA. The MS1500 exhibits orthotropic yield strengths, decreasing from 0° (1527 MPa) to 90° direction (1451 MPa). In contrast to that, UTS fluctuates around 1520 MPa within standard deviation. Due to decreasing yield strengths (from 0° to 90°) in combination with similar UTS for all directions, the hardening capability increases from 0° to 90° to RD. Isotropy in plastic strain behaviour is also observed by orientation independent Lankford-Coefficient of near unity.

Table 3-7: Mechanical properties obtained from standard tensile tests of MS1500 1.0 mm

Parameter	0°	22.5°	45°	67.5°	90°
Youngs Modulus [GPa]	196	197	198	199	202
Poisson-Number	0.28	0.29	0.28	0.29	0.28
Yield Strength [MPa]	1527	1515	1454	1429	1451
UTS _{tech} [MPa]	1533	1529	1506	1497	1531
UTS _{true} [MPa]	1547	1577	1549	1538	1575
Ratio YS / UTS _{tech}	1.00	0.99	0.97	0.95	0.95
Lankford-Coefficient R	0.96	0.97	0.97	0.95	0.94

In Figure 3-26 the force-displacements of standard tensile specimen of MS1500 are presented. They show a distinct yield strength in 0° to RD, which softens towards 90° direction. Only in 22.5° to RD a further distinct yield point is measured. The standard determination of the yield

strength at 0.2 % plastic strain misses the distinct yield point because of its sharp decrease. Hence, the calculation of the strength ratio (YS / UTS) is under- and therefore the hardening capability is overestimated. The definition of UTS as force-maximum leads to a hardening capability of 1.0 for the 0° and 22.5° orientation due to the equality of YS and UTS by definition. The UTS in 45° up to 90° to RD is reached at 19.2 kN. Fracture occurs within a displacement of 2.40 mm to 2.75 mm, where the lower end arises in 0°, the upper in 45° and 22.5° orientation. In between lie specimens in 67.5° and 90° to RD with similar force-displacement behaviour.

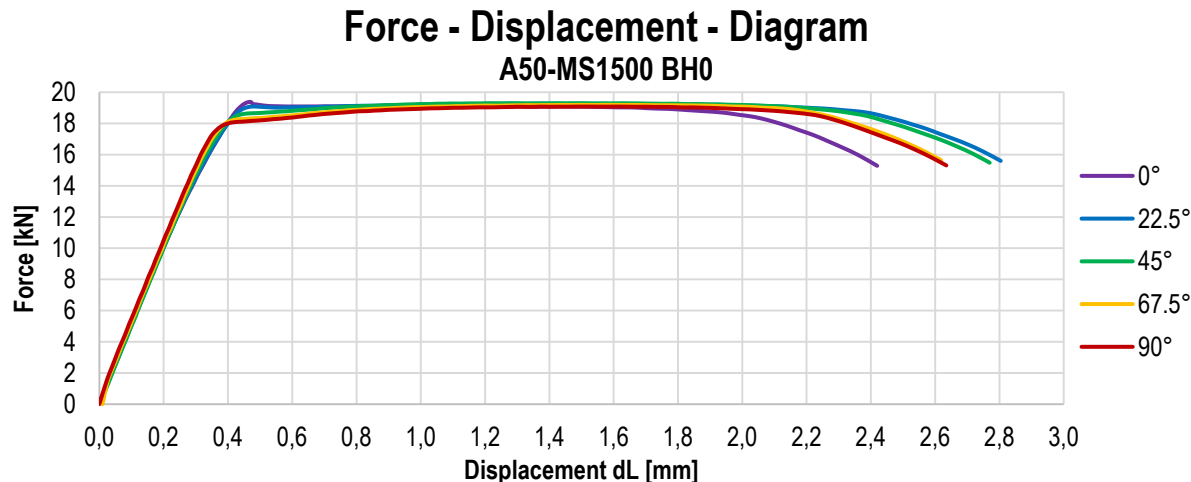


Figure 3-26: Force-Displacement - Diagram of standard tensile specimens of MS1500 BH0

Regarding notched specimens with a radius of 80 mm, they reveal similar yield behaviour as seen by A50 specimens (Figure 3-27). Similar to standard tensile specimen, all directions show a similar force maximum neglecting the distinct yield behaviour in 0° and 22.5°. In comparison to standard tension test, the notched specimens demonstrate only minor deviation in failure behaviour with failure displacements between 1.10 mm and 1.15 mm. The notched geometry of the NR80 specimens suppresses the development of uniform elongation in comparison to A50 specimens despite the fact that both specimen types represent similar initial stress states. It is concluded that the orientation dependent variations of the force-displacements mainly result from differing behaviour within uniform elongation.

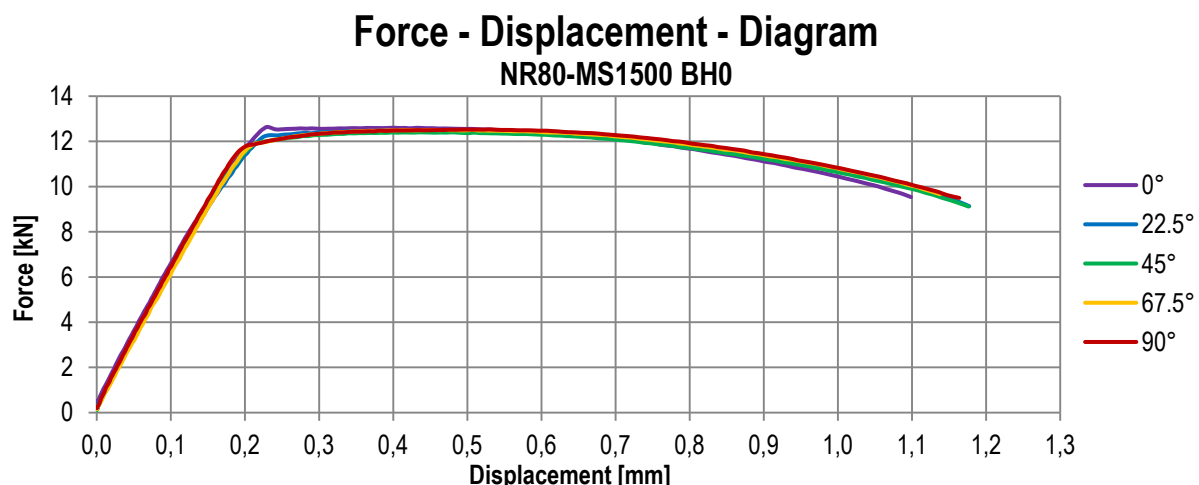


Figure 3-27: Force-Displacement - Diagram of NR80 specimens of MS1500 BH0

Figure 3-28 displays the force-displacement behaviour of specimens with 5 mm notch radius. A distinct yield point is observed again, but similar to NR05 specimens of CR340LA, it is less pronounced than for other investigated specimen types. All specimens show an equal force maximum of 12.6 kN and exhibit similar displacements to fracture with 0.45 mm except in 90° to RD, in which only 0.35 mm are witnessed.

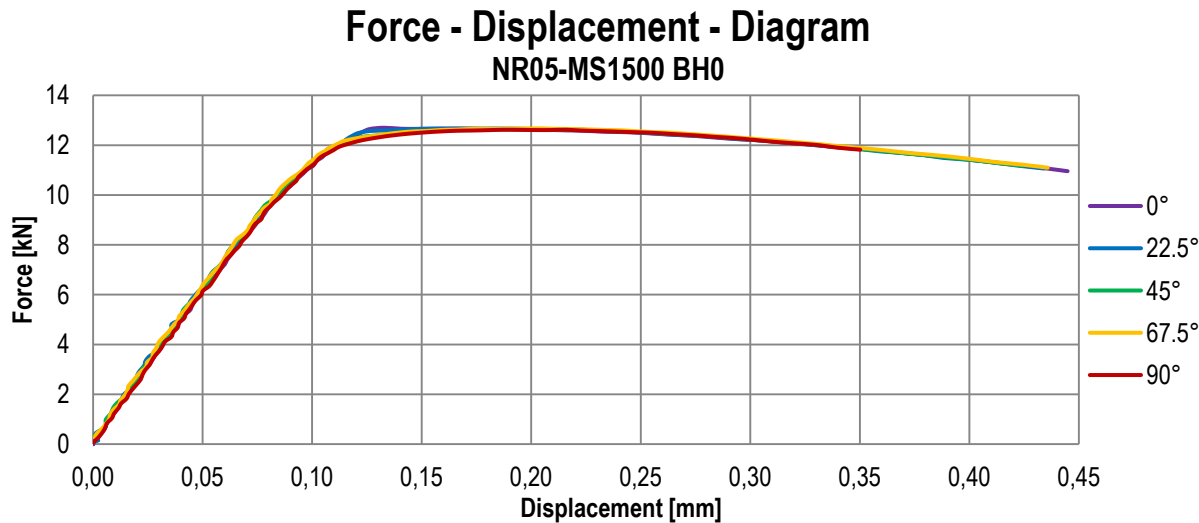


Figure 3-28: Force-Displacement - Diagram of NR05 specimens of MS1500 BH0

Figure 3-29 presents the MS1500 material behaviour under shear loading. The three investigated specimen directions show nearly similar behaviour regarding the yield point at 8.0 kN followed by only a slight increase in force level up to fracture. In comparison to previously investigated specimen types, the failure occurs abruptly at 2.4 mm without pronounced damage behaviour.

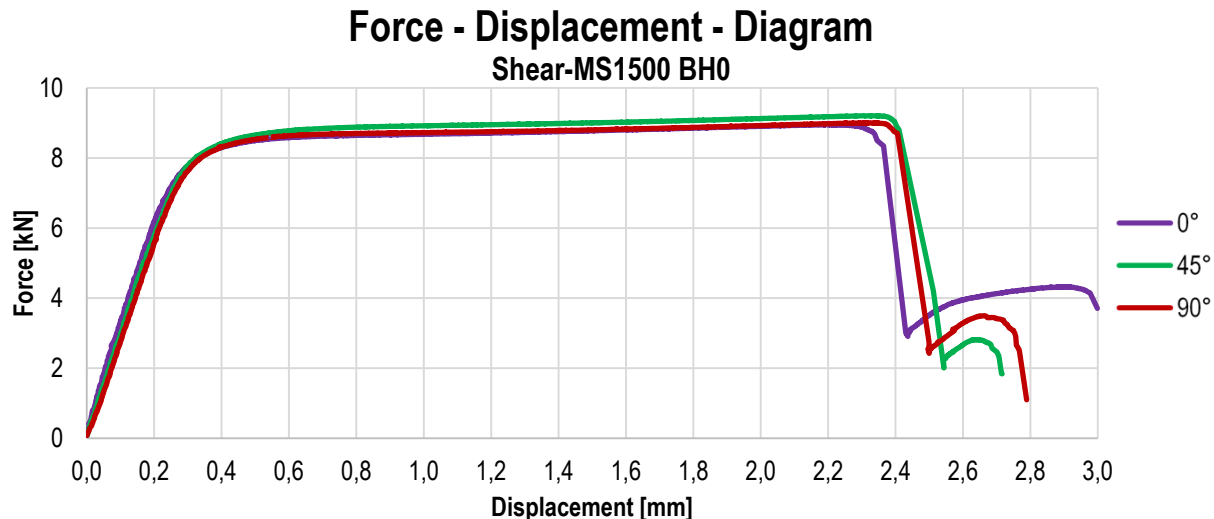


Figure 3-29: Force-Displacement - Diagram of SDR0302 shear-specimens of MS1500 BH0

The Bulge-test result, conducted with a 200 mm diameter, of MS1500 is displayed in Figure 3-30. The Bulge-dome proves a maximum displacement of 46.5 mm at a pressure of 18.2 MPa. As seen for shear specimens, no pronounced damage behaviour is observed; the material fails

at maximum pressure. The investigation of the surface strain fields reveals no development of a single localisation band as seen for CR340LA in 1.8 mm sheet thickness. Additionally, the maximum equivalent strains of 0.42 are obtained at the dome.

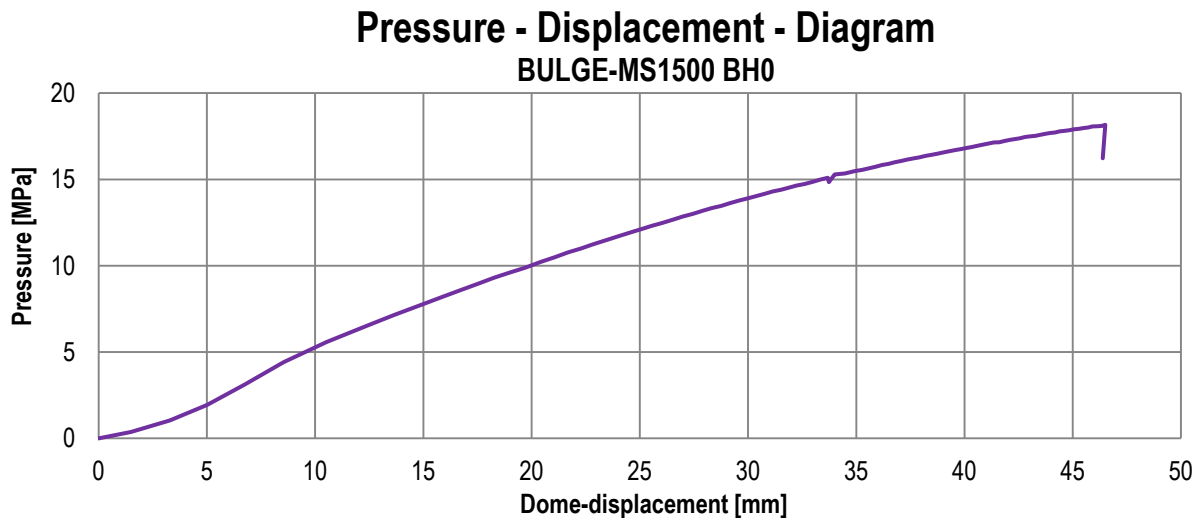


Figure 3-30: Pressure-displacement-diagram of the Bulge-test of MS1500 BH0

In Table 3-8 the obtained failure strains at material failure are depicted. The experimentally determined behaviour deviates from CR340LA. In 0° failure strains of A50 specimens are lower than of NR80. With an increasing angle to RD the failure strains of A50 specimens coincide (22.5° direction) and exceed (45° direction) the failure strains received from NR80 specimens. What is more, specimens with notch radii of 5 mm in 90° to RD exhibit significantly lower failure strains than other directions. This corresponds to the low displacements up to failure.

Table 3-8: True equivalent strains for the investigated specimen types for MS1500 PB 1.0 mm

Specimen	0°	22.5°	45°	67.5°	90°
Shear	0.82	-	0.80	-	0.79
A50	0.45	0.50	0.55	0.49	0.49
NR80	0.48	0.49	0.50	0.46	0.47
NR05	0.29	0.27	0.26	0.27	0.17
Bulge			0.42		

An explanation for the deviations of failure strains is the manufacturing process of the presented MS1500, which has undergone a stretch levelling process. The stretching occurs in 0° to RD with strains of 0.2 % to 0.5 % and can affect the A50 specimen with its 50 mm gauge and 75 mm parallel length. Especially plastic strain heterogeneities can have a strong effect on material behaviour resulting in mean variations of the displacements at failure of up to 25 %. Due to the loss of a uniform elongation zone of notched specimens, these material heterogeneities may not play a major role for loadings in 0° direction. The NR05 specimens in 90° direction exhibit stresses in RD, which may also be affected by heterogeneities.

3.2 Formation of Lüders-bands

All specimens investigated in chapter 3.1 exhibit a distinct yield point except the Bulge-test. Regarding standard tensile specimens, the distinct yield point is followed by the formation of Lüders-bands which start at the radii and run across the gauge length. Within the Lüders-bands no increase in force level is measured. With regard to NR80 specimens, the development of Lüders-bands is restricted to a narrow area at the notch ground. The development of these bands has only minor influence on the force-displacement curves except for 0.6 mm thick specimens. The surface strain fields at the distinct yield point are pictured in Figure 3-31a-c for NR80 specimens aligned in 0° direction for all three investigated sheet thicknesses.

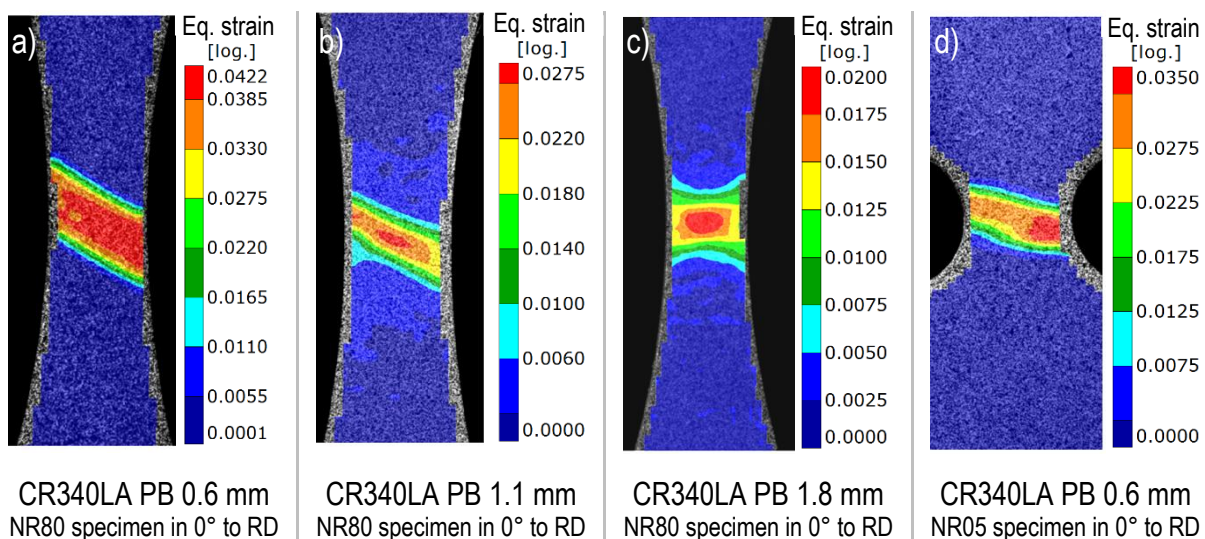


Figure 3-31: Strain localisation fields beyond the distinct yield point of NR80 specimens with material thicknesses a) 0.6 mm, b) 1.1 mm, c) 1.8 mm and NR05 specimens with material thickness of 0.6 mm

The NR80 strain fields of specimens in 0.6 mm and 1.1 mm material thickness form Lüders-bands with the onset of plastic straining. These are more pronounced for specimen with a sheet thickness of 0.6 mm. In contrast to that, NR80 specimens of 1.8 mm thick sheets show no formation of Lüders-bands. Furthermore, Figure 3-31d displays the formation of Lüders-bands of NR05 specimens of CR340LA with 0.6 mm thickness. For NR05 specimens in all other sheet thicknesses, no development of Lüders-bands is observed.

The orientation of Lüders-bands to the loading direction depends on the specimen geometry and therefore on the stress state. Lüders-bands, arisen at standard tensile tests, appear at an angle of 35° to the tensile direction, even though they occur at 30° in NR80 specimens. Specimens with a notch-radius of 5 mm form bands at 15° to loading direction.

The development of Lüders-bands is affected by different factors like microstructural properties as well as the specific testing parameters. Fujita and Miyazaki [Fuj78] investigated the separate effects of the grain size, the sheet thickness, the crosshead velocity and the temperature on the Lüders-strains. They observed a dependency of the formation of Lüders-bands on the specimen temperature and of the crosshead velocity. Furthermore, by increasing the sheet thickness, the upper and lower yield strengths are affected up to saturation, which is observed at high sheet

thicknesses. The investigation further revealed an exponential dependency on the grain size, whose decrease leads to an increase of the upper and lower yield strength.

Based on the results of Fujita and Miyazaki, the microstructural properties of the three previously investigated CR340LA sheet thicknesses are examined by OLM. Due to similar test conditions for all CR340LA specimens, the effects of crosshead velocity and specimen temperature are neglected in the continuing process. The resulting averaged grain sizes as well as the upper and lower normalised yield strength are presented in Table 3-9. For all three thicknesses a grain size below 10 μm is measured. An average size of 6.1 μm is observed for sheets with 0.6 mm thickness, whereas 1.1 mm and 1.8 mm sheets exhibit similar grain sizes with 8.5 μm and 8.7 μm respectively.

Table 3-9: Grain sizes and mechanical properties, obtained from uniaxial tension tests in 0°, for all three CR340LA sheet thicknesses

Parameter	$t = 0.6 \text{ mm}$	$t = 1.1 \text{ mm}$	$t = 1.8 \text{ mm}$
Averaged grain size $d [\mu\text{m}]$	6.1	8.5	8.7
Ratio t/d	98	129	207
Upper yield strength [MPa]	440	415	390
Lower yield strength [MPa]	415	380	370

Regarding the upper and the lower yield strength, an increase with lowering sheet thicknesses and grain size is observed. Due to the investigation of only three CR340LA sheets, no separate investigations of grain size and sheet thickness effect could be conducted. However, the dissimilarity in grain size of all researched steel sheets impedes a connection of yield strength and sheet thickness. To estimate the effect of the grain size variation at the observed length scale, the results of [Fuj78], ranging from 30 μm to 250 μm , are extrapolated to 9 μm and 6 μm (Figure 10-9, appendix). The extrapolation reveals an increase of 299 MPa for the upper and 94 MPa for the lower yield strength by lowering the grain size from 9 μm to 6 μm . Even though the extrapolation does not predict the observed rise of upper (+50 MPa to +299 MPa) and lower yield strength (+45 MPa to +94 MPa), it points to a dominant grain size effect. This dominant effect on the yield strength is further assumed to mask additional effects of the sheet thickness etc. These results correspond to the observed material behaviour and explain the differences between Lüders-strains of all three sheet thicknesses.

3.3 Microstructural Investigation

Microstructural investigations are performed with standard tensile specimens of CR340LA with 1.1 mm sheet thickness and in bake-hardening condition. OLM is applied as well as SEM to investigate the fracture surface. Additionally, the EBSD-method is utilised to obtain the texture.

The chemical composition of the investigated CR340LA in 1.1 mm sheet thickness is pictured in Table 3-10. The microstructure consists of a mixture of larger and smaller ferrite grains. The average grain size amounts to 8.5 μm whereas larger grains are measured up to 25 μm . OLM-

measurements of the microstructure depict ferrite grains with cementite precipitations as presented in chapter 10.2 (appendix).

Table 3-10: Chemical composition of CR340LA in 1.1 mm sheet thickness

Element	C	Mn	P	S	Al	Si
max. mass %	0.12	1.50	0.03	0.03	0.015	0.50

To investigate texture evolution during straining standard tensile specimens were pre-deformed and analysed by EBSD. The investigations were carried out at specimen aligned in 0°, 45° and 90° to RD with four pre-deformed specimen each. They were strained just beyond Lüders-strains (1), up to UTS (2), at 20 % global technical strain (3) and up to fracture (4). DIC-measurements were applied during pre-straining to obtain the surface strain field especially for 20 % global strain and fracture. The resulting ODFs of all three directions are presented in Figure 3-32. The typical sheet metal texture consists of a pronounced α - and γ -fiber, which both arise under $\varphi_2 = 45^\circ$. Therefore, the depicted ODFs are limited to the representation in the $[\varphi_1, \varphi_2 = 45^\circ, \Phi]$ – plane. Due to the statistical character of the ODFs, received from a representative microstructure, the EBSD-measurements of different pre-deformed specimens are also representative for the material behaviour of similar load paths.

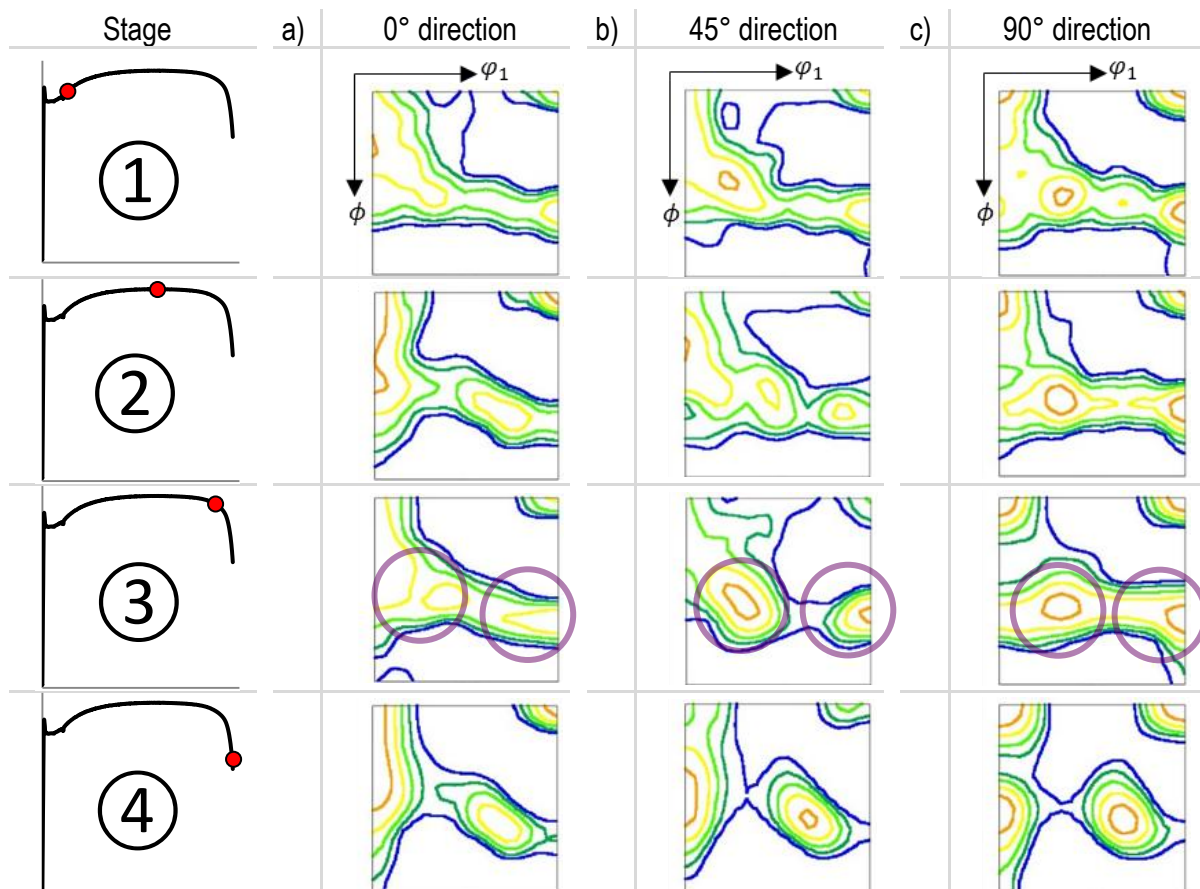


Figure 3-32: ODFs of the investigated CR340LA specimens (1.1 mm thickness) in 0°, 45° and 90° direction at four different strain stages, obtained from about 2000 grains

The investigations reveal a similar behaviour from stage ① to ③ with the formation of two spots of high orientation probability within the γ -fiber, marked by purple circles at stage ③. Parallelly conducted numerical simulations reveal uniaxial tension up to stage ③, which concurs with the similar texture evolution of all three stages. The simulations also reveal a stress state change beyond stage ③ towards plane strain, which is accompanied by strain localisation and the formation of localisation strain bands. This deviation from uniaxial tension with incorporated strain path change can explain the deviation in texture evolution, leading to a single spot concentration of grain orientation in the middle of the γ -fiber at stage ④.

Plastic orthotropy of sheet metals depends on its specific texture which defines possible glide directions. The grain orientations influence the required shear stress for dislocation movement, which influences the macroscopic stress and strain behaviour. The investigation reveals a significant change of the sheet metal texture during straining in all studied directions near fracture. Hence, straining is also assumed to change the yield surface shape of the investigated CR340LA as seen for IF-steel by An et al. [An13]. The effect of straining and microstructural evolution on the yield surface shape is investigated separately in chapter 3.4.

In addition to EBSD-measurements the composition of the grain boundaries is analysed at the same strain stages and depicted in Figure 3-33. The basic material is dominated by high angle grain boundaries (90 %). Only a small amount of low angle and sub angle grain boundaries (each 5 %) are measured. Furthermore, nearly no change is observed between the compositions of the basic material and stage ①. Yet, straining until point ③ leads to a conversion of the grain boundary composition. In addition, the increase in the number of LAGBs and SAGBs is accompanied by a relative decrease in high angle grain boundaries. This trend continues up to material failure (strain stage ④), but with an intensified generation of SAGBs. Consequently, the grain boundary evolution pictures a microstructural reorientation in addition to conducted EBSD-measurements.

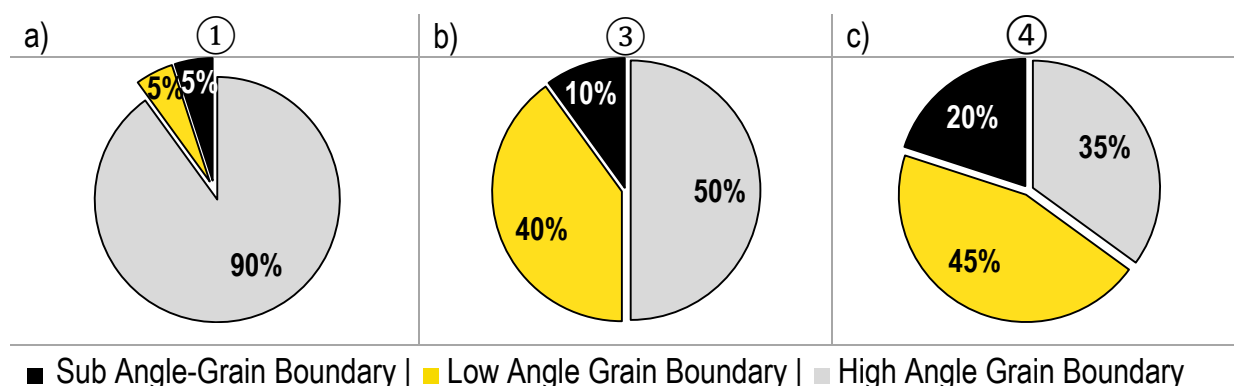


Figure 3-33: *Proportion of Grain boundary types and their evolution during straining measured at standard tensile specimens*

Furthermore, the grain boundaries are specified due to the individual grain orientations, which affect the slip transfer to neighbouring grains. Imperfect slip transfer leads to strain heterogeneities on grain size [Pat13] and affects intensified damage nucleation at these spots [Pat13], [Bie09]. During straining, for all grain boundary types (sub, low, high angle) an increase of the

absolute number but different evolution velocities are observed. Potential nucleation spots of voids arise with the increasing absolute number of high angle grain boundaries. Moreover, the rising sub angle as well as low angle grain boundaries are observed to arise mainly within the grains, impeding the inner grain slip transfer. The growing number of grain boundaries results in loading induced anisotropic damage in combination with straining induced texture evolution towards a tensile texture. In addition to that, a similar evolution of grain boundaries is witnessed for all specimen-directions.

Similar to CR340LA (1.1 mm), microstructural investigations incorporating OLM, SEM and EBSD are conducted for MS1500. In contrast to CR340LA, the microstructure consists of thin martensite needles instead of grains, which impede the EBSD-measurements (Figure 10-4, appendix). The ODFs, obtained from 500 grains, are pictured in Figure 10-3 in the appendix. Due to the reduced number of grains, the results are not representative and do not allow inference of the texture evolution during tensile straining.

3.4 Distortional Hardening

During straining the microstructure and the related mechanical properties undergo an evolution dependency on the straining direction. Affected mechanical properties are the yield strength and the plastic strain behavior, with regard to the Lankford-Coefficient R . Beyond UTS the Lankford-Coefficient is not further valid as a description of the plastic strain behaviour in uniaxial tension, but it is utilised here as a description of width to thickness strain ratio. A decrease of the Lankford-Coefficient up to fracture is measured due to stress state and conjoined strain state changes.

The microstructural evolution of aluminium was investigated by Savoie et al. [Sav95] and An et al. [An13], who also extended the investigation to IF-steel. For both materials decreasing R -values with increasing straining were observed. To picture the effect of the evolving Lankford-Coefficients on the yield surface, An et al. [An13] used the quadratic Hill yield criterion ([Hil48]) and determined its coefficients based on the Lankford-Coefficients. The evolution of the yield surface was investigated at technical tensile strains of 0 % and 25 % for the IF-steel. The resulting yield surfaces exhibited similar yield points in uniaxial tension but revealed decreasing biaxial yield points with increasing tensile strains.

Besides the conducted EBSD-measurements, presented in chapter 3.3, the microstructural evolution can also be described by the Lankford-Coefficient during tensile straining. Therefore, the Lankford-Coefficient is calculated, based on DIC-measurements, for every strain stage at the failure point during the whole test. The results for 0°, 45° and 90° to RD up to an equivalent local strain of 0.5 are presented in Figure 3-34a. Within elastic range, high R -values arise, which are called elastic R -values. The affiliated development of Lüders-bands, which occurs at stress states deviating from uniaxial tension, leads to a drop of the Lankford-Coefficient below the level obtained in uniaxial tension [Sav95]. Beyond the Lüders-strain range increasing R -values are measured for all directions up to UTS at plastic strains of about 0.15. The decrease of R -values is found not to start at UTS, but exhibits an orientation dependency. The increasing

R-values up to UTS are contrary to the results obtained by An. et al. [An13] for IF-steel, who measured a decreasing Lankford-Coefficient.

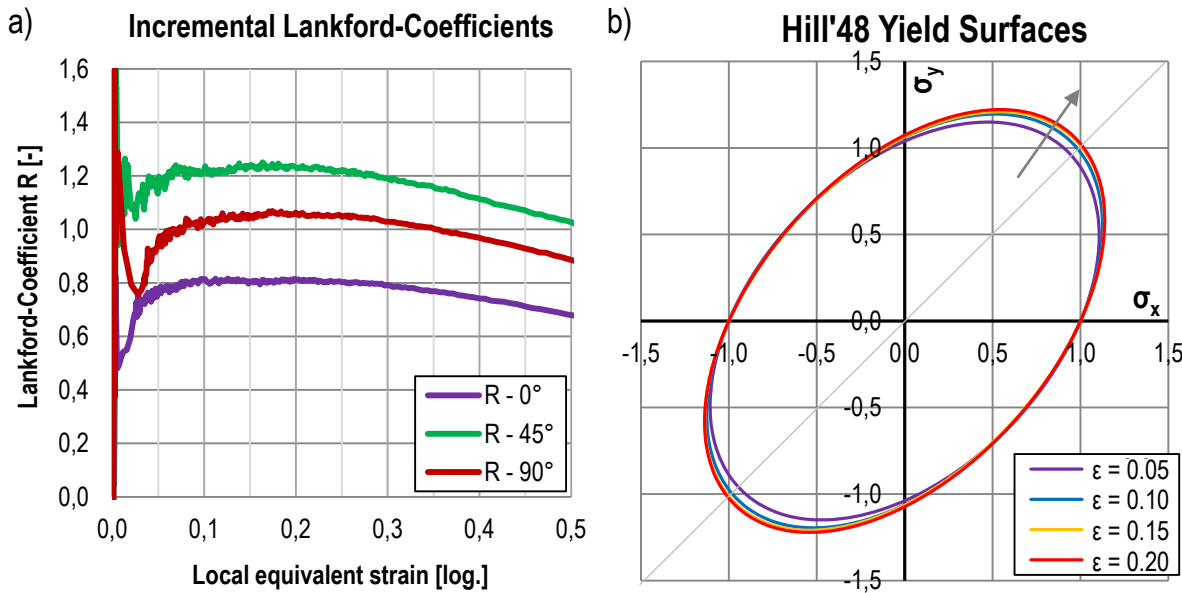


Figure 3-34: a) Lankford-Coefficients obtained in 0° , 45° and 90° dependent on the local equivalent strains obtained at the failure point, b) Hill'48 yield surface within the σ_{xx} - σ_{yy} -plane, incorporating the experimental Lankford-Coefficients at equivalent strains of 0.05, 0.10, 0.15 and 0.20

In Figure 3-34b the effect of experimentally obtained R-values at equivalent strains of 0.05, 0.10, 0.15 and 0.20 is demonstrated in combination with the Hill'48-yield criterion. On implying associated plasticity, the varying R-values result in a yield surface distortion. They lead to increasing biaxial stresses as well as changes of the strain vector. Besides this, Figure 3-34b pictures the effect on the uniaxial stresses, which increase in y-direction (90° to RD). In comparison to that, the x-direction (0° to RD) does not indicate changes of the uniaxial yield strength. Furthermore, the changing strain vector affects increasing strains in specimen width direction and a decrease of thickness strains when incorporating plastic incompressibility. They stabilise the strain localisation in combination with higher biaxial stresses [Sto16]. The investigation of the CR340LA (1.1 mm sheet thickness) reveals a slight distortion of the yield surface with a shift of the biaxial yield point of about +6 % at UTS in comparison to the yield surface at equivalent strains of 0.05.

Besides orthotropic strain behaviour, described by orientation dependent R-values, the yield surface distortion can also be influenced by orthotropic hardening. To quantify the impact of distortion hardening, the distortion-coefficient $\kappa(\varepsilon)$ is introduced and defined in equation (3-1). It describes the partial deviation of two flow curves Y_{S1} and Y_{S2} dependent on the plastic strains. In general both flow curves are defined for different directions e.g. uniaxial tension in 0° and 90° to RD. The distortion-coefficient ranges from $-\infty$ to ∞ , where $\kappa(\varepsilon) = 0$ marks no effect of strain hardening on the yield surface shape. What is more, the distortion-coefficient $\kappa(\varepsilon)$ is not affected by the initial orthotropy of the yield surface and only includes the strain hardening behaviour.

$$\kappa(\epsilon) = \frac{d\left(\frac{Y_{S1}(\epsilon)}{Y_{S2}(\epsilon)}\right)}{d\epsilon} \quad (3-1)$$

The investigated CR340LA with a sheet thickness of 1.1 mm revealed orthotropic hardening behaviour with orientation dependent variations of the yield strength and UTS. However, the distortion-coefficient up to UTS remains zero due to similar slopes of flow curves in 0°, 45° and 90° to RD. Therefore, no distortional effects arise due to strain hardening. This stands in contrast to results obtained from incremental R-value calculations. The divergence of yield surface expansion indicates non-associated plasticity during straining. For numerical simulation purpose, the effect of the evolving microstructure is neglected. Besides the minor effect on the yield surface up to UTS of 6 % in maximum for biaxial stress states, the R-values can only be experimentally obtained up to UTS. Beyond UTS, the Lankford-Coefficients have to be extrapolated, similar to the strain hardening behaviour. Due to similar effects of the Lankford-Coefficient and the strain hardening behaviour on the yield surface shape, the effect of the former is included into the extrapolation of the flow curves.

The investigation is extended to the MS1500 in 1.0 mm sheet thickness in paint-bake condition. As previously presented, the material exhibits orientation independent Lankford-Coefficients around 0.95. Similar behaviour is revealed for the trend of the incremental R-values at fracture point, which results in only minor yield surface distortions far smaller than seen for CR340LA. The introduced distortion-coefficient $\kappa(\epsilon)$ also remains near zero, indicating no distortion due to orthotropic strain hardening.

3.5 Behaviour of Double-Shear Specimens

Due to convention, the angle to RD of loadings is defined by the first principle stress. Figure 3-35 depicts different shear loading orientations, in which red arrows mark the first and blue arrows the third principle stress; the second is equal to zero. Green arrows point to shear stresses. The utilised flat shear specimens exhibit shear in specimen direction. Therefore, the specimen direction does not coincide with the direction of the first principle stress and is rotated 45° to the specimen loading direction.

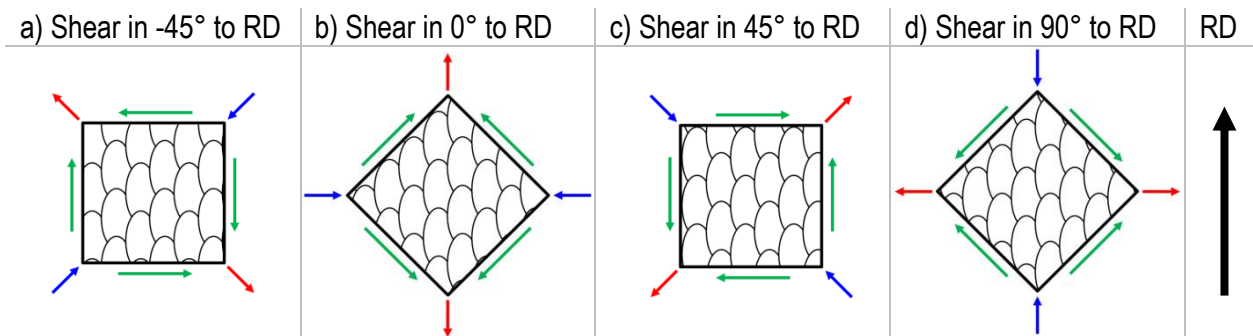


Figure 3-35: Pure shear stresses for different shear directions with schematic microstructure. The arrows in red, blue and green mark the first as well as the third principle and the shear stress.

Due to the specimen-composition of two shear zones, the results of one specimen represent the average force-displacement behaviour of two shear directions. At specimens aligned in 0° as well as 90° to RD shear appears at $\pm 45^\circ$ direction; specimens at $\pm 45^\circ$ to RD exhibit the shear directions 0° and 90° to RD.

In all tests failure did not occur simultaneously in both gauge sections. Hence, after the first failed gauge area an increase in force level is measured previously to the complete specimen failure. To understand the diverging fracture of both gauge sections as well as material behaviour within shear in 0° to RD, the equivalent strain fields of shear specimens in 0° and 45° orientation are presented in Figure 3-36. The local strain field of a 0° shear specimen is pictured in Figure 3-36a at a global displacement of 1.5 mm. Both gauge sections show equal equivalent strains. Subsequent loading leads to diverging local strain fields of both gauge sections as displayed in Figure 3-36b for a global displacement of 6.0 mm. Figure 3-36c presents the strain field of a 45° specimen at a displacement of 1.5 mm. As seen for 0° specimens at displacements of 6.0 mm, the equivalent strain fields of both gauge sections deviate, but the deviation arises at significantly lower global displacements.

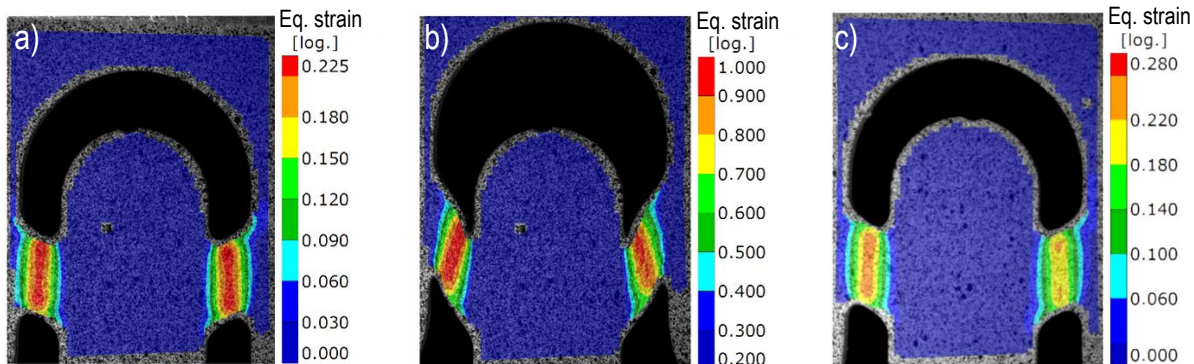


Figure 3-36: Local equivalent strain field of voest-shear specimens in different specimen directions a) 0° to RD with 1.5 mm of displacement, b) 0° to RD at displacement of 6.0 mm, c) $+45^\circ$ to RD at a displacement of 1.5 mm

For the utilised double shear specimen in 0° direction the arising shear strains are oriented in $\pm 45^\circ$ to RD. Due to the orthotropy assumption for metals, no deviation may occur and both gauge sections show an equal reaction to loading. Further straining leads to a reorientation of the shear zone which reorients the shear strain direction. The deviation from shear in $\pm 45^\circ$ to RD forces deviations in damage behaviour and leads to different equivalent strains in both gauge sections. The effect can be clearly observed in Figure 3-36c for a specimen in $+45^\circ$ direction. Regarding Figure 3-35, the specimen aligned in $+45^\circ$ to RD exhibits shear in 0° and 90° . As observed for standard tensile and notched specimens, these directions show different behaviour regarding yield strength and UTS as well as in local strain behaviour. These differences also reflect for shear specimens.

The differing loading directions within the shear zones of specimens aligned in 0° and $\pm 45^\circ$ direction respectively explain their deviating force-displacement behaviour. However, this explanation is insufficient to describe the deviations between specimens aligned in 0° and 90° to RD.

The microstructural investigation reveals non-equiaxed grains for the CR340LA. During the test, the microstructure is deformed in specimen loading direction. Therefore, the microstructure of both shear sections undergoes a straining in RD for specimens aligned in 0° to RD. In contrast to that, the microstructure of shear specimens in 90° orientation is strained in TD. In combination with non-equiaxed grains this results in an orthotropic microstructural evolution. In addition, numerical simulations reveal a load path change from nearly pure shear towards uniaxial tension due to deformations of the shear zone. The combination of non-equiaxed grains, its microstructural evolution and arising tensile stress proportions results in different loadings on the microstructure for 0° and 90°, which is supposed to affect the deviating material behaviour.

3.6 Strain Localisation and Failure

Analogous to the development of Lüders-bands of NR80 specimens, the three different CR340LA sheets exhibit variations in strain localisation behaviour. The localisation areas of standard tensile specimens at 0° to RD are displayed in Figure 3-37. In contrast to notched or shear specimens, the localisation zone of tensile specimens is not predefined and forms due to geometrical or material imperfections during straining. All tensile specimens exhibit the formation of two shear bands with an angle of $\approx \pm 55^\circ$ to RD, in which one band becomes dominant.

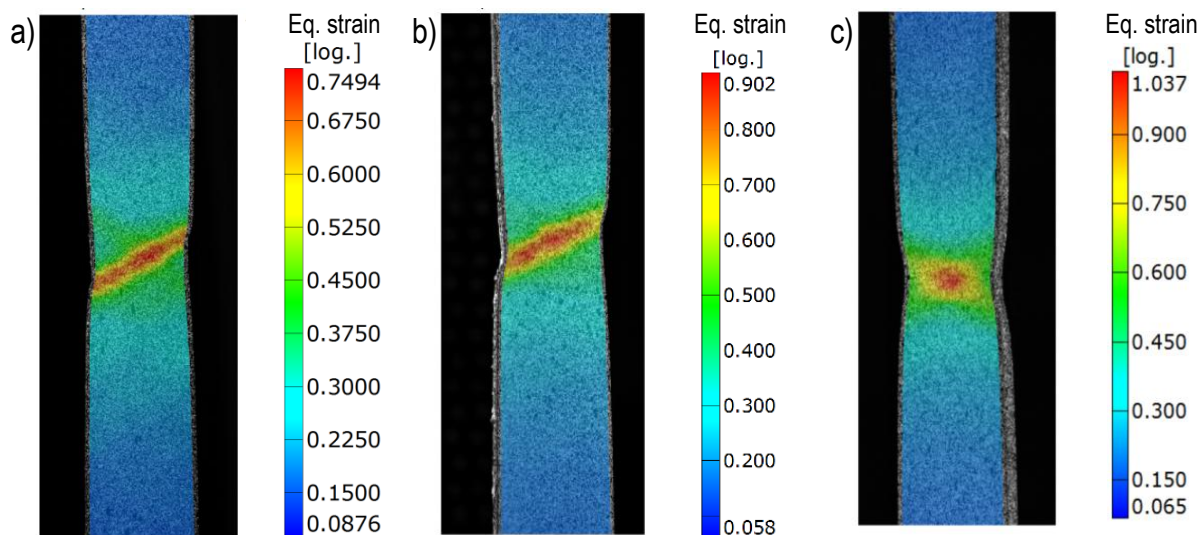


Figure 3-37: Strain localisation phenomena of CR340LA in 0° to RD with different sheet thicknesses in bake-hardening condition, a) 0.6 mm thickness, b) 1.1 mm thickness, c) 1.8 mm sheet thickness

This effect is found to be more pronounced the more the sheet thickness is reduced. Whereas the 0.6 mm thick specimens present high strains over the whole width of the band (Figure 3-37a), specimens with a thickness of 1.1 mm show a slight localisation of strains in the middle of the band (Figure 3-37b). The 1.8 mm thick specimens - as revealed in Figure 3-37c - exhibit a slightly dominant band with a clear strain localisation in the middle of the specimen.

Figure 3-38 exhibits a theoretically predicted and the experimentally observed development of localisation planes within different specimen geometries. The localisation planes indicate the orientations of the fracture surface. In Figure 3-38a the theoretically predicted localisation

planes for tensile loadings are presented in red and black. The blue line represents a plane perpendicular to loading direction. The theoretical basis can be found in [Ber04] and shall not be discussed here. Regarding uniaxial tension in direction 3, a localisation angle of 35° is predicted, which concurs with the experimental data. The localisation angle describes the rotation around the sheet metal normal direction (direction 2) of the plane perpendicular to the loading direction, resulting in both localisation planes. Figure 3-38b pictures the 3D-strain field of a standard tensile specimen of CR340LA (1.1 mm) within the strain localisation area. The DIC-measurement is performed on the sheet metal surface as well as over specimen thickness with a facet-size of 0.085 mm. Within the 1-3-plane a dominant localisation band is observed and highlighted in white, which exhibits an angle of 35° to the 1-axis as theoretically predicted. A second band, highlighted in purple, is also found. Both bands show elevated strains parallel to 2-direction over the specimen thickness. Both observed bands are tails of the localisation planes and agree with the theoretical predictions [Ber04], [Hil58].

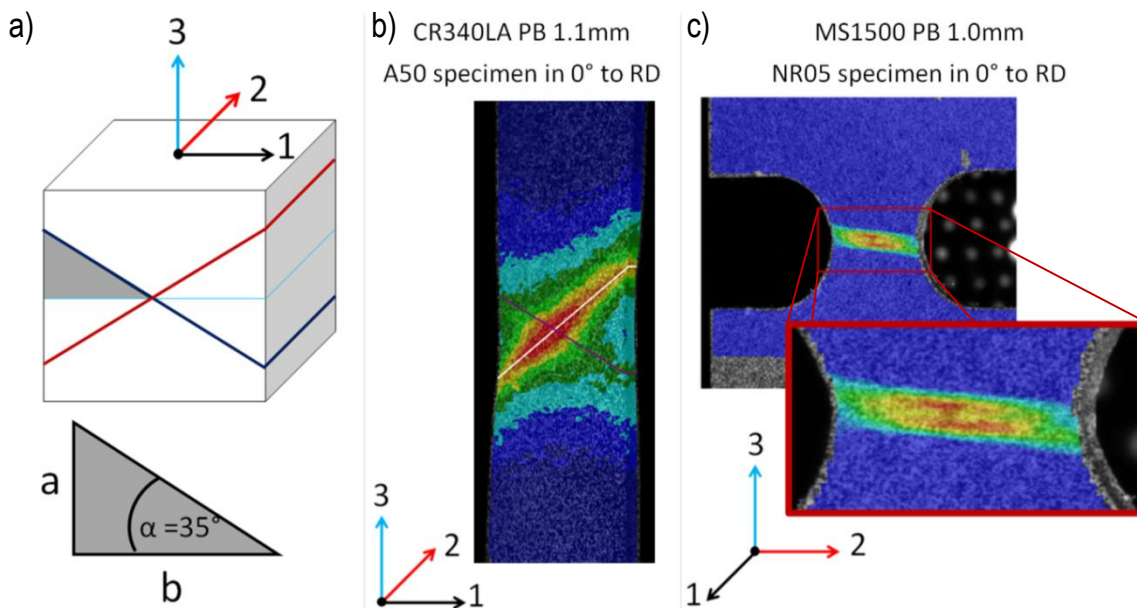


Figure 3-38: a) orientation of the failure planes within the 1-2-3-coordinate system, b) 3D strain localisation bands at CR340LA specimens with 1.1 mm sheet thickness with marked strain localisation bands (not dominant: purple, white: dominant), c) surface localisation bands at NR05 specimens of MS1500

Figure 3-38c illustrates the surface strain field of a specimen with 5 mm notch radius. The measurement is carried out on the MS1500-steel due to the minor ductility in comparison to CR340LA. Sheet metals with high ductility blur strain effects within the localisation zone of the notched specimens. The MS1500 resists constrictions and deforms mostly within localisation bands. In comparison to standard tensile specimens the fracture surface occurs also at 35° perpendicular direction to loading. However, the fracture plane runs across the sheet thickness unlike the observation of standard tensile specimens. On the specimen surface only two parallel lines are measured by the DIC-method. In combination with the orientation of the fracture surface, both lines indicate the orientation of the strain localisation in plane strain stress state. It

reveals a re-orientation of the localisation plane in comparison to the standard tensile specimen by a rotation of 90° around the tensile direction.

Figure 3-39 pictures the orientation of the fracture surfaces of the investigated standard tension specimens of CR340LA. Figure 3-39a-c displays the fracture surfaces within the RD-TD-plane, whereas Figure 3-39d-f shows the surfaces within the RD-ND-plane. The specimens with a thickness of 0.6 mm and 1.1 mm present a similar fracture surface orientation of about 57° to RD (0.6 mm: Figure 3-39a and d; 1.1 mm: Figure 3-39b and e).

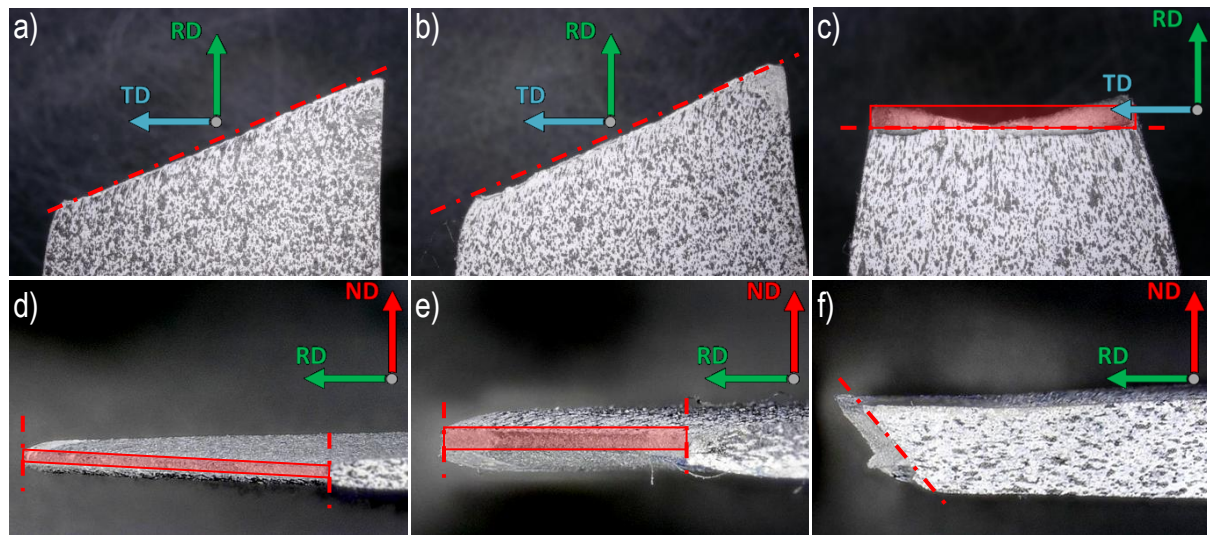


Figure 3-39: Fracture surface orientation of standard tensile specimens with different sheet thicknesses; a) 0.6 mm RD-TD-plane, b) 1.1 mm RD-TD-plane, c) 1.8 mm RD-TD-plane, d) 0.6 mm RD-ND-plane, e) 1.1 mm RD-ND-plane, f) 1.8 mm RD-ND-plane

Both surfaces demonstrate no further tilt within the RD-ND-plane. In contrast to that, specimens of 1.8 mm thickness exhibit a fracture surface orientation within the RD-ND-plane. The tilt angle amounts to 57° to RD; therefore, the fracture surface is rotated around RD with an angle of 90° in comparison to the other investigated material thicknesses.

Further observations of the fracture surface profile are conducted with OLM utilising 3D-measurements for standard tensile specimens with an initial sheet thickness of 1.1 mm. Figure 3-40a pictures the characteristic profile of the fracture surface, whereas Figure 3-40b presents the different position on the fracture surface. The OLM-measurements indicate strain localisation also to arise over the sheet thickness. The v-shape of the fracture surface alternates in specimen width direction, showing a maximum (profile down) or minimum (profile top) in the middle of the profile. Moreover, in the middle of the specimen the strongest thickness reduction is observed.

Numerical simulations with solid elements are carried out to examine the different strain localisation phenomena. The same material model is utilised for all three material thicknesses. The resulting distributions of the stress triaxiality and Lode Angle are depicted in Figure 10-5a and Figure 10-5b (appendix). The simulations reveal developing bands of increasing triaxiality and

decreasing Lode Angle respectively. These observed changes lead to a local decrease in plastic instability and failure strains. This decline influences damage accumulation within these bands and finally forces the material to fail within these developed bands. The resulting crack orientation for different sheet thicknesses of the numerical simulation agrees with the previous experimental results and is presented in Figure 10-6 in the appendix.

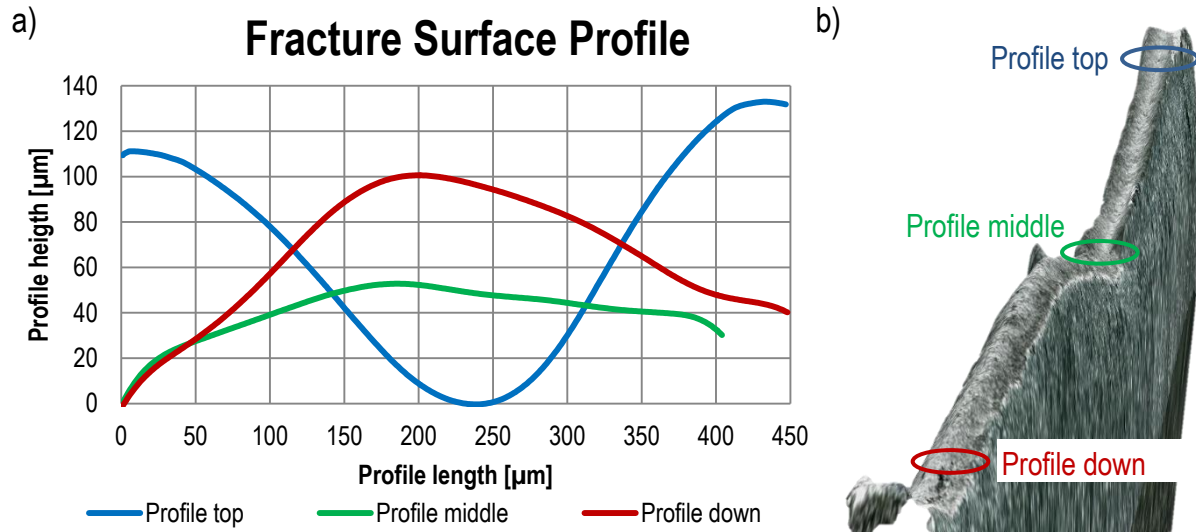


Figure 3-40: a) Profile of fracture surface in ND of specimens aligned in 0° to RD, b) 3D-OLM-measurement of fracture surface with marked measurement points

Besides OLM, SEM-images of the fracture surface are carried out for standard tension specimens in 0° to RD of CR340LA (1.1 mm) and MS1500, displayed in Figure 3-41.

Figure 3-41a pictures the fracture surface in the middle of the CR340LA specimen where a honeycomb structure indicates ductile failure. Some honeycombs prove particles on their ground which are presumed to be oxides. In Figure 3-41b SEM images of the fracture surface edge are displayed. In contrast to honeycombs at the specimen centre, near the specimen surface, the fracture surface exhibits shear comb-bands which are observed to arise with alternating band width (Figure 3-41b). The results reveal that material failure begins at the centre and spreads towards specimen surface. The SEM measurements indicate failure of the specimen surface under shear loading in contrast to its centre. Due to the development of very narrow bands in sheet thickness direction, they do not affect the DIC-measurements. Figure 3-41c represents the SEM-picture of the MS1500 specimen at its centre, where a honeycomb structure can be observed. The structure exhibits a distortion towards TD resulting from the development of shear bands during strain localisation. They lead to an opposed displacement of specimen halves in specimen width direction, which is equal to the TD for the present specimens. The distortion also affects shear combs near specimen edge. In comparison to CR340LA they are also arranged in width direction (TD). As seen for CR340LA, the SEM-results indicate material failure to start at specimen centre incorporating ductile failure as well.

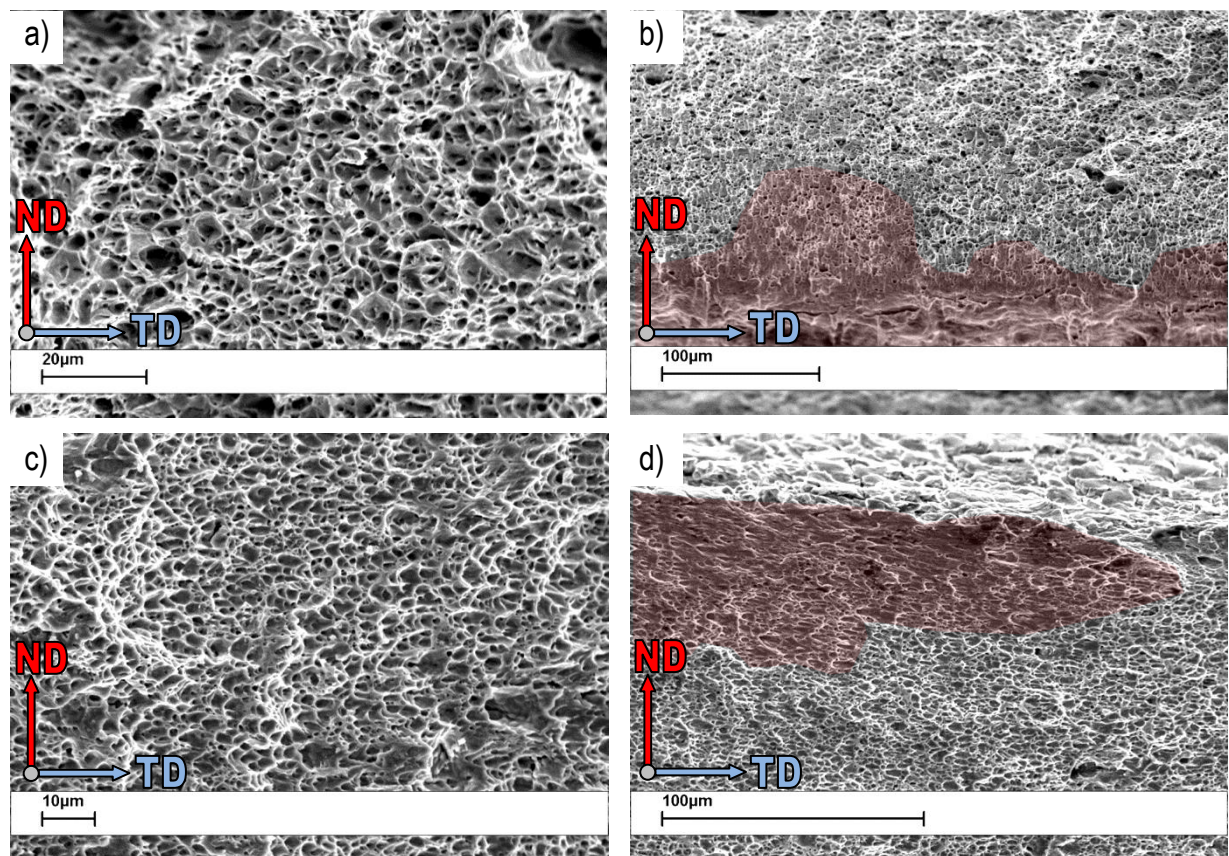


Figure 3-41: SEM-images of CR340LA in 1.1 mm and MS1500 in 1.0 mm sheet thickness at specimen centre of a): CR340LA and c): MS1500) and at the specimen edge in thickness direction of b): CR340LA and d): MS1500) with shear honeycombs marked in red

As previously presented, orientation dependent equivalent strains at fracture are obtained from DIC-measurements of standard tensile specimens of CR340LA and MS1500. Regarding the fracture surfaces of these specimens in 0°, 45° and 90° direction, SEM-images reveal a similar dependency on the honeycomb diameters than seen for equivalent strains for both materials (Table 3-11). The honeycomb diameters were determined according [Bru14] to 500 intersections of lines and honeycombs.

Additionally, the SEM-results are also depicted in the appendix in Figure 10-10. The results indicate a dependency of the size of honeycombs on the local deformation measured by DIC-method. The results concur with observations for aluminium, connecting the ductility with the honeycomb diameter [Ost14]. Furthermore, the comparison of CR340LA and MS1500 agrees with the definition that the former exhibits higher equivalent failure strains but also larger honeycomb diameters than the latter. The results further indicate an orientation dependency of ductility on all investigated levels (macroscopic / DIC, microscopic / SEM).

Table 3-11: Comparison of honeycomb diameter and failure strain

Parameter	CR340LA 1.1 mm			MS1500 1.0 mm		
Orientation to RD	0°	45°	90°	0°	45°	90°
Honeycomb diameter [μm]	2.81	3.16	2.92	1.31	2.09	1.61
True eq. failure strain [log.]	0.870	0.969	0.905	0.447	0.552	0.493

4 Plastic Instability

Elasto-plastic behaviour of metals can be subdivided into three parts: elastic, stable elasto-plastic and unstable elasto-plastic. The yield strength marks the end of elasticity and the beginning of plasticity. Due to plastic incompressibility tensile strains lead to a reduction of the materials cross section during loading. As long as the hardening rate of the material is higher than the decrease in the cross section the plastic deformation remains stable. Due to nonlinear hardening behaviour, a point exists where the reduction in cross section and work hardening cannot be balanced any longer, which leads to strain localisation and is defined as plastic instability. In standard tensile tests the uniform elongation turns into diffuse and after subsequent loading to localised necking. The transition to diffuse necking can be detected by the Considère criterion [Con85] based on the true stresses and strains.

It is widely assumed that the plastic instability marks the beginning of damage in sheet metal [Tho68]. For numerical simulation purpose an accurate prediction of the plastic instability strain is needed.

4.1 Experimental Procedure

To determine the plastic instability by DIC-measurements, different methods exist, e.g. based on the deviations of the local strain velocity. In that case, the angular bisector between two asymptotes, which approximate the strain velocity, is utilised to estimate the plastic instability point.

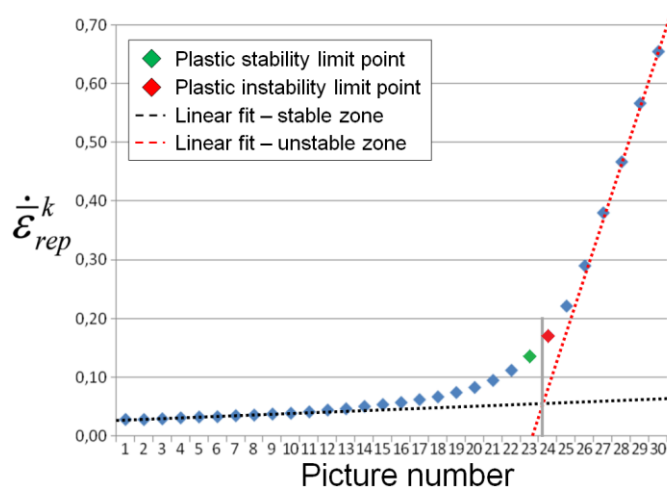


Figure 4-1: Determination of beginning plastic instability with linear curve fitting, using leastsquare method according Volk [Vol11]

For verification purpose as well as further investigations, DIC-measurements are coupled here with optical microscopy and SEM-images. To predefine the localisation zone, specimens with a notch radius of 80 mm (NR80) are used. The zinc coating was removed by hydrochloric acid and afterwards polished in 3-steps for microstructural investigations. To prepare the specimens for OLM, utilising a KEYENCE VHX-5000, the specimens were etched with Nital-2 % solution

for 30 seconds. SEM measurements are carried out with a LEO 1455VP SEM as well as a Tescan MIRA3 XMH. Both measuring devices use a Secondary Electron detector (SE-detector).

To compare macroscopic DIC-measurements with optical microscopy and SEM, a stochastic pattern is applied on one side of the uncoated and polished specimen. The tests are carried out stepwise to obtain the microstructural evolution at different strains. A picture of the microstructure is taken at each step on a predefined point on the specimen, see Table 4-1. The resulting force-displacement diagrams are presented in Figure 4-2. The arising plastic instability is initially assumed to determine the force-maximum. Therefore, the measurements are intensified around the maximum force. The testing speed conducts 0.2 mm/s, which results in 0.4 %/s referred to the initial gauge length of 50 mm.

Table 4-1: Test matrix for stepwise testing of NR80 specimens of CR340LAPB 1.1 mm

Displacement dL [mm]	0.00	1.90	2.20	2.50	2.55	2.75	3.15	3.45	3.95
Local eq. true strain [log.]	0.000	0.140	0.170	0.210	0.215	0.250	0.320	0.470	0.745

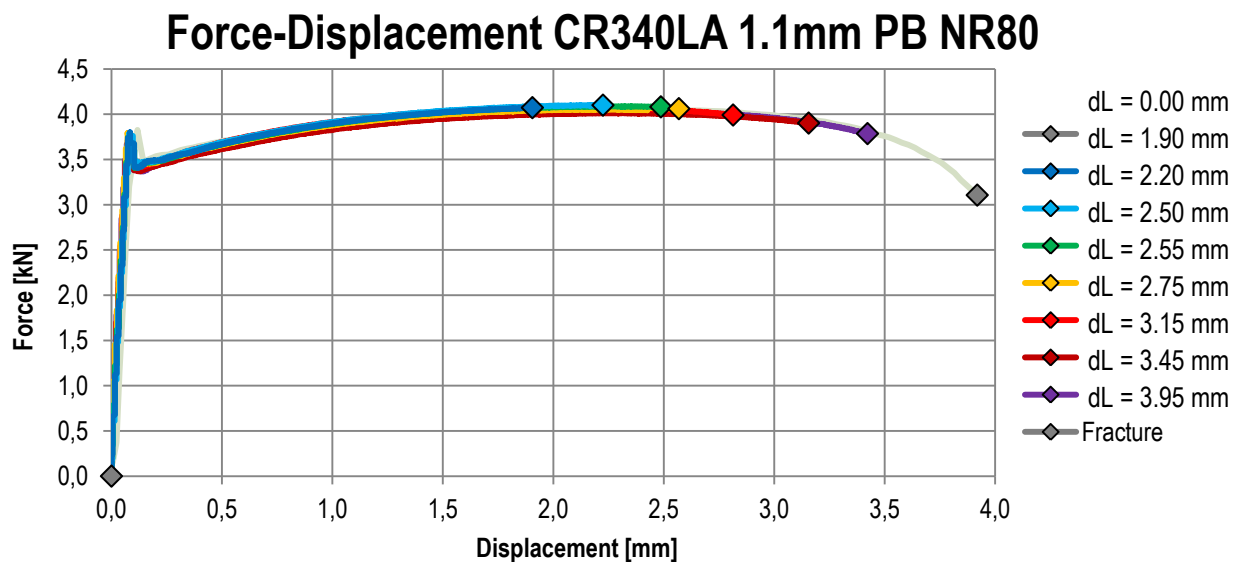


Figure 4-2: Force displacement diagrams of the investigated specimens, dots mark the end-point of loading

A fractured and polished NR80 specimen is investigated to determine the void size. The specimen shows a crack in the smallest cross section before total separation. Figure 4-3 displays the surface around the crack. Green ovals mark propagated cracks from the main crack towards the specimen edge. Around the main crack smaller (yellow rectangle) and larger (orange rectangle) ones can be seen. Small voids are also pointed out by blue triangles. Only the propagated cracks are larger than 5 μm , all others and voids measure a far smaller dispersed length. Therefore, the expected void size at plastic instability is in the range between 1 to 5 μm .

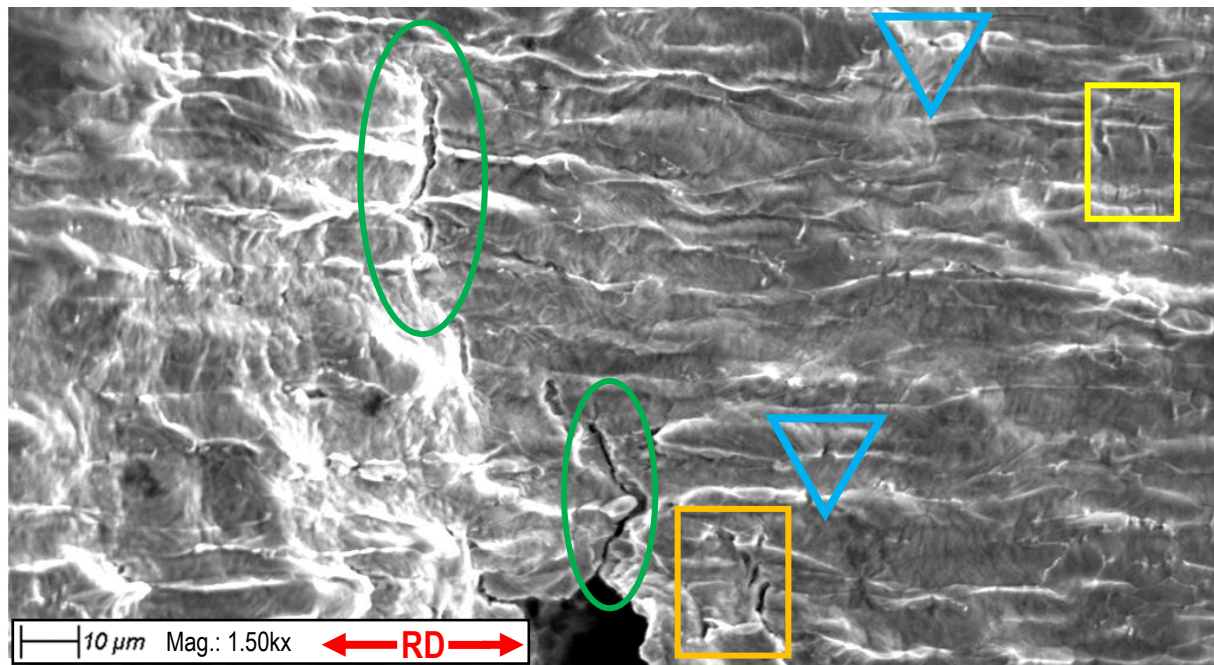


Figure 4-3: SEM-picture of fractured NR80 specimen on the polished surface, green ovals mark propagated cracks of the main crack, the yellow rectangle points small, the orange rectangle larger cracks, the blue triangles mark small voids

Figure 4-4 and Figure 4-5 present SEM-images at different pre-strain steps, which are additionally locally measured with DIC. This local measurement incorporates the strain heterogeneity of the notched specimen on macro-scale but is not able to dissolve the strain field on microstructure level. Figure 4-4 pictures the initial micro structure consisting of ferrite grains with pearlite at the grain boundaries and excavated cementite, highlighted with red circles. The undeformed material shows no signs of damage.

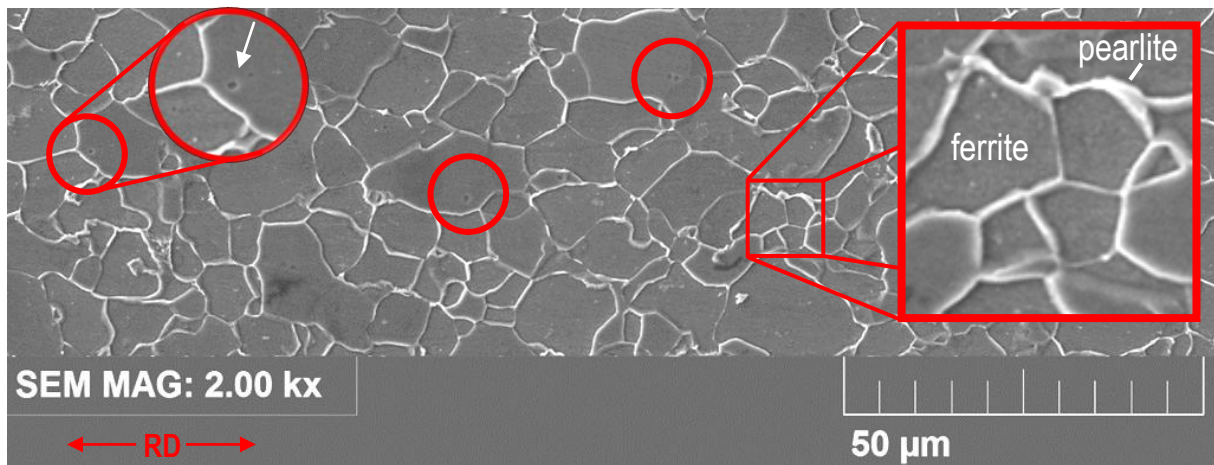


Figure 4-4: SEM-images of the initial microstructure of the investigated CR340LA in bake-hardening condition and 1.1 mm sheet thickness exhibiting ferrite grains, pearlite at the grain boundaries as well as etched cementite (red circles)

In contrast to that, first signs of damage are found after a pre-straining to 0.14 (dL = 1.90 mm). The corresponding SEM-images, pictured in Figure 4-5a and Figure 4-5b, reveal first cracks generated by cracking of pearlite on grain boundaries.

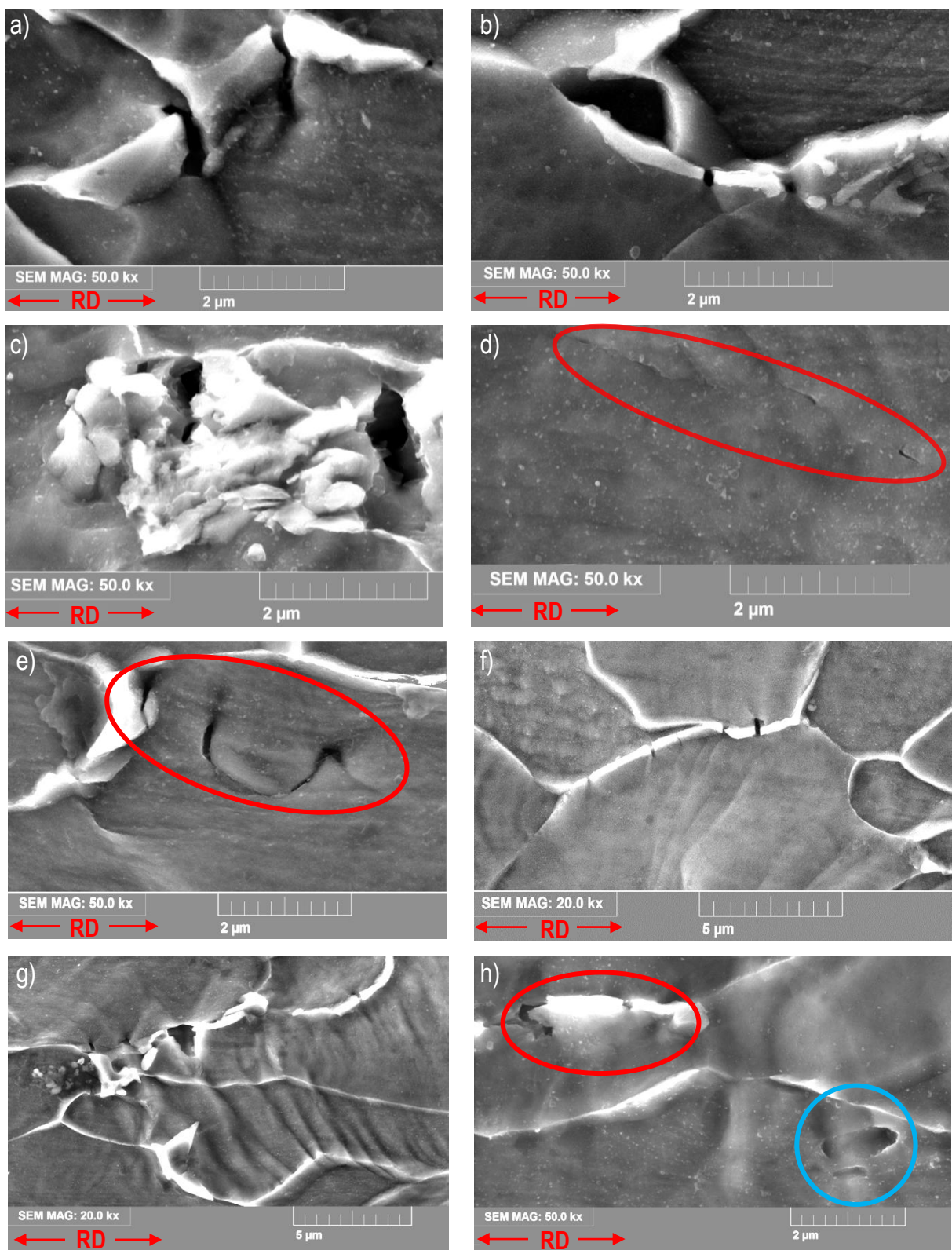


Figure 4-5: SEM-images within the strain localisation zone of NR80 specimens of CR340LA (1.1 mm) at different local pre-strains: 0.14 for a) and b), with cracked grain boundaries, 0.17 for c) and d), exhibiting a cracked grain boundary in c) and cracks within the grain in d), 0.21 for e) and f) with opened void within the grain in e) and crack grain boundaries in f), 0.32 for g) exhibiting opened voids at the grain boundary and 0.47 for h) with cracked grain boundary (red ellipsis) and crack within the grain (blue circle)

All observed cracks occur near grain boundary tripel points where strain incompatibilities can arise in conjunction with high local strains. The results of the SEM-analysis after a pre-strain of 0.17 ($dL = 2.20$ mm) are displayed in Figure 4-5c and Figure 4-5d. In comparison to a pre-strain of 0.14 ($dL = 1.90$ mm) an increase in the number of cracked grain boundaries is observed on the specimen surface. Besides the failure of pearlite on grain boundaries, first micro cracks within grains can be monitored, which are pictured in Figure 4-5d (red ellipsis). These cracks indicate the beginning damage within the grains. The assumption of beginning grain damage can be corroborated by further SEM-images. The specimen, pre-strained to 0.210 ($dL = 2.50$ mm), shows further micro cracks within the grain as well as opened cracks (Figure 4-5e, red ellipsis). Besides the development of micro cracks, the number of cracked pearlite on grain boundary increases further. In Figure 4-5f an additional cracked grain boundary is depicted, where the cracks not necessarily arise at the triple-boundary. Figure 4-5g depicts the micro-structure after a local pre-strain of equivalent strains of 0.32 exhibiting open voids at the grain boundary. In addition, Figure 4-5h pictures the pre-strained microstructure after local equivalent true strains of 0.47, where a cracked grain boundary (red ellipsis) and a neighbouring crack within the grain (blue circle) are witnessed.

Besides the evolution of voids and micro cracks, beginning inter-grain strain incompatibilities are monitored. Figure 4-6 exemplarily indicates the development of these incompatibilities. The involved grains are marked in green, red and blue. During straining, the grains in green and blue show only few slip lines, whereas the red grain exhibits a high density of them. The pile up of dislocations leads to high local stresses at the grain boundary supporting the nucleation of voids and promoting microstructural damage.

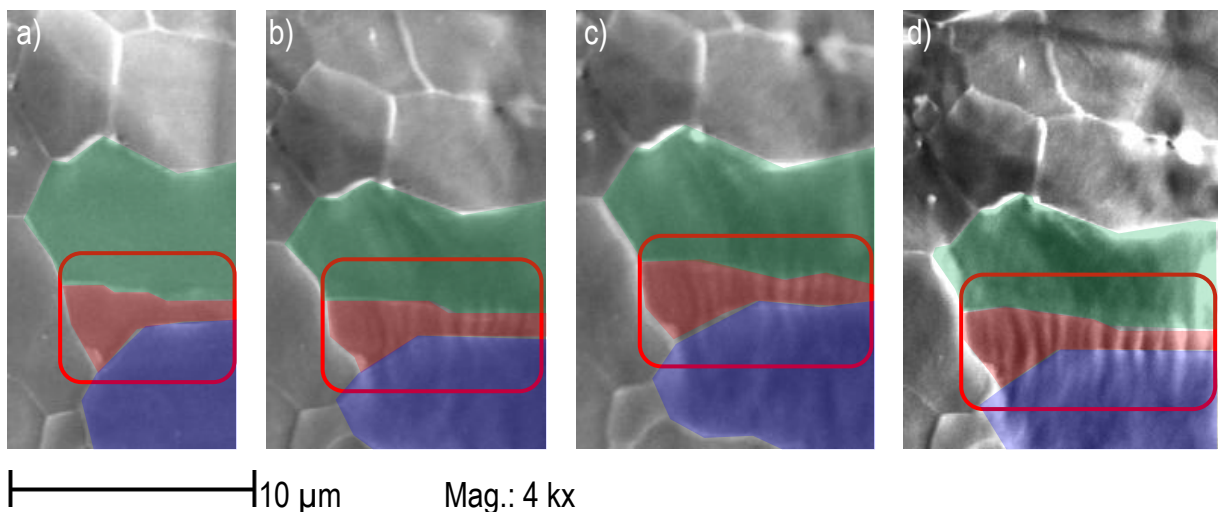


Figure 4-6: Evolving strain incompatibilities between three grains marked in green, red and blue (red rectangle) at different local true equivalent strains of one specimen a) 0.00, b) 0.14, c) 0.17, d) 0.30

In the light of the carried out SEM-results the DIC-strain fields, which are obtained in parallel, are evaluated, focussing on the local strain behaviour of the fracture zone. There, the local major versus minor strain behaviour is investigated further and depicted in Figure 4-7. The principle strain path subdivides into a linear and a non-linear part. The linear strain behaviour is obtained

at low, the non-linear strain path at elevated local strains. The deviation from linear strain path is accompanied by increasing strains in specimen thickness direction. The observed local strain state change is directly linked to a change of the local stress state irrespective of the assumption of associated or non-associated plasticity.

Regarding the depicted strain paths of the NR80 specimen, as depicted in Figure 4-7, the deviation from the linear strain path is observed at global displacements of 2.75 mm, which corresponds to local major strains of 0.25. The parallelly conducted SEM-images reveal the cracking of pearlite and micro cracks within grains within the linear strain range as well as prior to force maximum. Therefore, the observed onset of microstructural damage does not indicate damage of the continuum. The witnessed cracks result from arising strain incompatibilities between different grains. Mechanisms on micro-scale, e.g. strain hardening of single grains or microstructural reorientation, compensate damage of the microstructure and lead to unaffected macroscopic strain behaviour. These effects are captured on macroscopic scale by strain hardening. Moreover, straining affects the specimen geometry, but not the measured local strain paths and therefore the local stress state. Therefore, the onset of damage of the continuum and plastic instability respectively is further defined by the strains where micro-scale mechanism cannot balance out microstructural damage and becomes dominant for macroscopic material behaviour, leading to a strain state change. Hence, the arising deviation from linear strain path is further defined as the onset of plastic instability.

The determined instability point for the NR80 specimen arises at displacements beyond the force maximum. The definition of arising plastic instability by deviations from a linear strain path is applied to additional specimen types revealing a similar behaviour as observed by NR80 specimens. Figure 4-7 pictures the strain paths of A50, NR80 and NR05 specimens in 0° to RD, where the linear strain paths are marked by a dotted line. The local strain paths for all specimens, including shear- and Bulge-tests, are pictured in Figure 10-13 in the appendix.

Principle strain paths of CR340LA in 0° to RD

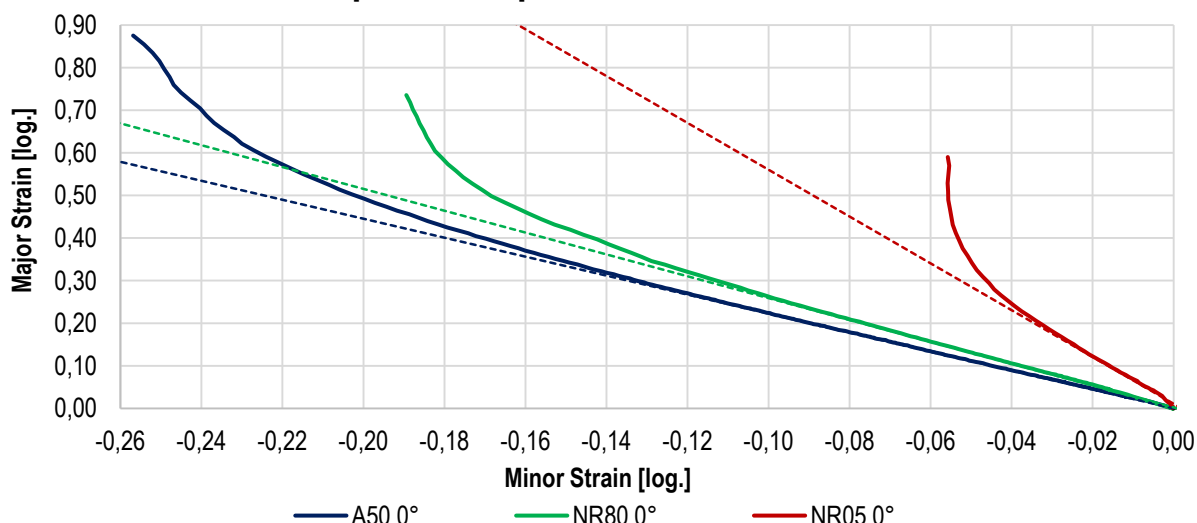


Figure 4-7: Major versus minor local strain behaviour of A50, NR80 and NR05 specimens 0° to RD with linear strain behaviour as dotted lines

Figure 4-8 shows the determined plastic instability points for different specimens and directions, depending on the estimated stress triaxiality. The investigation reveals decreasing plastic instability strains from uniaxial tension (A50 specimens, $\eta = \frac{1}{3}$) towards plane stress (NR05 specimens, $\eta = \frac{1}{\sqrt{3}}$). For biaxial tension, a strong increase of plastic instability strains is observed compared to NR05 specimens. The method is applied further on shear specimens for which no linear strain behaviour could be obtained. Conducted numerical simulations reveal a stress state change at even low equivalent strains. The stress state change affects the strain behaviour, which superimposes strain state change due to the onset of damage.

The determined plastic instability point arises beyond force maximum for standard tensile as well as NR80 specimens. The investigated A50 specimen in 0° to RD exhibits the UTS at 0.16 technical and 0.20 of true strains. Neither the representation in technical nor in true strains meets the onset of damage at true strains of 0.27 as predicted by local strain deviation method. The results indicate that the onset of diffuse necking is not connected to arising damage of the microstructure but only depends on material strain hardening. Thus, the Considère criterion only predicts the onset of diffuse necking which is strongly geometry dependent. The examination further reveals a discrepancy between onset of diffuse necking, corresponding to UTS for standard tension specimens, and plastic instability (Figure 10-17 to Figure 10-31, presented in the appendix).

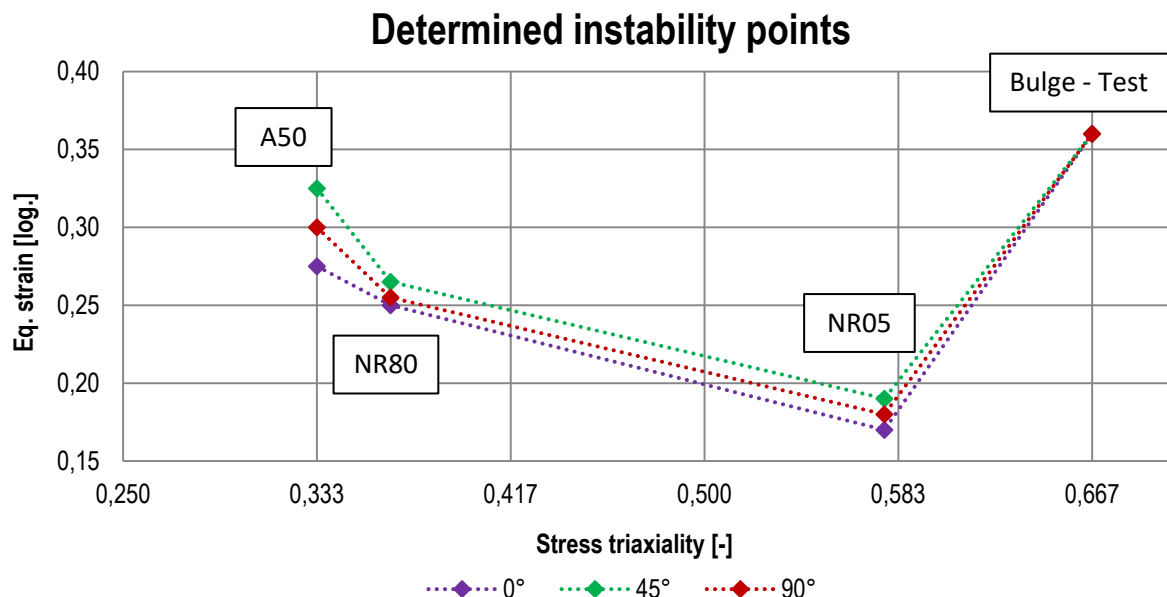


Figure 4-8: Determined instability points for standard tensile (A50), notched (NR05, NR80) and biaxial specimens in 0° , 45° and 90° to RD manufactured from CR340LA with a sheet thickness of 1.1 mm

Besides the strains at UTS, the predicted plastic instability point exhibits an orientation dependency. For the present CR340LA only small deviations of about 0.05 of equivalent strains are observed at A50 specimens (Figure 4-8). For all specimens except biaxial tension, the highest plastic instability strains occur in 45° , the lowest in 0° to RD. The results concur to the experimentally obtained Lankford-Coefficients, which exhibit their maximum in 45° to RD and their

minimum in 0° direction. The high R-values lead to plastic deformation mainly in specimen width- and not in sheet thickness direction. Especially arising strains in thickness direction facilitate plastic instability. This can be proven by the comparison of instability strains of standard tensile specimens, mainly deforming in specimen width direction, and NR05 specimens which exhibit only strains in sheet normal and nearly none in specimen width direction. The stabilising effect of high R-values on the strain behaviour is also reported by [Tas09], [Bee10], [Kan13].

The proposed method, based on strain state changes, is utilised for CR340LA with the three investigated sheet thicknesses of 0.6 mm, 1.1 mm and 1.8 mm to determine the dependency of the onset of plastic instability and sheet thickness. No differences of specimens in 1.1 mm and 1.8 mm concerning plastic instability strains are observed for all directions. In contrast to that, specimens with a sheet thickness of 0.6 mm show a drop of plastic instability strains of 0.04, see Figure 10-16 in the appendix. Due to similar strain hardening behaviour, neither the effect of deviating Lankford-Coefficients nor the geometrical aspects of differing sheet thicknesses are identified to mainly affect plastic instability. The results indicate the strain hardening behaviour as driving force affecting the onset of damage of the continuum.

The utilised method is applied further to the investigated MS1500 steel to determine plastic instability. Figure 4-9 presents the local strain behaviour of standard tensile, NR80, NR05 and Bulge-specimens. For A50, NR05 and Bulge specimens a nearly linear strain path is observed almost up to fracture. In contrast to that the local strain path of NR80 begins to deviate from linearity at relatively low strains, which results from the formation of localisation bands affecting opposed displacements of the specimen halves influencing measured surface strain behaviour. This opposed displacement as well as the connected specimen transverse strains are compensated by relating the transverse displacement to the specimen width. A linear strain path as a result follows for NR80 specimens too. The lack of strain path changes despite the development of strain localisation bands points to a similarity of plastic instability and failure strain surface.

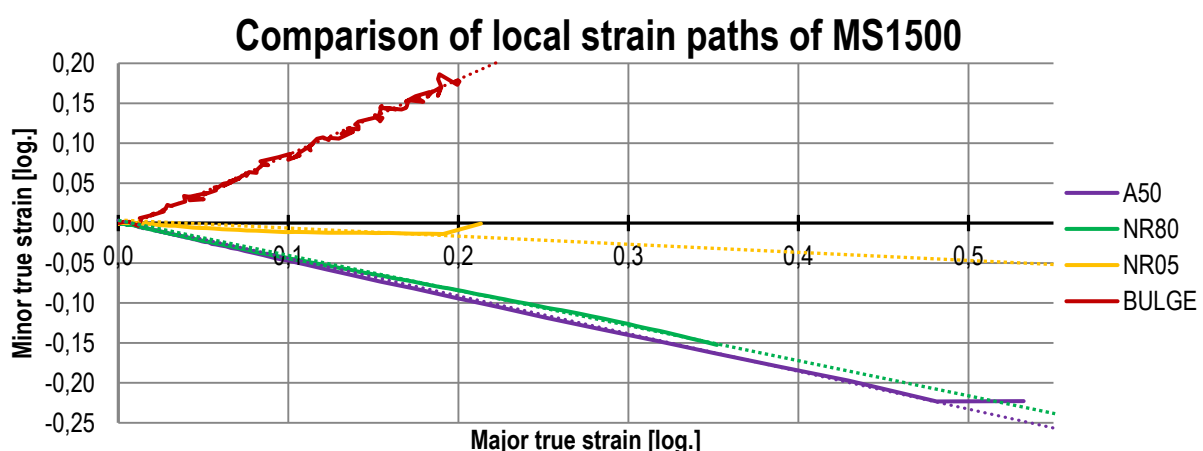


Figure 4-9: Local principle strain path of A50, NR80, NR05 and Bulge specimens of MS1500 in BH0 condition with linear strain behaviour as dotted lines

4.2 3D-Extension of the Marciniak-Kuczynski model

To predict the onset of plastic instability, different criteria have been developed over the years. A first simple criterion was proposed by Considère in 1885 which connects the onset of plastic instability in uniaxial tension with the hardening behaviour [Con85]. Based on shear stresses and incremental strains, Swift proposed an approach to predict plastic instability [Swi52]. In contrast to that, Hill [Hil58] defined the loss of uniqueness of a velocity boundary-value problem as instability point in 1958.

By considering geometrical heterogeneities, an approach for sheet metals was presented by Marciniak and Kuczynski in 1967 [Mar67]. The model approach assumes a grooved sheet with infinite width, pictured in Figure 4-10a. The ungrooved section is called section A, the grooved section calls section B. The model implies a force-equilibrium between section A and B in principle loading direction as well as a geometrical boundary condition leading to equal strains in width direction. Due to the force-equilibrium, the ratio of the first principle stresses of section A and B is equal to the inverse thickness ratio f of both sections. The initial thickness ratio f_0 typically ranges from 0.980 to 0.999. During straining the thickness ratio evolves dependent on strains in thickness direction (4-1).

$$f = f_0 \cdot e^{\int_0^t (d\epsilon_{zB} - d\epsilon_{zA})} = \frac{t_B}{t_A} \cdot e^{\int_0^t (d\epsilon_{zB} - d\epsilon_{zA})} \quad (4-1)$$

The equivalent strains of both sections, $d\epsilon_B$ and $d\epsilon_A$, are calculated based on the plastic potential, which defines the beginning plastic instability by a critical ratio of 10 of $d\epsilon_B$ to $d\epsilon_A$.

The Marciniak-Kuczynski model (MK model) only applies for the plane stress state and should therefore only be adopted by solid simulations for materials without a Lode Angle dependency. For numerical simulations with solids, using LS-DYNA and the GISSMo, the MK model is extended to obtain a Lode Angle dependent plastic instability surface within the mixed-stress-strain space. Therefore, additional stress and resulting strain components are introduced in z-, xz-, and yz-direction, see Figure 4-10a. Due to force equilibrium, the ratio of yz-shear stresses of section B to A results from the thickness ratio f . In contrast to that, the same stress components in z- as well as xz-direction are presented for both sections A and B. For each section the plastic potential for 3D-stresses follows the equation (4-2):

$$\sigma d\epsilon = \sigma_{xx} d\epsilon_{xx} + \sigma_{yy} d\epsilon_{yy} + \sigma_{zz} d\epsilon_{zz} + \sigma_{xy} d\epsilon_{xy} + \sigma_{xz} d\epsilon_{xz} + \sigma_{yz} d\epsilon_{yz} \quad (4-2)$$

To define the plastic instability surface within the mixed stress-strain-space, the stress triaxiality as well as Lode Angle Parameter dependency of the principle stresses is applied according to [Mar15a]. Due to convention, the first principle stress defines the loading direction. To define the local stress composition for 0° direction, the first principle stress is defined in material x-, the second principle stress in y- and the third principle stress in z-direction. For diverging directions, e.g. 45° or 90° to RD, the local stress tensor of the 0° direction is transformed by the rotation tensor $[Q]$, which describes a rotation around sheet metal normal direction.

The resulting plastic instability surfaces exhibit their maxima at Lode Angle Parameters of -1 and 1. The surface exhibits its minimum for Lode Angle Parameters of 0, which corresponds to

the plane stress state. Furthermore, the surface declines dependent on the stress triaxiality. The calculated instability surface, presented in Figure 4-10b, shows a good qualitative agreement with literature; see [Mar15b] and [Dun14].

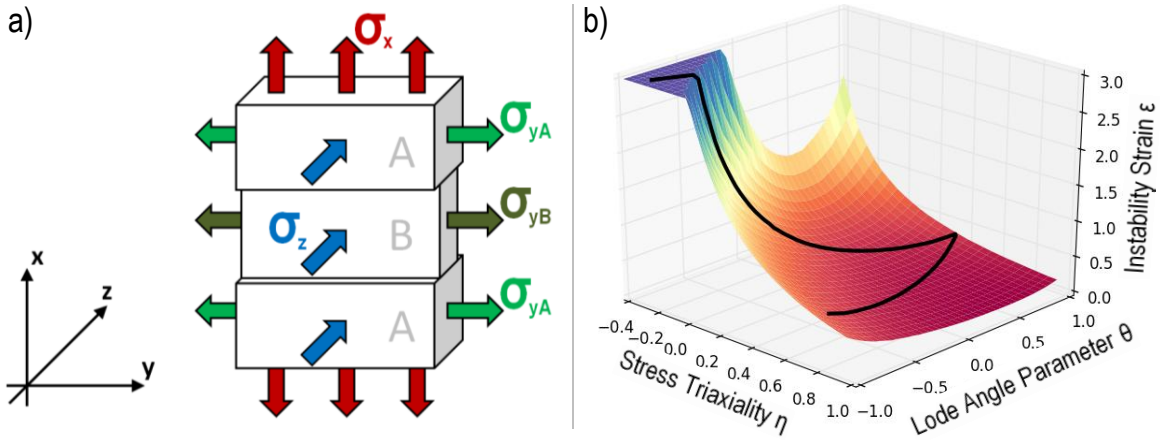


Figure 4-10: a) Schematic applied stress of extended Marcinia-Kuczynski model, b) Calculated plastic instability surface within the mixed-stress-strain-space, with a cut-off at strains over 3.0 for an 3D-stress state with highlighted plane stress state

In Figure 4-11, the orthotropic plastic instability curves for CR340LA in 1.1 mm sheet thickness and plane stress condition are presented. Coloured dots mark the experimentally obtained plastic instability points for the different directions. The predicted curves meet the experimental target points with a mean deviation of strains less than 0.04. Regarding the biaxial stress state, the three curves do not coincide, which is a model based short coming, resulting from varying stress states in section B during biaxial straining.

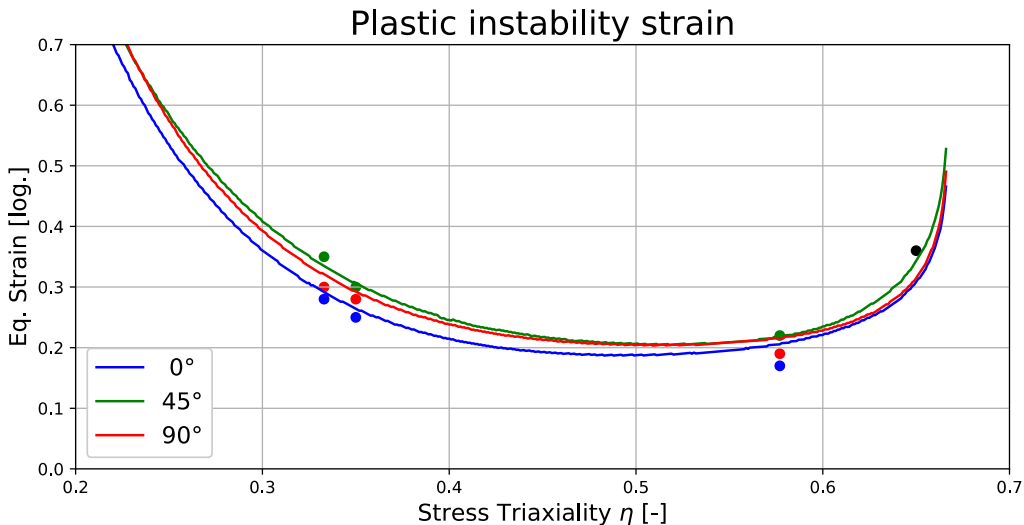


Figure 4-11: Comparison of experimental and proposed plastic instability strains for CR340LA with 1.1 mm sheet thickness with the plane stress state as basis

Due to its general formulation, the extended MK model is able to predict plastic instability strains for 6D- (e.g. Figure 4-10b) as well as plane-stress states (e.g. Figure 4-11). Their opposition along the plane stress path reveals similar behaviour for stress states between uniaxial and biaxial tension. Both exhibit their minimum dependent on the anisotropy, around the plane strain

stress state. For triaxialities lower than $\frac{1}{3}$ (uniaxial tension), the plastic instability strains of plane- and 6D-stress states differ. Whereas increasing plastic instability strains arise for plane-stress states, the 6D-pendant presents a local minimum in shear. The differences result from the definition of the principle stresses with $\sigma_1 \geq \sigma_2 \geq \sigma_3$. The plane stress state leads to one principle stress equal to zero. Both remaining principle stresses for stress states between uniaxial and biaxial tension are larger than zero, which results in $\sigma_1 \geq \sigma_2 \geq \sigma_3 = 0$. The shear stress state, in contrast, results in two principle stresses of equal absolute value but opposite sign. The order of the principle stresses of 6D-stress states follows $\sigma_1 \geq \sigma_2 = 0 \geq \sigma_3 = -\sigma_1$. In contrast to that, plane stress states (plane-stress states) do not exhibit a third principle stress component, resulting in $\sigma_1 \geq \sigma_2 = -\sigma_1$. Therefore, different loadings arise for plane- and 6D-stress states which explain the differences of the proposed plastic instability strains. Furthermore, a reordering of principle stresses to obtain similar behaviour for plane-stress states is not suitable due to arising jumps within the resulting plastic instability strain surface.

Additionally to CR340LA, the extended MK model is applied on the investigated MS1500-steel, calibrated by the experimental results of chapter 3.1.5. The yield surface shape is determined by the nominal stress maxima of A50, NR80, and NR05 specimens. Hence, strain hardening is determined in 0° , 45° and 90° to RD from standard tensile specimens. The resulting plastic instability strains overshoot the equivalent strains at material fracture, which coincides with the experimentally determined plastic instability point. Hence, for further material modelling, the definition of equivalent material failure strains is equal to equivalent strains at plastic instability.

5 Experimental Determination of Load-Paths

Recent failure criteria predict strain localisation as well as the fracture points based on the assumption of proportional load paths meaning constant stress triaxiality and Lode Angle Parameter. In contrast to that, the investigations of Behrens and Peshekodov [Beh16] revealed considerable load path changes for typical flat specimen geometries dependent on the specific geometry. Specimens with different initial triaxialities are utilised for material characterisation purpose to determine plastic behaviour and the failure point, despite exhibiting load path changes.

The Lankford-Coefficient R describes the strain behaviour in uniaxial tension by representing the plastic strain ratio in specimen width to thickness direction (chapter 2.2) and evolves during straining as described in chapter 3.4. The slight increase up to UTS is followed by a decrease with the onset of localised necking, incorporating a stress state change.

With regard to recent yield criteria for metals, which incorporate associated plasticity, the R-value describes the vector normal to the yield surface in uniaxial tension [Hil92] irrespective of isotropic or anisotropic plastic behaviour. This vector corresponds to the plastic strain increment. Thus, it can be calculated for any point on the yield surface but loses its validity as Lankford-Coefficient. The dependence of the Lankford-Coefficient on the principle loading direction as well as the stress state is utilised to estimate the surface load path and the surface failure point based on DIC-data. To describe the 3D surface strain state, the R- and the Γ -value have to be modified, which describe the ratio of in-plane shear strain to strain in loading direction. Both strain ratios are defined within the specimen coordinate system, which is substituted further by the material coordinate system. The resulting quotients R^* and Γ^* are presented in equation (5-1) and (5-2).

$$R = \frac{d\epsilon_{\text{Specimen TD}}}{d\epsilon_{\text{Specimen ND}}} \rightarrow R^* = \frac{d\epsilon_{\text{material TD}}}{d\epsilon_{\text{material ND}}} = \frac{\frac{\partial \bar{\sigma}(\sigma_{xx}, \sigma_{yy}, \sigma_{xy})}{\partial \sigma_{yy}}}{\frac{\partial \bar{\sigma}(\sigma_{xx}, \sigma_{yy}, \sigma_{xy})}{\partial \sigma_{zz}}} = \frac{d\epsilon_{yy}}{d\epsilon_{zz}} \quad (5-1)$$

$$\Gamma = \frac{d\epsilon_{\text{Specimen IPS}}}{d\epsilon_{\text{Specimen loading}}} \rightarrow \Gamma^* = \frac{d\epsilon_{\text{material IPS}}}{d\epsilon_{\text{material RD}}} = \frac{\frac{1}{2} \frac{\partial \bar{\sigma}(\sigma_{xx}, \sigma_{yy}, \sigma_{xy})}{\partial \sigma_{xy}}}{\frac{\partial \bar{\sigma}(\sigma_{xx}, \sigma_{yy}, \sigma_{xy})}{\partial \sigma_{xx}}} = \frac{d\epsilon_{xy}}{d\epsilon_{xx}} \quad (5-2)$$

Each plane stress state can be described by using R^* and Γ^* but both lead to identically modified strain ratios for similar principle loading directions in pressure and tension. Therefore, the sign of the strain component in rolling direction is utilised to identify the principle strain direction. Due to the assumption of associated plasticity, the components of $d\epsilon$, and therefore R^* and Γ^* , define the normal vector on the yield surface [Bar91]. For demonstration purpose the modified Lankford-Coefficients along the yield surface shape within the σ_x - σ_y -space, utilising the von Mises-yield criterion, are calculated. Due to constant shear stresses equal to zero, the Γ^* -value is not presented in Figure 5-1. The double occurrence of the modified Lankford-Coefficient is depicted in Figure 5-1a. In contrast to that, Figure 5-1b presents the trend of R^* along the yield surface. For both pictures, the two equally modified Lankford-Coefficients R_1^* and R_2^* are highlighted in red (tension) and green (pressure).

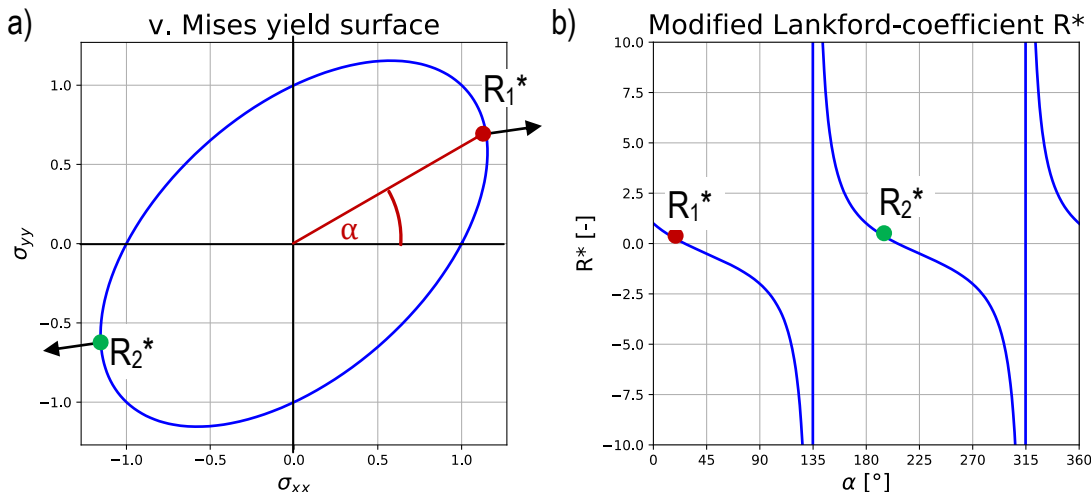


Figure 5-1: a) Same R^* -values on yield surface with pictured direction of angle α , b) modified Lankford-Coefficient R^* as a function of angle α with two marked stress states with identical absolute value of the stress triaxiality in pressure (green) and tension (red)

To couple the DIC-measurements with the stress states, an appropriate yield criterion has to be employed. Due to its coupling of stress state and plastic strain behaviour, it has to cover the main material effects, e.g. orthotropic yielding, the evolution of the yield surface during straining or pronounced non-associated plasticity. In the present investigation, the Barlat'91-plasticity model is applied, which accounts for orthotropic yielding and implies associated plasticity. The previous investigations revealed minor yield surface distortions during straining up to UTS. Therefore, a constant yield surface shape is assumed further, which is determined by the maximum of the nominal stress of the flat tension specimens (A50, NR80 and NR05) for all three directions.

To define the load paths on the basis of DIC-measurements, the local strain behaviour of the failure point is used, exhibiting the strongest strain path change. Moreover, the strong strain path change also indicates a strong load path variation in comparison to other, less affected, points of the surface strain field. The strain path, measured by DIC, shows a superimposed random noise which affects the resulting load paths. To minimize scattering, the local strain paths are smoothed. Figure 5-2a presents the determined load paths of CR340LA (1.1 mm) of all conducted specimen types, aligned in 0° to RD, which are coloured dependent on the specimen type. Except for shear loadings, all load paths initially exhibit a proportional load path at low equivalent strains, which tends stress state dependent towards the biaxial stress state except for the Bulge-test. The bending point concurs with the presented experimentally obtained plastic instability points in chapter 4.1. This observation is also valid for the plane stress state (NR05 specimens), in which the failure surface demonstrates its minimum. Moreover, the load path of the Bulge-test tends towards the plane strain stress state, exhibiting the smallest change of the stress triaxiality. The largest stress state change is found for shear-specimens, ranging from 0.05 to 0.45. As a result, a kink within the determined surface load paths in uniaxial tension is observed.

Figure 5-2b opposes the load paths of DIC-measurements and numerical simulation. The opposition reveals a shift of the experimentally determined load paths towards higher stress triaxialities. The shift results from e.g. diverging R-values in uniaxial tension of the experiment and the mathematical model due to the calibration by nominal stresses. However, both load paths reveal a similar trend up to failure.

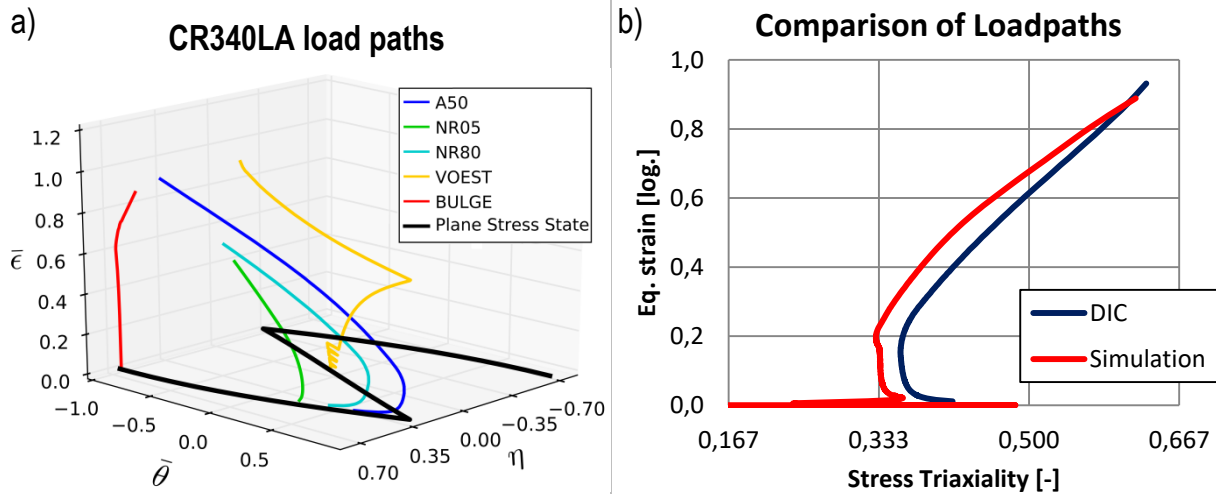


Figure 5-2: a) Load paths of A50, NR80, NR05, Bulge and shear specimens of CR340LA in 1.1 mm sheet thickness, b) opposition of experimental and computed load paths of standard tension specimens

For the standard tension test, due to the assumption of a proportional uniaxial load path ($\eta = \frac{1}{3} = \text{constant}$ and $\frac{d\epsilon_1}{d\epsilon_2} = \frac{\epsilon_1}{\epsilon_2}$), it is common to calculate the R-value directly from the plastic strains instead of the plastic strain increments, which is the case because of the equivalence of their ratios. The R^* - as well as Γ^* -values are also defined by the components of the natural plastic strain increment tensor. Therefore, both are linked to the actual trend of the load paths. To estimate the failure surface (6D-stress state) or curve (plane stress state) respectively of the non-proportional load paths, it is necessary to include their history.

To assess the main part of each load path, a linear dependency of the failure strain on the R^* - as well as Γ^* -value is assumed. Based on this approximation, the history of the non-proportional load paths is included by utilising the plastic strains instead of its increments. A detailed description can be found in the appendix in chapter 10.4. This definition weighs each calculated stress state and leads to an effective load path including the load path history. To visualise the weighing of the stress states, Figure 5-3 exhibits two proportional load paths and one non-proportional one incorporating linear damage accumulation. Failure strains of 2.0 and 1.0 respectively are defined for both proportional load paths and a linear behaviour of failure strains in between. The failure point, which conforms to 100 % of damage, is marked with a square; a circle highlights 50 % of damage.

Combining both proportional load paths, 1 (blue) and 2 (red), at 50 % damage leads to the two stage non-proportional load path highlighted in green. Due to the stress state dependent damage accumulation the predicted failure strain does not coincide with the pre-defined failure strain

curve. The non-proportional load path corresponds to the average of both proportional load paths, because of the linear relationship of failure strain and modified Lankford-Coefficient. To estimate the failure strains of proportional load paths the stress states are calculated from the local strains instead of their increments.

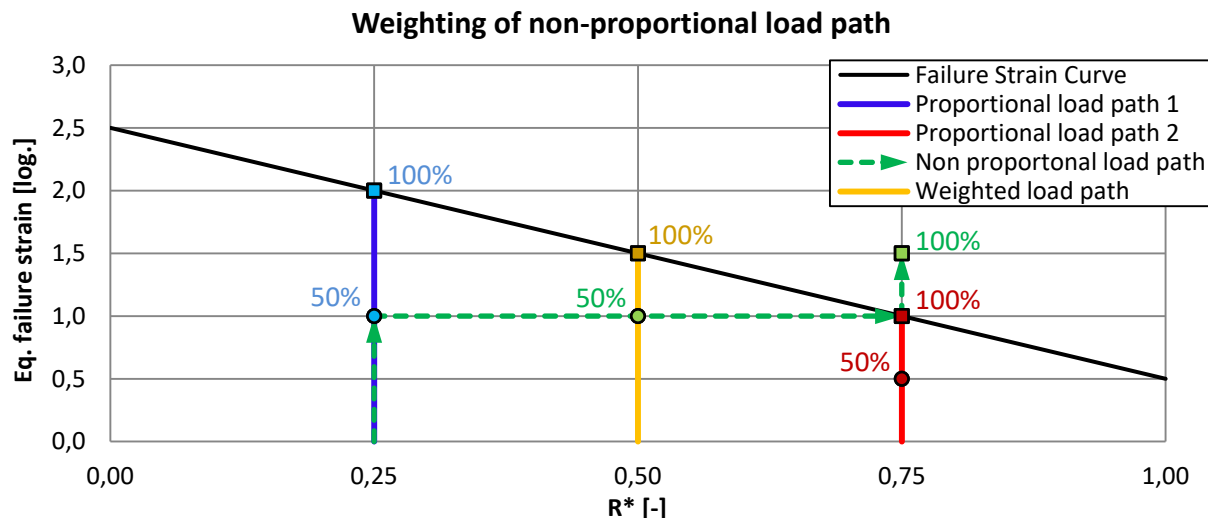


Figure 5-3: Visualisation of the weighting of the stress states by accumulating the plastic strain increments of linear strain paths

The surface strain fields of specimens with principle loading direction in 0° to RD are utilised to determine the load paths of CR340LA specimens with a sheet thickness of 1.1 mm. The resulting weighted load paths are depicted in Figure 5-4 including the applied failure curve for shell simulation (chapter 7.2.1). The criterion to define the failure strain curves for the numerical simulations is presented in chapter 6. For all specimens, except shear, the specimen loading direction coincides with the principle stress direction of the fracture zone. In contrast to that, shear specimens exhibit a principle stress direction, diverging from loading direction. Due to the use of a double-shear-specimen, both shear sections have to be regarded separately. They are named VOEST1 and VOEST2 for voest-shear specimens, and SDR1 and SDR2 for SDR-specimens. Therefore, their local strain tensors are transformed, applying a rotation of $+45^\circ$ for shear section VOEST1 and -45° for shear section and VOEST2 respectively. Hence, loading directions of 0° to RD for shear section VOEST1 and 90° to RD for shear section VOEST2 is obtained for shear specimens aligned in -45° to RD.

The determined fracture points, marked by coloured rectangles, and the applied failure curve are compared further. Both, NR05 and Bulge-test, reveal a relatively proportional weighted load path, resulting in a good correlation of failure point and failure curve. Regarding the A50 load path (standard tensile specimen), it reveals an overestimation of the failure strains of 0.075 as well as of the stress triaxiality of 0,02 at failure point. In contrast to $\frac{1}{3}$ (uniaxial tension), the initial triaxiality conducts 0.37. This indicates a slight deviation of plastic strain behaviour and yield surface shape, which can result from initial errors of yield surface shape, its evolution during straining or non-associated plasticity. In contrast to the weighted load paths of standard tensile, the ones of NR80 specimens agree with the applied failure surface, especially if it is shifted by a

stress triaxiality of -0.02 in the present case. The weighted load paths of voest-shear specimens are pictured in Figure 5-4 revealing an overestimation of the failure point. These results concur with the numerical simulations, conducted in chapter 7.2.1, in which too low failure strains are obtained from the numerical simulation to meet the force-displacements.

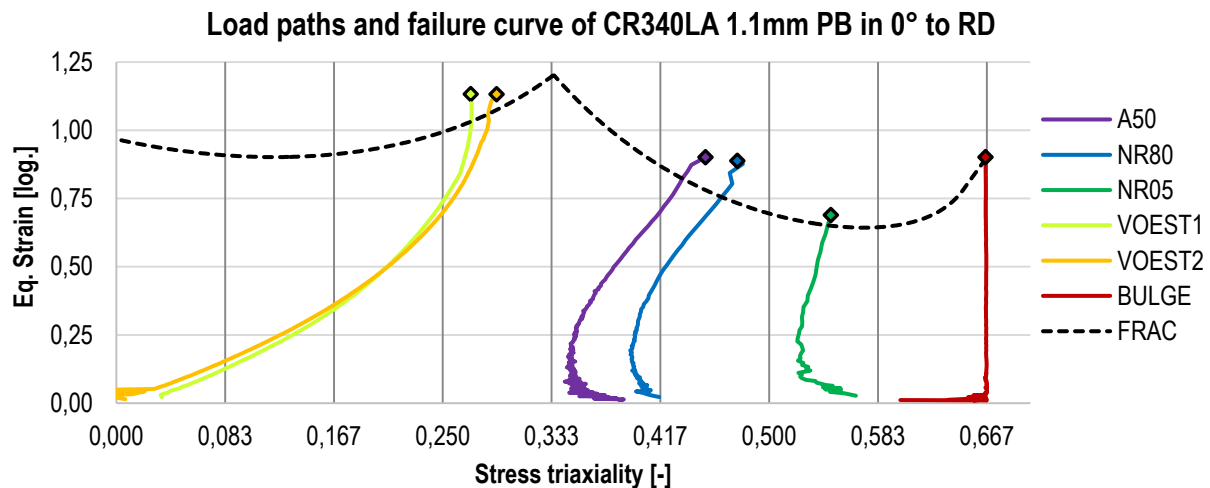


Figure 5-4: Determined effective load paths, based on DIC-measurements with additional defined fracture curve of CR340LA in 0° and bake-hardening condition

Moreover, the weighted load paths for the investigated MS1500 in 0° to RD are determined and depicted in Figure 5-5. As previously seen, the load path of the standard tensile test does not meet a stress triaxiality of $\frac{1}{3}$ (uniaxial tension). A50 specimens also exhibit lower failure strains than NR80 specimens, which cannot be captured by the failure surface. However, the determined failure points of NR80, NR05, SDR and Bulge test agree with the applied failure curve later on.

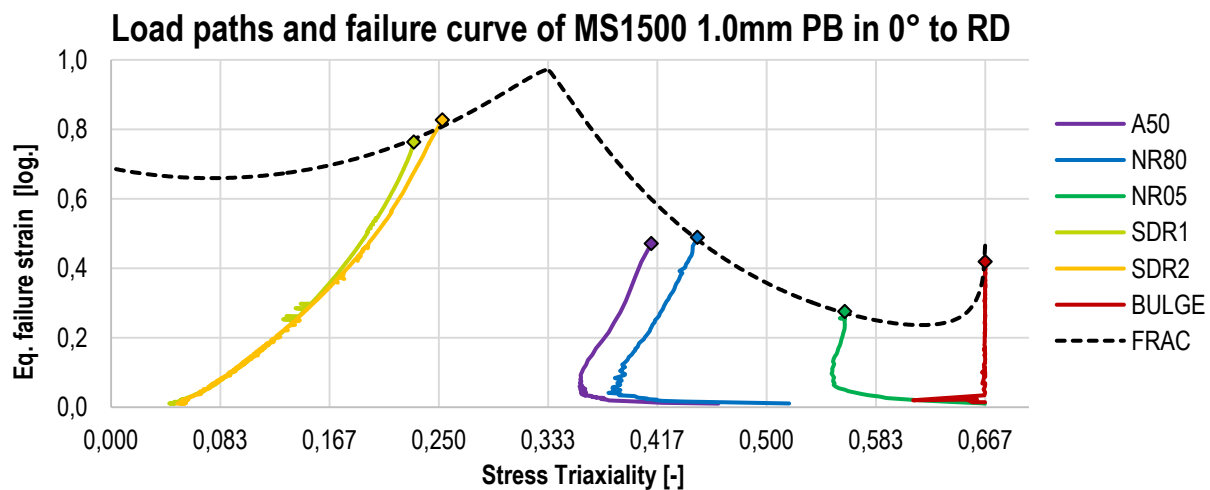


Figure 5-5: Determined effective load paths, based on DIC-measurements with additional defined fracture curves of MS1500 in bake-hardening condition and 90° to RD

6 Failure Characterisation

To describe failure of metals, different approaches have been proposed. As McClintock [McC68] observed, the main causes for ductile fracture are the growth and coalescence of voids. Based on this observation, Gurson [Gur77] proposed a model approach, which includes these mechanisms of failure. The model was refined by Tvergaard [Tve81] and Needleman [Nee87] who replaced the void volume fraction by a modified damage parameter [Fes08].

Further phenomenological approaches describe material failure directly by failure strain surfaces dependent on stress triaxiality and Lode Angle Parameter. To obtain this failure strain surface, Basaran [Bas11] utilised a Kriging-approach based on experimental results. A further approach bases on the Mohr-Coulomb model, which was originally used to describe soil mechanics, but was extended to describe ductile fracture of metals. A detailed description of the Extended Mohr-Coulomb model (EMC) can be found in [Wie10] and [Dun11].

A modification of the EMC model was proposed by Marcadet [Mar15b], in which the von Mises plasticity term is replaced by $\bar{\sigma}_{HF}$, the equivalent stress of the Hosford yield criterion. The resulting criterion is therefore called Hosford-Coulomb model (HC) and is presented in equation (6-1).

$$\bar{\sigma}_{HF} + c \cdot (\sigma_1 + \sigma_3) = \beta \quad (6-1)$$

The model describes the equivalent Hosford yield stress at fracture in correspondence to the Mohr's circles. The coefficient c signifies a type of friction-, β a type of cohesion coefficient. To describe anisotropic material failure, the HC model with an additional transformation of the stress tensor is utilised by Gu et al. [Gu15], basing on the transformation proposed by Karafillis and Boyce [Kar93].

6.1 Orthotropic Fracture Model

Based on numerical simulations of a unit cell, applying a Levy-von Mises material and including an initial porosity and different loadings, Marcadet [Mar15b] and Dunand [Dun14] presented the ability of the MC criterion to predict failure strains for different stress states. The Mohr-Coulomb model defines an isotropic failure surface within the mixed stress-strain-space. To contribute to the experimental results, which reveal orthotropic failure strains, the model is further extended. The extension is geared to the description of orthotropic plasticity.

In contrast to the experimental results, which reveal orthotropy of failure strains, the MC criterion is only able to predict an isotropic failure strain surface. To comprise orthotropy, a model extension is applied here, inspired by the orthotropic yield function of Barlat from 1991 [Bar91].

The MC criterion subdivides into a deviatoric and a principle stress dependent part. The orthotropic properties of the former are directly captured by the yield function. In order to include orthotropy of the principle stresses, the isotropic deviatoric stress tensor $[S_{iso}]$ is substituted by its orthotropic counterpart $[S_{ortho}]$, leading to equation (6-2).

$$[\sigma_{iso}] = [I] \cdot \sigma_m + [S_{iso}] \rightarrow [\hat{\sigma}_{ortho}] = [I] \cdot \sigma_m + [S_{ortho}] \quad (6-2)$$

The components of $[S_{ortho}]$ are defined by Barlat accordingly (6-3) [Liv16b]:

$$\begin{aligned} S_{xx} &= \frac{[C(\sigma_{xx} - \sigma_{yy}) - B(\sigma_{zz} - \sigma_{xx})]}{3}, & S_{yz} &= F \cdot \sigma_{yz} \\ S_{yy} &= \frac{[A(\sigma_{yy} - \sigma_{zz}) - C(\sigma_{xx} - \sigma_{yy})]}{3}, & S_{xz} &= G \cdot \sigma_{xz} \\ S_{zz} &= \frac{[B(\sigma_{zz} - \sigma_{xx}) - A(\sigma_{yy} - \sigma_{zz})]}{3}, & S_{xy} &= H \cdot \sigma_{xy} \end{aligned} \quad (6-3)$$

Based on these components, the principle values of the stress deviator lead to $\bar{\sigma}_{BARL91}$ which describe the equivalent stress dependent on the plastic exponent M according to Barlat and is presented in equation (6-4):

$$\bar{\sigma}_{BARL91} = \left(\frac{1}{2} \cdot (|S_1 - S_2|^M + |S_2 - S_3|^M + |S_3 - S_1|^M) \right)^{1/M} \quad (6-4)$$

The principle stresses of the orthotropic stress tensor $[\hat{\sigma}_{ortho}]$ as well as the equivalent Barlat yield stress $\bar{\sigma}_{BARL91}$ are included into (6-1) and lead to equation (6-5):

$$\bar{\sigma}_{BARL91} + c \cdot (\hat{\sigma}_{ortho\ I} + \hat{\sigma}_{ortho\ III}) = \beta \quad (6-5)$$

The material strain hardening behaviour couples the stress-strain behaviour. Isotropic hardening is included to obtain failure strains within the mixed stress-strain space. With focus on the investigated steels, the Swift hardening law is applied. The approach exhibits a good prediction quality up to UTS despite of its simple formulation (6-6).

$$\bar{\sigma}_{Swift} = k \cdot (\epsilon_0 + \epsilon)^n \quad (6-6)$$

Dissolving formulation (6-6) and replacing the equivalent strain ϵ by the equivalent failure strain of proportional load paths ϵ_f , it leads to equation (6-7):

$$\epsilon_f = \left(\frac{\beta}{k \cdot (\bar{\sigma}_{BARL91} + c \cdot (\hat{\sigma}_{ortho\ I} + \hat{\sigma}_{ortho\ III}))} \right)^{1/n} - \epsilon_0 \quad (6-7)$$

The investigation of Gu et al. [Gu15] revealed a similar controlling influence on the strains to fracture of the friction and cohesion coefficients β and c on the MC model. Gu et al. [Gu15] substituted the term $\left(\frac{\beta}{k \cdot (1+c)} \right)^{1/n}$ by the coefficient b , representing failure strains in uniaxial tension. On the basis of these results, the coefficient b is utilised to define the failure strains of uniaxial tension in rolling direction.

The predicted failure behaviour is affected by strain hardening as well as the yield surface shape. Orthotropy leads to distortion of the yield surface and shifts the yield points. For uniaxial tension in RD, the effect of strain hardening is already captured by the coefficient b . Therefore, only the yield surface distortion has to be included. Thus, the equivalent stress according to the Barlat'91 in uniaxial tension in RD is added to normalise the yield function. Thereby the equation (6-8) follows for coefficient b :

$$b = \left(\frac{\beta \cdot \bar{\sigma}_{\text{BARL91}}(\sigma_{xx}=1, \sigma_{yy}=\sigma_{zz}=\sigma_{xy}=\sigma_{xz}=\sigma_{yz}=0)}{k \cdot (1+c)} \right)^{1/n} \quad (6-8)$$

The orthotropic failure criterion therefore compounds to:

$$\epsilon_f^{\text{prop}} = b \left(\frac{(1+c)}{\bar{\sigma}_{\text{BARL91}} + c \cdot (\hat{\sigma}_{\text{ortho I}} + \hat{\sigma}_{\text{ortho III}})} \right)^{1/n} \quad (6-9)$$

The proposed failure criterion depends on all six components of the local stress tensor. Its representation requires a seven dimensional mixed stress strain space to picture the dependence of the failure strains on the local stresses. Even for the representation within the plane stress state, four dimensions are necessary. Hence, the failure surface is defined in dependence on the stress triaxiality η and the Lode Angle Parameter $\bar{\theta}$. Furthermore, the local stress composition is obtained from the principle stresses which directly base on η and $\bar{\theta}$ [Mar15a]. For the plane stress state, the Lode Angle Parameter can be related directly to the stress triaxiality.

The focus of the failure model is the generation of failure strain surfaces and curves for the GISSMo, implemented in LS-DYNA, in which the first principle stress defines the loading direction. This definition is further adopted for the transformation of the principle stress tensor $[\sigma]$ into the local stress tensor $[\tilde{\sigma}_\alpha]$, which depends on the material axis system. Hence, this work focuses on sheet metal; the rotation tensor $[Q]$ describes a rotation around sheet metal normal direction.

$$[\tilde{\sigma}_\alpha] = [Q] \cdot [\sigma] \cdot [Q]^T \quad \text{with } [\sigma] = \begin{bmatrix} \sigma_x = \sigma_1 & 0 & 0 \\ 0 & \sigma_y = \sigma_2 & 0 \\ 0 & 0 & \sigma_z = \sigma_3 \end{bmatrix} \quad (6-10)$$

With this definition, all generated failure surfaces for the GISSMo are independent of shear stress components in xz- and yz-direction. Therefore, the coefficients F and G are set to unity. Furthermore, the applied stress tensor transformation leads to differing failure behaviour in general stress and plane stress state below stress states of $\eta = \frac{1}{3}$.

The reason for this is based on the ordering of the principle stresses by $\sigma_1 \geq \sigma_2 \geq \sigma_3$. Stress states between uniaxial and biaxial tension lead to similar predicted failure strains of the plane stress and the general stress state. Stress states between uniaxial pressure and uniaxial tension exhibit one positive and one negative principle stress. Within the 6D stress space, the negative stress is aligned in sheet normal direction. In comparison to that, the negative principle stress lies within the loading plane for the plane stress state. For stress states between uniaxial and biaxial pressure, the loading direction is defined by a load free state in general stress state. In contrast to that, in plane stress state both pressure components arise within the sheet metal plane.

6.2 Parameter Study

The presented fracture model is affected by the implemented plasticity model as well as its fracture properties. The six weighting coefficients (A, B, C, F, G, H; equation (6-3)) as well as the

plastic exponent M (equation (6-4)) define the corresponding yield surface shape of the failure model. Furthermore, hardening behaviour is included by the Swift hardening law with its hardening exponent n . Consequently, both fracture coefficients b and c define the fracture envelope. The parameter study is conducted for the plane stress state. The reference fracture envelope of this study is defined by all plastic coefficients (A, B, C, F, G, H and M) equal to unity, a hardening exponent n of 0.20, an uniaxial failure strain b in RD of 1.0 and a friction coefficient c of 0.0. Due to the definition of the failure model in local stresses, its representation within the plane stress space is necessary, e.g. dependent on σ_{xx} , σ_{yy} and σ_{xy} . The fracture envelope is presented as a polar plot within the σ_{xx} - σ_{yy} -plane as well as within the perpendicular σ_{xy} - σ_b -plane, where σ_b -marks the biaxial stresses. The former is exemplarily presented in Figure 6-1 with different stress states pictured with respect to material direction. The perpendicular σ_{xy} - σ_b -plane is aligned along the green line connecting biaxial tension ($\eta = \frac{2}{3}$) and pressure ($\eta = -\frac{2}{3}$). Regarding isotropy, the σ_{xy} - σ_b - as well as the σ_{xx} - σ_{yy} -plane define the symmetry of the pictured fracture envelope.

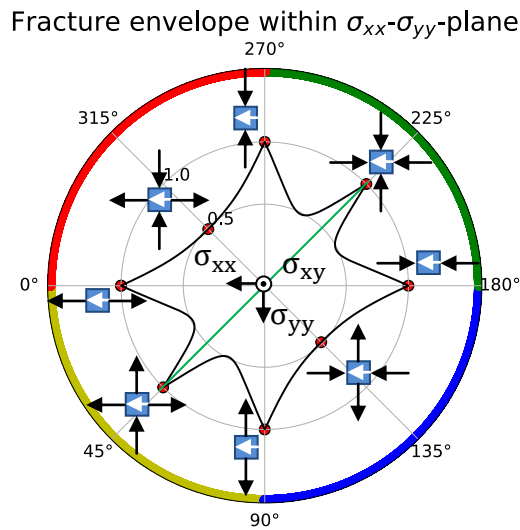


Figure 6-1: Stress states along fracture envelope within σ_{xx} - σ_{yy} -plane and different stress states. The angles define the principle loading direction to RD, whereas the concentric circles describe constant failure strains. The green line marks the line between biaxial pressure and tension. The first quadrant is marked in yellow, the second in blue, the third in green and the fourth in red

The plastic exponent M of the applied plasticity law has a major impact on the yield surface. To describe metal plasticity, exponents between 2 and 8 are commonly utilised. A plastic exponent of 1 leads to the Tresca yield surface, which applies to metal failure and is provided by the investigations of Stoughton [Sto11]. Similar results follow from the characterisations of Gu [Gu15] and Marcadet [Mar15a].

Figure 6-2 depicts the effect of the exponent M on the fracture envelope. It is neither affected by pure uniaxial as well as pure biaxial loading, meaning at Lode Angle Parameters of -1 and 1. In between the fracture envelope expands with increasing M , yet a decrease of M leads to a contraction. In both presented planes M has a similar effect on the failure strains. Decreasing M

contracts the fracture envelope mainly for stress states with Lode Angle Parameter of 0 (shear and plane strain).

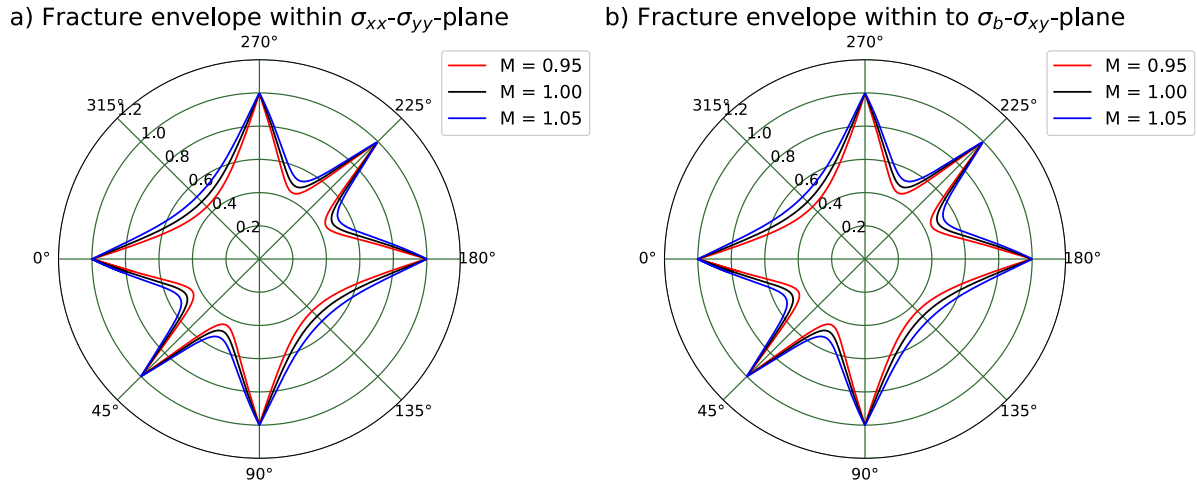


Figure 6-2: Effect of the plastic exponent M on the fracture envelope a) within the σ_{xx} - σ_{yy} -plane and b) within the σ_{xy} - σ_b -plane

Orthotropy of the presented failure model is represented by the six plastic weighting coefficients (A, B, C, F, G and H) of the utilised Barlat'91 model, see equation (6-3). The coefficients lead to the deformation and rotation of the yield surface and the fracture envelope. Due to the plane stress state only the four coefficients A, B, C and H affect the failure strains. Therefore, coefficient F and G are not further considered.

Coefficient A of the applied Barlat'91 yield surface weights stresses in y- and z-direction. Its influence on the fracture envelope is displayed in Figure 6-3a and b. The former presents failure strains within the σ_{xx} - σ_{yy} -plane, not affecting uniaxial tension in RD (0°) or shear. In contrast to that, coefficient A affects the failure envelope in TD (90°) as well as for biaxial stress states. The plot exhibits an increase in failure strains when reducing coefficient A, leading further to a shift of the maximum strain towards biaxial stresses.

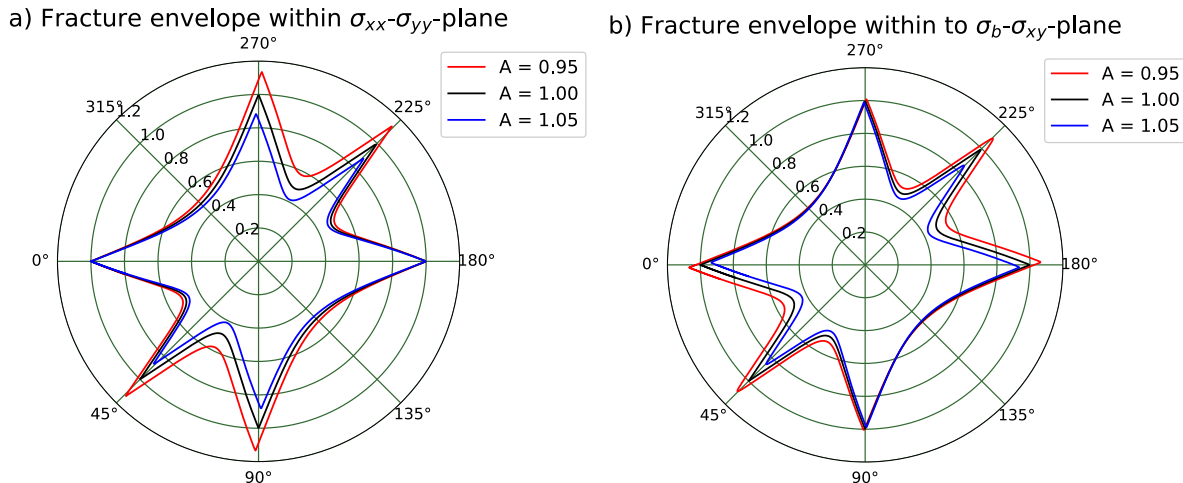


Figure 6-3: Effect of the plastic weighting coefficient A on the fracture envelope a) within the σ_{xx} - σ_{yy} -plane and b) within the σ_{xy} - σ_b -plane

Similar behaviour is found for the representation within the σ_{xy} - σ_b -plane (Figure 6-3b). Within it, uniaxial stress states in 45° to RD (0° in polar plot) as well as biaxial stress states are affected. Uniaxial stresses in -45° to RD (90° in polar plot) only present a minor effect on changes of coefficient A. Shear stresses are not affected at all.

In contrast to A, coefficient B weights stresses in x- and z-direction. Its effect on the fracture envelope is presented in Figure 6-4a for the σ_{xx} - σ_{yy} -plane and for σ_{xy} - σ_b -plane in Figure 6-4b. The yield surface is mainly affected in 0° direction by coefficient B. Due to the normalisation of coefficient b, presented in equation (6-9), the effect is shifted towards 90° to RD. As previously seen for A, variations of coefficient B lead to a shift of the maximum from uniaxial tension towards biaxial (decreasing B) or shear (increasing B). The major impact of coefficient B is revealed in uniaxial stress in TD, where a decreasing coefficient B leads to an increase in failure strains. This can be found alleviated also for shear within the σ_{xx} - σ_{yy} -plane ($135^\circ/315^\circ$). Within the σ_{xy} - σ_b -plane, the major impact of coefficient B is found for uniaxial tension and pressure stress states as well as for pure shear.

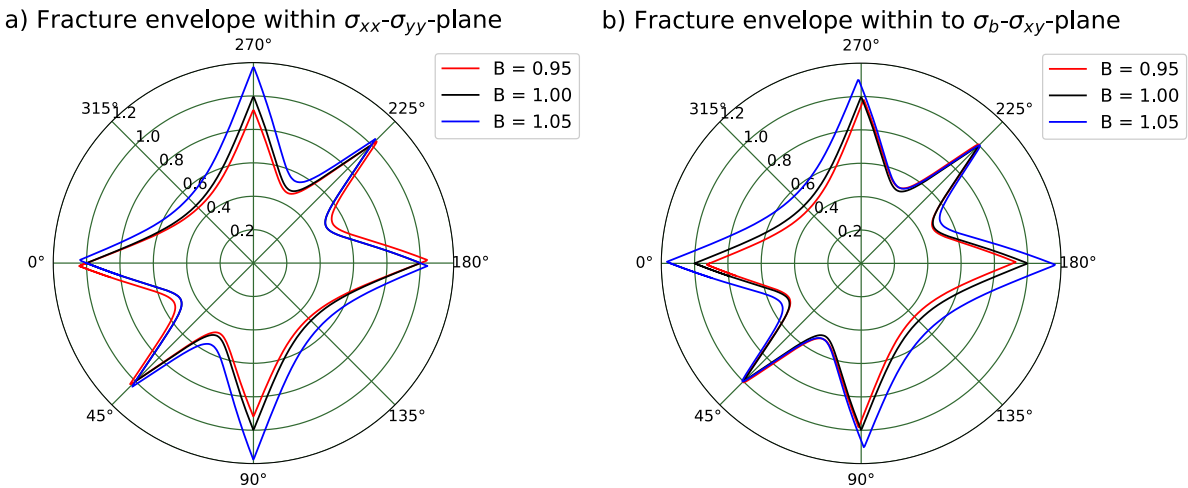


Figure 6-4: Effect of the plastic weighting coefficient B on the fracture envelope a) within the σ_{xx} - σ_{yy} -plane and b) within the σ_{xy} - σ_b -plane

In Figure 6-5a and b, the effect of coefficient C, which affects σ_{xx} and σ_{yy} , is pictured. Coefficient C exhibits no affect in uniaxial tension due to the definition of coefficient b. Despite this, variations of C lead to a shift of the maxima of the fracture envelope near uniaxial tensions towards shear (decreasing C) or biaxial stresses (increasing C). Decreasing C also induces higher failure strains in shear but lower ones in biaxial stress states and vice versa for increasing coefficient C. Regarding the σ_{xy} - σ_b -plane, coefficient C leads to an isotropic expansion (increasing C) or contraction (decreasing C) of the predicted fracture envelope. Coefficient C simultaneously affects σ_{xx} and σ_{yy} , therefore no variation in RD compared to TD is observed. Furthermore, coefficient b relativises the effect in uniaxial tension and intensifies the effect for biaxial stress state.

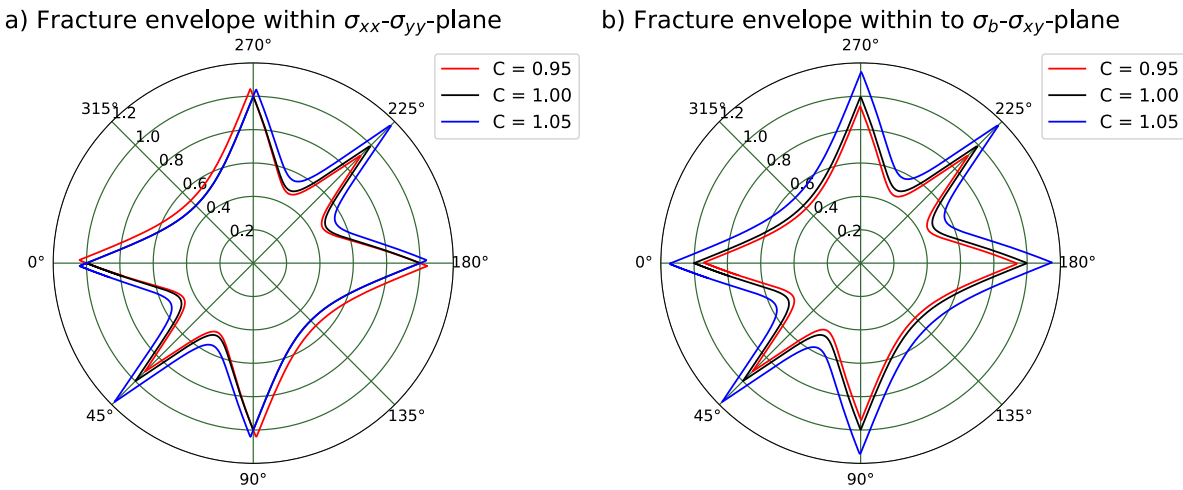


Figure 6-5: Effect of the plastic weighting coefficient C on the fracture envelope a) within the σ_{xx} - σ_{yy} -plane and b) within the σ_{xy} - σ_b -plane

As presented in Figure 6-6, coefficient H of the utilised Barlat model only weighs the shear stress components σ_{xy} and therefore has no effect on the fracture envelope within the σ_{xx} - σ_{yy} -plane. It only influences failure strains within the σ_{xy} - σ_b -plane, which incorporate shear stress components. By increasing of coefficient H , the fracture envelope expands except for biaxial stress states. The main effect is found for the directions of 135° and 315° respectively, corresponding to pure shear.

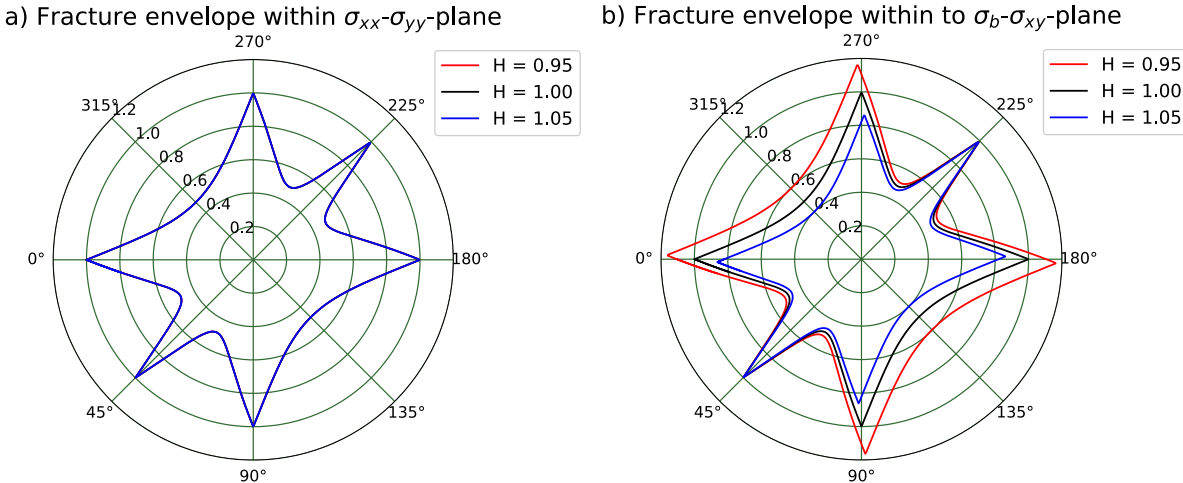


Figure 6-6: Effect of the plastic weighting coefficient H on the fracture envelope a) within the σ_{xx} - σ_{yy} -plane and b) within the σ_{xy} - σ_b -plane

The effect of the strain hardening exponent n is displayed in Figure 6-7, revealing a strong influence on the shape of the fracture envelope. Like the plastic exponent M , the hardening exponent n of the utilised strain hardening law by Swift exhibits no impact on the fracture surface for uni- and biaxial stress states or Lode Angle Parameters of -1 and 1 respectively. In comparison to that, the main influence is revealed for shear and plane stress states both corresponding to Lode Angle Parameters of 0. Decreasing the strain hardening exponent n , it leads to a con-

traction of the fracture envelope within shear and plane stress. In contrast to that, growing n results in increasing failure strains, predicted for shear and plane stress.

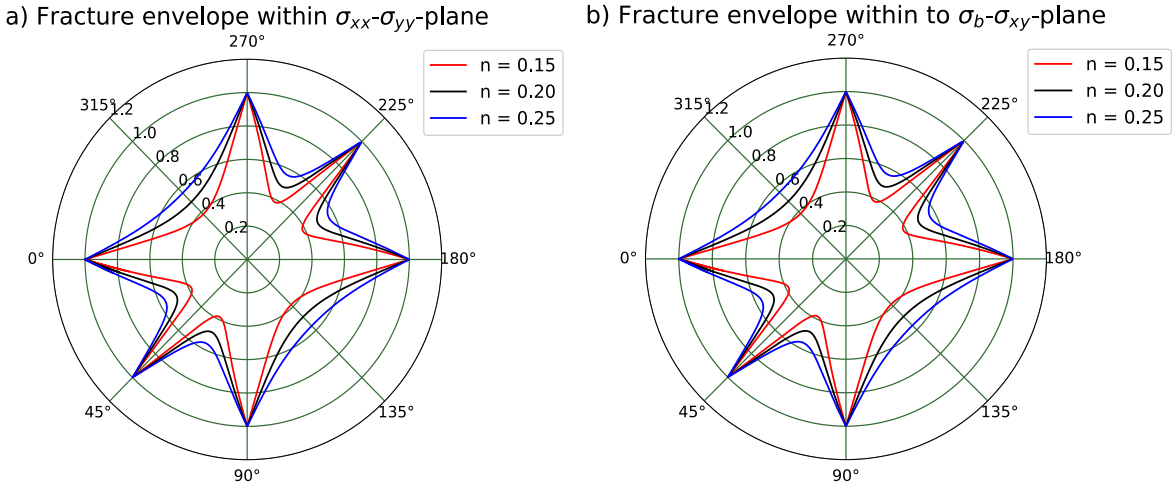


Figure 6-7: Effect of the hardening exponent n of the applied Swift hardening law on the fracture envelope a) within the σ_{xx} - σ_{yy} -plane and b) within the σ_{xy} - σ_b -plane

Coefficient b defines the failure strains of uniaxial tension in RD. Its effect on the fracture envelope is pictured in Figure 6-8. Due to its isotropic effect, the predicted failure strains within the σ_{xx} - σ_{yy} - as well as σ_{xy} - σ_b -plane are equally affected. Rising coefficient b results in an isotropic expansion of the failure envelope, whereas an isotropic contraction is found for decreased b .

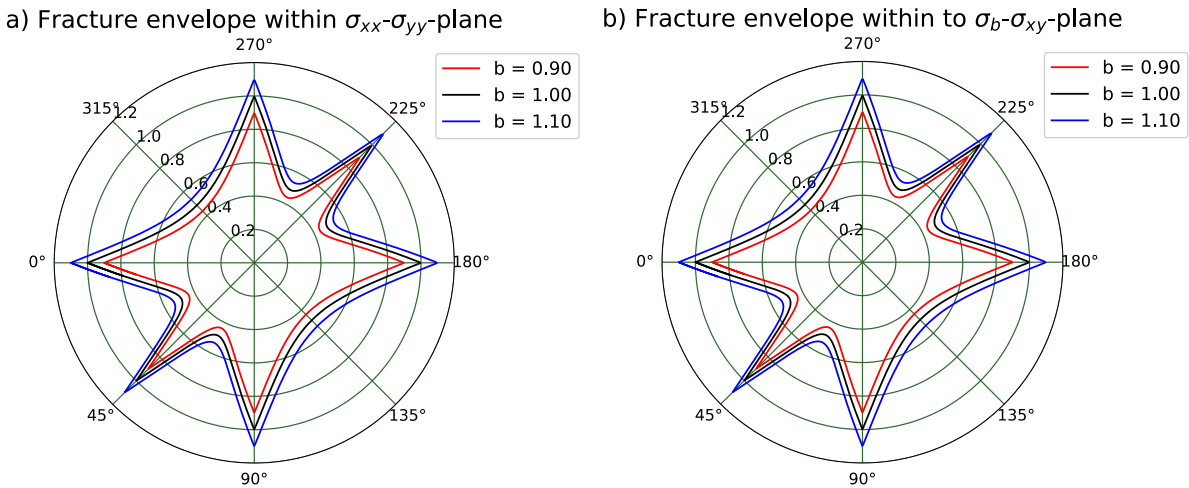


Figure 6-8: Effect of the uniaxial failure strain b in RD on the fracture envelope presented a) within the σ_{xx} - σ_{yy} -plane and b) within the σ_{xy} - σ_b -plane

The effect of the friction coefficient c is depicted in Figure 6-9, revealing no effect on stress states exhibiting $\eta \geq \frac{1}{3}$. That is why the polar plots within the first quadrant are not affected. Only failure strains for pressure dependent stress states ($\eta < \frac{1}{3}$) are influenced by coefficient c , e.g. shear, uni- and biaxial tension. The parameter study reveals an expansion of the fracture

envelope for increasing friction coefficients c . The fracture strains are mainly affected within the third quadrant, which corresponds to stress triaxialities of $\eta < -\frac{1}{3}$, e.g. uni- and biaxial pressure.

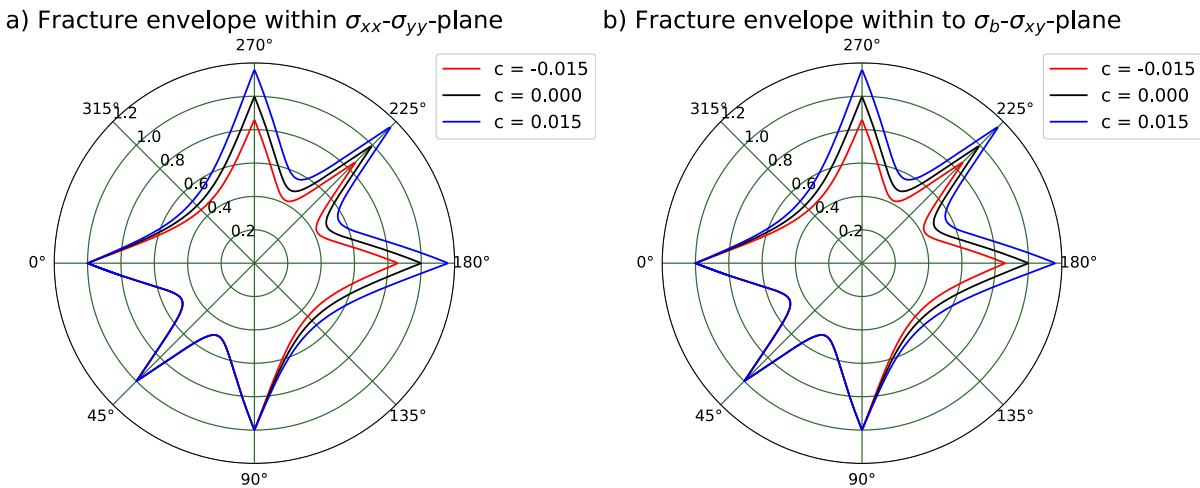


Figure 6-9: Effect of friction coefficient c on the fracture envelope a) within the σ_{xx} - σ_{yy} -plane and b) within the σ_{xy} - σ_b -plane

6.3 Parameter Identification

The parameter identification of the proposed failure criterion subdivides into four different steps, starting with an isotropic yield surface. As a first step the isotropic hardening behaviour has to be incorporated. Adapted from experimental hardening behaviour, the strain hardening exponent n of the Swift-law is defined. It determines the curvature of the failure strain surface and curve respectively. The investigated NR05 specimens show a nearly proportional load path on their surface. Its failure strain within the plane strain state is utilised to estimate the uniaxial tensile failure strain b . Coefficient c defines the rise of the failure surface with the occurrence of pressure stress components. It is adjusted to meet the failure strains in shear. To include orthotropy, all six components of the utilised Barlat'91-yield surface are determined in the fourth step. The adjusted plasticity model affects the failure surface within shear as well as within plane strain, which can lead to a readjustment of the coefficients b and c .

6.4 Orthotropic Hardening

The performed experiments reveal orthotropic hardening behaviour of the CR340LA specimens. The standard tensile test reveals a change in the ratio of the yield strength to the UTS with specimen orientation, although the trend up to UTS affects no yield surface distortion.

The hardening behaviour strongly influences the shape of the fracture surface, therefore an orientation dependent hardening exponent is taken into account which also includes strain hardening beyond UTS. In this work, orthotropic hardening is included by applying an orthotropic hardening exponent n_{ortho} on the Swift hardening law. The x-direction is aligned in 0° to RD, the y-direction in 90° to RD. For both directions the hardening exponent n_{xx} and n_{yy} , respectively can be defined directly. Regarding the 45° direction in this reference coordinate

system, uniaxial tension is composed of stresses in x-, y- as well as in xy-direction. Thus, strain hardening behaviour in 45° is defined by the x- and y-direction and completed by the hardening exponent n_{xy} . In analogy to these dominant stresses, the hardening behaviours in z-, xz- and yz-direction are applied. For the six dimensional stress space, orthotropic hardening follows the equation (6-11), which suppresses discontinuities due to its quadratic approach.

$$n_{\text{ortho}} = \frac{n_{xx}\sigma_{xx}^2 + n_{yy}\sigma_{yy}^2 + n_{zz}\sigma_{zz}^2 + n_{xy}\sigma_{xy}^2 + n_{xz}\sigma_{xz}^2 + n_{yz}\sigma_{yz}^2}{\sigma_{xx}^2 + \sigma_{yy}^2 + \sigma_{zz}^2 + \sigma_{xy}^2 + \sigma_{xz}^2 + \sigma_{yz}^2} \quad (6-11)$$

Figure 6-10a depicts the von Mises yield surface within the σ_{xx} - σ_{yy} -plane with coloured dedicated stress states, like uniaxial stress in 0° (black), and 90° (red) as well as biaxial stress states (green) and shear stresses (yellow). Due to orthotropy, material behaviour in pressure and tension is equal. For both uniaxial stresses in 0° and 90° , deviating n-values of the Swift hardening functions are defined to demonstrate orthotropic hardening. Additionally, the distribution of the n-values above the angle α in plane stress condition is shown in Figure 6-10b.

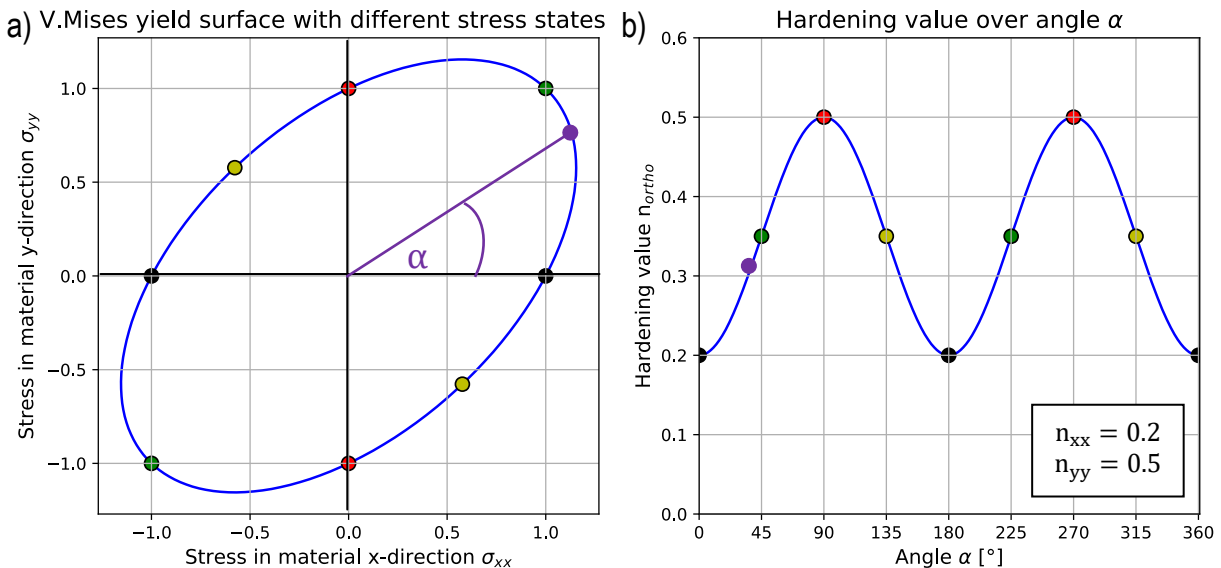


Figure 6-10: a) distinct stress states on von Mises yield surface, b) orientation dependent hardening value above the angle α with distinct stress states, black: uniaxial stress in x, red: uniaxial stress in y, green: biaxial stress, yellow: shear stress

The standard isotropic hardening models induce only an expansion of the yield surface but do not affect its shape. Contrary to that, orthotropic hardening behaviour leads to different expansion velocities along the yield surface. As a result, a distortion of the yield surface with a possible violation of the convexity criterion of the yield surface arises. Figure 6-11 pictures the effect of orientation dependent hardening in x- and y-direction on the von Mises yield surface. The different hardening states are computed according to the equations (6-6) and (6-11) with $k = 0.7$ GPa and $\epsilon_0 = 1.0$. For a better overview, the xy-direction is neglected in the depicted plot. In x-direction a lower hardening exponent is assumed than in y-direction. This leads to a slower expansion of the surface in material x- than in y-direction and leads to its distortion with accompanied loss of convexity.

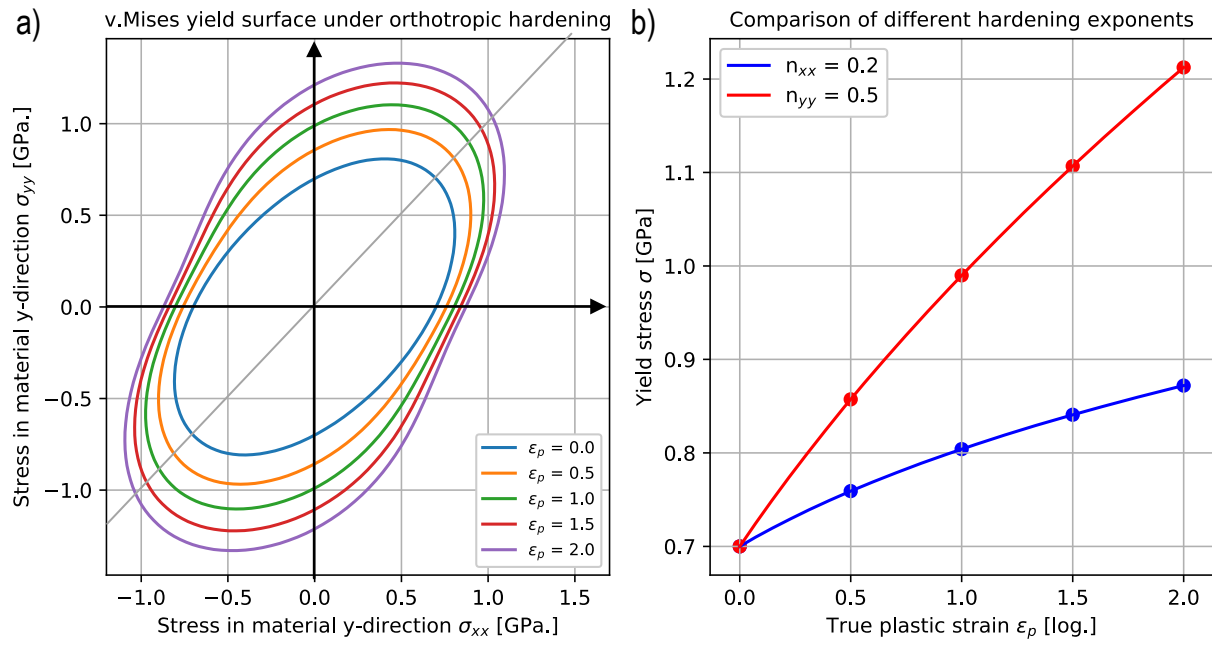


Figure 6-11: a) Effect of different hardening exponents in x- and y-direction, with resulting distortion of the yield surface and the loss of convexity near uniaxial stress in x-direction, b) both in a) applied Swift-strain hardening curves

6.5 Estimation of the Damage Parameters

Ductile fracture is characterised by evolving damage on microscale. According to McClintock [McC68] the evolution can be subdivided into the nucleation, the growth and the coalescence of voids in the material. The voids lead to a reduction of the effective cross section, which results in an increase in effective local stresses but a decrease in global force.

The damage accumulation as well as the reduction of the effective cross section have to be described on a macroscopic level for phenomenological modelling purposes. Therefore, different functions, based on plastic strains, have to be defined to model damage and stress fading behaviour. The former describes the local damage D and its evolution dependent on the local stress state and the plastic strain. The latter defines the effect of damage on the local stress level. Moreover, the characterisation of these damage or fading functions is focussed. The decrease in global force in dependence on the damage functions is described by the fading functions. De Faria [DeF16] proposed an optical measurement method on microscale to determine damage evolution. The method requires in-situ or stepwise performed tests. Damage measurement is based on the change in surface roughness investigated by optical microscopy.

There are different requirements on a specimen to determine the damage behaviour in macro scale. One of these requirements relates to a proportional load path to measure damage evolution accurately. In addition, the stress as well as the strain state has to be approximately constant over the cross section.

Regarding the investigated specimen, both tests, the NR05 specimen and the Bulge-test, show a favourable load path. The Bulge-test presents a nearly proportional load path with a homoge-

neous strain distribution at fracture point. Small changes of the load paths reveal large changes in plastic instability and fracture strains. In contrast to that, the NR05 specimen shows a higher robustness in fracture and instability strains, which can both be approximated as constant values. That is why the loss of the proportional load path does not affect large changes in specimen failure strains. Only the distribution of strains in the fracture cross section is not as homogeneous as in the Bulge-test. Hence, the NR05 specimen is taken into account for a hybrid experimental-numerical method to determine phenomenological damage evolution.

All investigated NR05 specimens depict a maximum load followed by a decrease in their force-displacement curves. The three main reasons for this decrease are an insufficient hardening behaviour, a cross section reduction due to necking or material damage. To divide material damage from necking and hardening, numerical simulations without damage are carried out. The tensile forces as well as the local strains can be obtained from numerical simulations and experiments including DIC-measurement. In contrast to the strains, the force is a global measure. Including local strain measurement, they enable the calculation of the current cross section. With this current cross section the measured force is interpreted as an average stress, which is constant over the cross section. For a better comparison the averaged stress is connected to an averaged equivalent strain. Due to the small material thickness, a small gradient in sheet normal direction of local strains is assumed. Thus, the surface strains are an accurate representation of the cross section strain field, see Figure 6-12. The averaged equivalent strain is obtained from the arithmetic mean along the smallest specimen cross section.

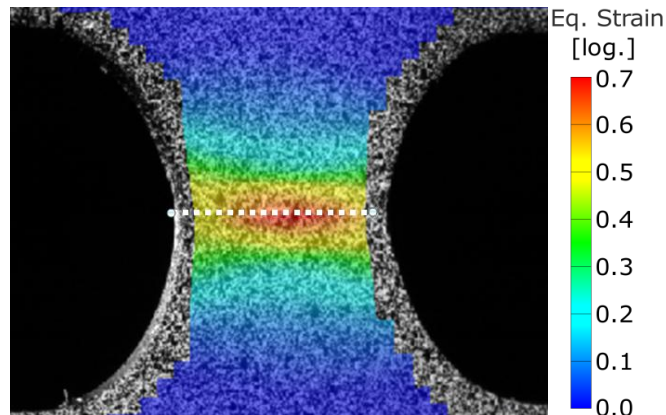


Figure 6-12: Effective strain field on NR05 specimen with marked cross section (white line)

To characterise phenomenological damage evolution and stress fading functions have to be defined. Both functions are based on the present work on the GISSMo in [Liv16b]. This allows a direct comparison between predicted damage evolution and simulation result. The damage increment is given by equation (6–12). The integral leads to a dependence of the damage value on the equivalent strain ϵ_f and can be solved directly for linear damage accumulation (6–13). The damage value \tilde{D} ranges from 0 to 1 in which the former describes a completely undamaged and the latter a completely damaged material. The load path is determined by the stress triaxiality and the Lode Angle Parameter as well as equivalent plastic strain $\tilde{\epsilon}_p$. Moreover, the damage exponent D_{exp} defines the exponential function of the damage accumulation. The assumption of a proportional load path results in constant failure strains $\epsilon_f(\eta, \theta)$.

$$\Delta D = \frac{D_{\text{exp}} \cdot D^{1-D_{\text{exp}}}}{\epsilon_f(\eta, \theta)} \Delta \epsilon_p \rightarrow D^{D_{\text{exp}}-1} dD = \frac{D_{\text{exp}}}{\epsilon_f(\eta, \theta)} d\epsilon_p \quad (6-12)$$

$$\int_0^{\tilde{D}} D^{D_{\text{exp}}-1} dD = \int_0^{\tilde{\epsilon}_p} \frac{D_{\text{exp}}}{\epsilon_f(\eta, \theta)} d\epsilon_p \rightarrow \tilde{D} = \left(\frac{\tilde{\epsilon}_p}{\epsilon_f(\eta, \theta)} \right)^{D_{\text{exp}}} \quad (6-13)$$

With the damage value \tilde{D} the stress fade out follows by equation (6-14):

$$\sigma_{\text{SIM}} = \tilde{\sigma} \left[1 - \left(\frac{D - D_{\text{crit}}}{1 - D_{\text{crit}}} \right)^{F_{\text{exp}}} \right] = \tilde{\sigma} \left[1 - \left(\frac{\left(\frac{\tilde{\epsilon}_p}{\epsilon_f(\eta, \theta)} \right)^{D_{\text{exp}}} - D_{\text{crit}}}{1 - D_{\text{crit}}} \right)^{F_{\text{exp}}} \right] \quad (6-14)$$

In this case of characterising damage- and stress fading behaviour, $\tilde{\sigma}$ is equal to the averaged stress of the numerical simulation without damage. The stress σ_{SIM} in equation (6-14) defines the average of predicted stress of the numerical simulation including damage. With σ_{EXP} the average stress of the experiment is presented in equation (6-15). The applied Finite-Element-failure model requires a Damage-Exponent equal unity. Therefore, only the Fading-Exponent is characterised adapting the experimentally obtained force-averaged equivalent strain behaviour. A non-linear optimisation algorithm is utilised to minimize the quadratic deviation of the predicted and the experimental averaged stress due to (6-15).

$$\min \Delta = \min \sum_{i=1} (\sigma_{\text{SIM}} - \sigma_{\text{EXP}})^2 \quad (6-15)$$

The predicted average stress-average strain behaviour is depicted in Figure 6-13 in red. This result is compared to the result of the numerical simulation (solids) using the characterisation methods described in the chapters 5 and 6. The result of the numerical simulation (solid) of the investigated CR340LA of 1.1 mm thickness is plotted in green dots and shows a good agreement with the predicted curve. Only the average equivalent strains differ at failure point. The method was adopted for further orientations as well as materials which show similar prediction quality when applied at results of solid simulations. However, shell simulations underestimate the fading-exponent due to diverging stress states of shell at the specimen inside.

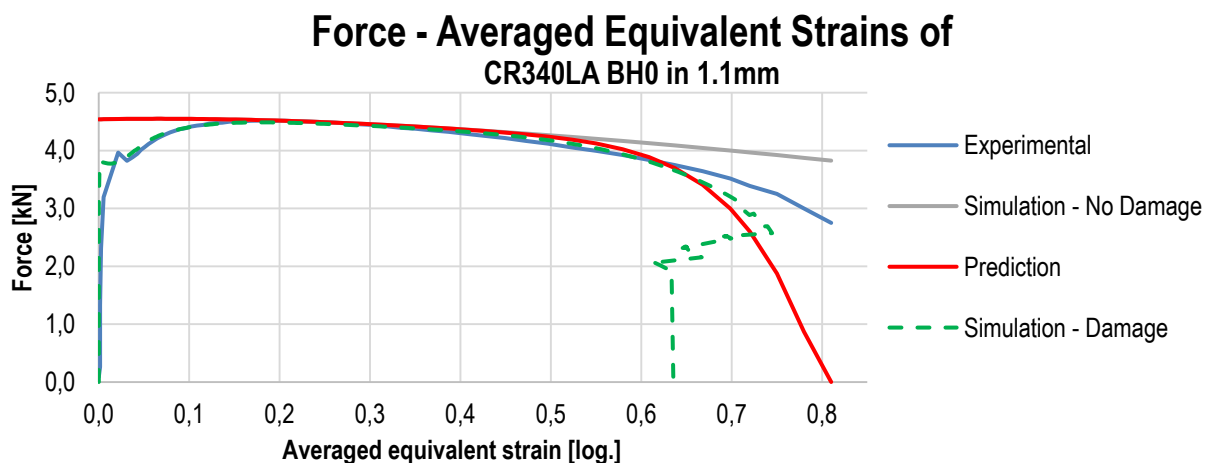


Figure 6-13: Predicted as well as experimentally obtained force over averaged equivalent strains on NR05 specimen surface and solid simulation

7 Numerical Simulations

All four investigated materials have been characterised based on the previously presented experimental results. Explicit numerical simulations have been conducted with LS-DYNA, version R 9.0 and fully integrated shell elements (LS-DYNA: Element type 16). The applied element size constitutes 0.5 mm. The local stresses of sheet metals can be approximated in wide ranges of material deformation by the plane stress state. Therefore, shell elements are a suitable simplification to simulate sheet metals within the automotive crash simulation.

Material characterisation subdivides into the separate definition of elasto-plastic and failure properties. To capture the former *MAT_036 was employed to capture isotropic elasticity and to include the Barlat'89 yield surface. Strain hardening in uniaxial tension in 0°, 45° and 90° to RD was involved by three flow curves. They were determined up to UTS directly from the conducted uniaxial tension tests, which could be represented by the analytical strain hardening function, proposed by Swift [Swi46]. For flow curve extrapolation beyond UTS, a mixture of different analytical strain hardening functions $\bar{\sigma}_i$, e.g. Swift [Swi46], Voce [Voc45], El-Magd [ElM94] etc., is applied. The flow curve extrapolation with the weighting coefficient w_i follows by equation (7-1).

$$\bar{\sigma} = \sum_{i=1}^n w_i \cdot \bar{\sigma}_i \quad (7-1)$$

The equivalent stress and the deviation of the experimentally determined flow curve at UTS are boundary conditions of the extrapolation. The mixture of different analytical approaches leads to an increasing degree of freedom for the extrapolation of the flow curve to fit experimental strain hardening behaviour. For direct utilisation of the different flow curves, a yield potential of 1 was adjusted for uniaxial tension in 0°, 45° and 90°. Due to limitations of the implemented model, the orthotropic strain hardening excludes the application of the strain rate dependency.

Orthotropic material failure is described by the generalisation of the isotropic GISSMo (LS-DYNA: *MAT_Add_Generalized_Damage / *MAT_MAGD). For the present numerical simulations the material behaviour in 0°, 45° and 90° to RD is described separately. In each direction plastic instability as well as failure strains are defined additionally to the damage evolution and the stress fading. Within the present model utilisation, the first principle strain defines the loading direction, which is done by the first principle stress in contrast to the previous definition. Furthermore, linear damage accumulation ($D_{exp} = 1$) is necessary for a proper prediction of orthotropic failure.

7.1 Bake-hardening Effect

There are different approaches to include the bake-hardening effect, which are described in detail in [Lin13], [Koc17] and [Rie16]. In this work the bake-hardening effect is captured by modifying the flow curve as described by Riemensperger [Rie16]. The definition of flow curves enables a better fitting quality on the experimental strain hardening behaviour and more flexibil-

ity of the flow curve-extrapolation. In [Rie16], the bake-hardening effect is modelled by a linear range with low slope. In contrast to that, the Swift hardening function is applied here to model the strain hardening behaviour up to UTS without the bake-hardening effect and to add an exponential term, similar to [Bal09], see equation (7-2). The coefficients α , β and γ define the additional flow potential by pinned dislocations.

$$\sigma = k \cdot (\epsilon_0 + \epsilon)^n + \alpha \cdot e^{-\beta \cdot \epsilon + \gamma} \quad (7-2)$$

The approach is able to reproduce a strain hardening behaviour up to UTS and includes the paint baking. It is also able to describe the distinct yield strengths with subsequent decrease in flow stress during Lüders-band propagation. The approach further represents the microstructural behaviour more realistically than the previously adopted approaches. Prior to Lüders-strains the bake-hardening effect raises the required local stress. Vaulting this threshold leads to further resolving dislocations.

The approach of nearly constant flow-stress within Lüders-strain and the presented method with additional flow potential are compared by modelling the CR340LA in 0° to RD with a sheet thickness of 1.1 mm. The distinct yield strength with Lüders-strains occurs within the plastic strains up to 0.04. The decrease in the flow curve can influence the stability of the numerical simulation. In order to avoid numerical instabilities the development of Lüders-strains is modelled as linear increasing with small slopes. This contributes to the missing hardening behaviour during the occurrence of Lüders-strains. The effect of both flow curves is pictured in Figure 7-1.

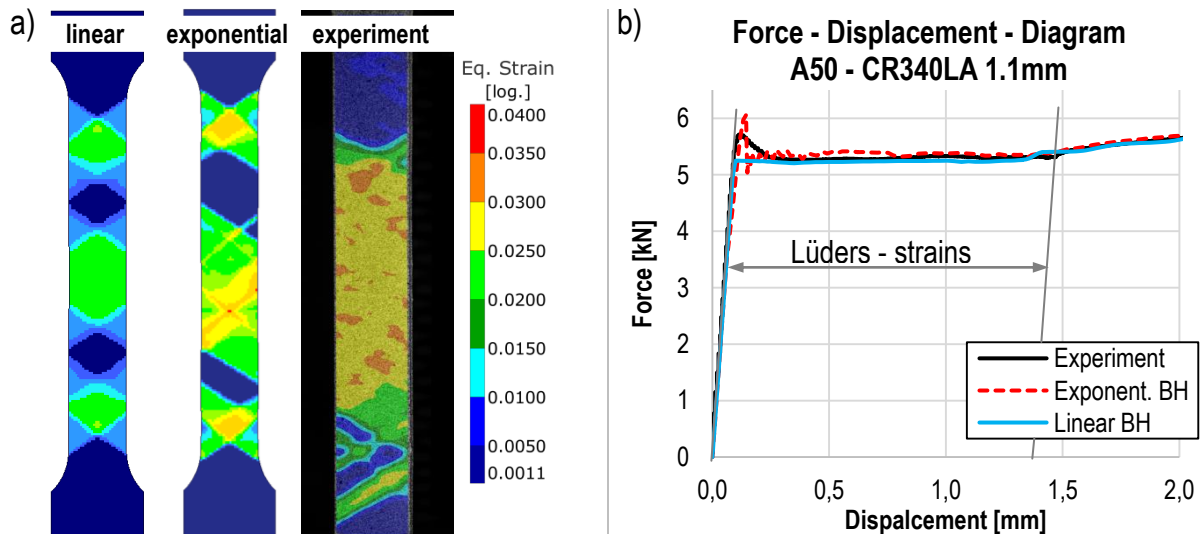


Figure 7-1: Influence of linear and exponential approach of modelling the Lüders-strains; a) comparison of strain fields obtained from DIC and numerical simulation, b) opposition of numerical and experimental force-displacements at the Lüders-band development

Only the decreasing flow curve is able to model the distinct yield strength of the bake-hardening effect. Regarding the force-displacements during the development of Lüders-strains both flow curves agree with the experimental data. The DIC-strain fields reveal differences in both model-

ling methods. The strain field of the exponential approach shows a good agreement with experimental surface data. It is able to reproduce the development of the Lüders-bands commencing at the outer radii. The linear approach exhibits a different propagation of the Lüders-bands along the parallel length than obtained from DIC-measurements.

On the other hand, this effect should not be completely neglected. Besides the CR340LA-steels, also the investigated full martensitic Ultra High Strength Steel (UHSS) MS1500 exhibits the formation of Lüders-bands observed at standard tensile specimens in 0° and 22.5° to RD. In combination with a low hardening rate and only small material inhomogeneities the pronounced yield point causes an increase of failure near the radii outside the gauge length. At these points local strain measurement reveals slightly higher strains than in the parallel length.

7.2 Simulation Results

Based on the previously described methods as well as including experimental specimen behaviour, all investigated materials of chapter 3.1 have been characterised. The failure surface can be directly determined by incorporating DIC-strain fields; the flow curve extrapolation has to be estimated based on the material behaviour beyond force maximum. In this section force-displacements and local strains of numerical simulation and experiment are contrasted. The local strains represent the distribution along the middle axis on the surface in loading direction, where the DIC-strain fields are obtained from the last picture prior to fracture. The comparison is conducted between CR340LA in 1.1 mm and MS1500 in 1.0 mm sheet thickness, the remaining CR340LA thicknesses can be found in the appendix (chapter 10.6 and 10.7). To visualise the scattering of the tests, coloured bands are utilised to picture the variations in displacements at failure and maximum failure strains.

7.2.1 CR340LA 1.1 mm in Bake-hardening Condition (Shell)

This section opposes the observed experimental and simulated material behaviour in 0° , 45° and 90° of CR340LA with a sheet thickness of 1.1 mm. The obtained force-displacements of A50 specimens are presented in Figure 7-2.

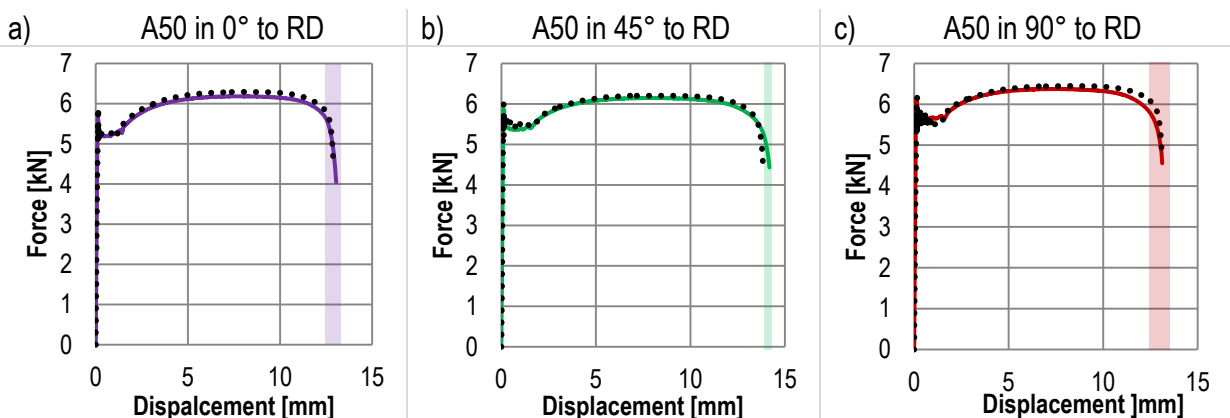


Figure 7-2: Comparison of experimental with numerical determined force-displacement behaviour of standard tensile tests of CR340LA in a) 0° , b) 45° and c) 90° to RD

The simulation results agree with the experimental behaviour regarding elasto-plastic behaviour and failure point. The utilised exponential approach of modelling the distinct yield point as well as material behaviour during the development of Lüders-bands meets the experiment. Furthermore, the determined hardening behaviour (prior to UTS based on experiment and after UTS as extrapolation) meets the experimental trend. The applied failure model is able to reproduce the displacements at fracture for all directions within the scattering bands.

The equivalent strain profile along the specimen middle axis for tensile specimens aligned in 0° , 45° and 90° to RD are depicted in Figure 7-3. Scattering of failure strains within the localisation zone ($-10 \leq x \leq 10$) of 0.08 is recorded whereas outside of the localisation zone the scattering restricts to 0.01. The applied orthotropic failure model is able to represent the orthotropic failure strains of standard tensile specimens. The numerical simulation predicts failure strains of 0.87 arising for tensile specimens in 0° and 90° to RD, which concurs with the experimentally obtained scattering. For specimens aligned in 45° direction the predicted failure strains of 1.02 meet the experiment. Furthermore, the localisation band width of numerical simulation and DIC-data agree. Outside of the localisation zone the three investigated specimen directions also meet the experiment.

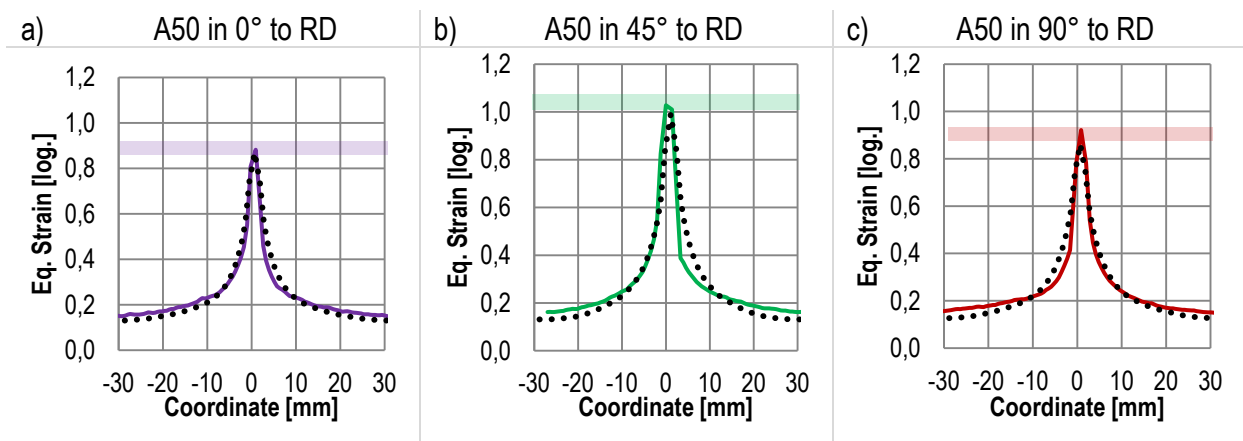


Figure 7-3: Comparison of experimental with numerical determined local strain behaviour of standard tensile tests of CR340LA in a) 0° , b) 45° and c) 90° to RD

Figure 7-4 displays the contrasted force-displacement behaviour of experiment and numerical simulation. The utilised model approach in general is able to reproduce the distinct yield point, but cannot predict the elevated point in 90° to RD, which overshoots the maximum in force during strain hardening. Additionally, the maximum force is met comparably and the experimentally observed curvature beyond force maximum is reproduced for NR80 specimens. Regarding the displacements at failure, the characterised material model is able to predict the displacements at failure in 0° and 45° to RD. Only in 90° direction the displacements are overestimated by 0.1 mm.

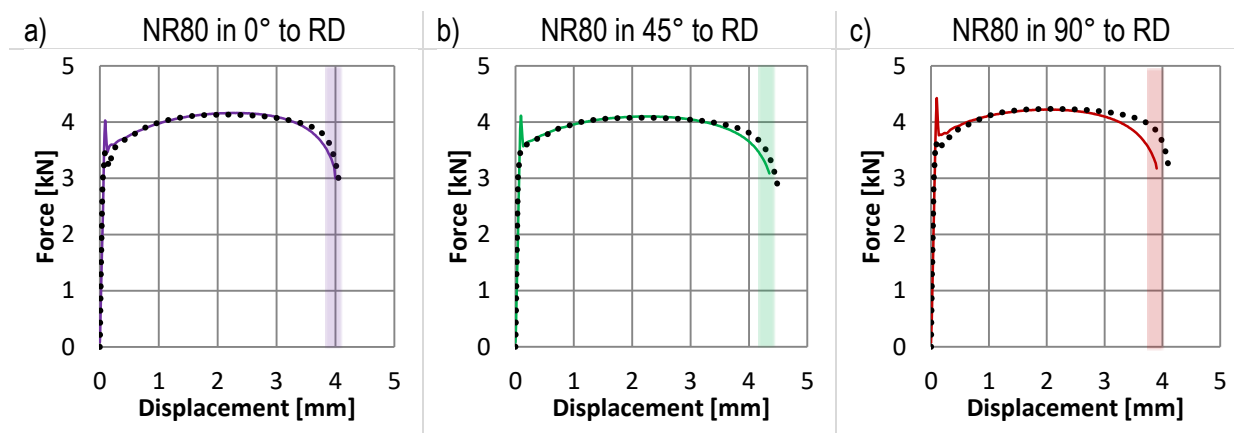


Figure 7-4: Comparison of experimental with numerical determined force-displacement behaviour of NR80 specimens of CR340LA in a) 0° , b) 45° and c) 90° to RD

Regarding the local strain field of NR80 specimens, all three directions of the numerical simulation meet the experimental data within the scattering band width as displayed in Figure 7-8. The characterised material model is able to represent the experimental fracture strain behaviour and the localisation band width for all investigated directions.

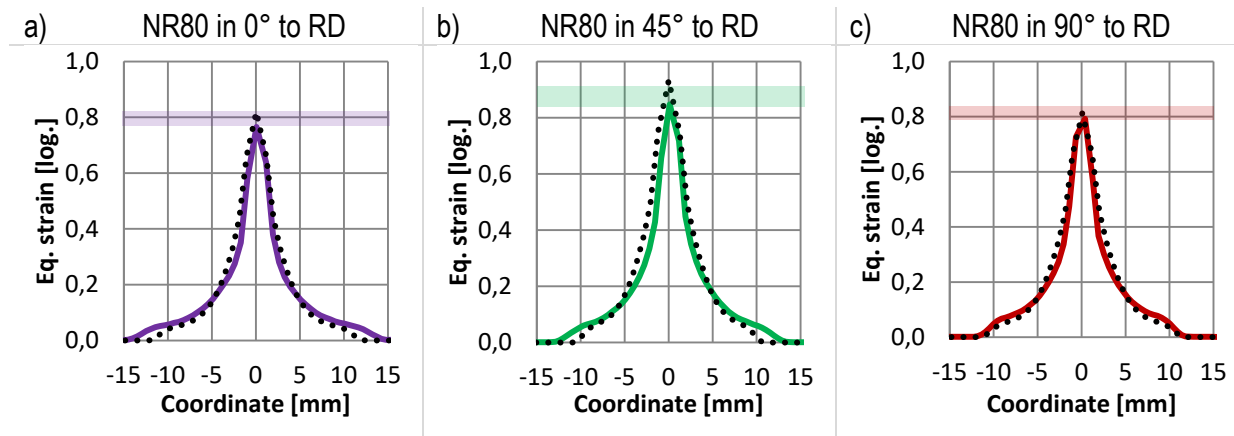


Figure 7-5: Comparison of experimental with numerical determined local strain behaviour of NR80 specimens of CR340LA in a) 0° , b) 45° and c) 90° to RD

Figure 7-6 and Figure 7-7 present the experimental and numerical behaviour within approximately plane strain achieved by NR05 specimens. The material model catches the distinct yield point, but is not able to reproduce its elevated force-level. Beyond force-maximum, the force-displacement trend of the numerical simulation does not meet the curvature of the experiment, but is able to predict the displacements at material failure within the experimental scattering. The differing force-displacement trends result from varying stress states of numerical simulation and the experiment. The numerical simulation is restricted to the plane stress state. In contrast to that, solid-simulations prove arising stresses in sheet normal direction, which can have a stabilising effect on the specimen behaviour due to a shift of the yield point towards higher equivalent stresses. This effect has to be compensated either by strain hardening behaviour or by a shift of the plastic instability point. Both result in differing force-displacement trends of experi-

ment and numerical simulation but enable the reproduction of the displacements at material failure.

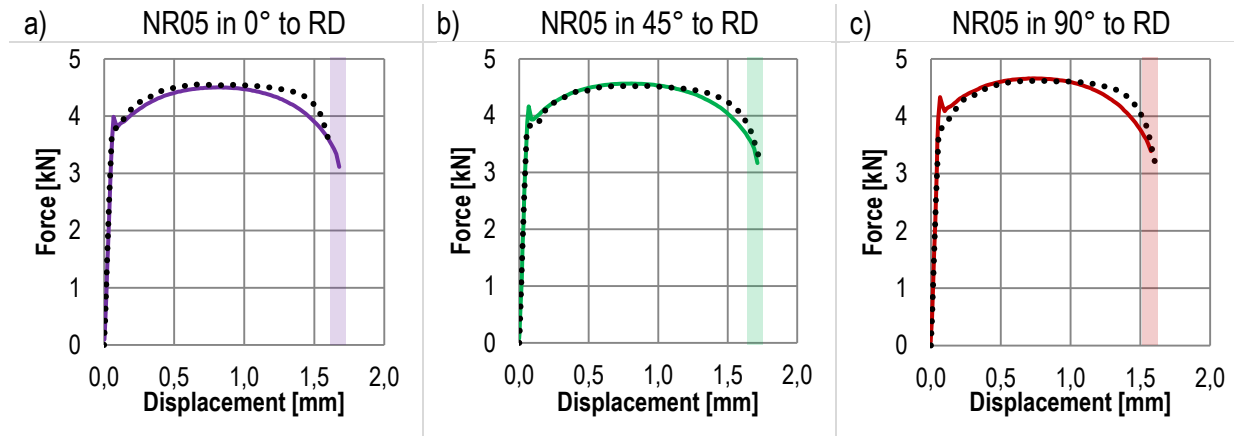


Figure 7-6: Comparison of experimental with numerical determined force-displacement behaviour of NR05 specimens of CR340LA in a) 0° , b) 45° and c) 90° to RD

Moreover the strain fields of the NR05 specimens are depicted in Figure 7-7. For all three presented directions nearly no deviations of experimental and numerical results are observed. The localisation band width is met for all directions, assisted by the specimen-geometry. Furthermore, the applied orthotropic failure model is able to predict the equivalent strain at failure correctly for NR05 specimens.

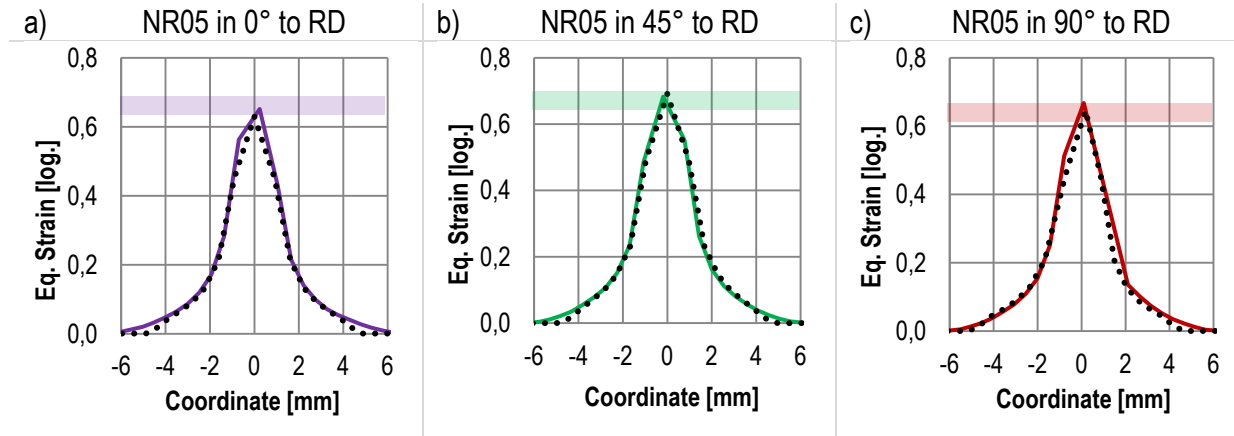


Figure 7-7: Comparison of experimental with numerical determined local strain behaviour of NR05 specimens of CR340LA in a) 0° , b) 45° and c) 90° to RD

Material behaviour under approximate shear is juxtaposed in Figure 7-8 and Figure 7-9. The utilised modelling approach shows a good correlation at the onset of yielding and also represents the slight elevated force-peak of the distinct yield point. However, the material model cannot reproduce the experimental force-displacement trend beyond 2 mm of global displacement leading to an overestimation of force. The obtained gradual decrease prior to failure of the numerical simulation is not as pronounced as seen in the experiment. However, the highest displacements up to failure are witnessed in 0° to RD (6.5 mm), whereas specimens in 45° and 90° exhibit only 6.0 mm of displacement. Even though the utilised material model overestimates

the force-level, the displacements at failure are within the scattering range. Moreover, the experimental force-displacement curve exhibits a kink only for 0° specimens, which is reproduced by the numerical simulation.

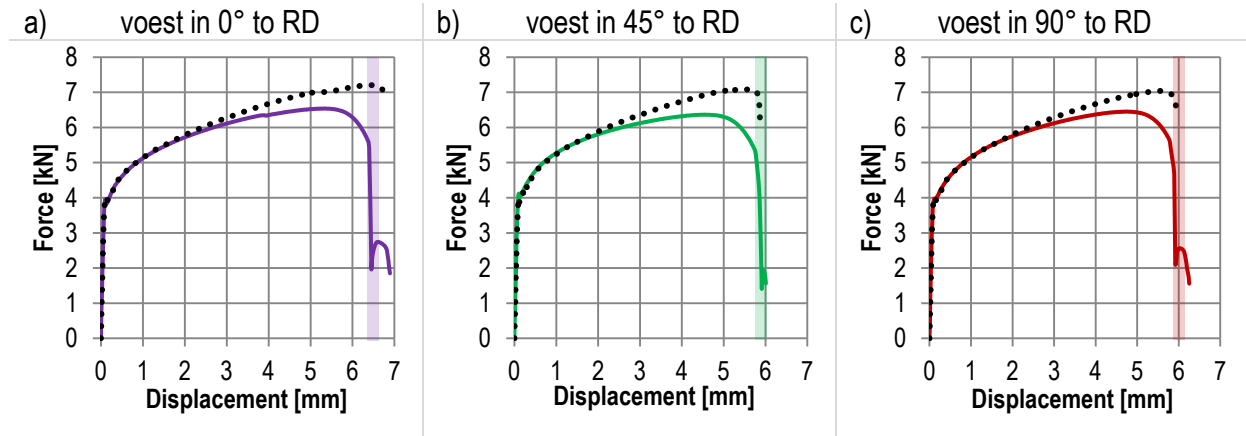


Figure 7-8: Comparison of experimental with numerical determined force-displacement behaviour of voest-shear-specimens of CR340LA in a) 0° , b) 45° and c) 90° to RD

In addition to the force-displacements, Figure 7-9 depicts the local strain fields over both shear sections. It pictures a strong underestimation of the failure strains for all three specimen directions. The reduced equivalent failure strains of the failure model are applied to capture the displacements at failure due to an unappropriated description of plastic behavior during shear loading.

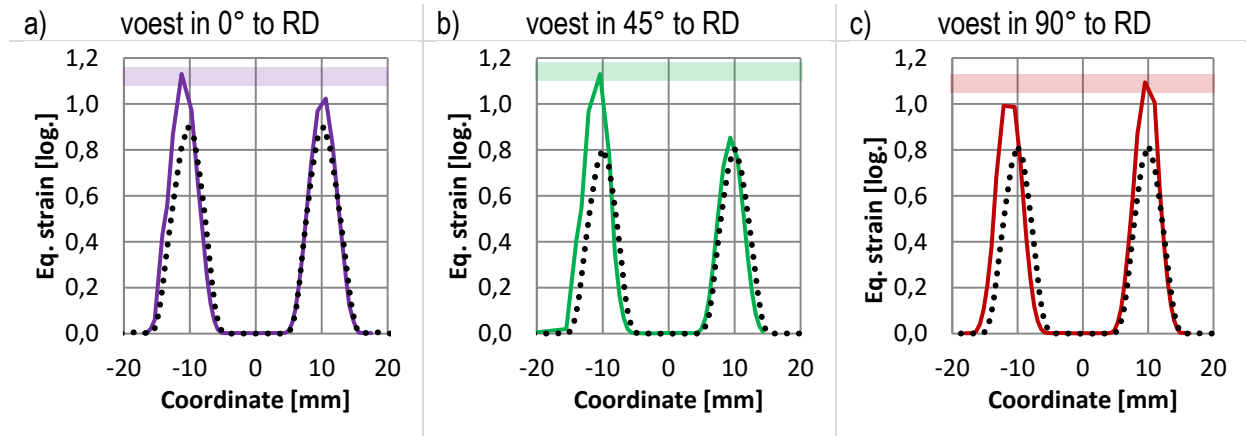


Figure 7-9: Comparison of experimental with numerical determined local strain behaviour of voest-shear-specimens of CR340LA in a) 0° , b) 45° and c) 90° to RD

Experimental as well as numerical simulation results of the conducted Bulge-test are contrasted in Figure 7-10. Besides the pressure-dome-displacement diagram the strain- and the displacement profiles in rolling direction are also investigated. Regarding the pressure-displacement behaviour, it reveals similar slopes of experimental and numerical data of the Bulge-test. Both show similar displacements at fracture, however, the simulation exhibits a higher maximum pressure than the experiment. The opposition of the local strains along RD reveals a good correspondence of experimental data and numerical simulation. Similar behaviour is found for the

dome displacement in rolling direction. As seen for pressure-displacements similar deflections are obtained from the experiment and the numerical simulation.

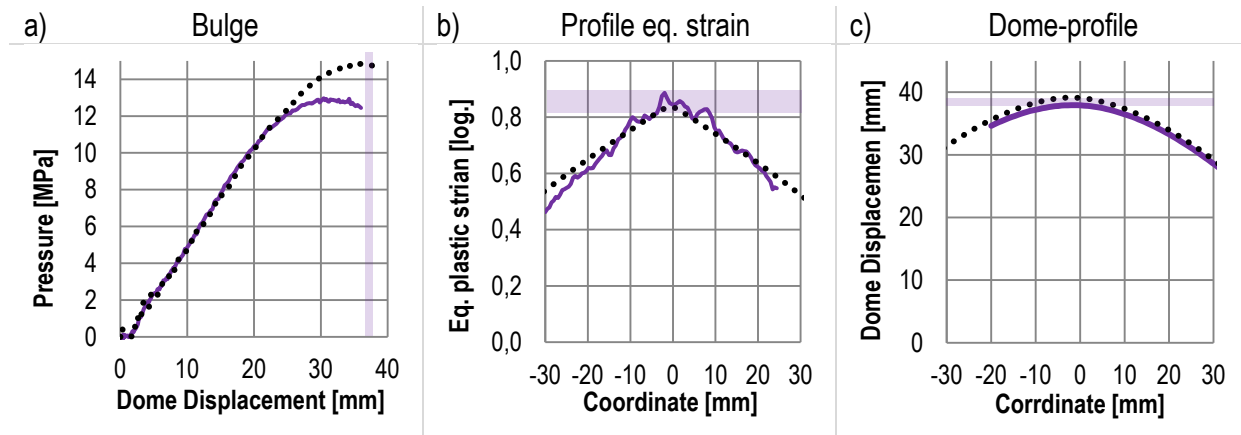


Figure 7-10: Comparison of experimental with numerical determined behaviour of CR340LA under biaxial loading, a) pressure-displacements at the dome, b) local equivalent strain profile in RD, c) dome-displacement profile in RD

7.2.2 MS1500 1.0 mm in Bake-hardening Condition (Shell)

The conducted numerical results of MS1500 in 0°, 45° and 90° to RD are pictured below. A plastic exponent M of 6 is chosen to meet the experimentally obtained force maxima of the NR05 specimens which approximate the plane strain stress state. The parameters are set to unity, which leads to a representation of the Hosford-yield surface by the Barlat'89 yield criterion. Including the experimental results of chapter 4.1, material failure is modelled with equal plastic instability and failure strains. With the utilised model approach a good correlation of experimental and numerical force-displacement behaviour could be obtained.

Figure 7-11 and Figure 7-12 compare the resulting material behaviour of standard tensions tests of experimental and numerical simulation. Figure 7-11 presents the force-displacements in 0°, 45° and 90° to RD. With the application of a flow curve in 0°, 45° and 90° to RD each, the characterisation is able to represent the experimental behaviour with its distinct yield strength in 0° as well as the yield behaviour in 45° and 90°. Furthermore, the force-displacement behaviour beyond maximum force is met with a good correlation of displacements at failure.

The local strain behaviour, displayed in Figure 7-12, reveals a similar width of the localisation bands. For all three directions, the numerical simulation is able to represent the DIC-strain fields within the scattering band width and predict material behaviour of the standard tension specimens.

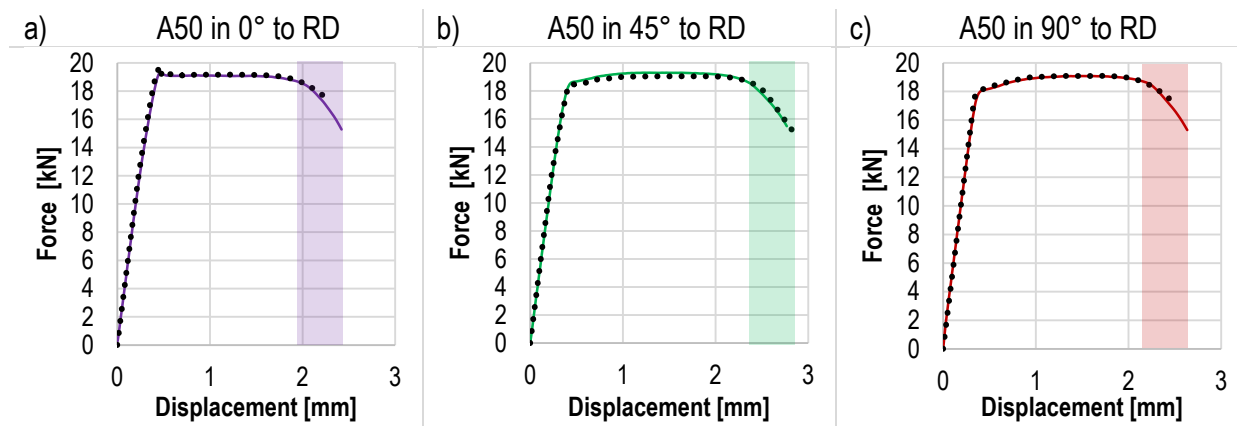


Figure 7-11: Comparison of experimental with numerical determined force-displacement behaviour of standard tensile tests of MS1500 in a) 0° , b) 45° and c) 90° to RD

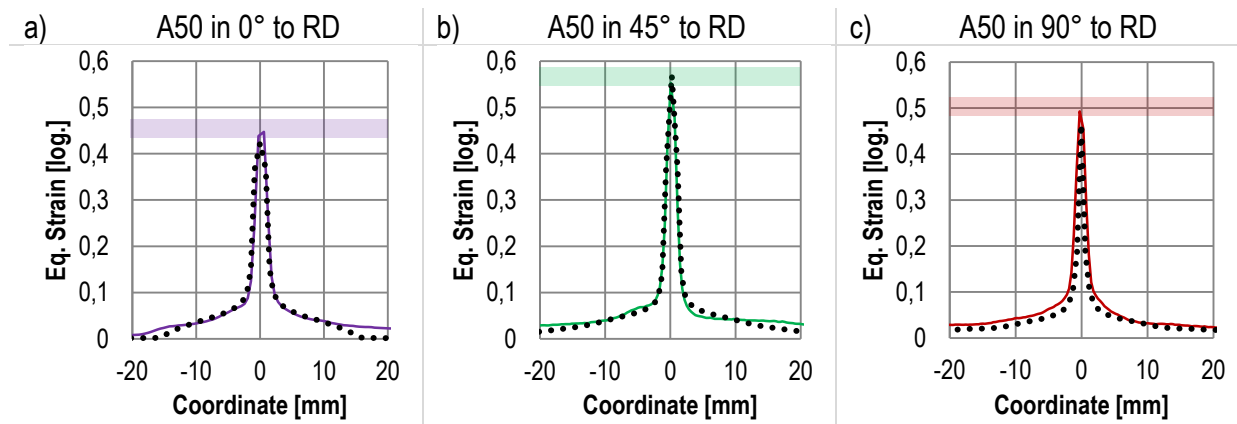


Figure 7-12: Comparison of experimental with numerical determined local strain behaviour of standard tensile tests of MS1500 in a) 0° , b) 45° and c) 90° to RD

The force-displacement behaviour of the experiment and the numerical simulation are contrasted in Figure 7-13. The characterisation is able to predict the distinct yield point for specimens in 0° to RD and shows no formation in 45° and 90° direction. For all directions, the displacements at failure are underestimated.

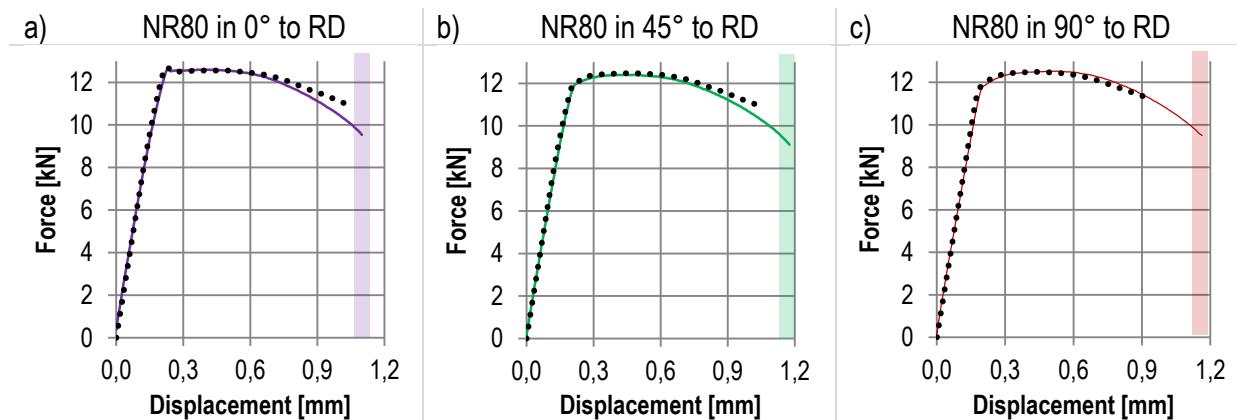


Figure 7-13: Comparison of experimental with numerical determined force-displacement behaviour of NR80 specimens of MS1500 in a) 0° , b) 45° and c) 90° to RD

Figure 7-14 depicts the local strain behaviour of NR80 specimen. The numerical simulation predicts the trend of the local strains along the specimen middle axis for 0° and 45° to RD. Only for specimens in 90° orientation it underestimates the fracture strains as well as the localisation band width.

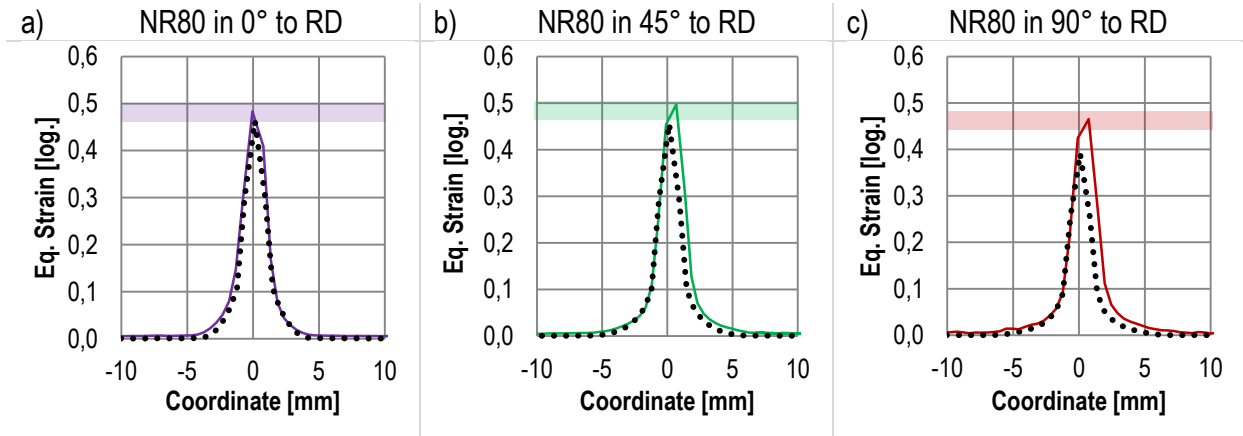


Figure 7-14: Comparison of experimental with numerical determined local strain behaviour of NR80 specimens of MS1500 in a) 0° , b) 45° and c) 90° to RD

Figure 7-15 and Figure 7-16 juxtapose the experimental material behaviour with numerical simulation results of NR05 specimens. The former presents the force-displacements in 0° , 45° and 90° to RD, the latter local strain behaviour. For all directions the maximum force levels are met with only a slight overestimation of the maximum. Additionally, the displacements at material fracture are underestimated with 0.05 mm for each direction. Regarding the local equivalent strains, the profiles along the specimen middle axis are met in 0° and 45° RD. In contrast to that, maximum strains in 90° are overestimated which marks an outlier with its significant lower failure strains. Moreover, the double-peak, resulting from the development of the failure surface over specimen thickness, cannot be reproduced with shell elements.

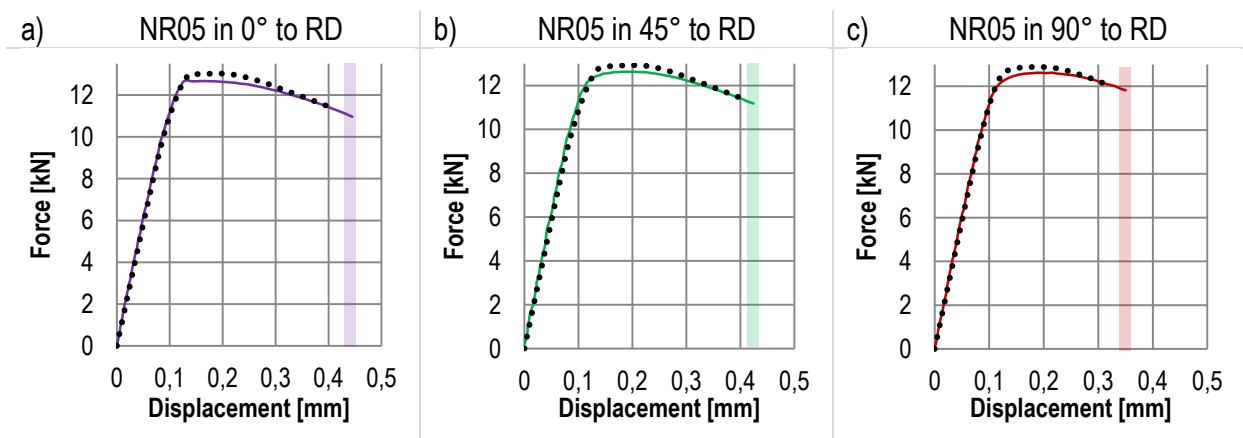


Figure 7-15: Comparison of experimental with numerical determined force-displacement behaviour of NR05 specimens of MS1500 in a) 0° , b) 45° and c) 90° to RD

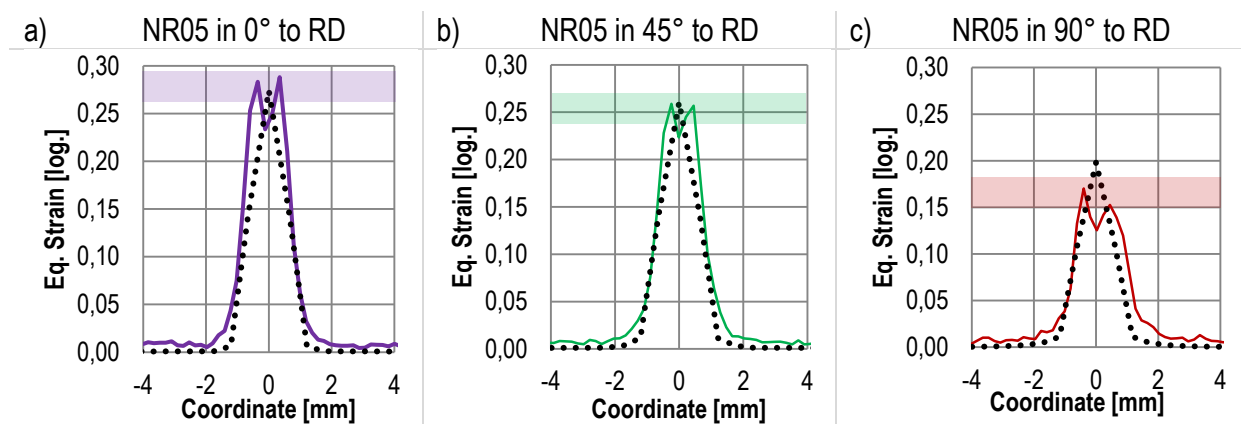


Figure 7-16: Comparison of experimental with numerical determined local strain behaviour of NR05 specimens of MS1500 in a) 0° , b) 45° and c) 90° to RD

The experimental behaviour of MS1500 and its characterisation under shear loading is presented in Figure 7-17 and Figure 7-18. The force-displacement behaviour as well as the local strain profiles are met for all investigated directions. Only numerical simulations of specimens orientated in 45° to RD exhibit a lower displacement (-0.15 mm) at failure and failure strain (-0.09).

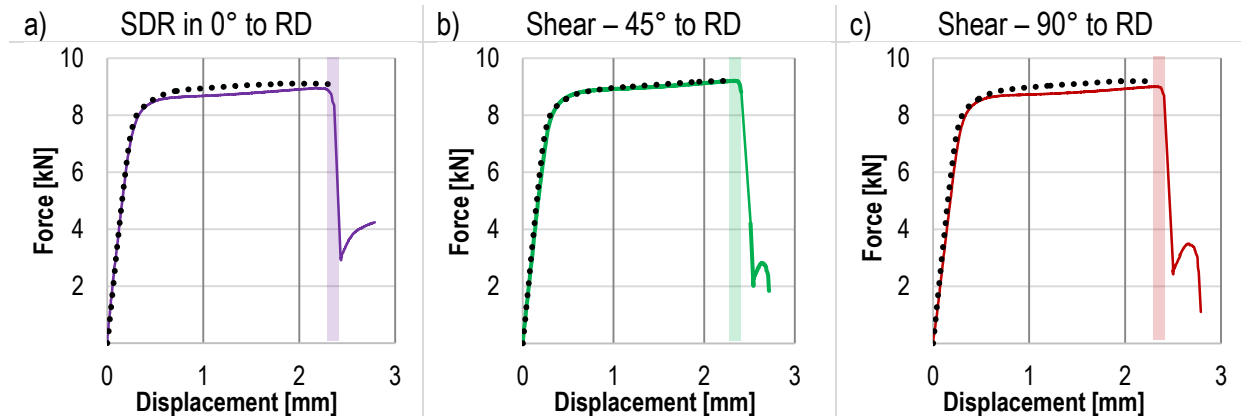


Figure 7-17: Comparison of experimental with numerical determined force-displacement behaviour of SDR0302-specimens of MS1500 in a) 0° , b) 45° and c) 90° to RD

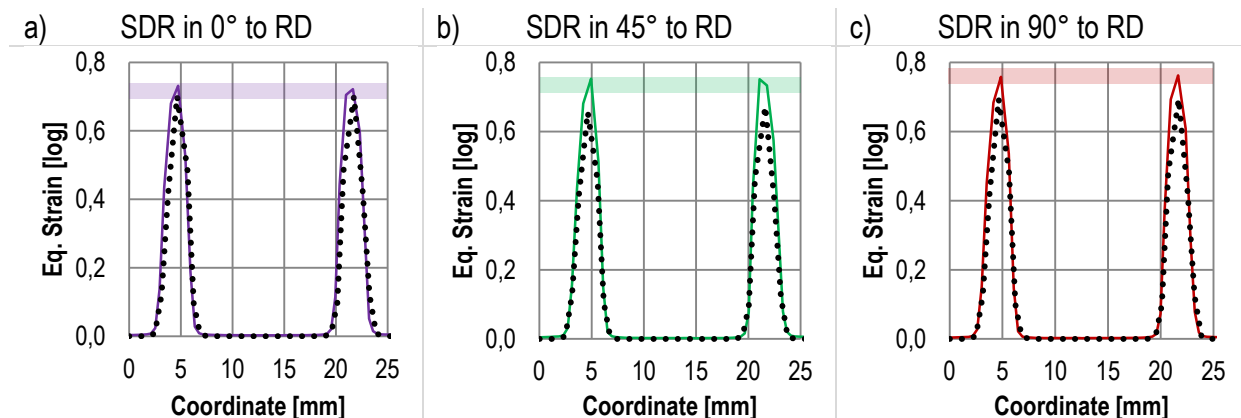


Figure 7-18: Comparison of experimental with numerical determined local strain behaviour of SDR0302-specimens of MS1500 in a) 0° , b) 45° and c) 90° to RD

Figure 7-19 depicts the opposition of experimental and numerical simulation results of the conducted Bulge-tests. The pressure in dependency to the dome displacement, the equivalent strains and the displacement profile in rolling direction are contrasted. The obtained pressure-displacement curve from numerical simulation agrees with the experiment, regarding maximum pressure, displacements at failure as well as general trends. Besides the fracture point, the trend of equivalent strains and displacements of the numerical simulations corresponds to the experiments. The contrasted curves show only minor deviations along the whole profile.

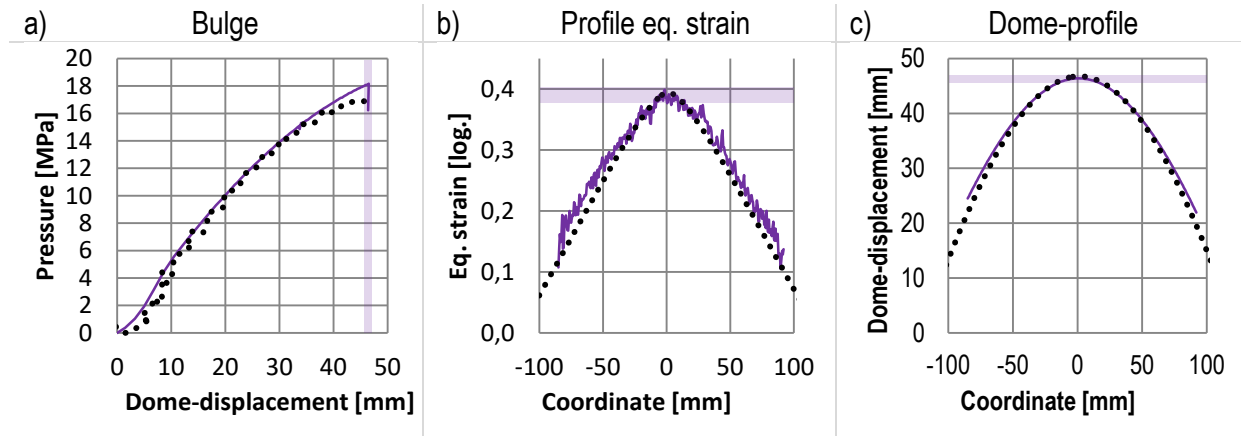


Figure 7-19: Comparison of experimental with numerical determined behaviour of MS1500 under biaxial loading, a) pressure-displacements at the dome, b) local strain profile, c) dome-displacement profile

7.3 Model Validation

The material characterisations conducted in chapter 7.2.1 and 7.2.2 base on the definition in 0° , 45° and 90° to RD. To verify the present material characterisation numerical simulations of specimens in 22.5° and 67.5° are carried out and compared to experimental results. Furthermore, force-displacements as well as local strain behaviour of numerical simulations and experimental tests are compared.

7.3.1 Validation of CR340LA 1.1 mm-Material Model

In this section the opposition of the material behaviour of A50 (Figure 7-20), NR80 (Figure 7-21) and NR05 specimens (Figure 7-22) in 22.5° and 67.5° to RD is investigated for validation purpose of the material characterisation.

The conducted numerical simulations of standard tension specimens in both directions match the experimental force-displacement behaviour. Hardening behaviour and displacements at failure are also met besides the development of Lüders-bands with its distinct yield point. Regarding the local strain fields, the numerical results agree with the experimental data. This applies for the 22.5° as well as the 67.5° specimens.

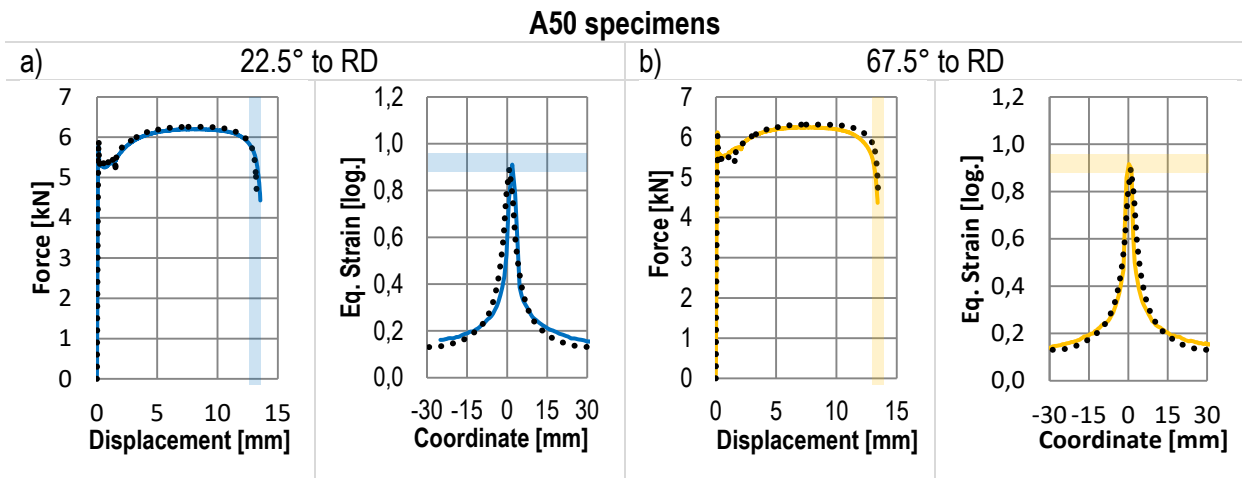


Figure 7-20: Validation of material model for CR340LA PB 1.1 mm at A50 specimens in a) 22.5°; left: force-displacements, right: local strain field) and b) 67.5°; left: force-displacements, right: local strain field)

The opposition of the force-displacement behaviour of NR80 specimens in 22.5° and 67.5° to RD is depicted in Figure 7-21. As previously seen for specimens in 0°, 45° and 90° to RD, the experimental force-displacements are overestimated by the numerical simulations, which overshoot the scattering band widths of the displacements. Regarding the onset of plastic deformation, the pronounced yield point is only partly captured. The numerical simulation is only able to reproduce a less pronounced yield point than obtained from the experiment. However, force-maximum is captured for both specimens in 22.5° and 67.5° direction.

Moreover, the numerical simulations in 22.5° and 67.5° to RD meet the experimental strain behaviour. The failure strains meet the DIC-data within the scattering as well as the localisation band width.

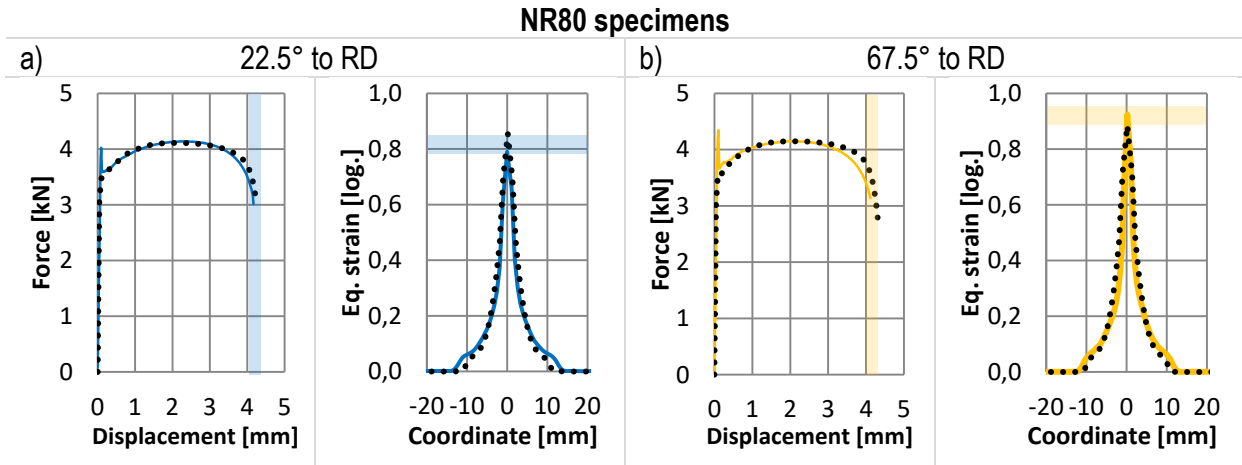


Figure 7-21: Validation of material model for CR340LA PB 1.1 mm at NR80 specimens in a) 22.5°; left: force-displacements, right: local strain field) and b) 67.5°; left: force-displacements, right: local strain field)

In addition to A50 and NR80, the material model is validated for NR05 specimens. As previously detected already for 0° , 45° and 90° , the model does not reproduce the elevated force-level of the distinct yield point. The hardening behaviour as well as the maximum force is met by the numerical simulations. Material behaviour beyond force-maximum, however shows a drop too early, which results in slightly lower displacements at failure. The opposition of the local strain fields reveals an agreement of numerical simulation and DIC-strain field for both additional specimens in 22.5° and 67.5° direction.

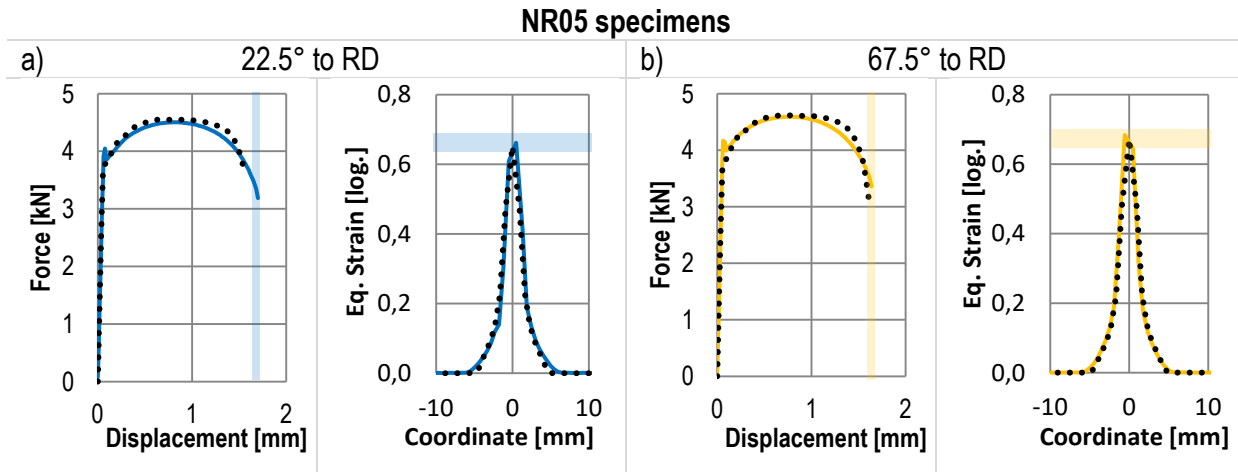


Figure 7-22: Validation of material model for CR340LA PB 1.1 mm at NR05 specimens in a) 22.5° ; left: force-displacements, right: local strain field) and b) 67.5° ; left: force-displacements, right: local strain field)

7.3.2 Validation of MS1500-Material Model

This section presents the model validation of the characterised MS1500. The experimental and numerical simulation results are contrasted in Figure 7-23 (A50 specimens), Figure 7-24 (NR80 specimens) and Figure 7-25 (NR05 specimens).

Comparing the force-displacements results of standard tensile specimens (Figure 7-23), they reveal a correlation of numerical simulation and experimental test. With the three applied flow curves, the yield behaviour could be reproduced. The numerical simulation in 22.5° direction exhibits the same slight distinct yield point as can be seen experimentally. The yield point in 67.5° is also met lying between those in 45° and 90° . Additionally, the force-displacement behaviour of numerical simulations agree with the experiments. Furthermore, the displacement at failure in 22.5° to RD matches the experimentally determined trend within the scattering range. Regarding the local strain behaviour, lower equivalent strains at failure are obtained by the numerical simulation than by DIC-measurements. Moreover, the localisation band width is slightly smaller than seen in the experiment. The lower failure strains are connected to 0° , which are also at around 0.4, and dominate failure in 22.5° to RD. In 67.5° the absolute value of failure strains as well as the localisation band width could be reproduced.

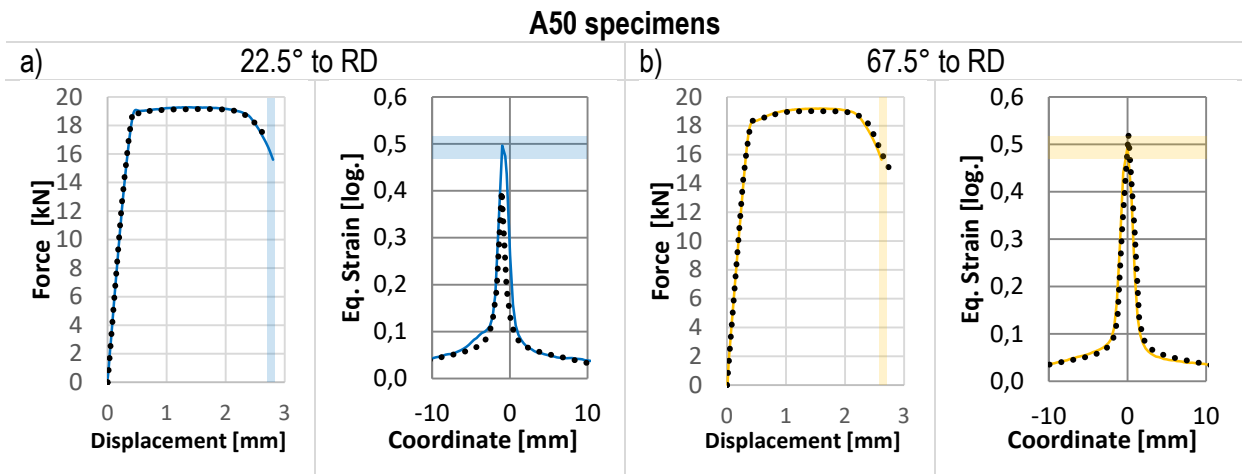


Figure 7-23: Validation of material model for MS1500 at A50 specimens in a) 22.5°; left: force-displacements, right: local strain field) and b) 67.5°; left: force-displacements, right: local strain field)

The opposition of the force-displacement behaviour obtained from the experiments and the numerical simulations for NR80 specimens is presented in Figure 7-24. The yield point as well as the force-maximum are met for both directions. However, the displacements up to failure are underestimated for 22.5° as well as for 67.5° to RD. Moreover, the local strain fields are reproduced for both directions. Also the width of the localisation bands as well as the failure strains agree with experimental results.

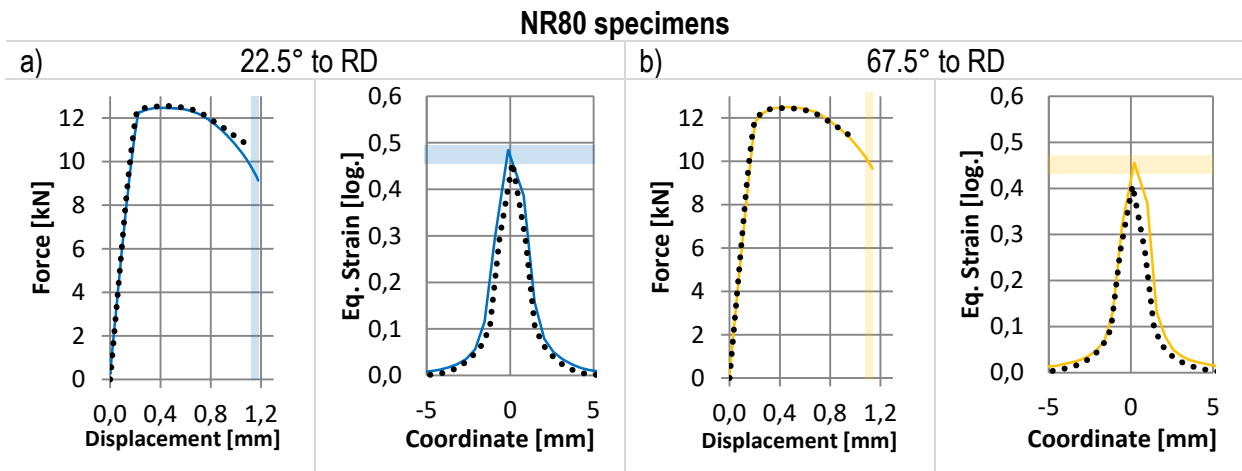


Figure 7-24: Validation of material model for MS1500 at NR80 specimens in a) 22.5°; left: force-displacements, right: local strain field) and b) 67.5°; left: force-displacements, right: local strain field)

Figure 7-25 displays the characterisation in nearly plane stress in 22.5° and 67.5° to RD. The force-displacements as well as local strain fields match for both directions. As previously seen for 0°, 45° and 90° specimens, the maximum force is slightly over- and displacements at failure slightly underestimated. The strain fields obtained from numerical simulations exhibit the same localisation band width as well as failure strain than from DIC-measurements. As described in 7.2.2 it is not possible to reproduce the double-peak with shell simulations.

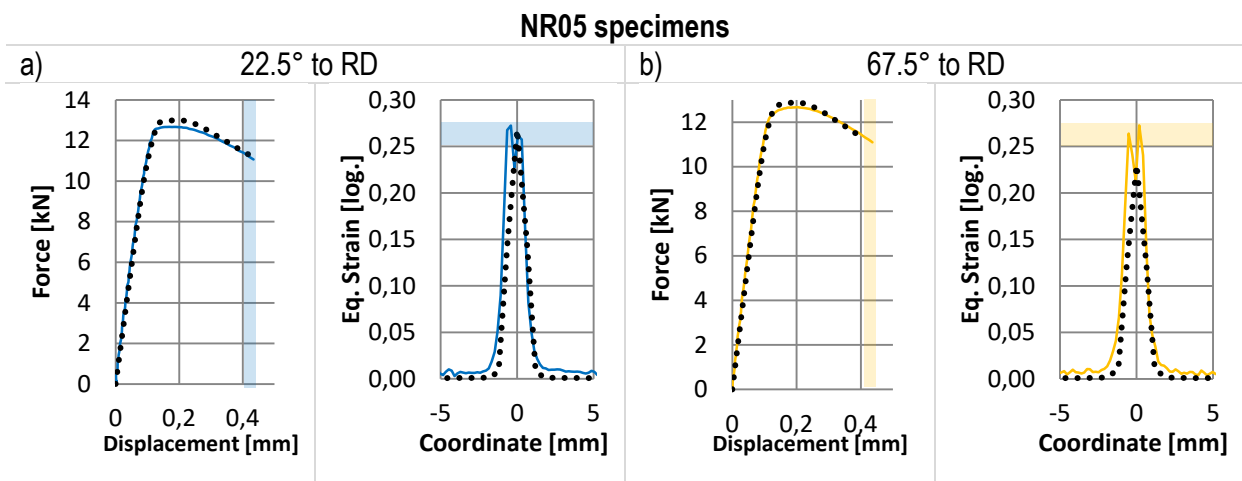


Figure 7-25: Validation of material model for MS1500 at NR05 specimens in a) 22.5°; left: force-displacements, right: local strain field) and b) 67.5°; left: force-displacements, right: local strain field)

Regarding the comparison in this section as well as the results presented in chapter 7.2.2, the numerical simulations are able to reproduce the experimental results. The characterisation provides no evidence for material behaviour for pressure. Therefore in this stress triaxiality range, no conclusion can be drawn. Besides, due to neglecting rate dependencies the model is only valid for quasi-static tests and triaxialities between shear and biaxial tension.

7.4 Investigations of Virtual Components

The previously conducted orthotropic material characterisation bases on flat specimen with different initial stress triaxialities under tensile loading. As presented in chapter 3, material effects like the development of Lüders-bands or pronounced orthotropy are stress state dependent (e.g. deviating behaviour in uniaxial tension and plane strain stress state). In contrast to that, various stress states arise during component tests, which also depend on the specific geometry or the loading.

To estimate the effect of orthotropic material behaviour, different components are virtually investigated. These tests are not correlated with experimental results due to a partly massive effect of outer influences, e.g. friction. Two different test setups are chosen and depicted in Figure 7-26; a hole expansion test and the compression of a double-hat profile. Drawings of the specific geometries of these setups can be found in chapter 10.8. For both components numerical simulations with material variations, e.g. orthotropic plasticity and failure, orthotropic plasticity and isotropic failure and isotropic plasticity and failure, are carried out to rate the effect of orthotropy. The simulation results of the hole-expansion tests are compared in regard of force-displacement behaviour and crack orientation. For the double-hat-profile, a robustness analysis is conducted, which includes, besides material variations as well as sheet thicknesses, impactor velocity and impactor angle. Furthermore, the effect of the distinct yield point on the component behaviour is investigated.

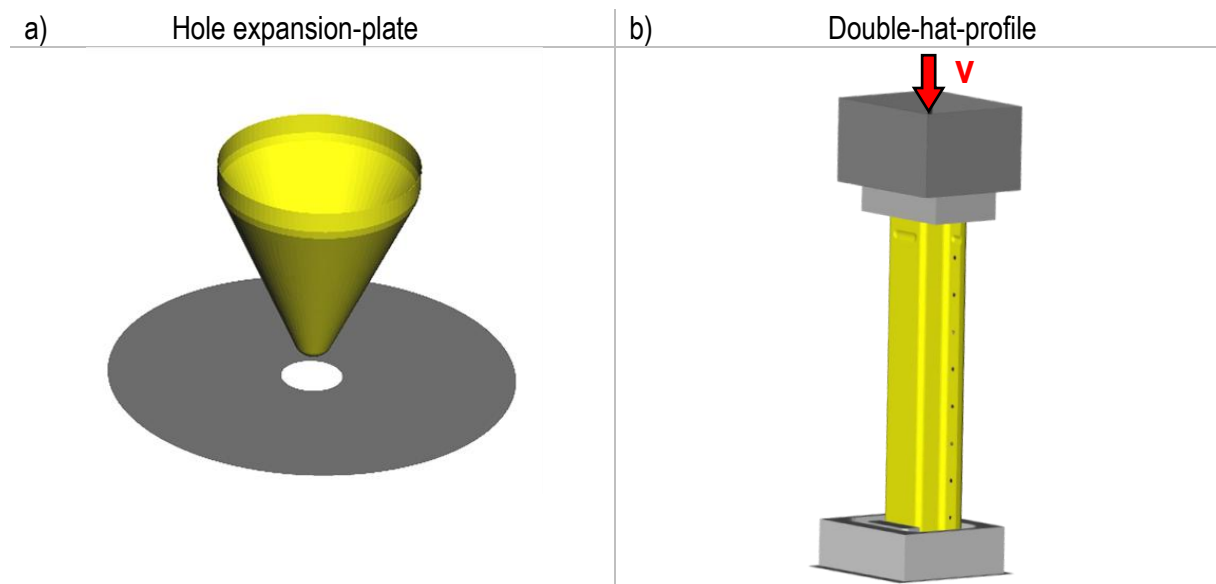


Figure 7-26: Different test setups for virtual component tests; a) hole expansion test and b) compression of a double-hat profile

7.4.1 Influence of Orthotropy on Hole Expansion Test

To investigate the influence of orthotropy on the hole expansion tests, three different materials based on the experimental data are defined, contributing to orthotropy as well as isotropy of plasticity and failure. What is more, orthotropic plastic behaviour with isotropic failure is utilised for the holed plate. The resulting force-displacement-diagrams are pictured in Figure 7-27. All three simulations exhibit similar force-displacement behaviour up to 37 mm punch displacement. Beyond, failure arises for isotropic plasticity coupled with isotropic failure. Furthermore, both numerical simulations incorporating orthotropic plasticity exhibit equal force-displacement as well as similar failure behaviour, with material failing at punch displacements of 41 mm.

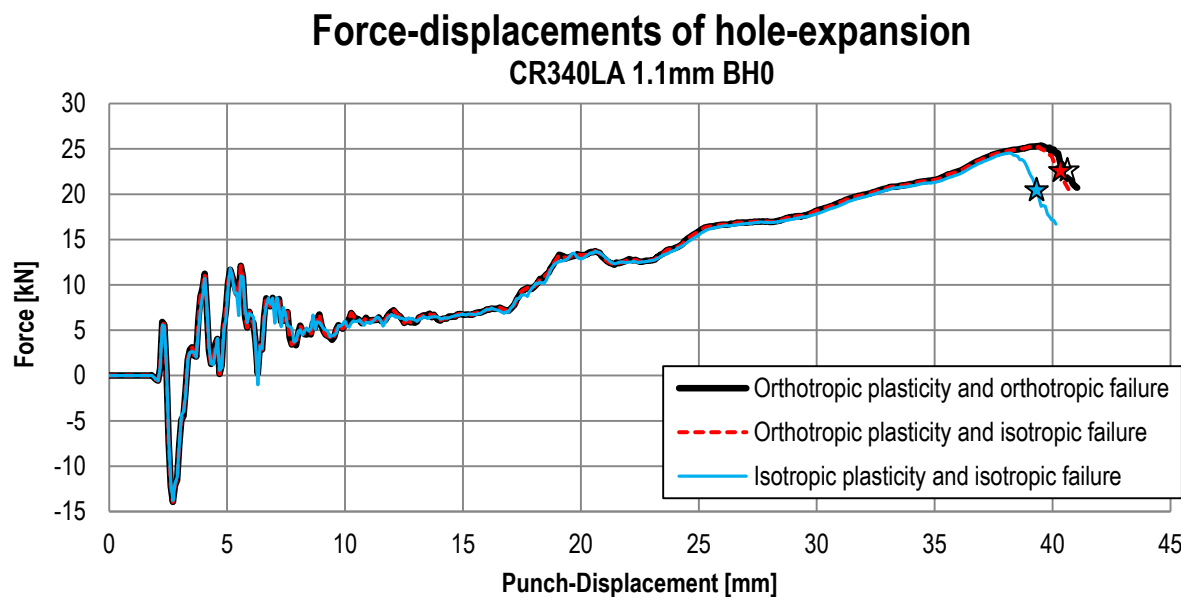


Figure 7-27: Force-displacement behaviour of the hole-expansion test for different material compositions with marked onset of failure (star)

The results only show an ancillary effect of orthotropic failure on the simulation results in comparison to the utilisation of orthotropic plasticity, especially orthotropic strain hardening. However, all three material definitions include the properties of the 0° direction and both orthotropic material definitions additionally possess the properties of the 45° and 90° direction. Within the 0° orientation, the lowest strain hardening capability as well as the lowest plastic instability and failure strains arise. Despite this, simulations incorporating orthotropic plasticity demonstrate higher punch-displacements at failure. This indicates a stabilising influence of other directions, namely 45° and 90° to RD, which exhibit a higher strain hardening behaviour.

7.4.2 Robustness Analysis of Double-Hat Profile

The robustness analysis bases on the comparison of the plastic strain behaviour according to Diez et al. [Die16] and is applied to the numerical simulations of the double hat profile. The model reduction is conducted by projecting the plastic strains onto the middle-axis of the double-hat profile, see Figure 7-28.

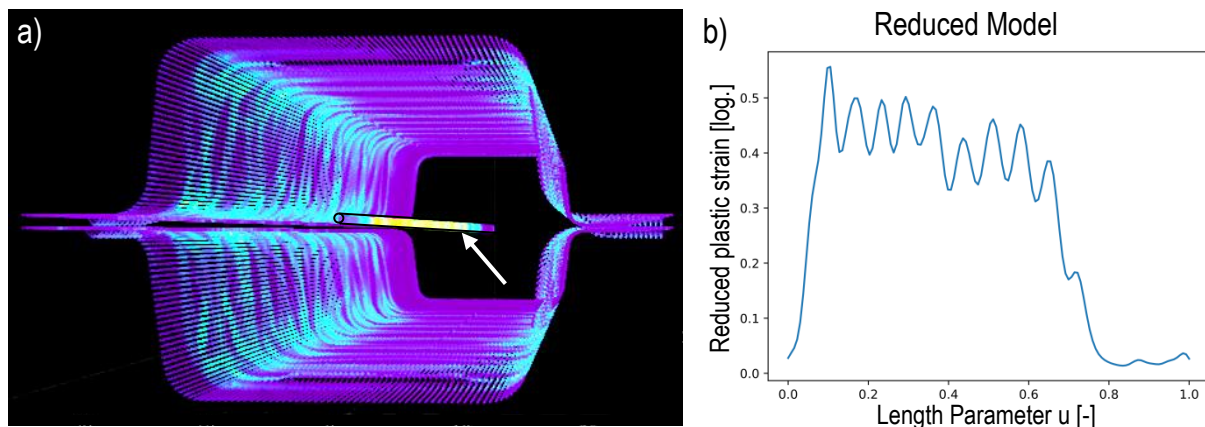


Figure 7-28: a) Visualisation of the plastic strains along the double-hat profile and their projection onto the middle axis (white arrow), b) Plastic strain profile of the middle axis, utilised for model reduction

Based on the resulting plastic strain profiles of various numerical simulations, Diez et al. [Die16] calculate the similarity between simulation results ranging from 0 (completely diverse) to 1 (identical). Each result is displayed as a single point within a 3D Cartesian coordinate system, in which the Euclidean distances between different points are complementary to their similarity (1 - completely diverse and 0 - identical [Die16]). Furthermore, the resulting trends of the plastic strains are classified based on their similarity and form different clusters which indicate similar deformation behaviour. Moreover, the force-displacement behaviour is regarded.

To investigate the effect of orthotropy, the material definition is varied. The variations are applied to each numerical simulation with a material orientation of 0° , 45° and 90° to RD. Besides orthotropic plasticity and failure, orthotropic plasticity is combined with isotropic failure; isotropic plasticity and isotropic failure are included as well. To rate the arising variations of the component behaviour, additional parameters like the flow curve, the failure strains but also the sheet thickness or the impactor velocity and impactor angle are varied. Moreover, flow curves without

distinct yield points are utilised to exclude the effect of bake-hardening. The variations are presented in Table 7-1.

Table 7-1: Parameter variations of the conducted robustness analysis

Parameter	Initial	Variation
Orthotropic plasticity and orthotropic failure	Base run	
Orthotropic plasticity and isotropic failure (angle to RD)	0°	45°, 90°
Isotropic plasticity and isotropic failure (angle to RD)	0°	45°, 90°
Distinct yield point	Including	Excluding
Impactor velocity	5m/s	±0.5 m/s
Impactor angle	0°	+2.5°
Sheet thickness	1.1 mm	±0.05 mm
Offset flow stress	0.0 MPa	±20 MPa
Scaling of flow stress	100 %	±10 %
Scaling of failure strains	100 %	±10 %

The resulting multi-dimensional similarity plot is pictured in Figure 7-29 with the similarity axes S_x , S_y and S_z . The presented robustness analysis bases on the results of the time step in which the base run exhibits 30 mm impactor displacement. The sixty-six simulation results are grouped into six clusters, which are depicted as coloured single points within the multi-dimensional similarity plot. Within these clusters no orientation dependency is observed. Cluster0 groups the three simulations which include an offset of the flow stress of -20 MPa. In contrast to that, cluster1 represents the simulation results by lowering the impactor velocity towards 4.5m/s. Moreover, cluster2 includes simulations with increased impactor velocity of 5.5m/s or an impactor angle around the y-axis of 2.5°. Furthermore, cluster2 incorporates the simulation result with the material orientation in 45° and fully orthotropic material behaviour (plasticity and failure). In contrast to that, cluster3 represents all simulations, which neglect the Lüders-Effect. These simulations are conducted for isotropic as well as orthotropic plasticity. In cluster4 the three simulations with an impactor angle of 2.5° around the z-axis are represented. The remaining variations group into cluster5, which incorporates the sheet thickness variations or the change from orthotropic towards isotropic material behaviour and failure strain scaling.

Regarding the calculated similarity values, only minor differences between all conducted simulations are revealed. The calculated similarities remain below 0.05, which indicates only minor impact of the single parameter variations. Especially the comparison of orthotropic and isotropic material behaviour leads to no significant strain field variations.

In addition to these results, the local plastic strain fields of each cluster are presented exemplarily in Figure 7-30. Except for cluster3 only minor variations of the strain fields are observed. The visualised plastic strain fields confirm the results of the conducted robustness analysis.

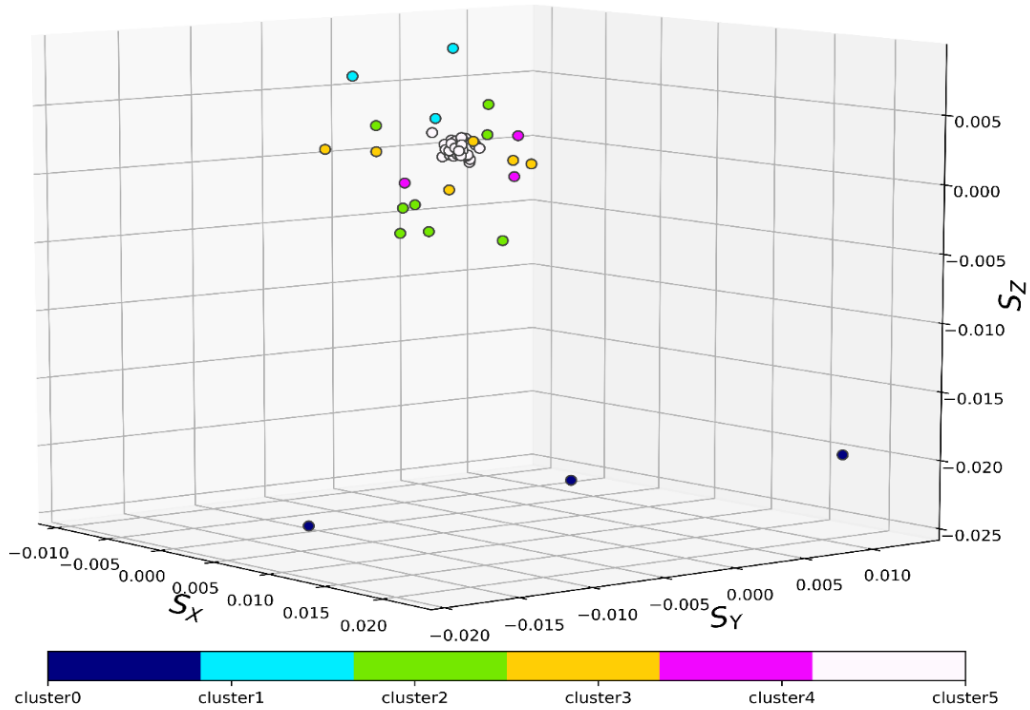


Figure 7-29: Results of the robustness analysis of the double-hat profile with six highlighted clusters, which represent the flow curve offset of -20 MPa (cluster0), lowered impactor velocity (cluster1), raised impactor velocity (cluster2), neglecting of the Lüders-Effect (cluster3), impactor angle variations (cluster4) and all other variations (cluster5)

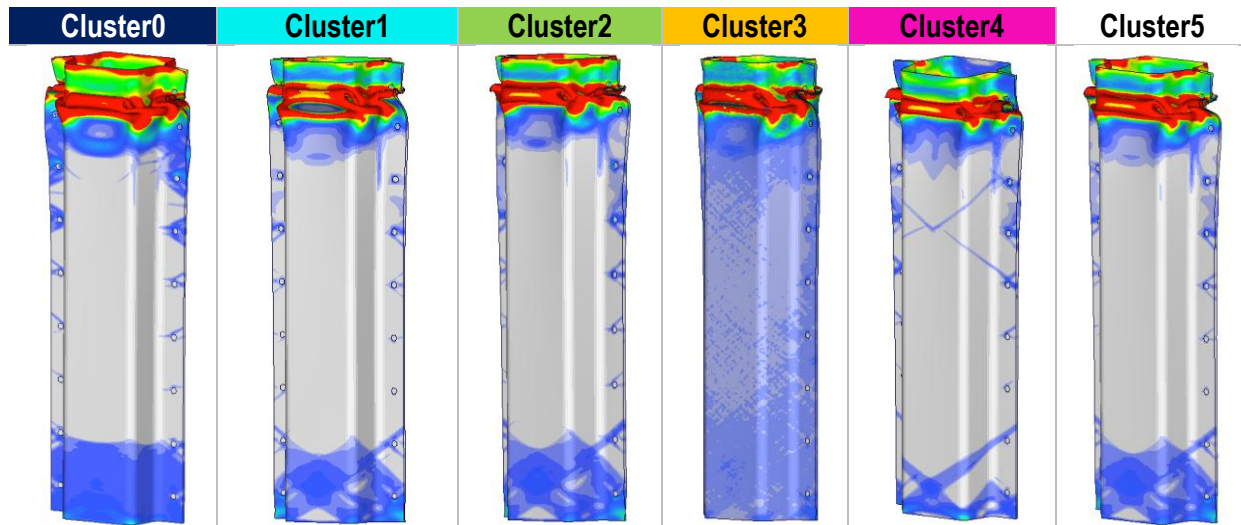


Figure 7-30: Exemplary strain fields for the different clusters at the same time-step (refers to 30 mm impactor displacement in cluster 5) with the plastic strain cut off at 0.20 (red)

In addition to the time step with 30 mm impactor displacement, further time steps of the simulation with displacements up to 90 mm are investigated. At these steps similar material behaviour also remains and no major differences are observed. Moreover, the resulting plastic strain fields

equal with ongoing impactor displacement. As a result, the clear grouping into cluster with similar parameter variations disappears.

The influence of the Lüders-Effect with its accompanied elevated yield strength on the double-hat profile is regarded separately. In Figure 7-31, the force-displacements of the double-hat-profile with and without distinct yield point in 0° as well as 90° to RD are presented. The displacements are obtained at the impactor; the force is measured at the top of the profile.

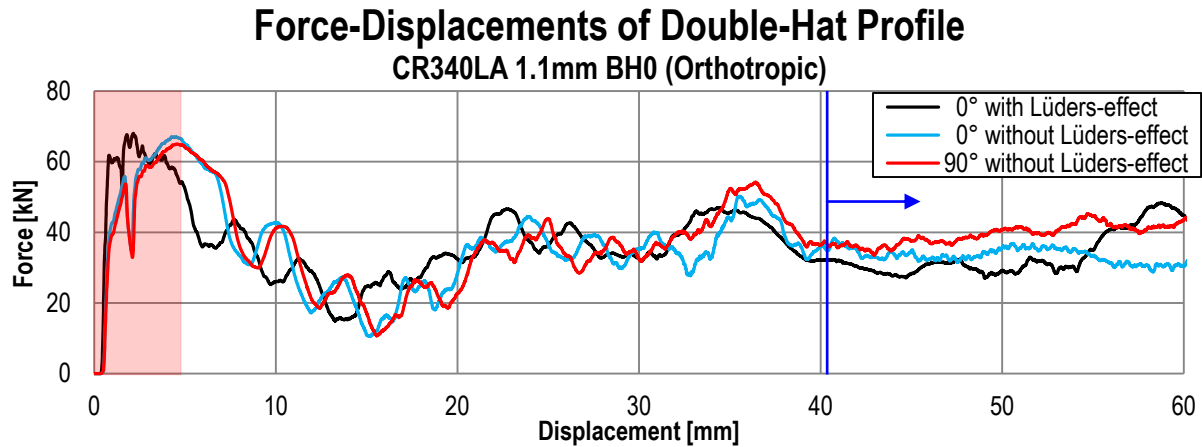


Figure 7-31: Force-displacement-diagrams of the double-hat profile in 0° and 90° incorporating as well as neglecting the Lüders-Effect. Arising plastic deformation is highlighted in red. The deviating behaviour of both simulations without Lüders-Effect is marked by a blue line

The onset of plastic deformation of all three presented numerical simulations is marked within a red rectangle. The application of the distinct yield point leads to the onset of yielding at 60 kN followed by an increase up to 70 kN, which represents the maximum of the measured forces. Beyond force maximum a drop of the force level is observed which oscillates around 35 kN. Regarding both numerical simulations, which neglect the Lüders-Effect, the onset of plastic deformation arises at 40 kN. As seen for numerical simulations with distinct yield point, both simulations without Lüders-Effect exhibit also a maximum force of 70 kN. This maximum, however, is shifted towards higher impactor displacements from 2 mm towards 4 mm. This shift remains for the force-displacements beyond force-maximum. Both simulations without Lüders-Effect show similar behaviour up to 40 mm. Beyond that point, marked by the blue line, the two simulations begin to differ and the double-hat profile in 0° exhibits a decreasing force-displacement trend, whereas in 90° an increase is observed.

Moreover, the simulation results at impactor displacements of 90 mm are pictured in Figure 7-32. The numerical simulation, which includes the Lüders-Effect within its flow curve, leads only to dents at the top of the profile. In addition, the resulting strain field features areas with no or very low true plastic strains (<0.01). However, the investigation proves the influence of the Lüders-Effect in conjunction with plastic orthotropy on the denting behaviour of the double-hat profile but only at late stages of deformation.

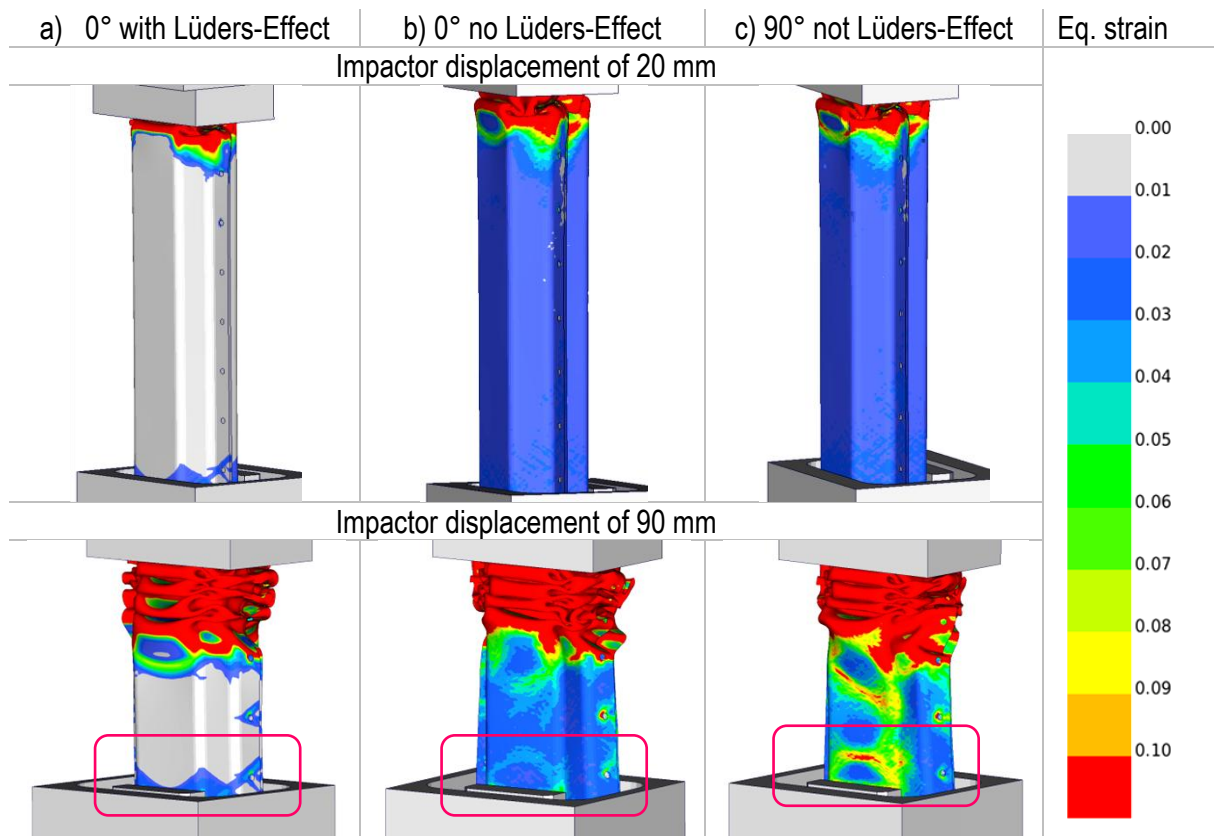


Figure 7-32: The local strain fields at displacements of 20 mm (upper) and 90 mm (lower) for double-hat-profiles with orthotropic plasticity and failure, utilising flow curves a) with and b)/c) without a distinct yield point in material orientations of 0° and 90° to RD

7.4.3 Comparison of the CR340LA Fracture Properties

In chapter 7.2 the resulting material characterisation of CR340LA in 1.1 mm sheet thickness was presented. In addition to that, both remaining CR340LA sheet thicknesses (0.6 mm, and 1.8 mm) are characterised; their results are depicted in chapter 10.6 and 10.7. Also the characterised material properties of all three investigated sheet thickness of CR340LA are also compared. The comparison includes the different flow curves, the plastic instability as well as failure strain curves and the damage- and fading exponent.

As presented in chapter 3.1.4 the different sheets demonstrate varying distinct yield points. They are considered within the material characterisations and lead to varying flow curves within the Lüders-Effect. Equal strain hardening behaviour is observed beyond this up to UTS. The major variation of the flow curves arises beyond UTS, at which point the plastic behaviour has to be estimated. As pictured in chapter 4.1 the plastic instability strains are equal for sheet thicknesses of 1.1 mm and 1.8 mm yet 0.04 lower for 0.6 mm sheets. In addition, equal damage and fading exponents are identified for CR340LA in 0.6 mm, 1.1 mm and 1.8 mm. Despite equal damage and fading exponents, all three sheet thicknesses show different failure strains. A dominant effect of the utilised plasticity model is revealed due to high fading exponents, leading to dominant damage effects at relatively high strains for all three characterisations.

8 Summary and Discussion

This work focused on the orthotropic material characterisation of selected high strength and ultra high strength steels. Beside the experimental investigation of different measuring techniques, the experimental results were conveyed into mathematical models. With focus on automotive crash simulation the solver LS-DYNA was chosen. Different modelling approaches were utilised to describe the elasto-plastic behaviour and material failure separately. To describe elasto-plastic material behaviour, the Barlat models from 1991 for 6D (solids) and from 1989 for 3D stress states (shells) were chosen. Especially the implementation of the latter with a separate definition of the flow behaviour in up to three directions enables an accurate description of the elasto-plastic material behaviour, even though more advanced models, like e.g. the YLD2000 are able to describe the yield surface more precisely. To describe material failure the orthotropic extension of the GISSMo, the *MAT_ADD_GENERALIZED_DAMAGE, was selected to provide the separate definition of failure properties in up to three directions. Within this work, different isotropic models were extended to describe material orthotropy. For extension purpose, the plasticity Barlat model from 1991 was utilised. It represents the generalisation of the model approach from 1989 and therefore enables the consistency of the utilised models.

The experimental investigation focussed on the quasi-static behaviour of CR340LA in three thicknesses (0.6 mm, 1.1 mm and 1.8 mm) and MS1500 (1.0 mm). The initial stress triaxialities of the tested specimens ranged between 0.00 (shear) and $\frac{2}{3}$ (biaxial tension). In addition to the force-displacement behaviour, the DIC-technique was utilised to determine surface strain behaviour. Furthermore, the microstructure of selected specimens was investigated by OLM, SEM and EBSD-method.

Beside the separate investigation at different stress states or specimen orientations, the experimental results of all CR340LA sheet thicknesses were contrasted. To account for the different sheet thicknesses, the force-level was normalised by the minimum cross section leading to the normalised stress. For all three CR340LA sheets, similar material behaviour up to the maximum of normalised stresses was found except for the onset of plastic deformation. All sheets exhibited a distinct yield point accompanied by the development of Lüders-bands. However, the connected stress and the strain level differed. For 0.6 mm sheets the highest yield strength as well as the highest strain during Lüders-band development arose. Both remaining sheet thicknesses revealed significantly lower yield strengths.

To investigate the dependency of Lüders-band development on the sheet thickness, OLM-measurements were conducted. They revealed similar grain sizes (8.5 μm and 8.7 μm) for 1.1 mm and 1.8 mm thick sheets but a significant reduction (6.1 μm) for 0.6 mm sheets. With regard to the work of Fujita and Miyazaki [Fuj78], the increasing sheet thickness increases the upper and lower yield strength up to a saturation level. Additionally, the presented experimental results revealed an exponential dependency of the yield strength on the grain size. The application of these results on the investigated CR340LA-types proved the dominant effect of the grain

size reduction from 1.1 mm and 1.8 mm thick sheets to 0.6 mm sheets on the upper and lower yield strengths. The differing grains sizes resulted from the specific sheet metal manufacturing process with different rolling and annealing steps. In addition, the pronounced grain size effect disguised a possible thickness effect.

Affiliated with the diverging development of Lüders-bands, all three CR340LA sheets showed similar strain hardening behaviour up to UTS, which can be best expressed by the Swift strain hardening law. Regarding the normalised stress-displacement behaviour beyond the stress-maximum of standard tensile specimens, no regularities were found for all three thicknesses and orientations. The conducted standard tension tests in RD, in which material behaviour is specified, exhibited similar behaviour for all CR340LA steels. In contrast to that, the lowest displacements up to fracture were observed for the 0.6 mm thickness for standard tension specimens in 45° and 90° to RD. However, 1.1 mm thick specimens showed higher displacements up to fracture than their 1.8 mm counterparts. In contrast to the displacements, the obtained surface strains at material failure were larger with increasing sheet thickness. The effect of different grain sizes was captured phenomenologically by the separate definition of plasticity and material failure.

The standard tensile specimens exhibit a parallel length of 75 mm in which the localisation zone is not geometrically predefined. Strain localisation forms due to geometric or material heterogeneities. These heterogeneities can be balanced out by the strain hardening behaviour and affect the global displacements as well as local strains. Regarding the displacements at UTS, much lower differences were observed than for the displacements at material failure. Even though the displacements at failure showed irregular behaviour, a clear thickness dependency of the failure strains was observed. Additionally, all three CR340LA sheets displayed similar plastic instability strains, which define the onset of damage of the continuum. In contrast to that, differing displacements at the onset of plastic instability were obtained. Therefore, differing strain hardening behaviour between UTS and the onset of plastic instability strains must cause the irregular behaviour of the standard tensile specimens, which stabilises the material behaviour beyond UTS especially for the 1.1 mm sheets more than for both other sheet thicknesses. The strain hardening behaviour is related to microstructural properties, e.g. the texture, the grain size, precipitations at the grain boundaries and grain elongation. Besides these OLM-measurements, no further microstructural measurements were conducted for all three sheets.

In addition to standard tensile specimens, representing uniaxial tension, additional specimens with varying initial stress triaxiality were investigated, e.g. shear or notched specimens. In comparison to standard tensile specimens, these specimens exhibited a more pronounced thickness dependency leading to higher displacements up to failure with rising sheet thickness. Furthermore, the equivalent failure strains on the surface showed a dependency on the sheet thickness. In addition, increasing failure strains were observed with the rise of the sheet thickness.

In contrast to standard tensile specimens, the zone of plastic deformation and strain localisation is geometrically predefined. Therefore, damage arises only in a narrow zone. Furthermore, the geometry forces strain localisation, which is consistent with a stress state change. At the speci-

men surface, the stress state tends towards the plane strain stress state. Regarding the specimen centre, the strain localisation leads to increasing stress in sheet normal direction, leading to higher yield strengths in comparison to the plane stress state on the specimen surface. The increasing yield strengths stabilises material behaviour during strain localisation. Numerical simulations proved this effect to be more pronounced with increasing sheet thickness. The strain localisation as well as the stress state change at the specimen centre is more intense for notched specimens with 5 mm than for those with 80 mm notch radius. The stronger stress state heterogeneity with decreasing notch radius and increasing sheet thickness leads to the observed more regular behaviour of specimens with notch radius of 5 mm in comparison to those of 80 mm notch radii or standard tensile specimens.

Besides these three CR340LA thicknesses, the MS1500-steel in 1.0 mm sheet thickness was investigated. Both steels represented two different steel-types; The CR340LA possessed a ferritic microstructure with small amounts of pearlite and ranks within the HSLA-group. In comparison to that, the MS1500, with its fully martensitic microstructure, belongs to the MS-group. Regarding the results of the MS1500, a strong orthotropy of the yield point was observed. All specimens in 0° direction displayed a distinct yield point, which was less pronounced in 22.5° orientation and disappeared for specimens in 45° to RD. Regarding the ratio of UTS to yield strength, ranging from 0.95 in 90° and 1.00 in 0° to RD, all directions exhibited only low hardening potential. In comparison to CR340LA, significantly lower displacements as well as equivalent failure strains were monitored at material failure. Moreover, the strain localisation was found to arise at early strain stages. With Lankford-Coefficients slightly lower than unity, nearly isotropic strain behaviour was determined for A50 specimens.

Regarding local strain behaviour, the 0° direction of the MS1500 showed lower equivalent failure strains at standard tensile tests than NR80 specimens. Furthermore, the distinct yield point of specimens in 0° is more intense than for other directions. These experimental results can be related to the rolling but also the stretch-levelling process during manufacturing of the MS1500. The resulting material behaviour was found to demonstrate bands of heterogeneities, e.g. pre-strains and affiliated pre-damage, in rolling direction.

The standard tensile specimens show a gauge length of 50 mm without the geometrical predefinition of the failure point, which forms due to specimen heterogeneities (geometry or material). In contrast to that, the failure point of NR80 specimens is predefined by the 80 mm notch. Plastic deformation of NR80 specimens occurs mainly within the notch ground and makes the specimen insensitive to small bands of material heterogeneities. In contrast to that, the A50 specimens with its 50 mm gauge length are sensitive to material heterogeneities and fail within the identified bands of pre-strain and pre-damage.

In addition, the NR05 specimens in 90° to RD exhibited significantly lower failure strains and displacements than all other directions. The NR05 specimens represent the plane strain-stress state with arising stresses in specimens-transverse direction. For NR05 specimens in 90° direction, these stresses were found to arise in 0° to RD, where pre-damage was identified. The pre-damage triggered failure at lower equivalent strains also incorporating lower displacements at

failure. In contrast to that, no effect of pre-damage was found for NR05 specimens, resulting from the small localisation zone which is unaffected by material heterogeneities. In addition, all NR05 specimens indicated the development of small localisation bands orthogonal to loading direction, pointing at the localisation surface through the specimen thickness. The resulting fracture surfaces revealed the same orientation as all CR340LA-specimens, though these did not show the localisation bands due to too-high ductility of the steel.

The experimental results of the investigated MS1500 proved a pronounced effect of the manufacturing process on the material behaviour. A dominant effect on the behaviour of standard tensile specimens in 0° orientation was observed, affecting lower failure strains than for NR80 specimens in 0° to RD. Moreover, also notched specimens with 5 mm aligned in 90° direction were also affected, exhibiting significantly lower failure strains as well as displacements at failure. Due to the unaffected NR80 and NR05 specimens with their geometrically predefined failure zone, the heterogeneities have to arise as banded structure. Additionally, both specimens were also influenced by pre-strain and pre-damage respectively induced by the manufacturing process. The material heterogeneities in combination with the low hardening potential leads to high scattering of the failure of standard tensile specimens.

The initial plastic orthotropy was characterised by the yield strengths of the conducted quasi-static tests as well as on basis of the local strain behaviour of standard tension tests. The Lankford-Coefficients ranged, dependent on their orientation, from 0.85 to 1.21 (CR340LA 1.1 mm) and revealed only minor orthotropy (isotropic: $R = 1.0$). In comparison to the strongly orthotropic strain behaviour of, e.g. aluminium extrusions with R -values between 0.3 and > 3.0 [DuB16], the investigated steels exhibited approximately isotropic strain behaviour. To estimate the effect of straining on the yield surface, the ratio of width to thickness strains were calculated at the later fracture point of standard tensile specimens in 0°, 45° and 90°. This ratio corresponds to the R -values up to UTS. Incorporating the Lankford-Coefficients at true equivalent strains of 0.05 (directly beyond Lüders-strains), 0.10, 0.15 (approximately UTS) and 0.20 (remaining constant R -value), the coefficients of the Hill'48 yield surface were directly calculated. The resulting yield surfaces only exhibited a distortion of +6 % in relation to biaxial stresses and between strains of 0.05 and 0.10. No further distortions were measured within a strain-range of 0.10 and 0.20. The distorted yield surface was found to stabilise localised necking with its increasing stress triaxialities compared to the yield surface of the unstrained material. The applied material model in LS-DYNA is capable of including the dependency of the Lankford-coefficient on the plastic equivalent plastic strain and enables the evolution of the yield surface with plastic straining. However, the yield surface evolution was negligible due to its minor impact of 6 % for biaxial stresses and its decreasing towards uniaxial tension. Moreover, the determination of R -values is only valid up to UTS; beyond UTS they have to be extrapolated. The effect of Lankford-Coefficients, dependent on the plastic strains, was investigated in [Sto16] and revealed only minor effects on the strain behaviour at the fracture point as well as on macroscopic force-displacement behaviour.

The obtained results contradicted the investigation of [An13] for IF-steel, in which a decreasing biaxial yield strength had been observed during straining yet could not be generalised for all steels. In addition to the Lankford-Coefficients, the CR340LA demonstrated orthotropic hardening behaviour leading to three different flow curves. The distortion-coefficient κ was proposed to rate the diverging hardening behaviour in 0° , 45° and 90° to RD. The investigation revealed no yield surface distortion due to the utilised orthotropic strain hardening. Therefore, all the experimentally obtained flow curves only varied at their stress level but not their principle trend.

Additional to DIC-measurements, the EBSD-method is applied to standard tensile specimens (CR340LA 1.1mm), aligned in 0° , 45° and 90° direction, at four different strain states, e.g. directly beyond Lüders-strains, at UTS, between UTS and fracture and at fracture. The former three strain states for all specimen directions show an evolution within the α - and γ -fiber. Only EBSD-measurements near fracture point reveal a significant change of both fibers, from a rolling- towards a tension-texture. The texture evolution also depends on the stress state besides microstructural properties. The diverging texture evolution for the first three strain stages of all three directions can be related to the specimen orientation and the microstructural orientation towards loading direction. Near fracture, DIC-measurements point dominant strains in loading direction, which can explain the development of similar ODFs with a maximum within the γ -fiber. In addition, conducted numerical simulations prove a multi-axial stress-state at material failure. In opposition to fracture, the continuous texture evolution beyond Lüders-strains and beyond UTS indicates similar stress- and strain-states respectively. The results of the EBSD-measurement accorded with the previously presented DIC-measurements. Due to the focus on a pure continuums mechanical material description the EBSD-measurements were not included in the material characterisation

Finally, regarding the failure behaviour of all three sheet thicknesses, a realignment of the fracture surface was revealed. For standard tension specimens, it was aligned within the sheet metal plane, where in contrast, the fracture surface of 1.8 mm specimens was oriented toward the sheet normal direction. Conducted numerical simulations with equally sized solid elements, including the same material model, for three sheet thicknesses (0.6 mm, 1.2 mm and 1.8 mm) indicated a thickness effect on the failure behaviour of standard tension specimens. By increasing the sheet thickness, a non-homogeneous stress state in sheet normal direction was obtained, leading to arising stress triaxiality and simultaneously decreasing Lode Angle Parameter. For sheets with a thickness of 0.6 mm and 1.1 mm the effect was negligible but became dominant for sheets in 1.8 mm. The shift of η and $\bar{\theta}$ affected decreasing failure strains for the arising stress state and supported a reorientation of the failure surface.

Moreover, the investigation of A50 and NR05 specimens revealed a similar effect resulting from the initial stress state. DIC-measurements, conducted within the sheet metal plane as well as over sheet thickness at A50 specimens of CR340LA (1.1 mm), pointed to a clear localisation band within the sheet metal plane but also to constant extensions over the sheet thickness. These bands accorded with the orientation of the fracture surface. The high ductility of the CR340LA blurred the local strain behaviour. Therefore, the investigated NR05 specimens were

manufactured from the MS1500, which exhibits a significantly lower ductility but similar fracture behaviour. In that case, the surface measurements prove two constant bands of elevated strains orthogonal to loading direction and within the sheet metal plane. In addition, material failure occurred over sheet metal thickness, not only for MS1500, but also for all CR340LA NR05 specimens.

The similar localisation behaviour for A50 and NR05 specimens arising at different orientations, indicated a stress state dependency of the fracture surface. The fracture behaviour of standard tensile specimens in three sheet thicknesses also proves the dominant effect of the stress state. As previously presented, the localisation affects a stress state heterogeneity over the sheet thickness and is more pronounced with increasing sheet thickness. However, the diverging orientation of the fracture surface, resulting from stress state heterogeneities, had only minor influence on the strains at material failure. Therefore, the sheet thickness is not the driving force of the increase of failure strains with growing sheet thickness.

The onset of plastic instability, which was defined as onset of damage of the continuum, was treated in chapter 4, in which plastic instability was defined on the basis of DIC-measurements. Specimens with 80 mm notch radius were utilised to investigate the surface strain behaviour. Additionally to DIC-measurements, the microstructure of the specimen surface was studied by SEM-images at different technical strain stages, revealing cracking grain boundaries and opening voids for every strain stage even prior force-maximum, except for the basic material. Due to no observable effect on the local strain behaviour prior force-maximum, the arising cracks and voids did not indicate the onset of plastic instability. Moreover, the local strain path remained linear even beyond force-maximum, which arose at 2.2mm, and started deviating with subsequent loading at displacements of 2.75mm.

There are different mechanisms which can affect the observed strain path change, e.g. the microstructural evolution leading to a change of the yield surface or the local stress state. Based on the previous investigations of CR340LA, only minor yield surface distortions arose due to orthotropic hardening or varying Lankford-Coefficients during straining up to UTS. These observations were supported by the conducted EBSD-measurements which revealed only a minor evolution of the ODFs even beyond force-maximum of standard tensile specimens in comparison to the ODF at material failure. Even though no effect of arising cracks of grains and grain boundaries was observed during plastic deformation prior force-maximum, the microstructure was identified to balance the microstructural damage. Furthermore, the onset of damage on the scale of the microstructure did not indicate damage of the continuum. Moreover the linear strain path was not influenced by the evolution of the NR80 geometry during straining, which leads to a deformation of the radius. Additionally, numerical simulations provided constant stress triaxiality for NR80 specimens during straining up to force-maximum. Regarding the onset of plastic straining revealed a deviation from the linear strain path during the development of Lüders-bands. Numerical simulations provided the development of Lüders-bands to be accompanied by stress state changes, which affect the local strain behaviour. Irrespective of associated or non-associated plasticity, the strain behaviour is connected to the stress state. In general, a stress

state change effects a change of the strain behaviour. Only special stress state changes within the 6D-stress space do not show a strain state change. Due to the focus on sheet metal, these load paths which are accompanied by a strong increase of stress components in sheet normal direction can be neglected.

If and when the evolution of the specimen geometry and damage on micro-scale did not impact local strain behaviour, yet material inherent properties have to induce the observed strain and stress-state change. Therefore, the deviation from linear strain behaviour has been identified as strains where microstructural effects became dominant and were defined as plastic instability strains. With this method the plastic instability of thin structures, e.g. sheet metals which exhibit the plane stress state, can be determined based on the surface strain measurements. Moreover, this approach does not require additional equipment like OLM, SEM or EBSD and can be directly obtained from standard material testing with a DIC-system.

The definition of plastic instability strains was applied to all of the previously investigated CR340LA (1.1 mm) specimens except for shear. The studied stress states, between $\frac{1}{3}$ and $\frac{2}{3}$ exhibited a minimum in plastic instability strains in approximate plane strain, obtained from NR05 specimens. Increasing strains were observed towards stress triaxialities of $\frac{1}{3}$ and $\frac{2}{3}$. The resulting curvature is similar to the predicted localisation strain surface of Marcadet [Mar15b] taken from unit-cell-simulations. The results contradict the predictions by Swift [Swi52] which forecasted the minimum plastic instability strains for uniaxial stress.

The presented definition of plastic instability was also applied to the DIC-results of specimens in 0°, 45° and 90° to RD. The highest plastic instability strains were received for specimens aligned in 45° to RD, whereas the lowest arose in 0° to RD. The obtained plastic instability strains for the 90° direction were found to lie in between the strains in 0° and 45°. All three directions demonstrated different Lankford-Coefficients, ranging from 0.85 (0° to RD) over 1.06 (90° to RD) to 1.21 (45° to RD). Despite these low variations, growing plastic instability strains went along with increasing R-values. The results accorded with previous observations in literature, e.g. [Tas09], of rising formability with growing R-values. Increasing Lankford-Coefficients lead to decreasing out-of-plane strains, e.g. in sheet normal direction, which destabilise the material and support necking.

Regarding both additionally surveyed CR340LA sheet thicknesses, slightly lower (0.6 mm) and similar (1.8 mm) plastic instability strains were maintained in comparison to the 1.1 mm thick specimens. The sheets in 0.6 mm and 1.8 mm, however proved deviating Lankford-Coefficients, e.g. for 45° specimens, ranging from 0.90 (0.6 mm) over 0.96 (1.8 mm) up to 1.21 (1.1 mm). The observations indicate additional effects to be responsible for the onset of plastic instability rather than only the absolute value of Lankford-Coefficients, e.g. the differing grain sizes, differing strain hardening behaviour beyond UTS or geometrical effects resulting from the sheet thickness.

The proposed method to define plastic instability was executed on the MS1500 steel. The investigated specimens exhibited a linear dependence of major to minor strains up to the occurrence

of localisation bands, which lead to a shift of the specimen halves in specimen transverse direction. An additional width strain, based on the deflection in specimen transverse direction, was included to eliminate this effect. For all investigated specimens, no deviations from linear strain paths were observed, which indicates coinciding plastic instability and failure surfaces.

The proposed method determines plastic instability strains on basis of the surface strain path and the connected stress state change. It further assumes a homogeneous behaviour over the sheet thickness prior plastic instability. However, based on numerical simulations Mohr et al. [Moh09] concluded material failure to start at the specimen centre. This may be true also for the onset of plastic instability but could not be investigated due to the limitation of the measurement techniques on the specimen surface. However, conducted solid simulations proved a deviation from homogeneous stress state over the sheet thickness higher strains than observed at the plastic instability point of the investigated CR340LA sheets. For specimens, especially notched specimens, considerably thicker than the investigated materials this must not apply.

Moreover, the proposed method determines the onset of plastic instability at displacements beyond force-maximum. For standard tensile specimens, the force-maximum determines the onset of diffuse necking and the end of the homogeneous distributed strains over the gauge length. The determined displacements at plastic instability of standard tensile and NR80 specimens were higher than the displacements at force maximum. Plastic instability and force maximum accorded only for NR05 specimens.

As previously described a coupling of stress and strain state by the plasticity models exist, which is utilised to determine the load paths of CR340LA and MS1500 based on DIC-measurements. The associated plasticity model of Barlat from 1991 was applied and calibrated by different stress states, e.g. uniaxial and biaxial tension as well as the plane strain stress state. The partial derivative of the yield surface within the stress space leads to the local strain increment vector, defining the local strain composition described by the introduced modified Γ -value and modified R-value (Γ^* and R^*). On basis of the experimentally obtained Γ^* and R^* the local load paths were determined. A direct comparison of load paths obtained from numerical simulations and DIC-measurements revealed a strong dependency on the flow potential. For both materials, the experimentally determined load path exhibited a shift towards higher stress triaxialities for specimen representing uniaxial tension in comparison to numerical simulations but they showed a similar trend.

The determined non-proportional load paths could not be utilised to calibrate the fracture strain surface due to the dependence of the fracture strains on the stress state. Therefore, so-called weighted load paths were introduced, relating the non-proportional load paths to an equivalent proportional load path. Instead of the local strain increment the local strains were utilised to determine the stress state. Furthermore, piecewise linear failure strains between single strain stages, measured by DIC, were approximated. In contrast to the previously presented determination of the load paths, the strain increments were integrated for weighting purpose. The weighted load paths were calculated from the resulting local strains in analogy to the local strain increments and determined the target points for the failure strain surface. Applied to specimens

of CR340LA (1.1 mm) and MS1500, it revealed a good correlation with the adopted failure curve of the shell simulation later on.

The presented method is highly dependent on the yield surface and the predicted strain increment. The yield surface determines the composition of the plastic strains for each stress state and has to be defined accurately for a proper prediction of the stress states on basis of the DIC-measurements. The yield surfaces were also used for the numerical simulations and were primarily adapted to meet the stress level and secondarily on the plastic strain behaviour. The resulting load paths overestimate the stress triaxiality, e.g. in uniaxial tension.

Moreover, the failure points, predicted by weighting of the non-proportional load paths, correspond to the later on applied failure curves of the material characterisation. The approach enables the determination of these curves for all three directions directly on experimental results. The accuracy of the prediction, however, depends on the representation of the plastic strain behaviour. Especially for standard tensile specimens of CR340LA an overestimation of the failure strains was observed. In contrast to that the plastic strain behaviour within biaxial tension and plane strain stress state was accurately determined by the yield surface and meets the utilised failure curve.

To capture orthotropic fracture a new the failure criterion, the Barlat-Coulomb model, has been developed based on the Mohr-Coulomb model [Wie10]. The resulting failure strain surfaces and curves were defined within the mixed stress-strain space. Orthotropy of the failure strains was included by linear transformations of the isotropic stress tensor on basis of the Barlat plasticity model proposed in 1991. When focussing on the experimental results of CR340LA, orthotropic strain hardening was integrated into the applied Swift-hardening law, which was utilised for conversions from equivalent stresses to equivalent strains.

The resulting failure criterion is applicable to plane and general stress states and predicts failure curves or surfaces within the mixed stress-strain-space. These curves or surfaces show consistent behaviour, e.g. equal failure strains for biaxial tension, due to one criterion for all directions using the Barlat-Coulomb model. In contrast, a separate definition of failure strains for each direction, employing an isotropic failure criterion, cannot guarantee these equalities. However, the Swift hardening criterion, utilised to couple the stress-strain behaviour, represents the strain hardening behaviour up to UTS of the investigated CR340LA-steels but deviates beyond UTS from the characterised flow-curves. The deviation can be balanced out by fitting the parameters of the Swift law, leading to a discrepancy of experiment and model prediction even prior UTS.

Beside the definition of plastic instability and failure strains, the applied orthotropic failure model in LS-DYNA includes non-linear damage accumulation and stress fading described by two exponents for each direction. Due to the model implementation, orthotropic failure requires linear damage accumulation. To estimate the fading exponent, a hybrid criterion has been proposed based on DIC measurements as well as numerical simulation results without damage. The NR05 specimens initially represented the plane strain-stress state, in which the plastic instability and failure strain surfaces showed their minimum within the mixed stress-strain-space. Only

minor deviations were observed on regarding the effective surface load paths of NR05 specimens. Furthermore, the plastic instability as well as the failure strain surface demonstrated only minor variations for these load paths. Therefore, changes of the load path were assumed not to affect large changes of the failure properties, which can be approximated as constant. This assumption is not valid for near material failure, however, where the failure point indicates large changes of the load paths. To minimize this effect, the average strains along the minimum cross section were applied and compared to the averaged equivalent strains obtained from numerical simulations without damage. The nominal stresses dependent on the averaged local strains were defined separately for numerical simulation and experiment to couple global and local material behaviour. On applying the equations of the GISSMo on the resulting nominal-stress-averaged equivalent strain curve, the damage and stress-fading exponents could be estimated by fitting on the experimental curve. The hybrid approach, including the nominal stress-averaged equivalent strain curves of the numerical simulation, leads to failure parameters dependent on the flow curve extrapolation. The proposed hybrid method was able to balance these effects when the numerical simulation (solids) results were integrated as well. However, the hybrid approach was only able to predict the fading-exponents for solid simulations and underestimated the fading-exponents for shell simulations. The shell simulations were not able to represent the stress state changes at the specimen inside, which can be related to a stabilising increase in yield stress. Moreover, numerical simulations without damage exhibit diverging stress states compared to simulations including damage. For solid simulations, these stress state divergence was balanced out by the solids in the specimen inside which could not be represented by shells and leads to a miscalculation of the fading exponent.

The numerical simulation results of CR340LA in 1.1 mm and MS1500 in 1.0 mm sheet thickness were presented in chapter 7. All investigated steels demonstrated a distinct yield point, which was included into the numerical simulation by the definition of the flow curve. Material behaviour has been divided into strain hardening and dislocation break free, in which the former was reproduced by the Swift hardening law and the latter was modelled by adding an exponential term to the strain hardening function. The applied approach was able to represent a distinct yield point as well as a following constant force-level during Lüders-band propagation. Furthermore, the flow curve lead to a good correlation of experimental and numerical strain behaviour, including the development of strain bands during the development of Lüders-strains.

The approach includes a decrease of the flow-stress during the development of the Lüders-bands. This decrease in combination with the negligence of strain rate effects can cause oscillations of the force-level during the Lüders-band development.

Orthotropic material behaviour has been defined for the 0°, 45° and 90° direction, which applied to the plasticity- (Barlat'89 - LS-DYNA: *MAT_036) and for the failure model (LS-DYNA: *MAT_MAGD). Strain hardening behaviour was included by three flow curves for uniaxial tension. The definition of orthotropic failure is based on the isotropic GISSMo. The orthotropic failure model enables various definitions of failure, e.g. LIAD. In the present utilisation, separate GISSMo's were specified in 0°, 45° and 90° to RD. Damage was accumulated within three di-

reactions separately, unlike material failure, which was based on an equivalent damage variable. Moreover, linear damage accumulation is necessary for a proper prediction of material failure.

Besides the Barlat'89 plasticity model, the *MAT_MAGD, an orthotropic failure model in LS-DYNA, was applied to model the CR340LA steel. The material behaviour was described in 0°, 45° and 90° to RD. For validation purpose numerical simulations in 22.5° and 67.5° orientation were also conducted. The characterised material model was able to represent the force-displacement behaviour of standard tensile as well as the notched-specimens in all investigated directions. Moreover, the local strain along the specimen middle axis of experiment and numerical simulations agreed within the scattering bands. The numerical simulation was not able to reproduce the experimentally observed orthotropic Lankford-Coefficients of the CR340LA due to a focus of the characterisation on the reproduction of the force-displacement behaviour and failure strains. However, the force-displacements of the shear tests were not represented accurately, which was also true for the pressure displacement curve of the Bulge-test. For these specimens, the force and pressure levels during strain localisation were overestimated by the numerical simulation. Despite this, the local strains at material failure were represented by the utilised material model within the experimentally scattering bands.

The used specimens exhibit a stress state change during strain localisation, which is more pronounced at the specimen centre than at its surface. The stress state change during strain localisation stabilises the material behaviour with increasing yield strengths. The utilised shell elements are only able to represent the stress state at the specimen surface. The stabilisation of the specimen centre is utilised by the flow-curve extrapolation and overestimates the strain hardening behaviour to capture the behaviour of standard tensile or notched specimens. For shear or biaxial tension with less pronounced stress state differences over the sheet thickness this leads to an overestimation of the force- and pressure levels respectively during strain localisation. For a better representation within shear or biaxial tension, a separate definition of the strain hardening behaviour within these stress states is needed.

Also the material behaviour of the investigated MS1500 was also modelled by the Barlat'89 plasticity model, as well as the *MAT_MAGD failure model. For most of the specimens, a good correlation quality has been achieved regarding force-displacements and local strain profiles along the specimens. Moreover, the numerical simulation is able to reproduce the experimentally observed Lankford-Coefficients of the MS1500 in all directions. The investigated MS1500 steel revealed microstructural effects which could not be simulated without further modelling steps or with shell elements. Opposing the behaviour of A50 and NR80 specimens aligned in 0° direction, they revealed higher equivalent strains at failure for the notched specimen, which could be explained by pre-damage resulting from manufacturing steps like stretch levelling. Furthermore, the applied numerical model was not able to describe the development of localisation bands over the sheet thickness and therefore of capturing the local strain profile along the loading axis. Despite these material inherent factors, the numerical simulations proved the applicability of the proposed failure criterion on the MS1500.

Even though the numerical simulation is not able to model over thickness effect, resulting in strains over the sheet thickness, of the MS1500, as seen for NR05 specimens, the deviation of experimental and numerical simulation results within shear or biaxial tension is less than seen for CR340LA. Numerical simulations proved minor stress state heterogeneities over the sheet thickness than seen for the ductile CR340LA, leading to a better representation of the strain hardening behaviour. Moreover, the observed localisation bands over the sheet thickness did not dominate material behaviour. Their approximation with shell elements as band orthogonal to the loading direction represented material behaviour sufficiently.

Beside material characterisation, the impact of orthotropy was investigated on the hole-expansion tests as well as on the compression behaviour of a double-hat profile. The results, depicted in chapter 7.4, indicated a pronounced impact of the plastic behaviour on the regarded components. However, other material inherent properties, e.g. failure strain, exhibited only a minor effect on the virtual component behaviour. In addition, a distinct yield point could dominate the material behaviour especially.

Regarding the conducted robustness analysis a very minor impact on the component behaviour was observed. Although standard tensile or shear specimens demonstrated significant orthotropic properties, nearly no effect was observed within the plane strain stress state. Material failure of the conducted compression tests arose mainly under plane strain, in which only minor effects of material orthotropy were witnessed.

In addition, the material characterisations of the three different CR340LA sheet thicknesses were contrasted. Besides varying failure strain curves, all other failure properties remained similar for all directions, e.g. instability strains as well as damage- and fading-exponents. Similar yield surfaces, calibrated by R-values and by nominal stresses, were obtained on regarding the plastic behaviour. Main variations arose with the flow curves exhibiting deviations beyond UTS besides the included Lüders-Effect. These observations were independent from the modelling technique regarding (high fading exponents) or disregarding (low fading exponents) additional regularisation. For both characterisation methods the definition of plasticity and especially of strain hardening had a major influence. In addition, the dominant effect of the flow curves agreed with the observations of the conducted robustness analysis.

DuBois et al. [DuB16] presented the characterisation of an aluminium extrusion (AW6060-T66), including orthotropic plasticity and failure. Strong R-value variations, ranging from 0.27 to 1.69, are identified and lead to deformation of the yield surface compared to its isotropic counterpart. Additionally, different strain hardening behaviour in 0°, 45° and 90° to RD as well as failure strain variations up to 100 % were described which enable an accurate prediction of the conducted tests. Moreover, the investigations of [DuB16] revealed a similar dominant effect of plasticity on the material behaviour as seen in the presented investigation conducted for different steels. Therefore, a proper description of plastic strain behaviour is necessary for an adequate material description. This is especially true for materials with only minor orthotropy of the failure strains as proven by the investigated steels.

9 Outlook

The experimental procedure focussed on the quasi-static testing to characterise orthotropy. Yet real crash-loadings are highly dynamic. Beside inertia effects, the arising high strain rates lead to nearly adiabatic heating during plastic deformation and result in material softening. In contrast to that, increasing yield and ultimate tensile strengths are observed at higher strain rates. Therefore, the full characterisation of an orthotropic failure model with application in the crash simulation has to consider orthotropic effects for all strain rates. Consequently, a future work can focus on the experimental investigation of orthotropy at elevated strain rates incorporating crash relevant material behaviour.

In the present work, the plastic instability point is defined by DIC-measurements and compared to SEM-images. For further verification, additional in-situ non-destructive testing-methods, like the evolution of magnetic properties [Dob10], could be exercised. Measuring the evolution of magnetic behaviour enables the inclusion of the properties over the whole material thickness and can add further aspects besides the consideration of the surface behaviour only. Furthermore, the proposed method has to be applied on further materials, e.g. aluminium or plastics. Besides the extension on further material groups and materials, the DIC-based method could also be adopted to cyclic tests. The observed onset of plastic instability for quasi-static tests arises beyond force-maximum, whereas cyclic tests examine the maximum load cycle by decreasing force-levels. It is also observed further that load histories with high loadings for only a few load cycles reduce the number of stress cycles with decreased loading. This observation could be connected to the shift of the onset of plastic instability beyond force maximum at quasi-static tests.

In addition to the previous, the material behaviour could be investigated with representative volume elements (RVE) which represent the contrast to the executed continuums-mechanics in this work. Utilising RVEs enables the investigation of material behaviour for various stress and strain states, which cannot be depicted by specimens.

10 Appendix

10.1 Additional Experimental Results of MS1500

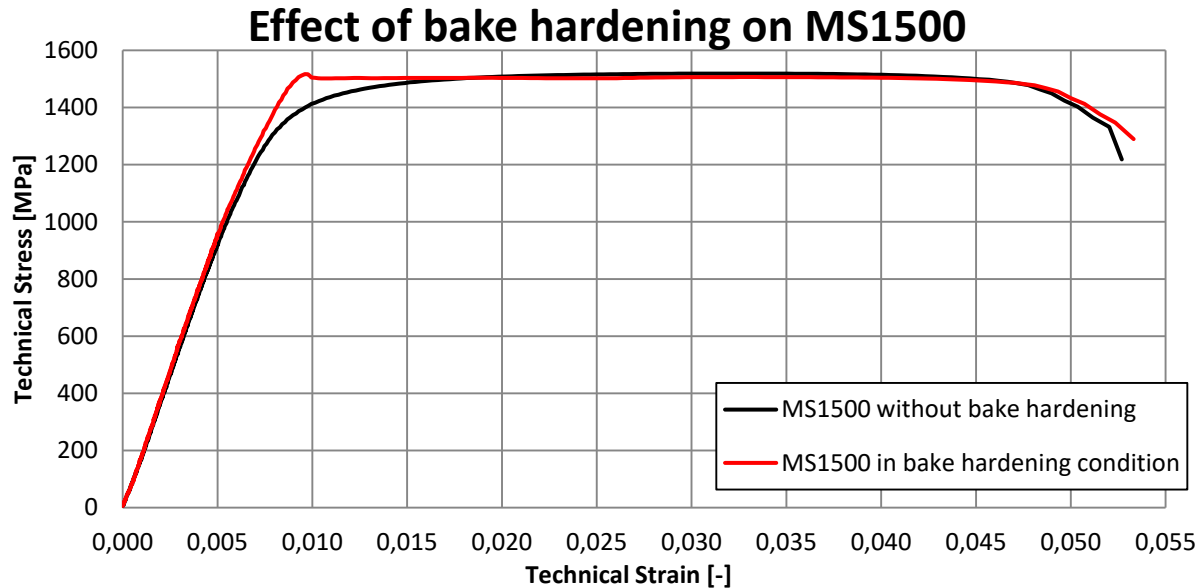


Figure 10-1: Force-Displacement curves of MS1500 with and without bake-hardening condition

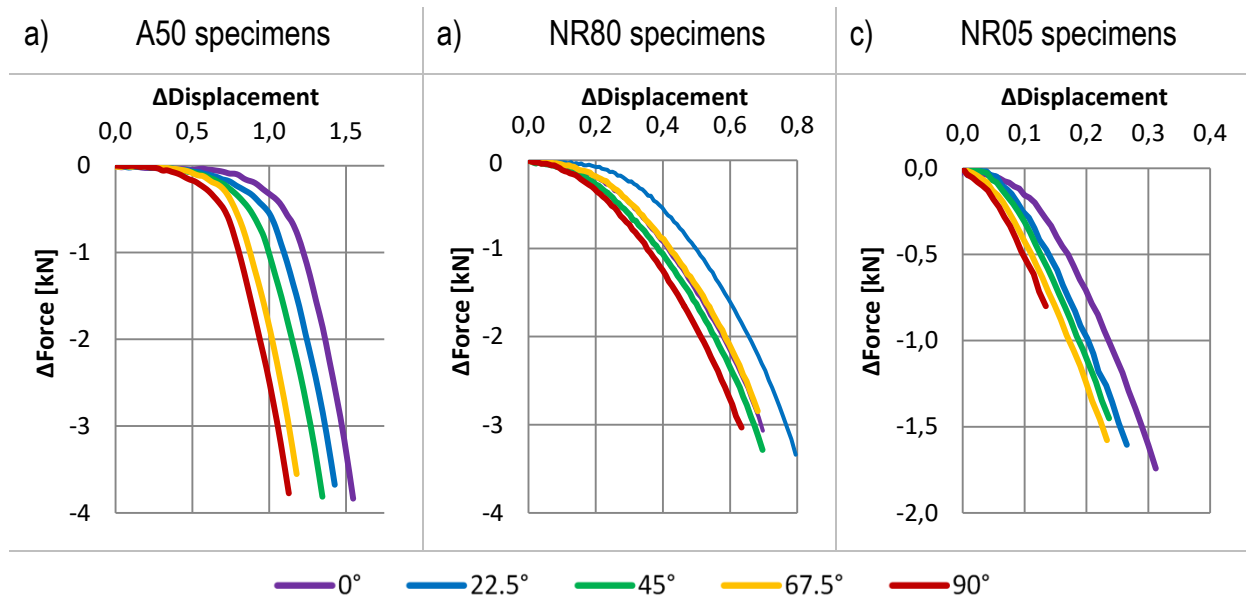


Figure 10-2: Post-UTS-behaviour obtained from MS1500 1.0 mm obtained of a) A50, b) NR80 and c) NR05 specimens, represented as force- and displacement difference related to UTS

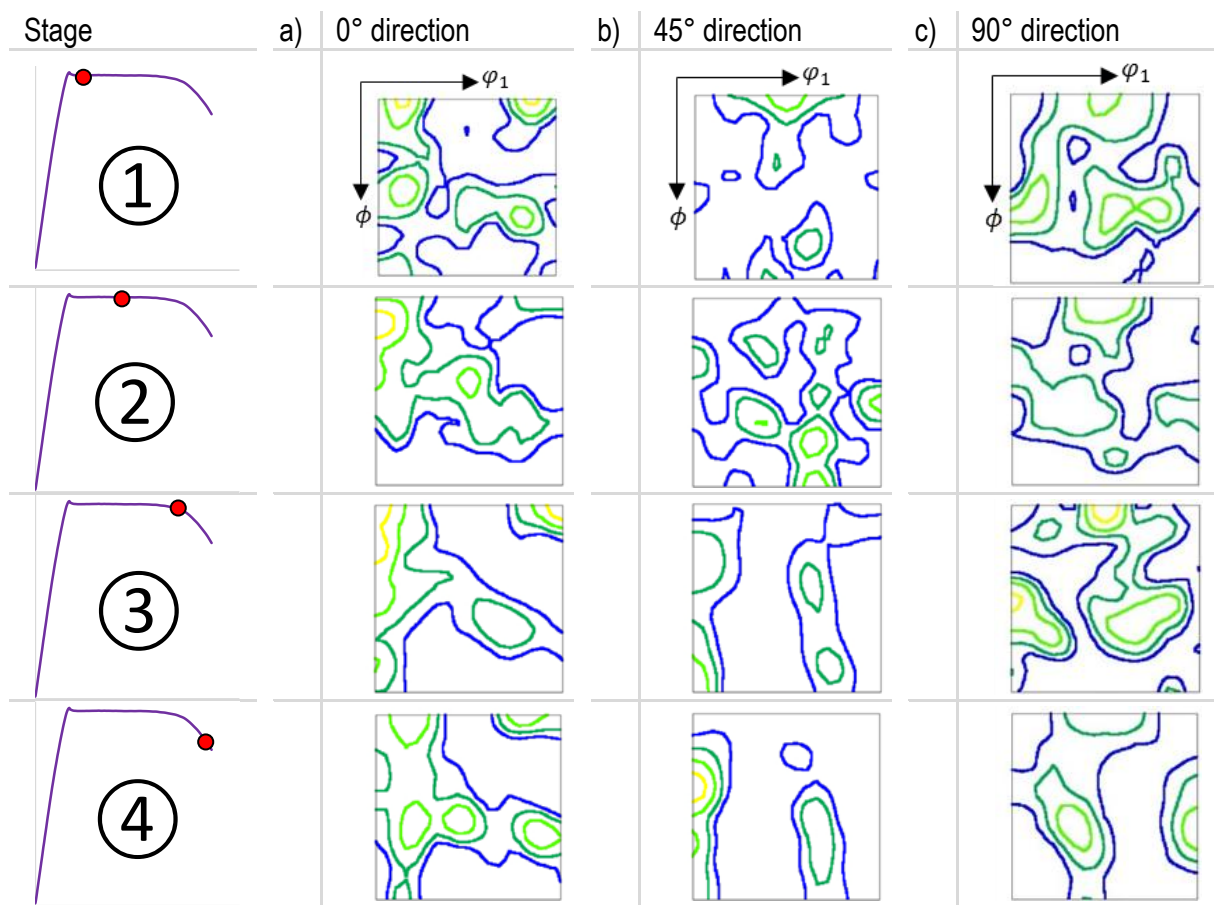


Figure 10-3: ODFs of the investigated specimens of MS1500 in 0°, 45° and 90° at four different strain stages

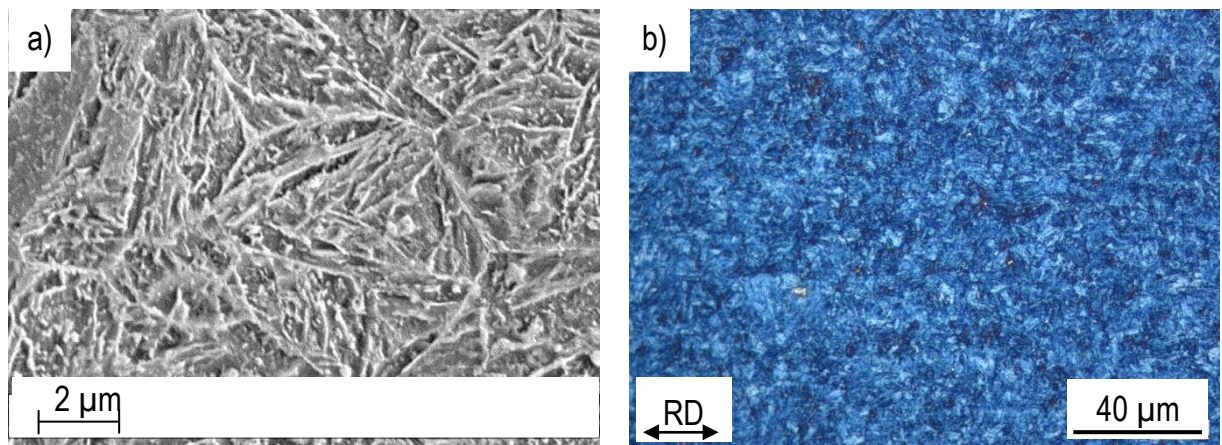


Figure 10-4: a) SEM surface measurement of MS1500, etched with Nital 2 % for 8 seconds, revealing direction independent martensite needles, b) MS1500 surface, etched with Klemm I resulting in blue martensite needles of various orientations and white cementite dispersions

10.2 Microstructural Investigations

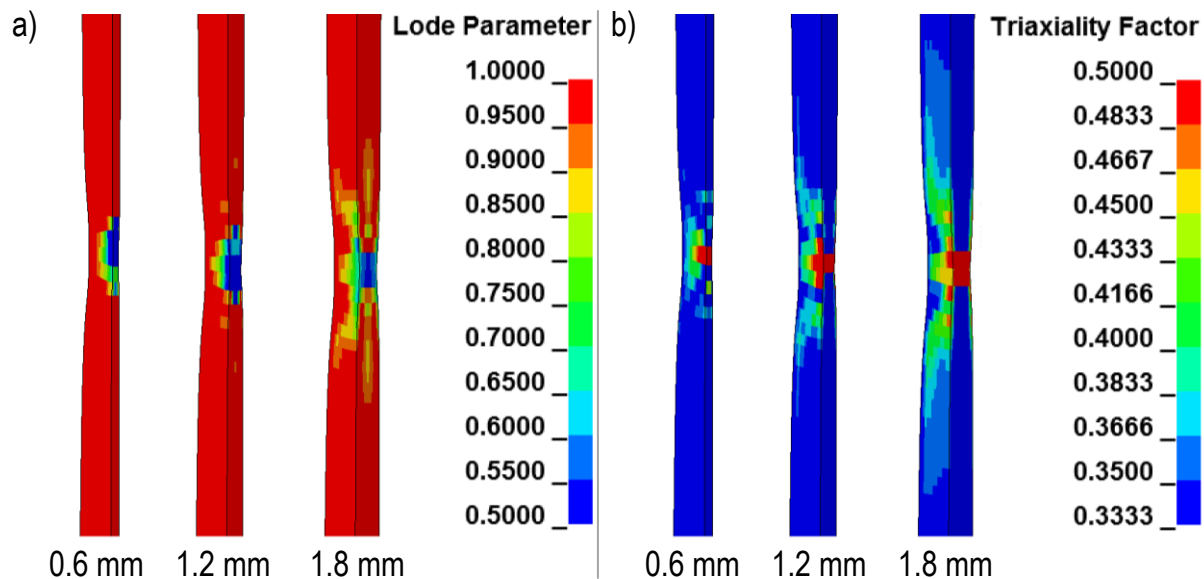


Figure 10-5: Numerical simulation ($0.5 \text{ mm} \times 0.5 \text{ mm} \times 0.075 \text{ mm}$ solid elements) results of A50 specimens in three sheet thicknesses with the same material model, presented as cut through the specimen; a) Lode Angle Parameter, b) stress triaxiality

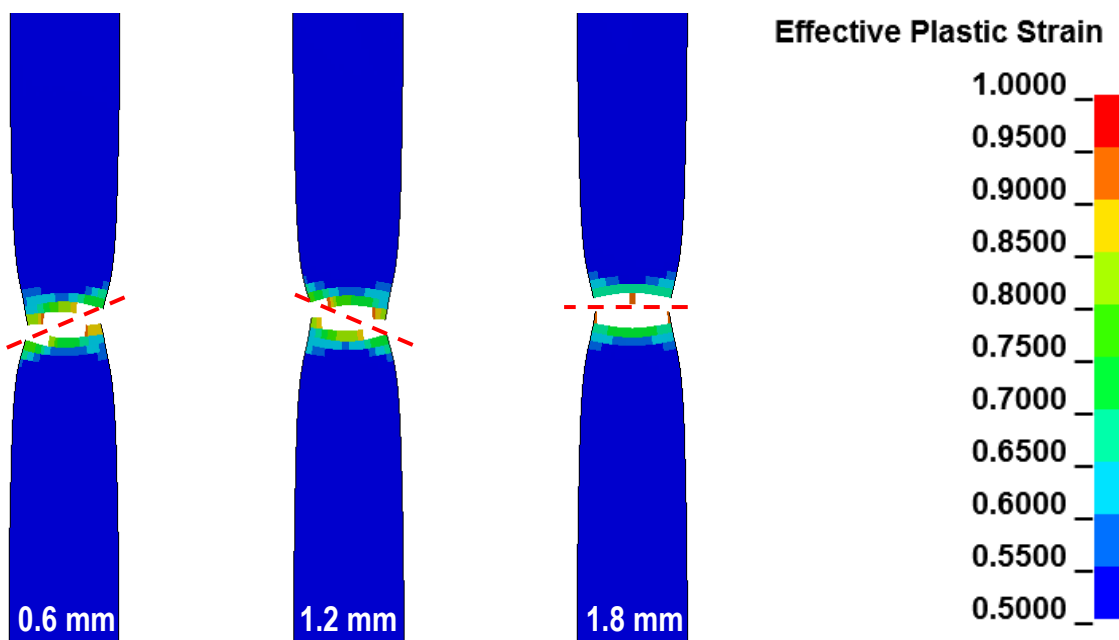


Figure 10-6: Thickness dependency of failure surface orientation (dashed line) of numerical simulations with $0.5 \text{ mm} \times 0.5 \text{ mm} \times 0.075 \text{ mm}$ solid elements

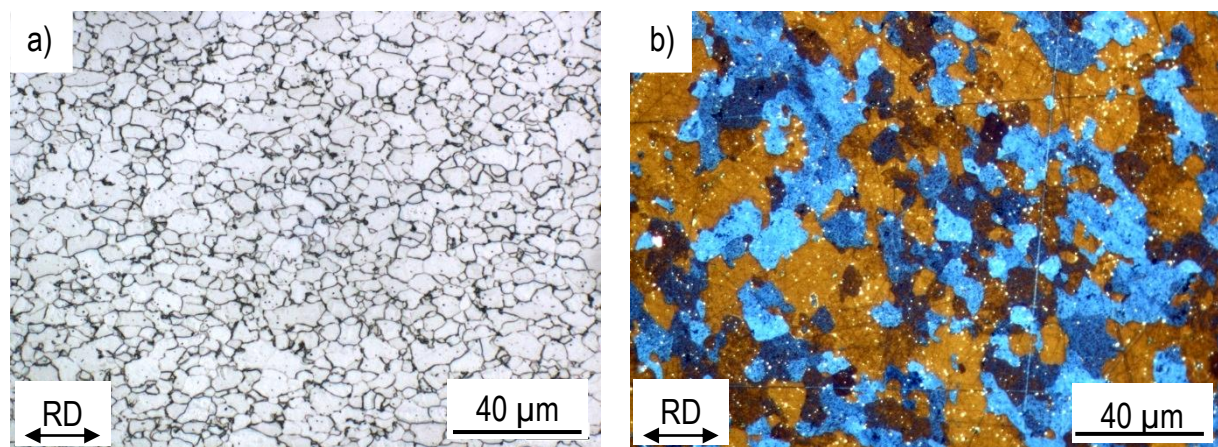


Figure 10-7: a) Microstructure of CR340LA (1.1 mm) with ferrite matrix and cementite dispersions; b) CR340LA microstructure, etched with Klemm I leading to blue and brown coloured ferrite grains (depending on their orientation) and cementite dispersions in white

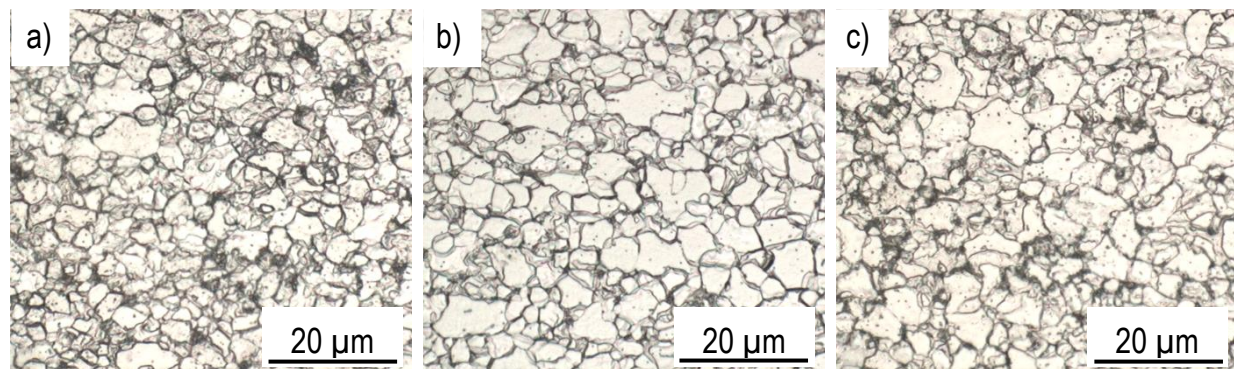


Figure 10-8: Microstructure of CR340LA in the sheet thicknesses of a) 0.6 mm, b) 1.1 mm and c) 1.8 mm

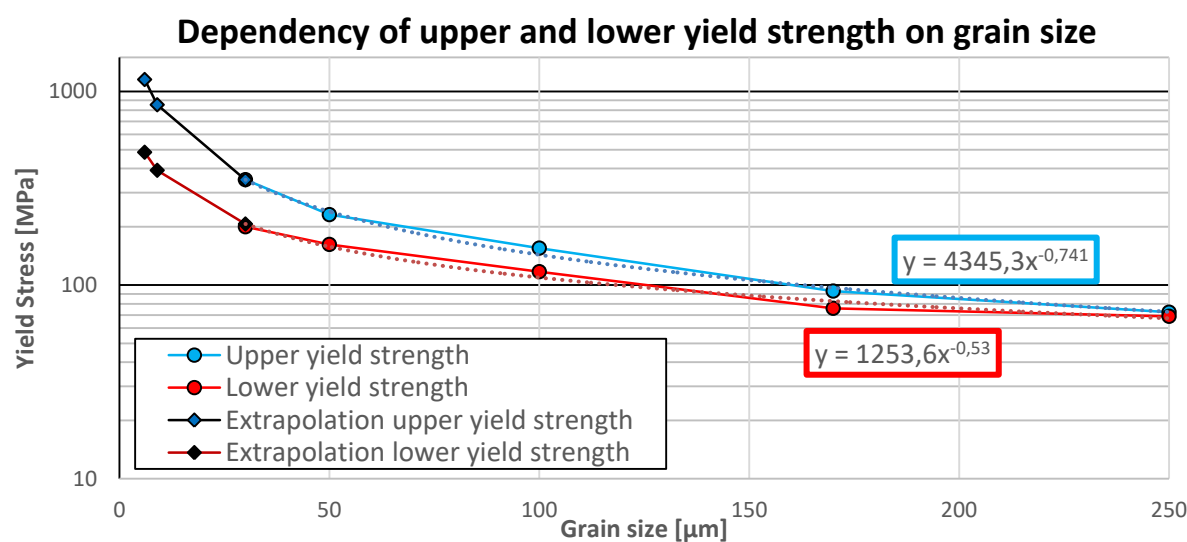


Figure 10-9: Experimental results of upper and lower yield strength, depending on the grain size, obtained from [Fuj78] with additional exponential extrapolation functional to estimate both yield strengths for grain sizes of 6 μm and 9 μm

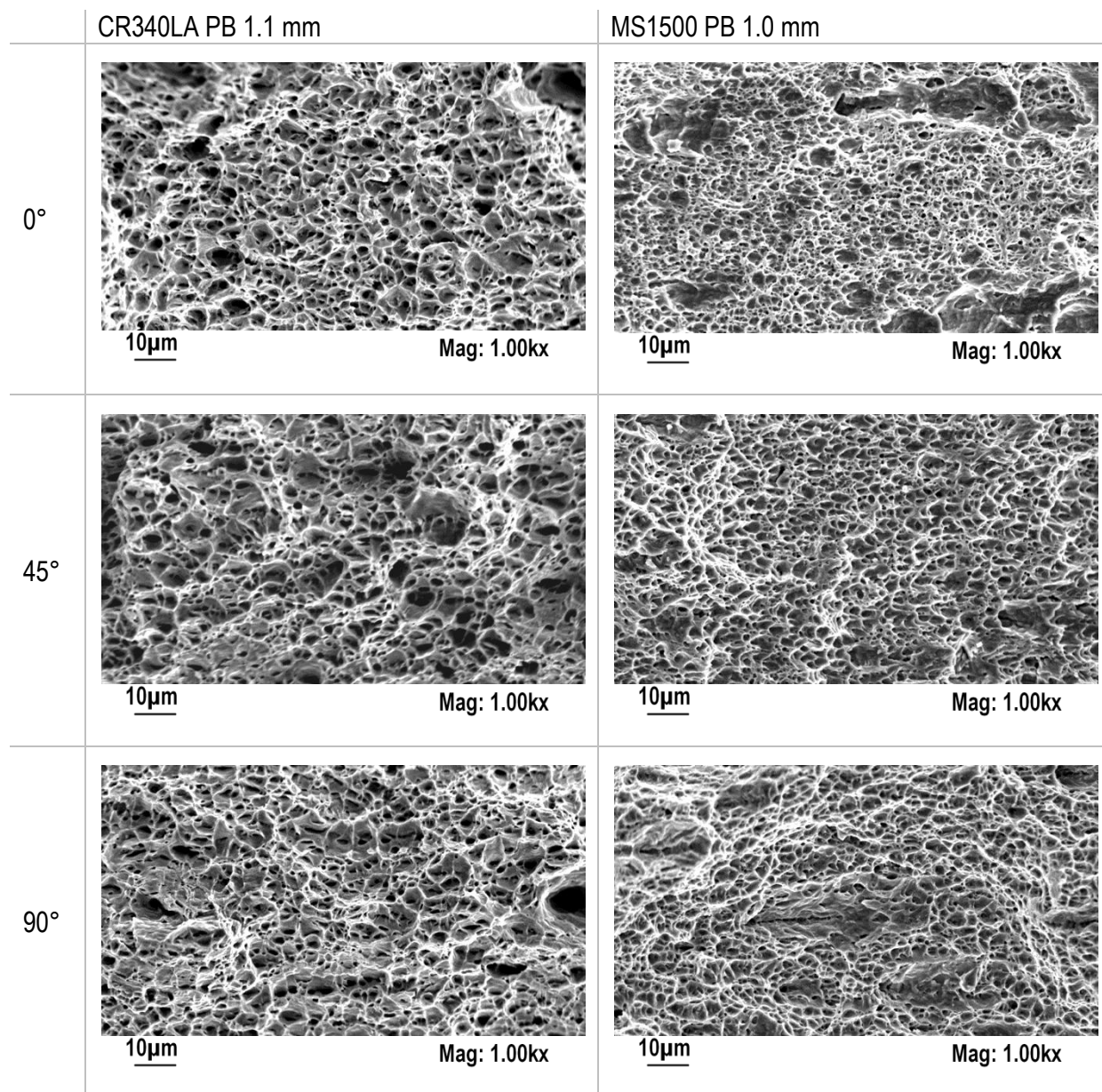


Figure 10-10: SEM-images at the centre of the fracture surfaces of CR340LA 1.1 mm PB and MS1500 PB 1.0 mm in 0°, 45° and 90° to RD at a magnification of 1000

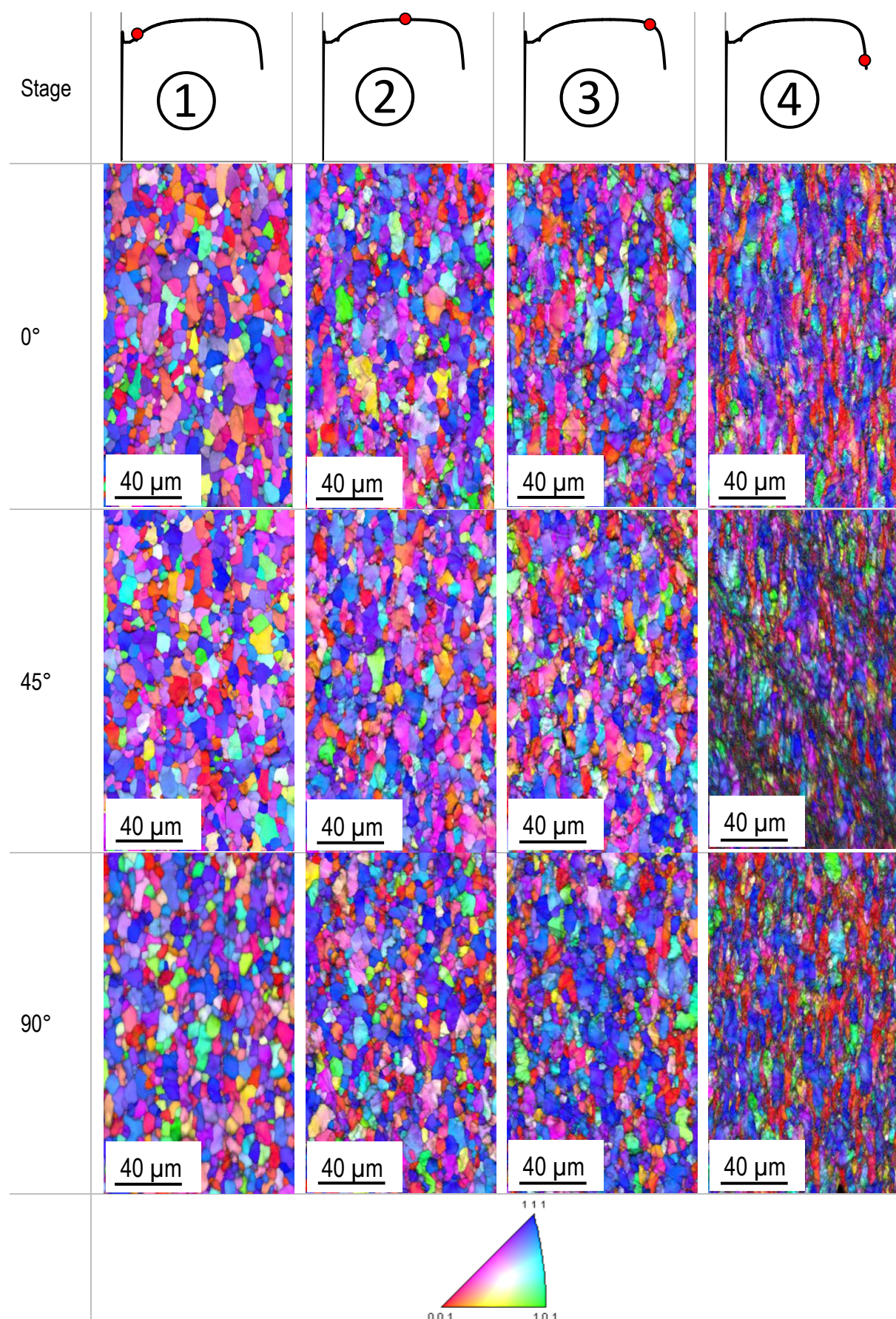


Figure 10-11: Orientation dependent coloured microstructure, obtained from EBSD-measurements of standard tensile specimens in 0°, 45° and 90°

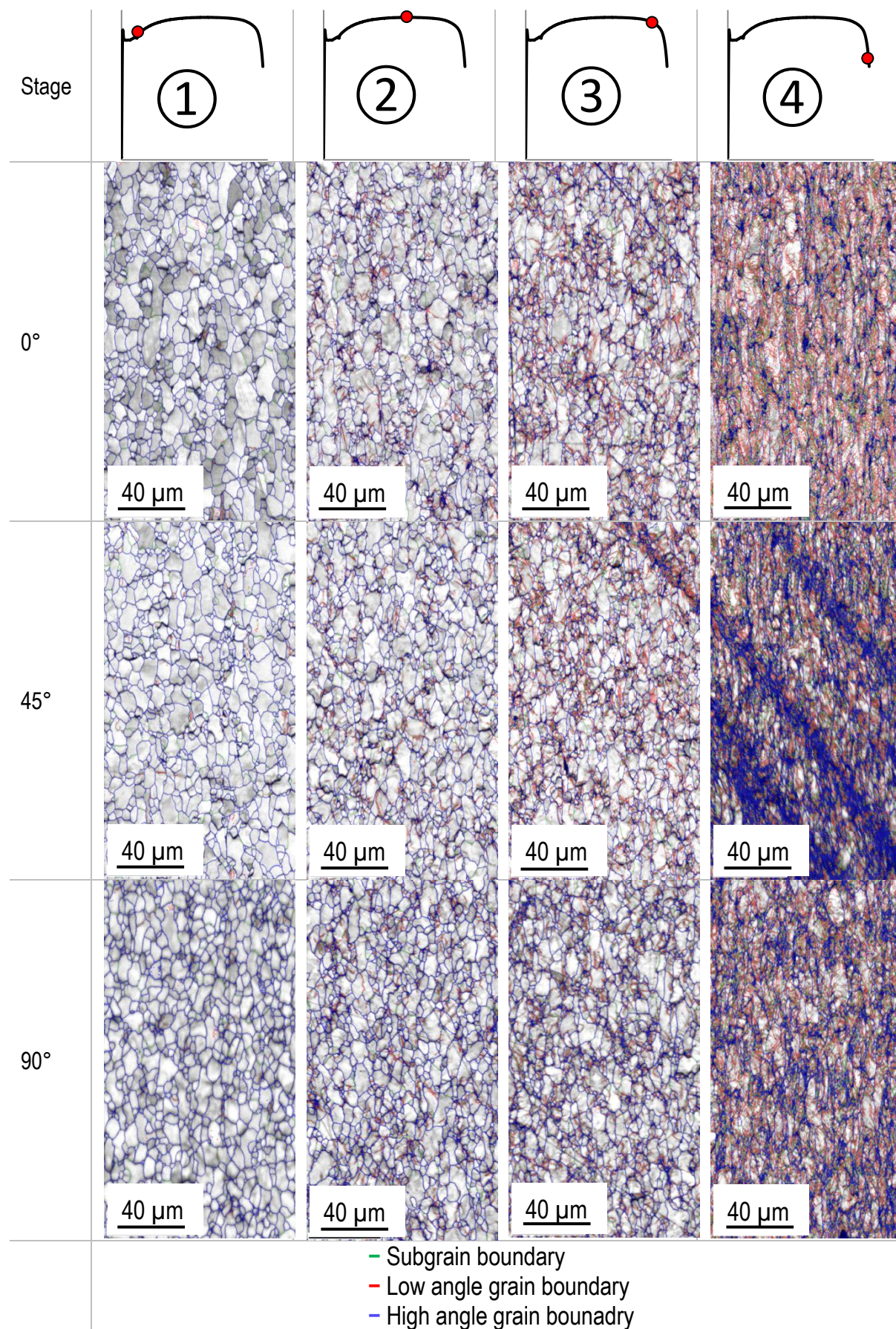


Figure 10-12: Grain boundary evolution, obtained at different strain stages for A50 specimens in 0°, 45° and 90°

10.3 Additional Measurements to Determine the Plastic Instability Point

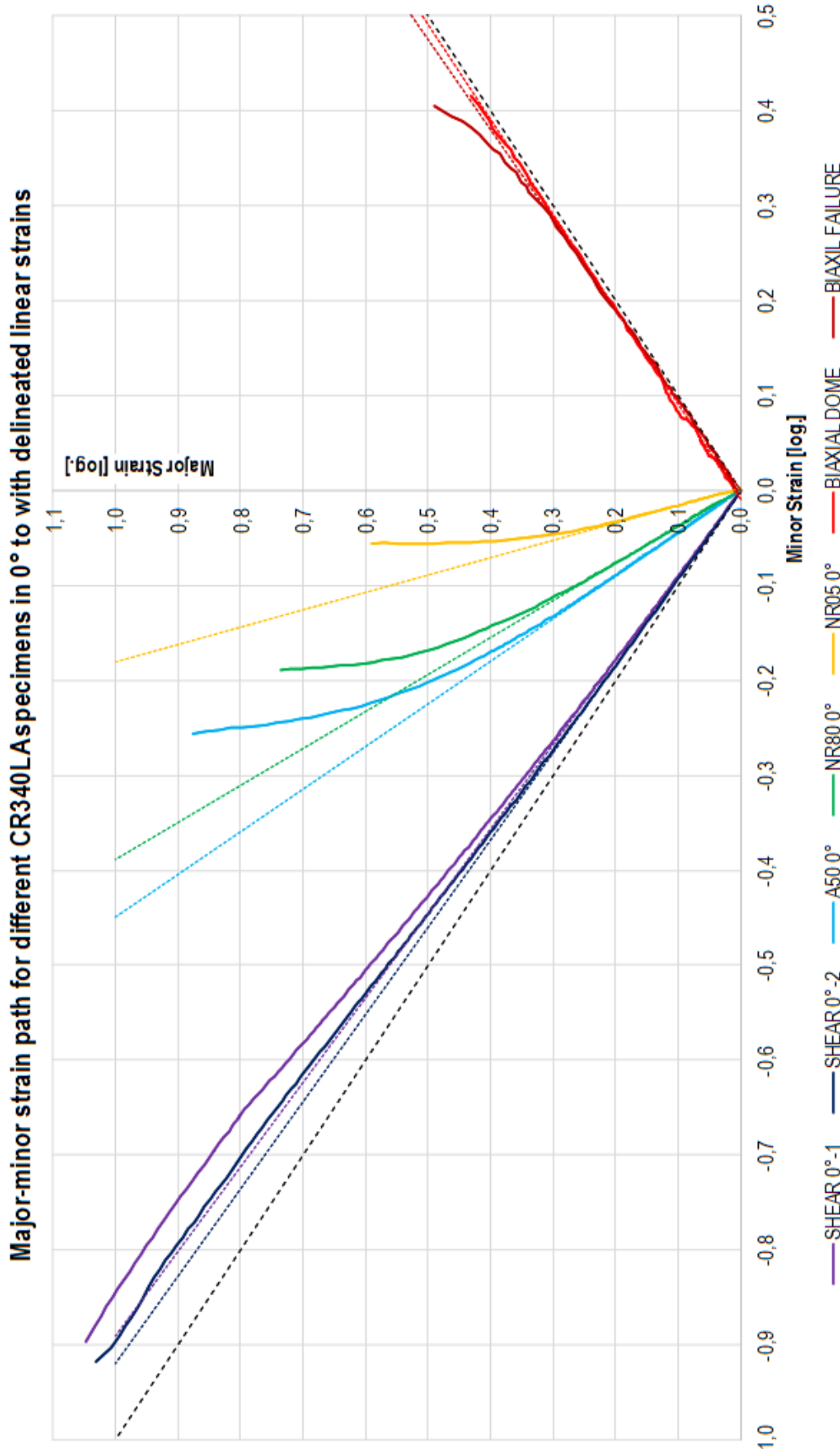


Figure 10-13: Major vs. Minor strains of all investigated specimens (VOEST-shear, A50, NR80, NR05 and Bulge)

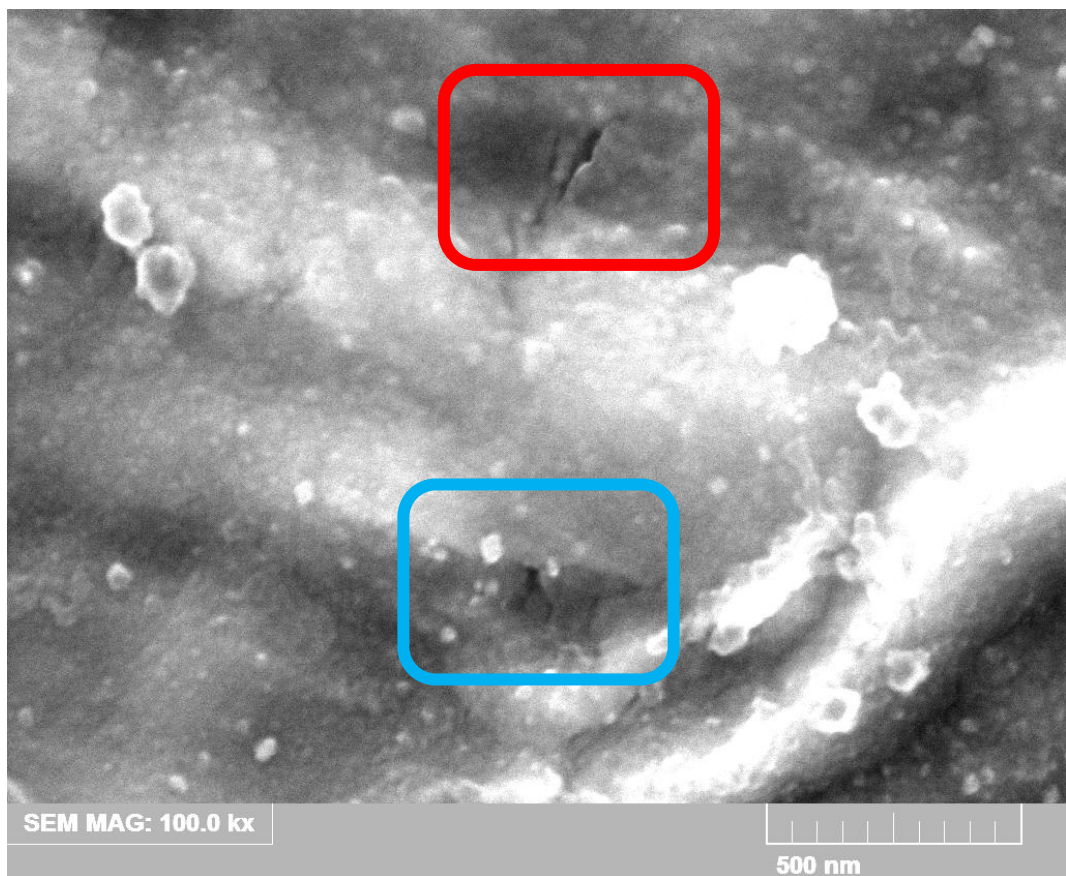


Figure 10-14: SEM-picture at local equivalent true strains of 0.17, picturing first micro-cracks within the grains

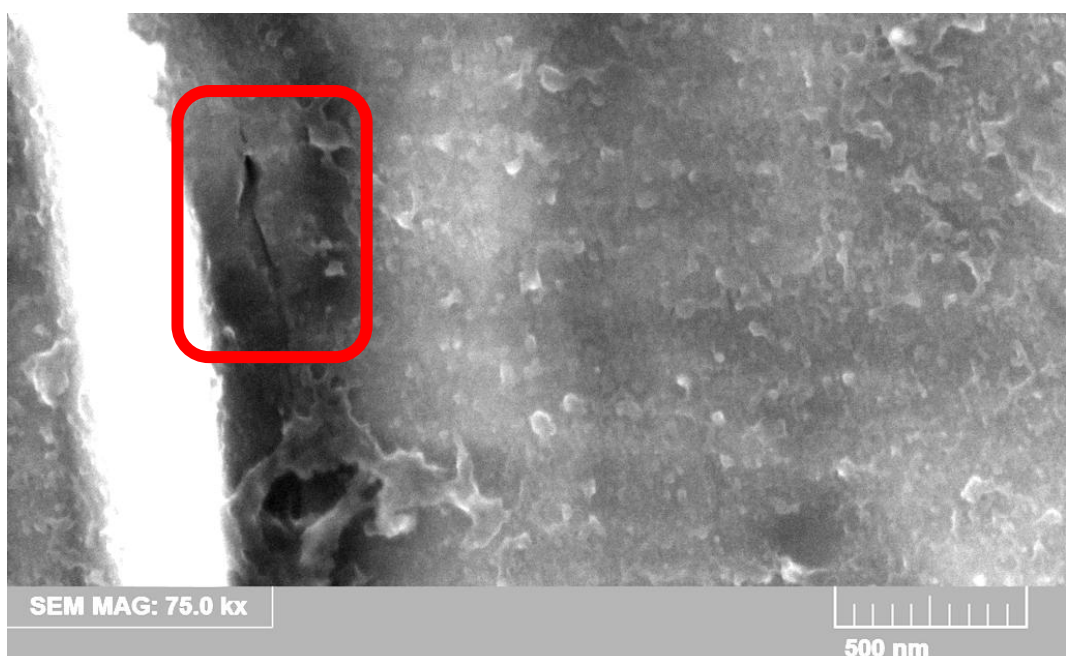


Figure 10-15: SEM-picture at local equivalent true strains of 0.21, micro-cracks near pearlite at a grain boundary (white)

Determined Instability Points of CR340LA

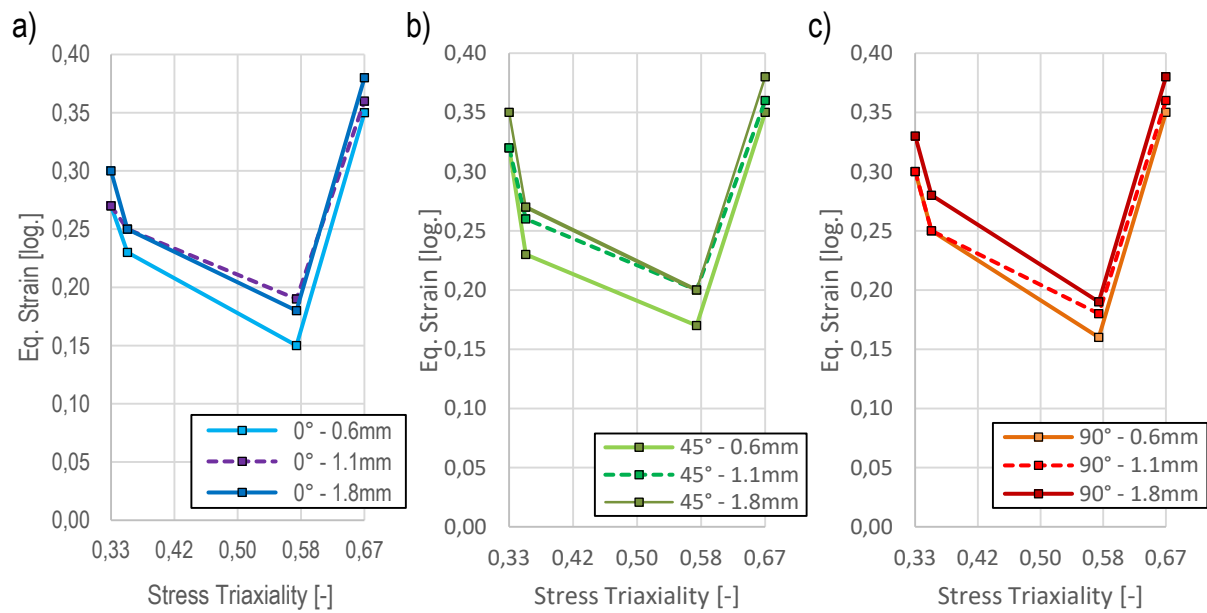


Figure 10-16: Opposition of the determined plastic instability strains for the three thicknesses of CR340LA



Figure 10-17: Force-displacement behaviour of standard tensile specimens of CR340LA (1.1 mm), aligned in 0°, 45° and 90° to RD with marked force-maxima (coloured diamonds) and marked determined instability points (coloured dots)

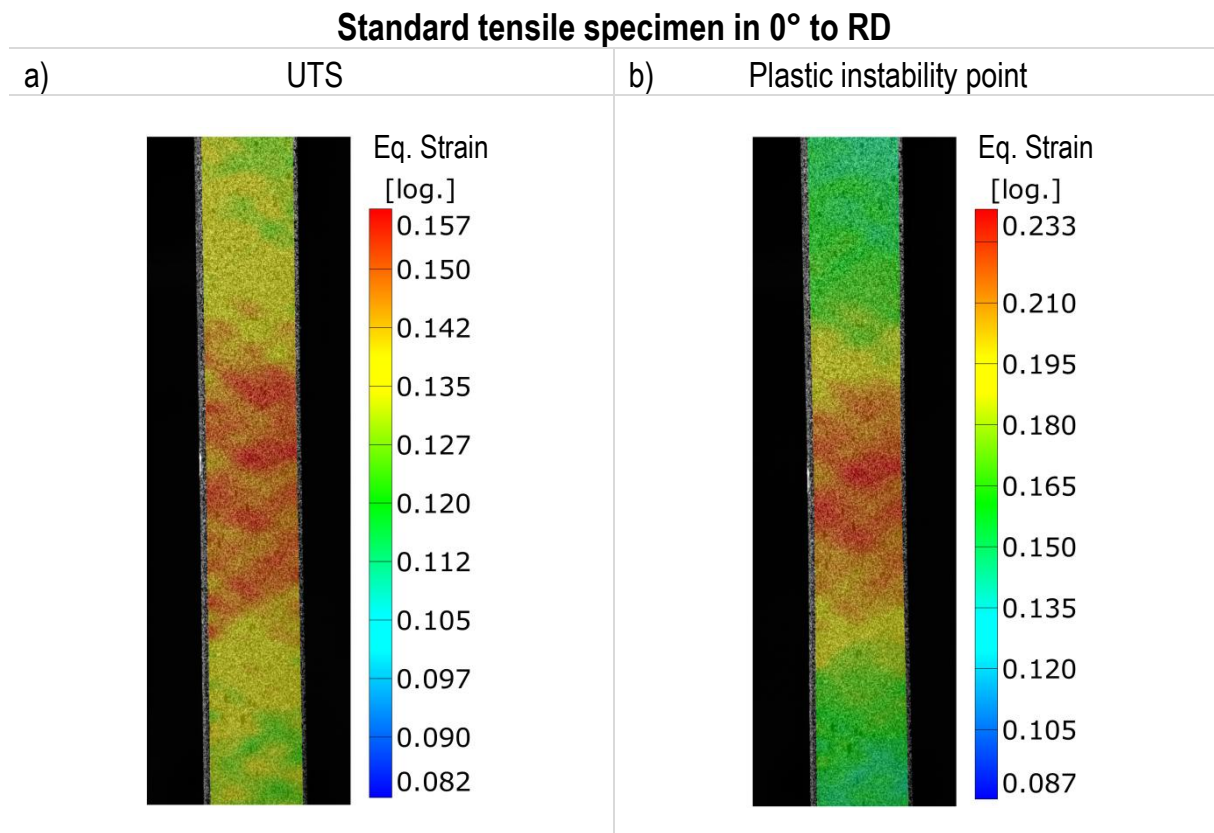


Figure 10-18: Local strain fields of CR340LA (1.1 mm) obtained from standard tensile specimen aligned in 0° to RD at a): UTS and b) determined plastic instability point

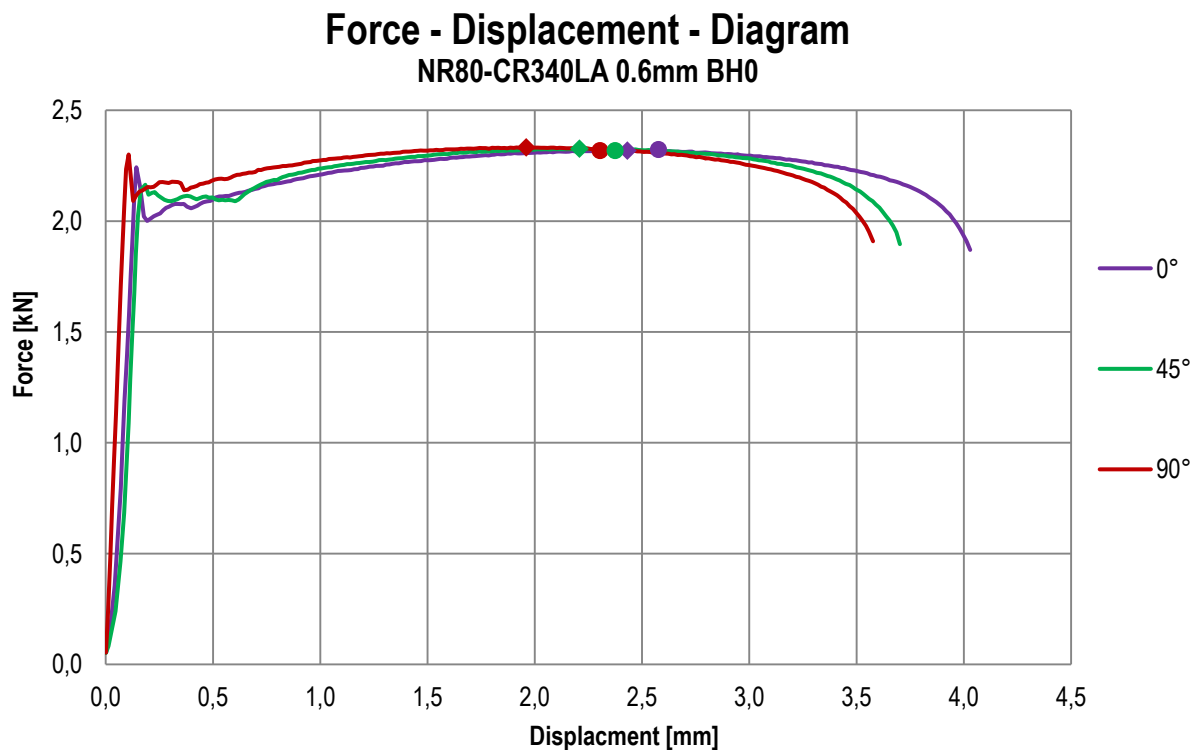


Figure 10-19 Force-displacement behaviour of NR80 specimens of CR340LA (1.1 mm), aligned in 0°, 45° and 90° to RD with marked force-maxima (coloured diamonds) and marked determined instability points (coloured dots)

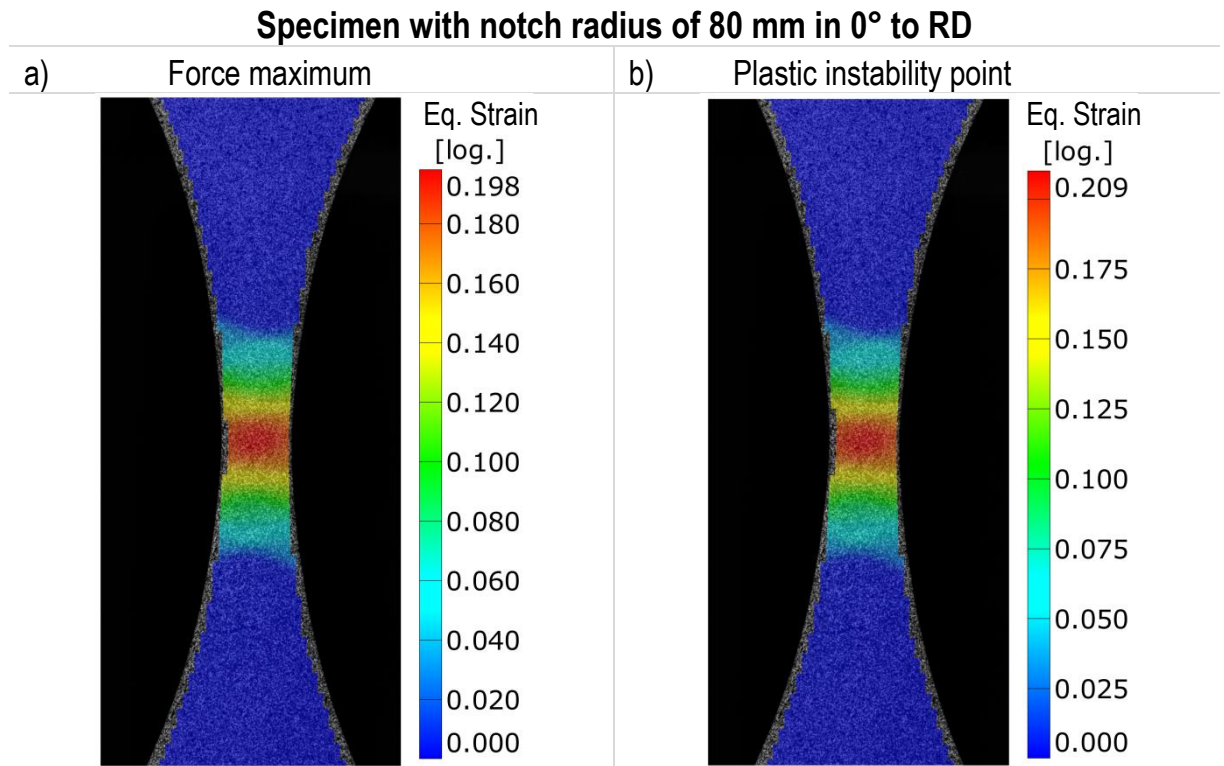


Figure 10-20: Local strain fields of CR340LA (1.1 mm) obtained from a NR80 specimen aligned in 0° to RD at a) UTS and b) determined plastic instability point

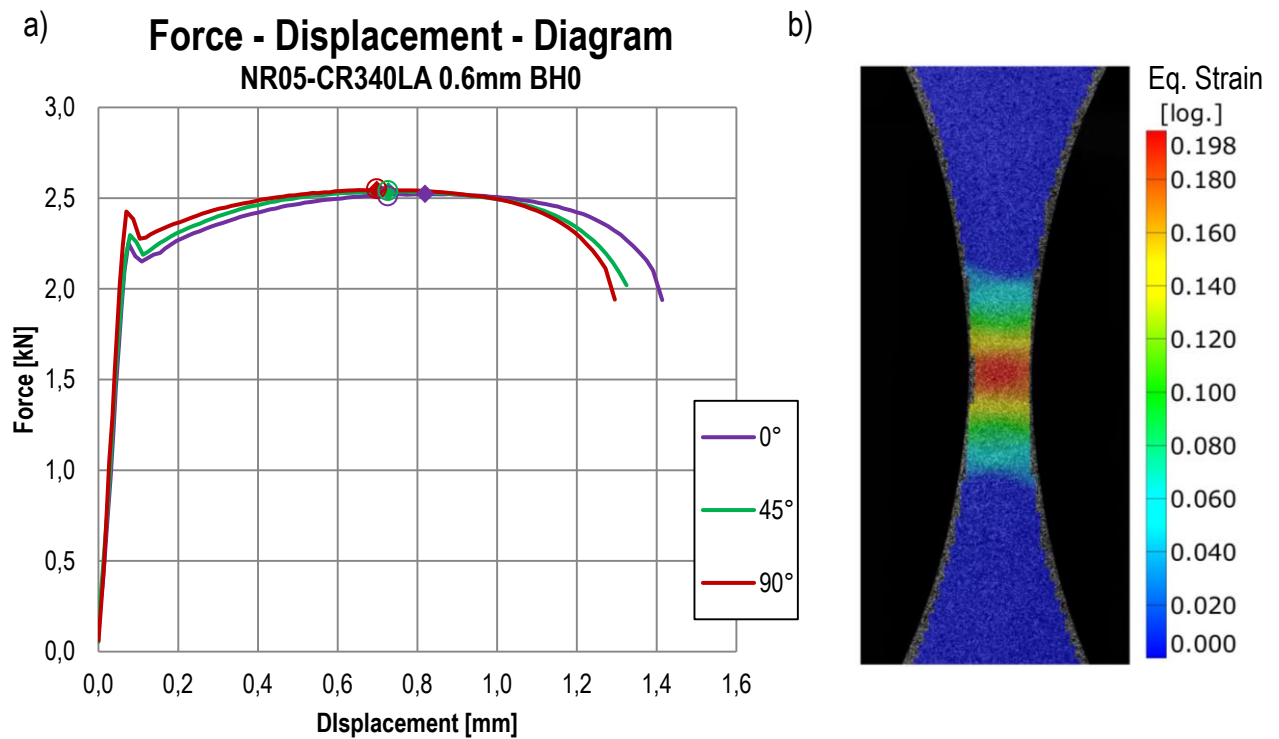


Figure 10-21: a) Force-displacement behaviour of NR05 specimens of CR340LA (0.6 mm), aligned in 0°, 45° and 90° to RD with coinciding marked force-maxima (coloured diamonds) and marked determined instability points (coloured dots), b) local strain field of NR05 specimen in 0° to RD at force maximum

Force - Displacement - Diagram

A50-CR340LA 1.1mm BH0

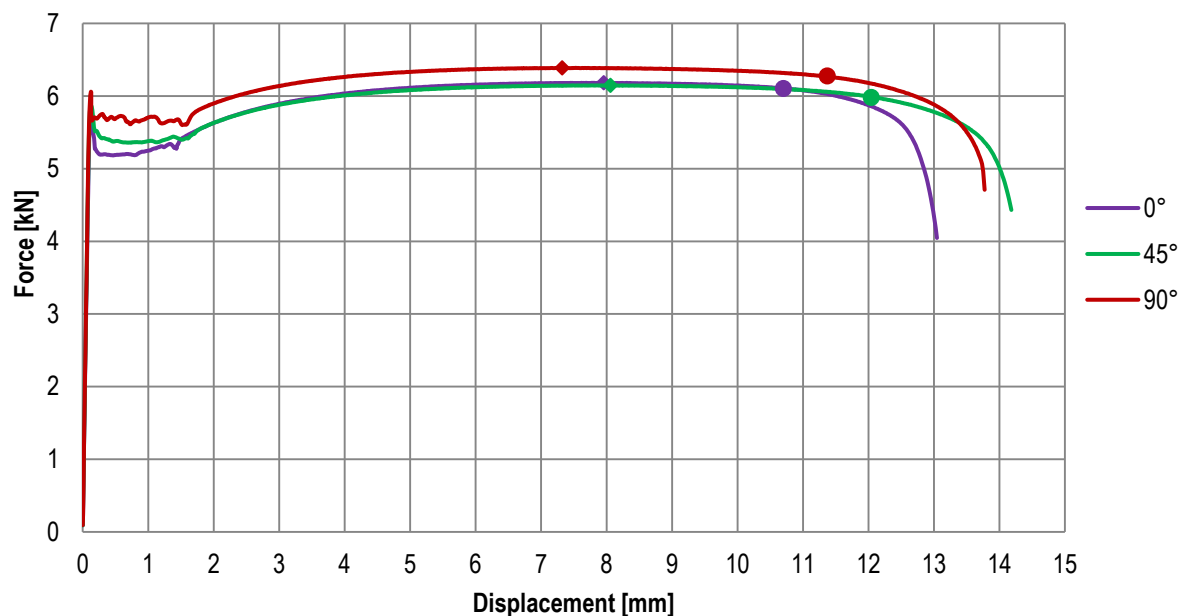


Figure 10-22: Force-displacement behaviour of standard tensile specimens of CR340LA, aligned in 0° , 45° and 90° to RD with marked force-maxima (coloured diamonds) and marked determined instability points (coloured dots)

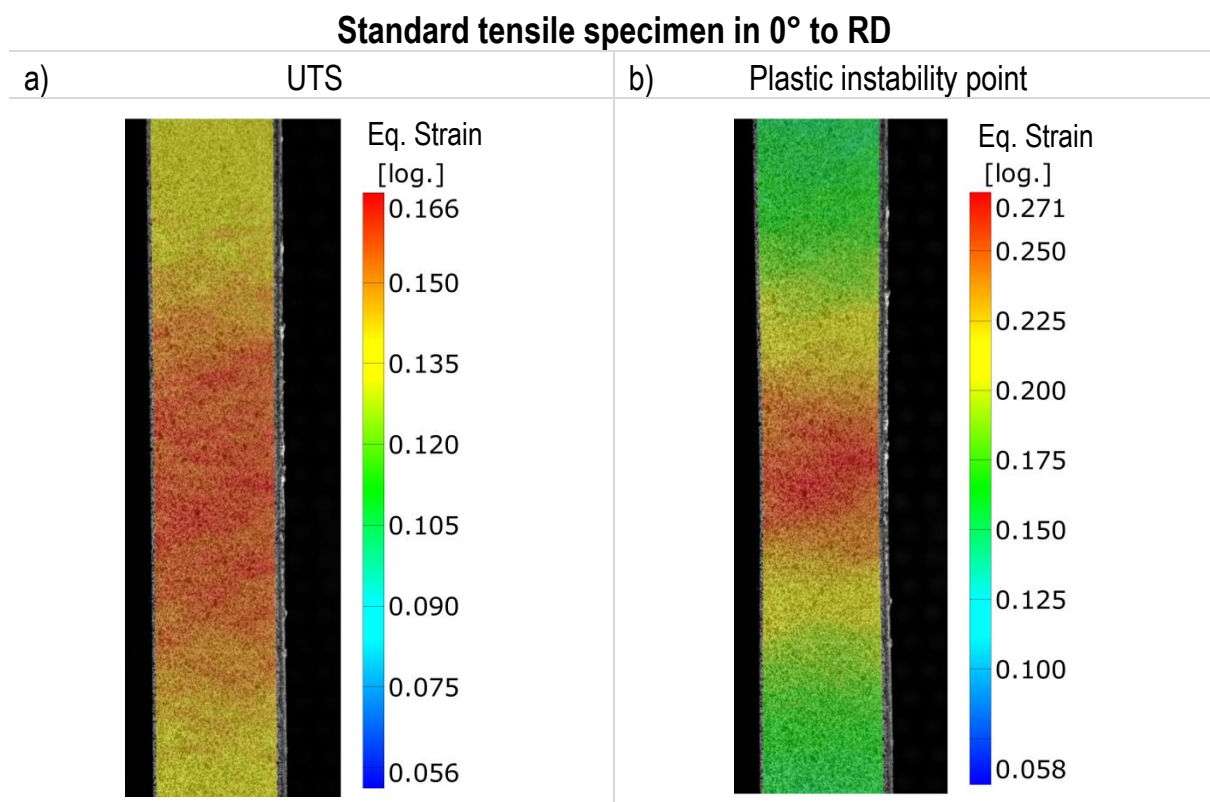


Figure 10-23: Local strain fields of CR340LA obtained from standard tensile specimen aligned in 0° to RD at a): UTS and b) determined plastic instability point

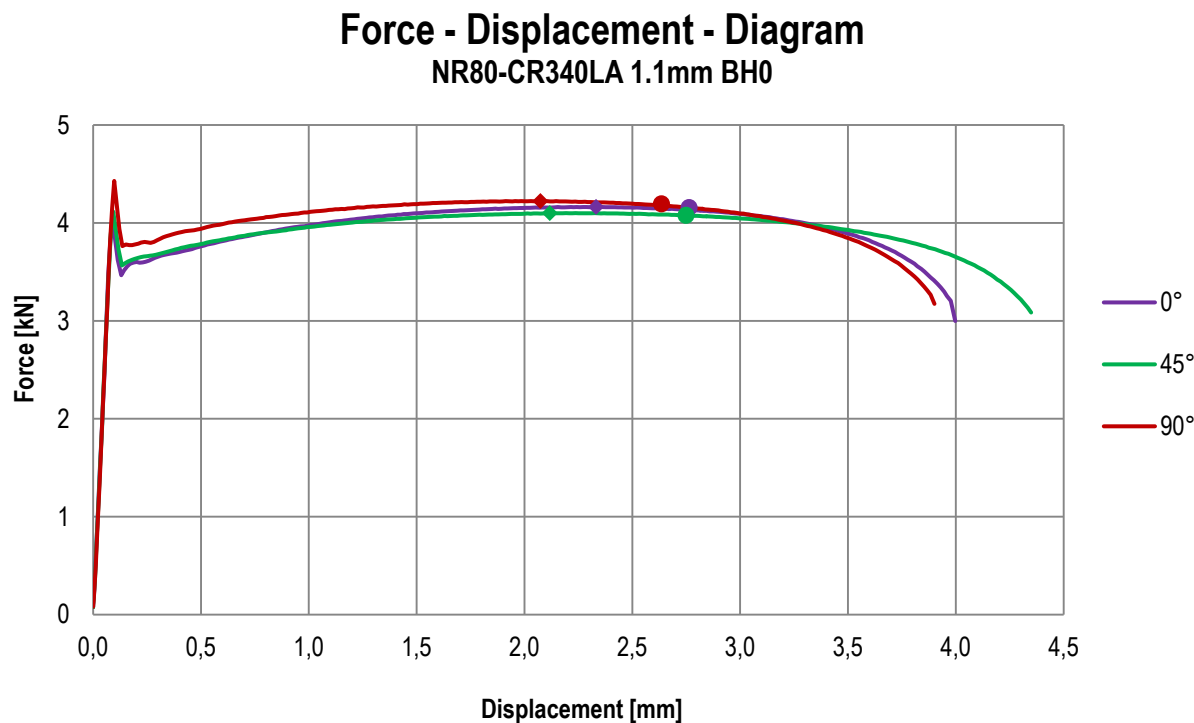


Figure 10-24 Force-displacement behaviour of NR80 specimens of CR340LA, aligned in 0° , 45° and 90° to RD with marked force-maxima (coloured diamonds) and marked determined instability points (coloured dots)

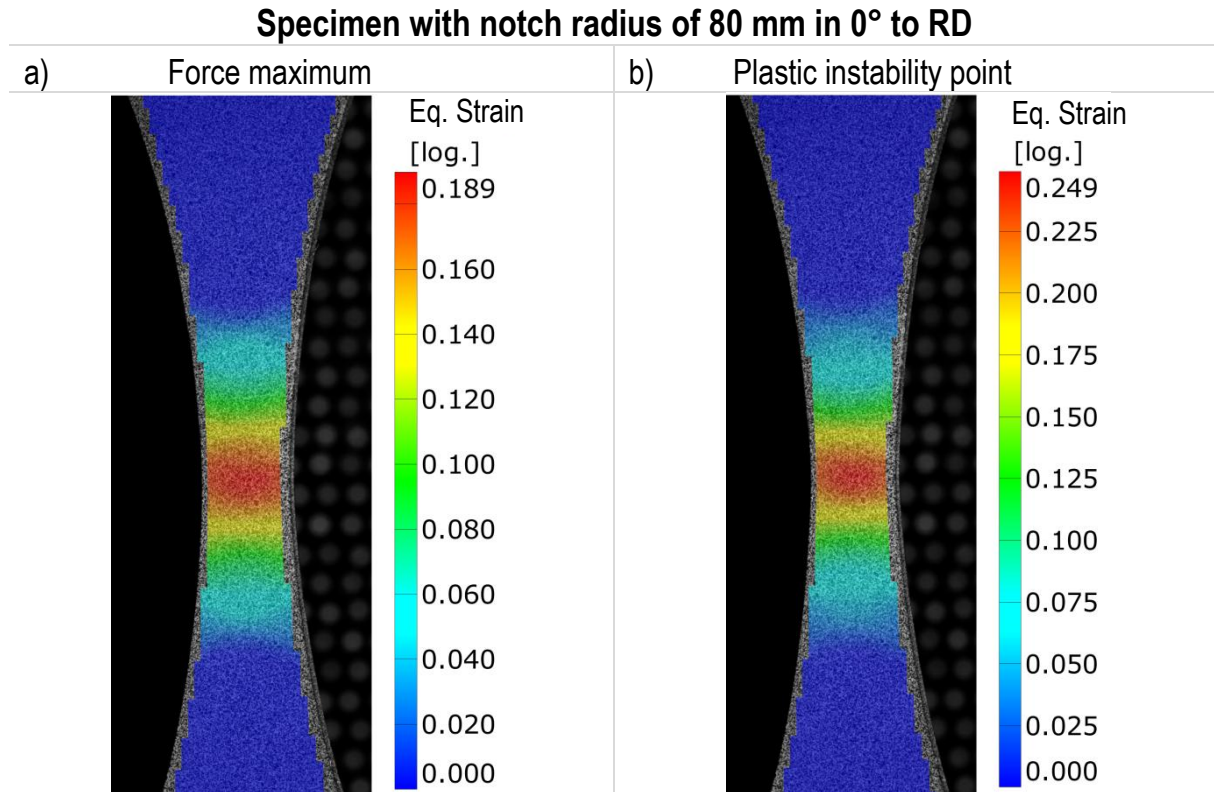


Figure 10-25: Local strain fields of CR340LA obtained from a NR80 specimen aligned in 0° to RD at a): UTS and b) determined plastic instability point

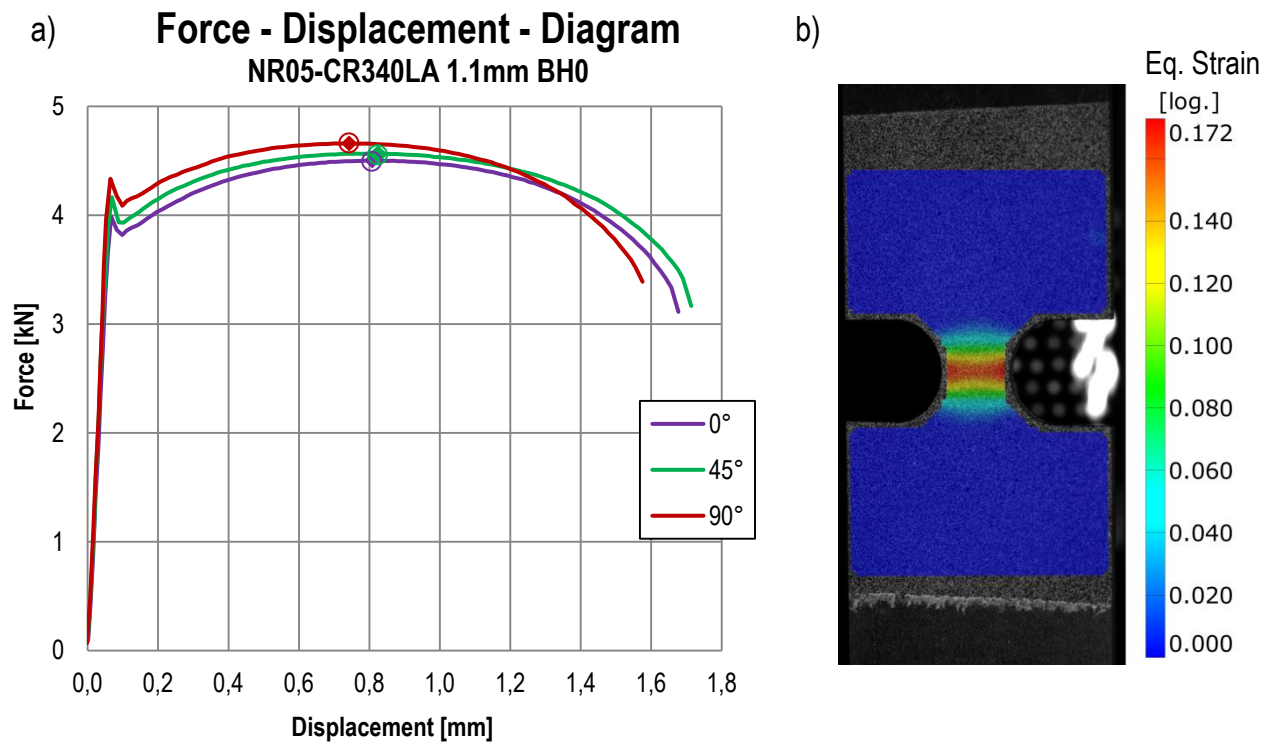


Figure 10-26: a) Force-displacement behaviour of NR05 specimens of CR340LA, aligned in 0°, 45° and 90° to RD with coinciding marked force-maxima (coloured diamonds) and marked determined instability points (coloured dots), b) local strain field of NR05 specimen in 0° to RD at force maximum

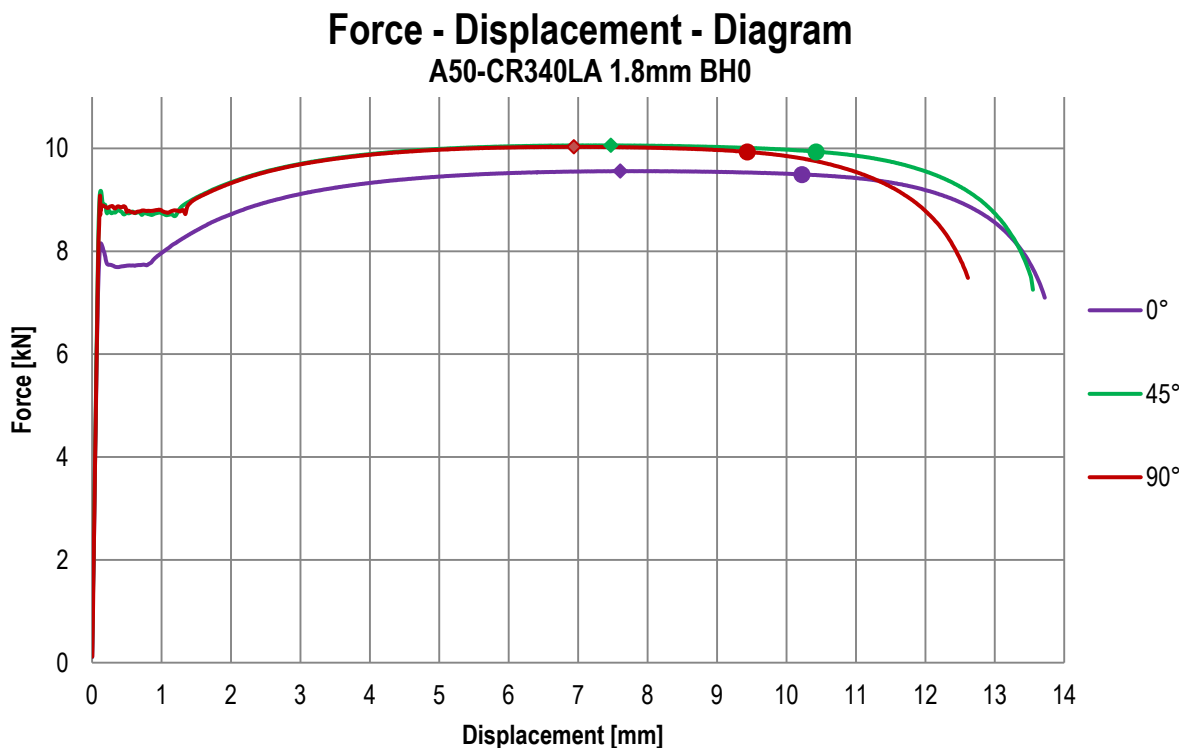


Figure 10-27: Force-displacement behaviour of standard tensile specimens of CR340LA, aligned in 0°, 45° and 90° to RD with marked force-maxima (coloured diamonds) and marked determined instability points (coloured dots)

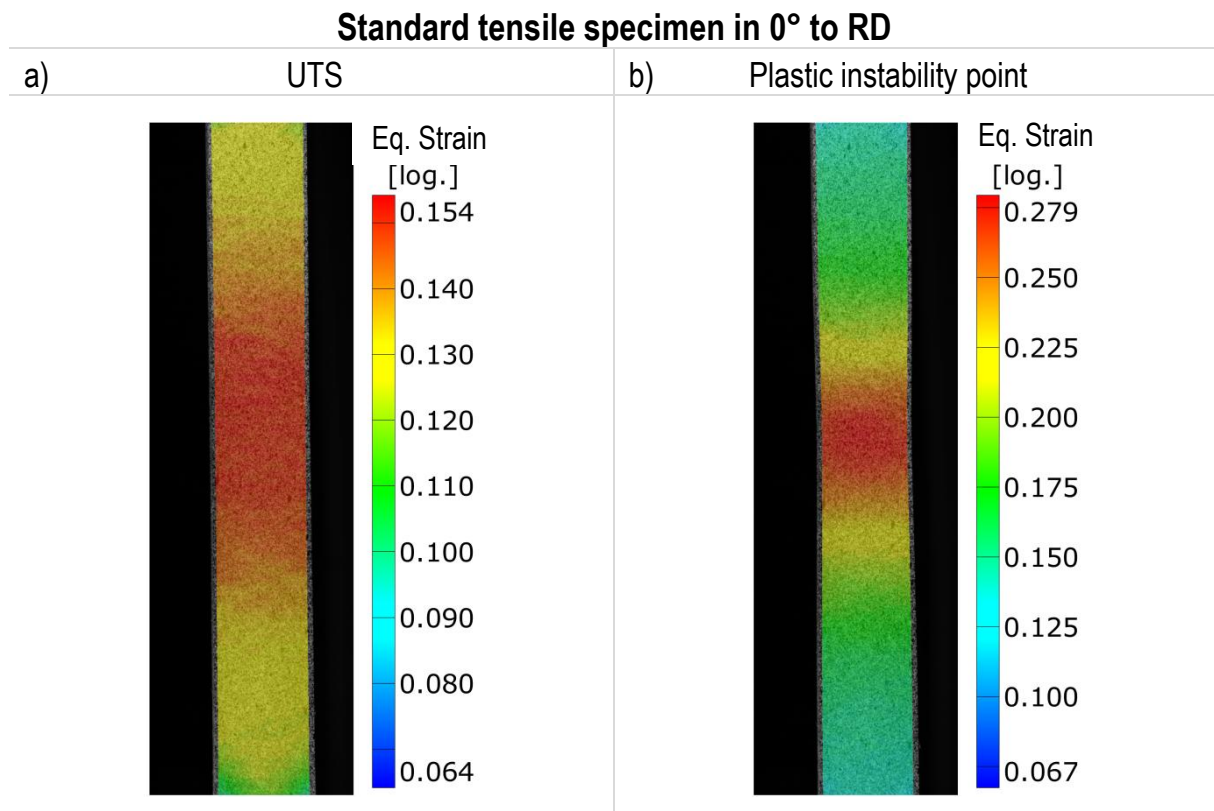


Figure 10-28: Local strain fields of CR340LA obtained from standard tensile specimen aligned in 0° to RD at a): UTS and b) determined plastic instability point

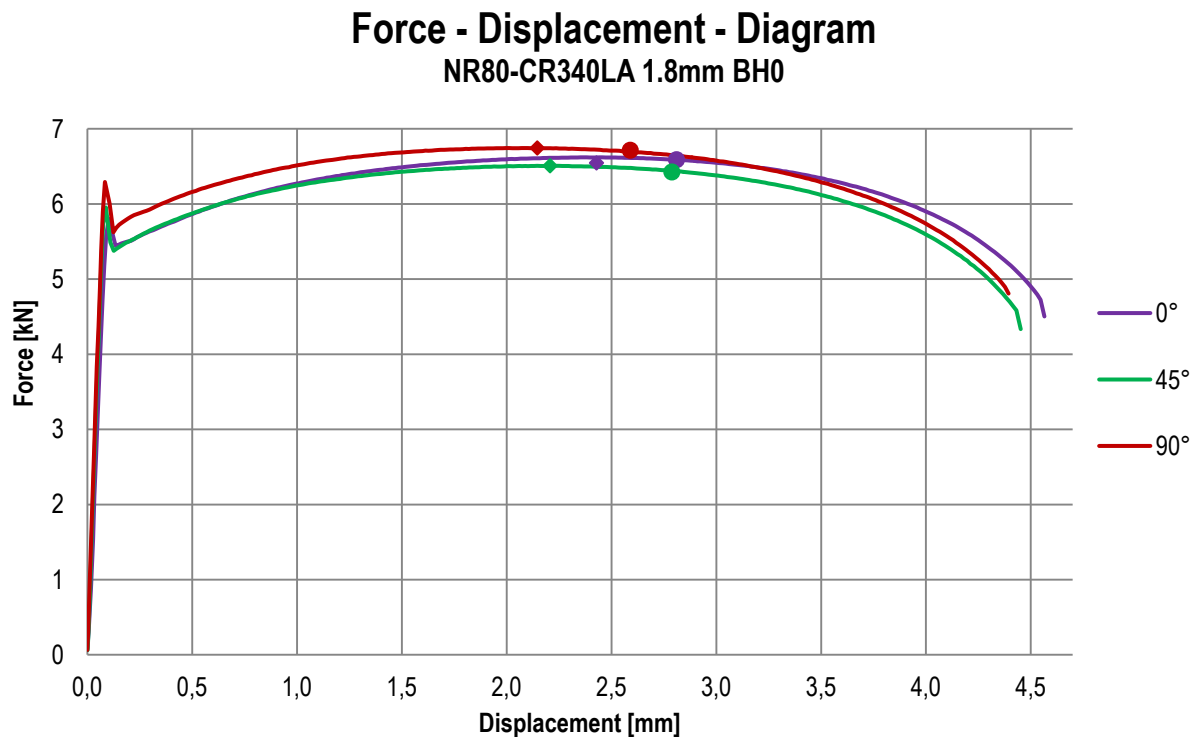


Figure 10-29: Force-displacement behaviour of NR80 specimens of CR340LA, aligned in 0°, 45° and 90° to RD with marked force-maxima (coloured diamonds) and marked determined instability points (coloured dots)

Specimen with notch radius of 80 mm in 0° to RD

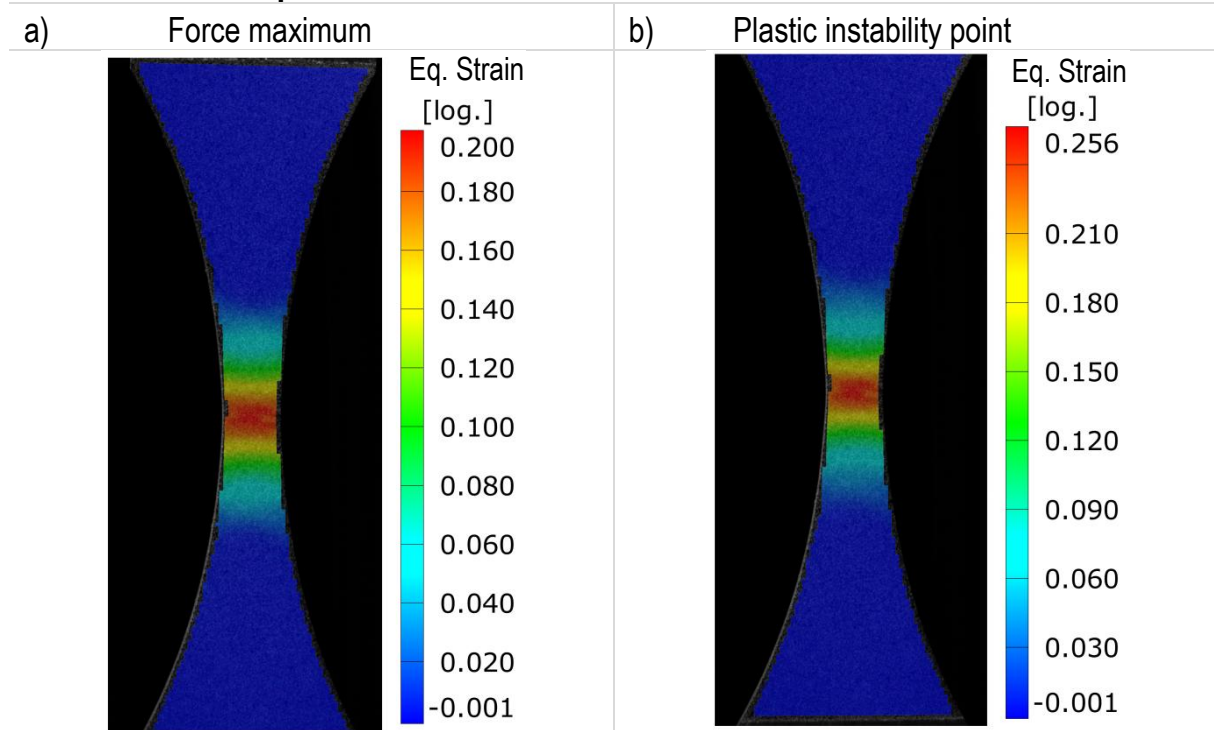


Figure 10-30: Local strain fields of CR340LA obtained from a NR80 specimen aligned in 0° to RD at a): UTS and b) determined plastic instability point

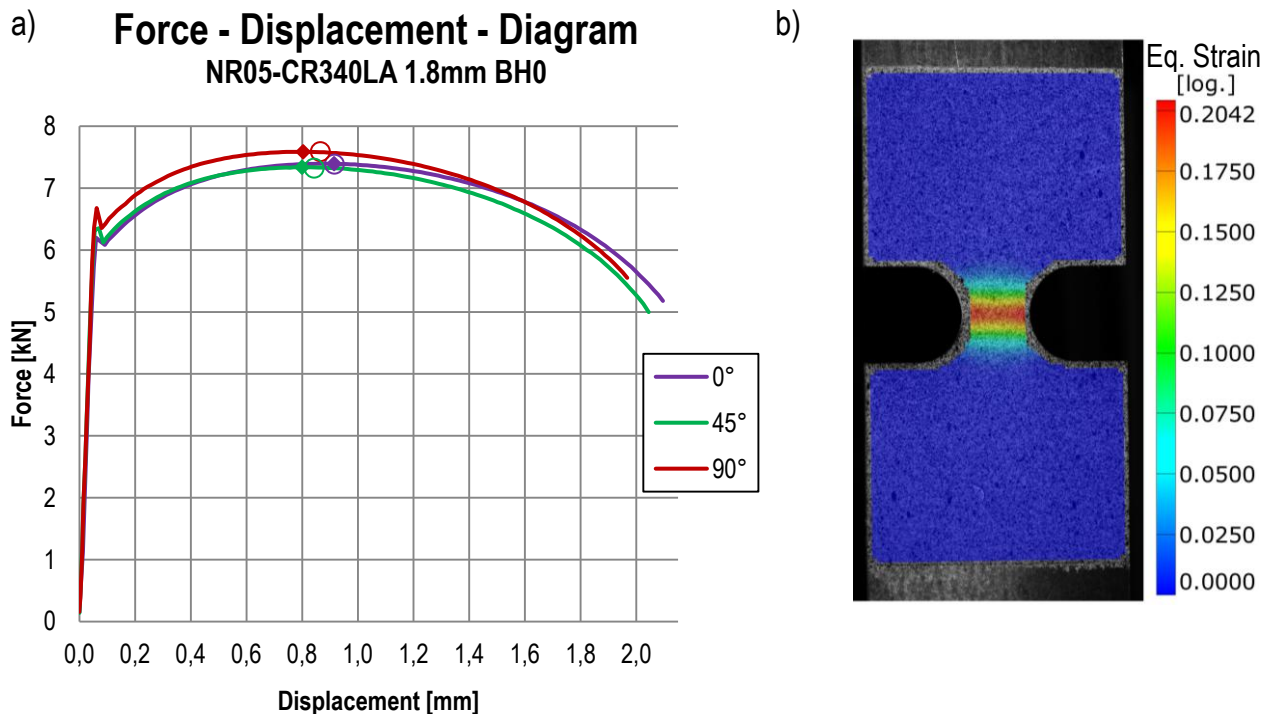


Figure 10-31: a) Force-displacement behaviour of NR05 specimens of CR340LA, aligned in 0°, 45° and 90° to RD with coinciding marked force-maxima (coloured diamonds) and marked determined instability points (coloured dots), b) local strain field of NR05 specimen in 0° to RD at force maximum

10.4 Weighting of non-proportional load paths

The modified Lankford-Coefficient according formula (5-1) of the two stress states 0 and 1. Stress state 0 exhibits the strains $d\epsilon_{y0}$ and $d\epsilon_{z0}$, whereas stress state 1 is defined by $d\epsilon_{y1}$ (10-1) and $d\epsilon_{z1}$ (10-2).

$$d\epsilon_{y1} = (d\epsilon_{y0} + \Delta y) \text{ with } \Delta y \ll d\epsilon_{y0} \quad (10-1)$$

$$d\epsilon_{z1} = (d\epsilon_{z0} + \Delta z) \text{ with } \Delta z \ll d\epsilon_{z0} \quad (10-2)$$

The accumulated strains of both stress states follows by the formula (10-3) and (10-4).

$$\epsilon_{y1} = d\epsilon_{y0} + d\epsilon_{y1} = 2 \cdot d\epsilon_{y0} + \Delta y \quad (10-3)$$

$$\epsilon_{z1} = d\epsilon_{z0} + d\epsilon_{z1} = 2 \cdot d\epsilon_{z0} + \Delta z \quad (10-4)$$

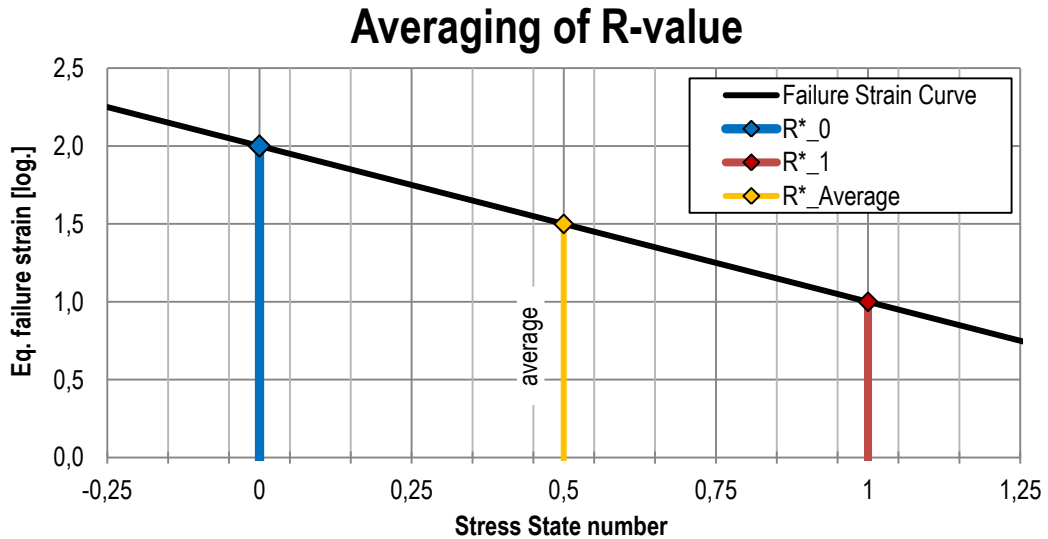


Figure 10-32: Visualisation of the weighting of two stress states

For weighting purpose the average modified Lankford-Coefficient R_{av0-1}^* is defined by (10-5):

$$R_{av0-1}^* = \frac{1}{2} \cdot (R_0^* + R_1^*) = \frac{1}{2} \cdot \left(\frac{d\epsilon_{y0}}{d\epsilon_{z0}} + \frac{d\epsilon_{y1}}{d\epsilon_{z1}} \right) = \frac{1}{2} \cdot \left(\frac{d\epsilon_{y0}}{d\epsilon_{z0}} + \frac{d\epsilon_{y0} + \Delta y}{d\epsilon_{z0} + \Delta z} \right) \quad (10-5)$$

Simplifying formula (10-5) leads to:

$$R_{av0-1}^* = \frac{2 \cdot d\epsilon_{y0} + \Delta y}{2 \cdot d\epsilon_{z0} + 2 \cdot \Delta z} + \frac{\frac{d\epsilon_{y0} \cdot \Delta z}{d\epsilon_{z0}}}{2 \cdot d\epsilon_{z0} + 2 \cdot \Delta z} = \frac{2 \cdot d\epsilon_{y0} + \Delta y}{2 \cdot d\epsilon_{z0} + 2 \cdot \Delta z} + \frac{1}{2} \cdot R_0 \cdot \frac{\Delta z}{d\epsilon_{z0} + \Delta z} \quad (10-6)$$

Assuming $\Delta z \ll d\epsilon_{z0}$, formula (10-6) simplifies to:

$$R_{av0-1}^* = \frac{2 \cdot d\epsilon_{y0} + \Delta y}{2 \cdot d\epsilon_{z0} + 2 \cdot \Delta z} + \frac{1}{2} \cdot R_0 \cdot \frac{\Delta z}{d\epsilon_{z0} + \Delta z} \approx \frac{2 \cdot d\epsilon_{y0} + \Delta y}{2 \cdot d\epsilon_{z0} + \Delta z} = \frac{\epsilon_{y1}}{\epsilon_{z1}} \quad (10-7)$$

For N discrete stress states, the weighting follows by formula (10-8), based on formula (10-7):

$$R_{av0-N}^* = \frac{1}{N} \sum_{i=0}^N R_i^* \approx \frac{\frac{1}{N} \sum_{i=0}^N d\epsilon_{yi}}{\frac{1}{N} \sum_{i=0}^N d\epsilon_{zi}} = \frac{\epsilon_{yN}}{\epsilon_{zN}} \quad (10-8)$$

The weighting of the Γ^* -value is identically to the presented calculation of R_{av}^* .

10.5 Characterised Material Models

10.5.1 Characterisation of CR340LA in 0.6 mm Sheet Thickness

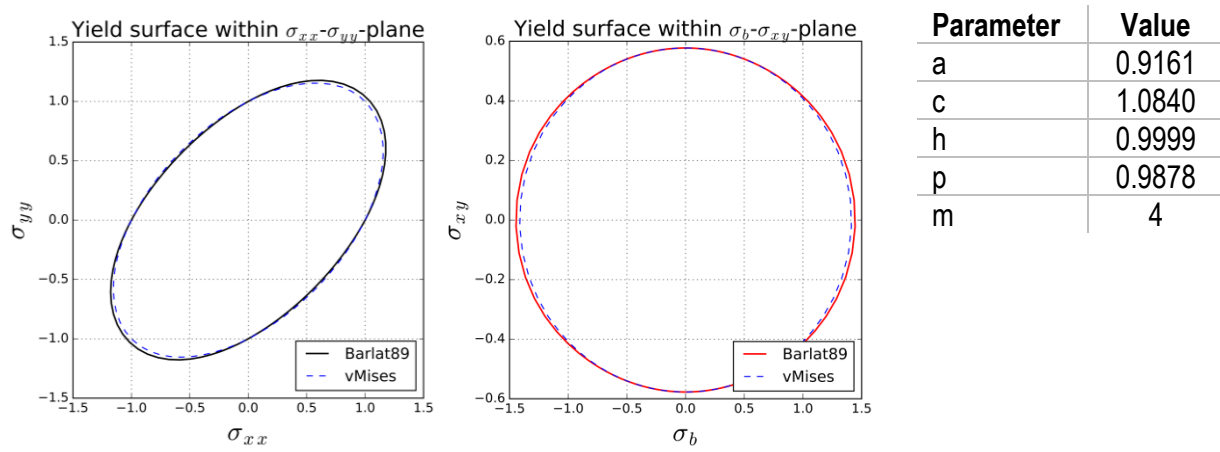


Figure 10-33: Defined yield surface within a) the σ_{xx} - σ_{yy} -plane and b) within the σ_{xy} - σ_b -plane as well as the applied parameters of the Barlat'89 yield surface of the CR340LA with a sheet thickness of 0.6 mm

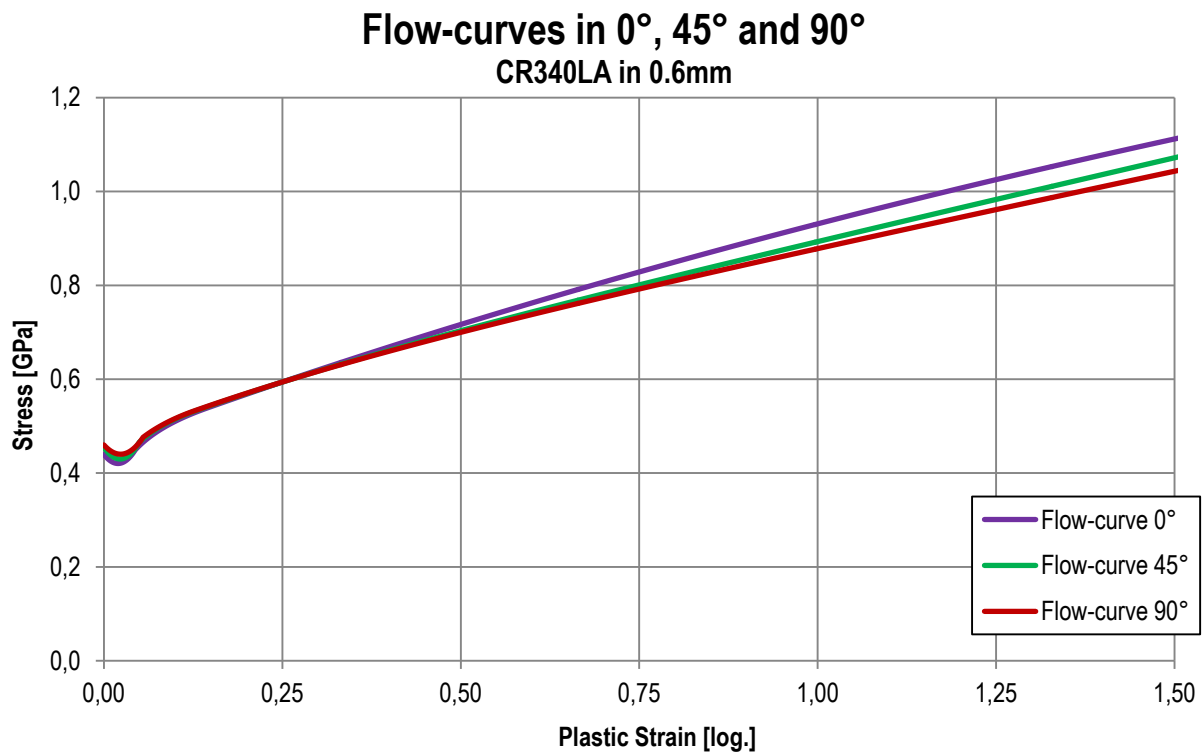


Figure 10-34: Characterised flow curves in 0° , 45° and 90° to RD of the investigated CR340LA with a sheet thickness of 0.6 mm

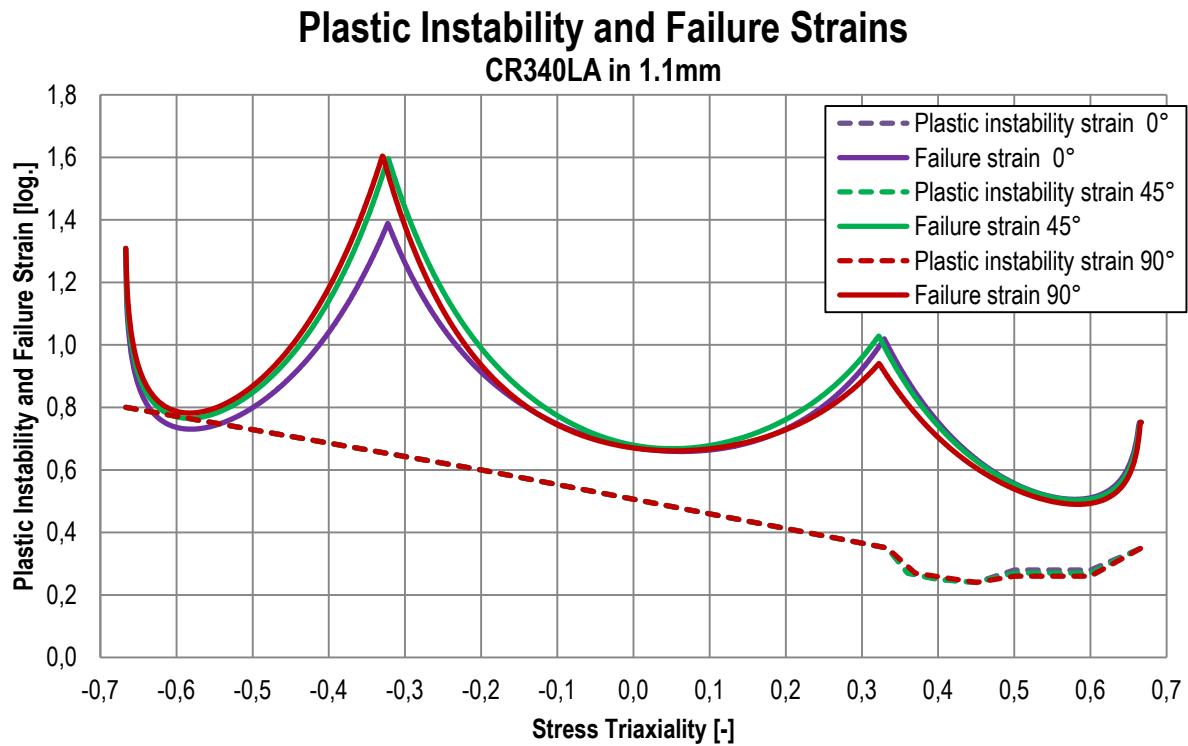


Figure 10-35: Characterised plastic instability as well as failure strain curves in 0° , 45° and 90° to RD of the CR340LA in 0.6 mm sheet thickness

Table 10-1: Applied Damage and Fading Exponents of the CR340LA in 0.6 mm thickness

Exponent	0°	45°	90°
Damage exponent	1.0	1.0	1.0
Fading exponent	6.9	7.1	7.0

10.5.2 Characterisation of CR340LA in 1.1 mm Sheet Thickness

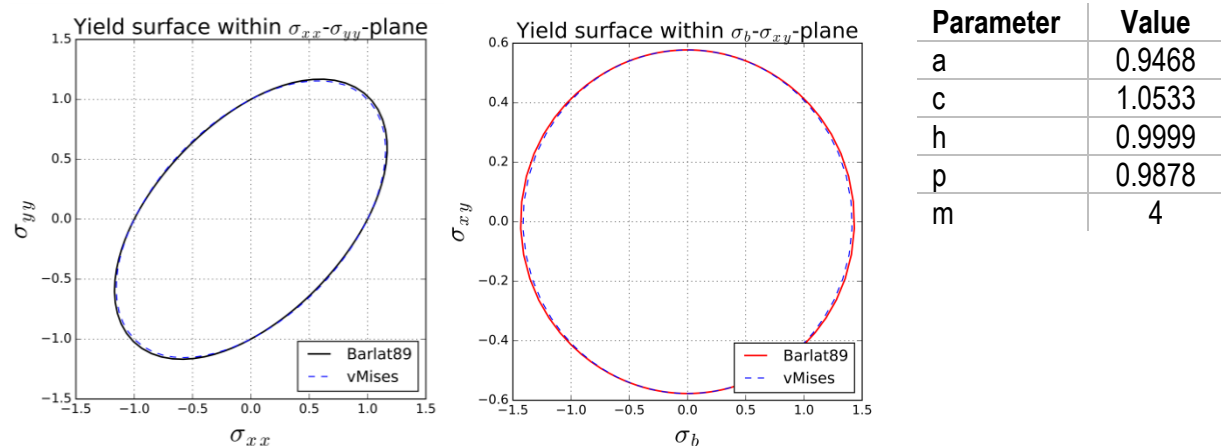


Figure 10-36: Defined yield surface within a) the σ_{xx} - σ_{yy} -plane and b) within the σ_{xy} - σ_b -plane as well as the applied parameters of the Barlat'89 yield surface of the CR340LA with a sheet thickness of 1.1 mm

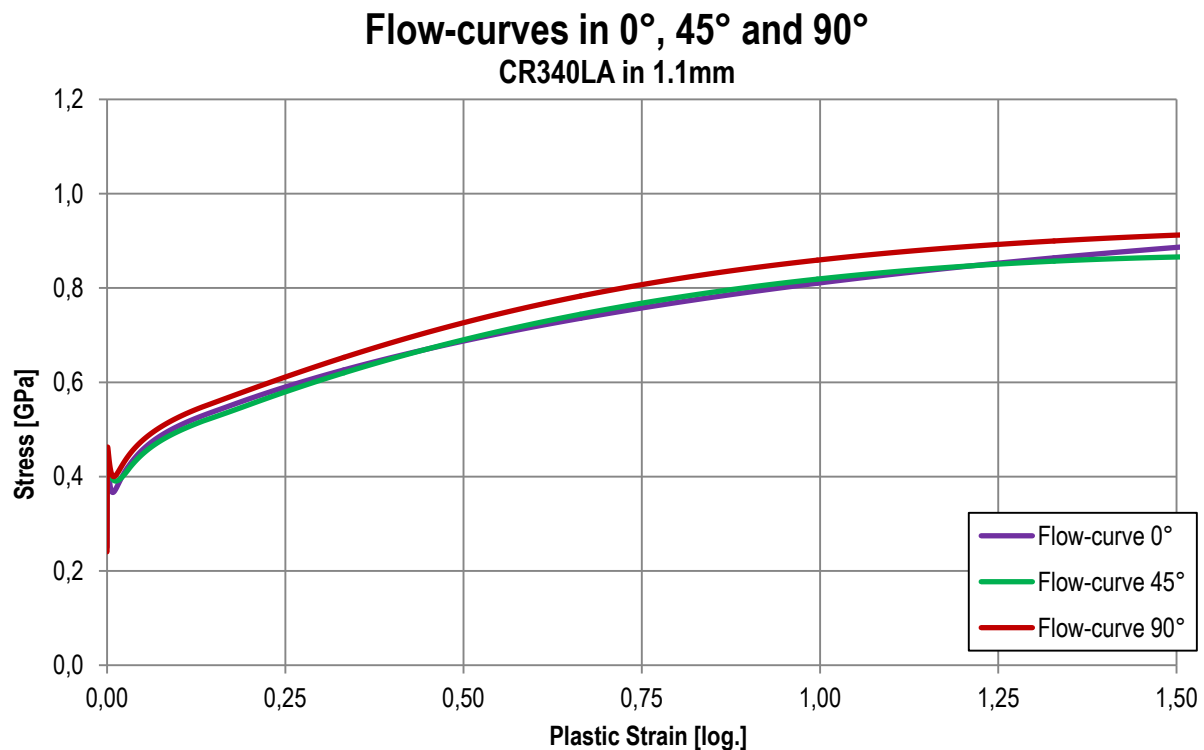


Figure 10-37: Characterised flow curves in 0°, 45° and 90° to RD of the investigated CR340LA with a sheet thickness of 1.1 mm

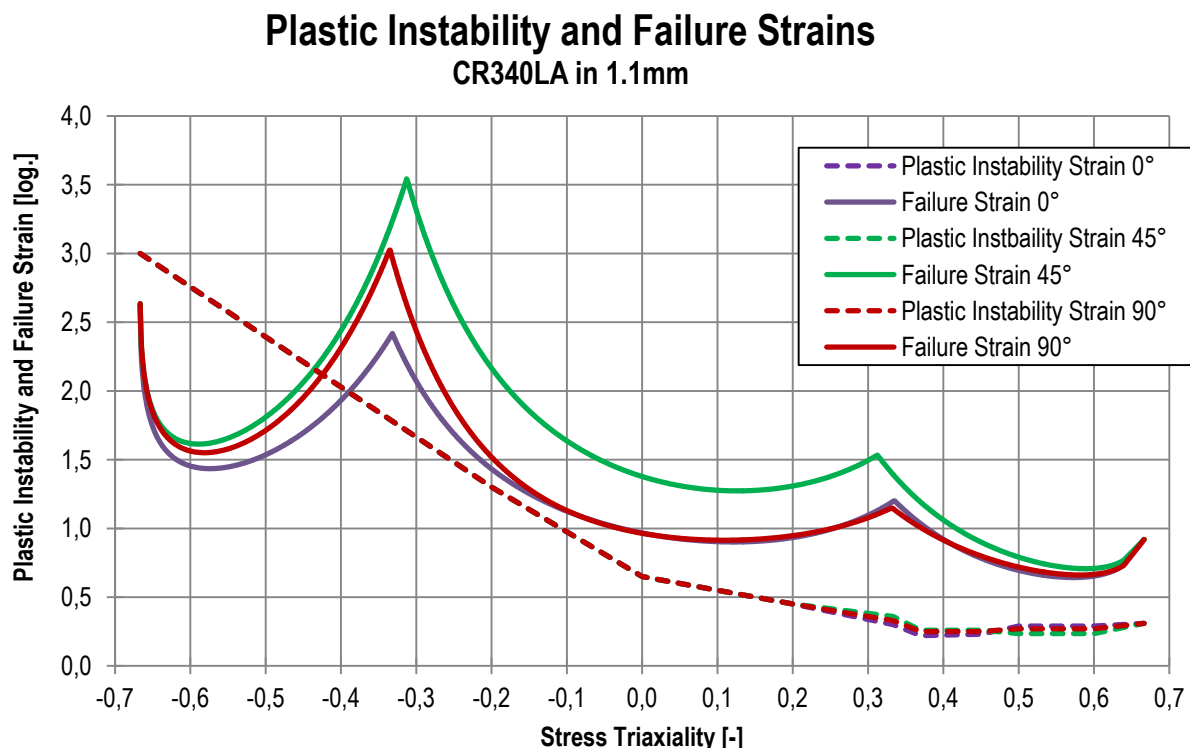


Figure 10-38: Characterised plastic instability as well as failure strain curves in 0°, 45° and 90° to RD of the CR340LA in 1.1 mm sheet thickness

Table 10-2: Applied Damage and Fading Exponents of the CR340LA in 1.1 mm thickness

Exponent	0°	45°	90°
Damage exponent	1.0	1.0	1.0
Fading exponent	6.9	7.1	7.0

10.5.3 Characterisation of CR340LA in 1.8 mm Sheet Thickness

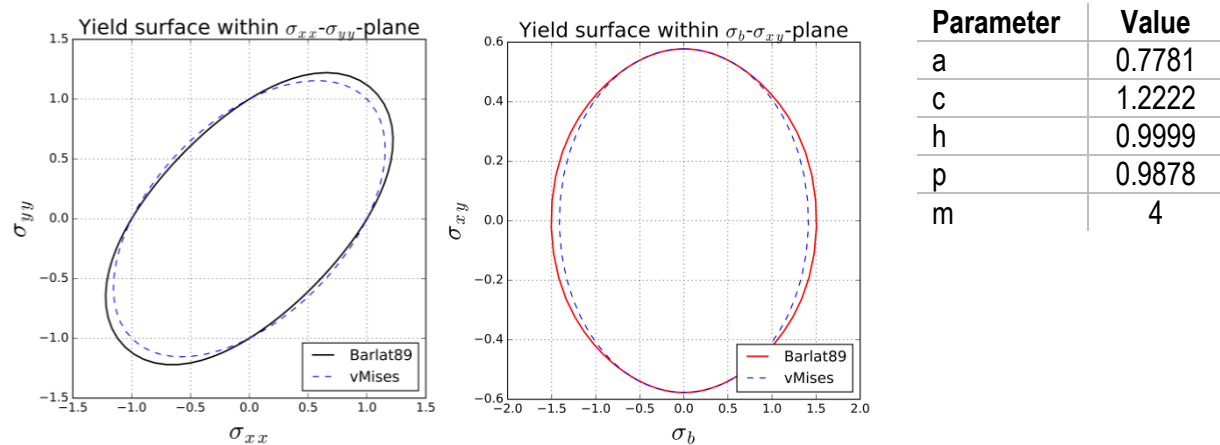


Figure 10-39: Defined yield surface within a) the σ_{xx} - σ_{yy} -plane and b) within the σ_{xy} - σ_b -plane as well as the applied parameters of the Barlat'89 yield surface of the CR340LA with a sheet thickness of 1.8 mm

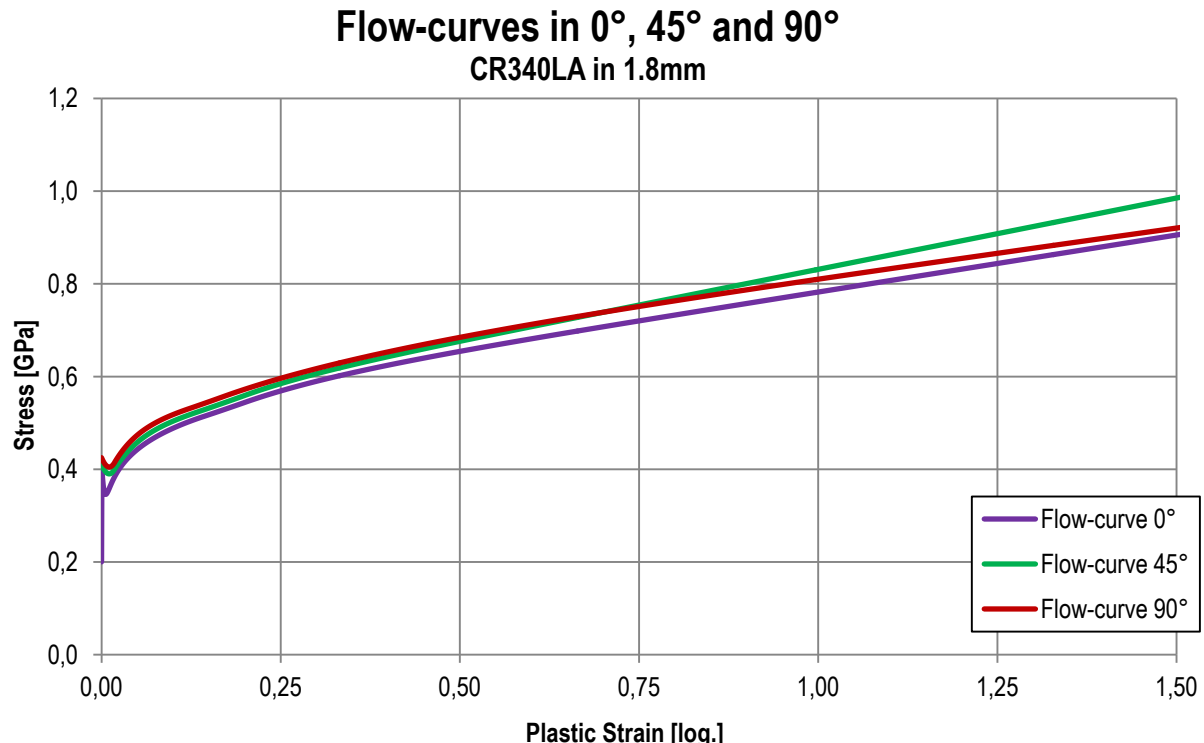


Figure 10-40: Characterised flow curves in 0°, 45° and 90° to RD of the investigated CR340LA with a sheet thickness of 1.8 mm

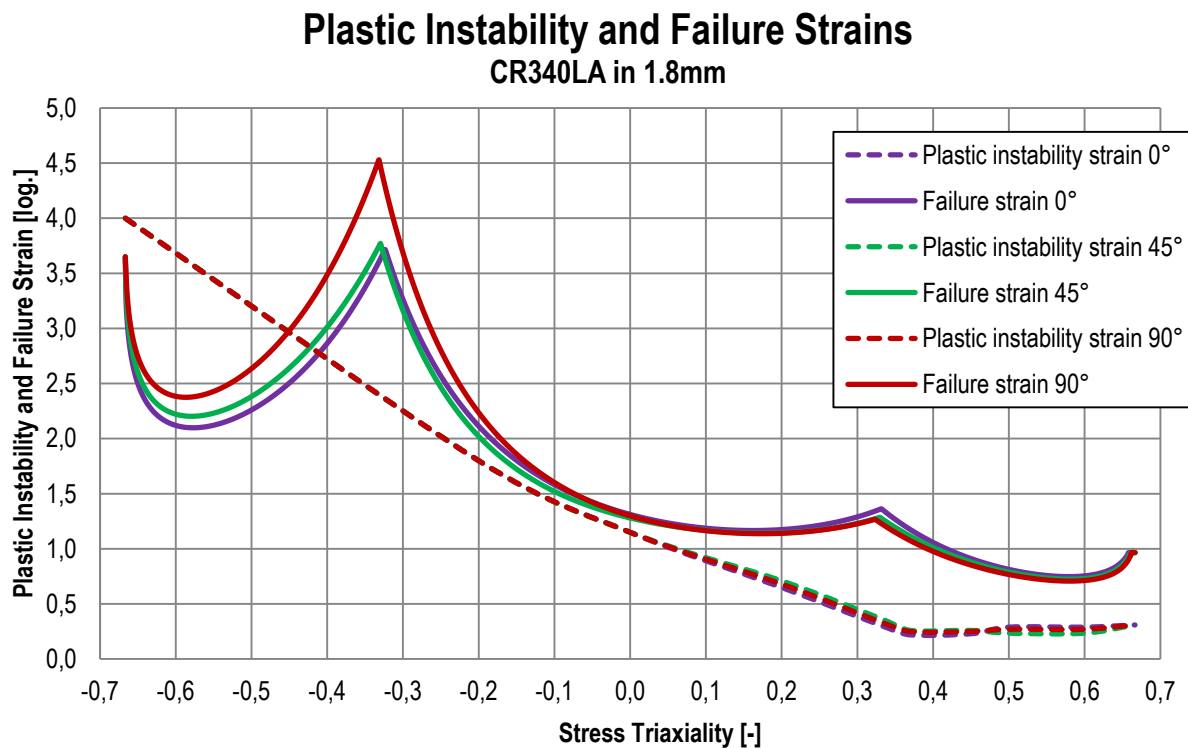


Figure 10-41: Characterised plastic instability as well as failure strain curves in 0°, 45° and 90° to RD of the CR340LA in 1.8 mm sheet thickness

Table 10-3: Applied Damage and Fading Exponents of the CR340LA in 1.8 mm thickness

Exponent	0°	45°	90°
Damage exponent	1.0	1.0	1.0
Fading exponent	6.9	7.1	7.0

10.5.4 Characterisation of MS1500 in 1.0 mm Sheet Thickness

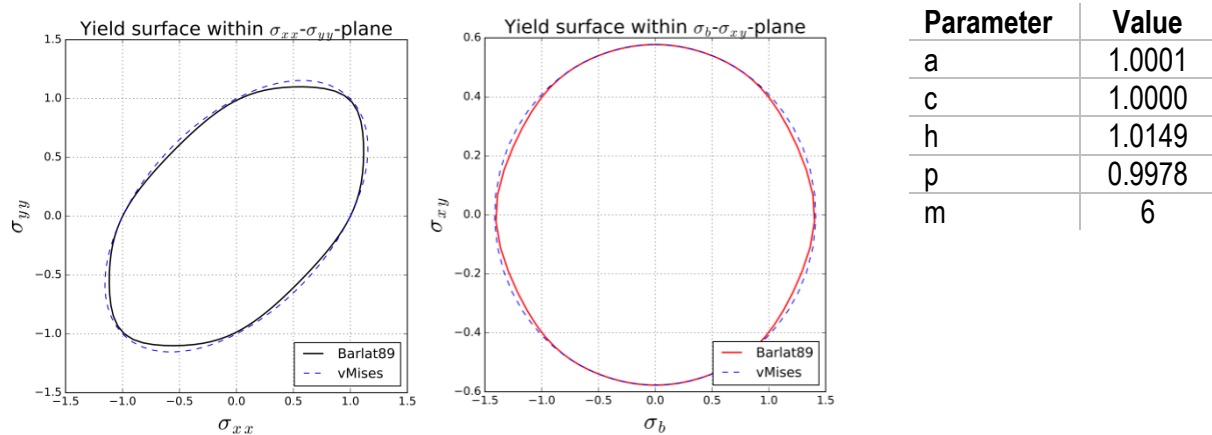


Figure 10-42: Defined yield surface within a) the σ_{xx} - σ_{yy} -plane and b) within the σ_{xy} - σ_b -plane as well as the applied parameters of the Barlat'89 yield surface of the MS1500 with a sheet thickness of 1.0 mm

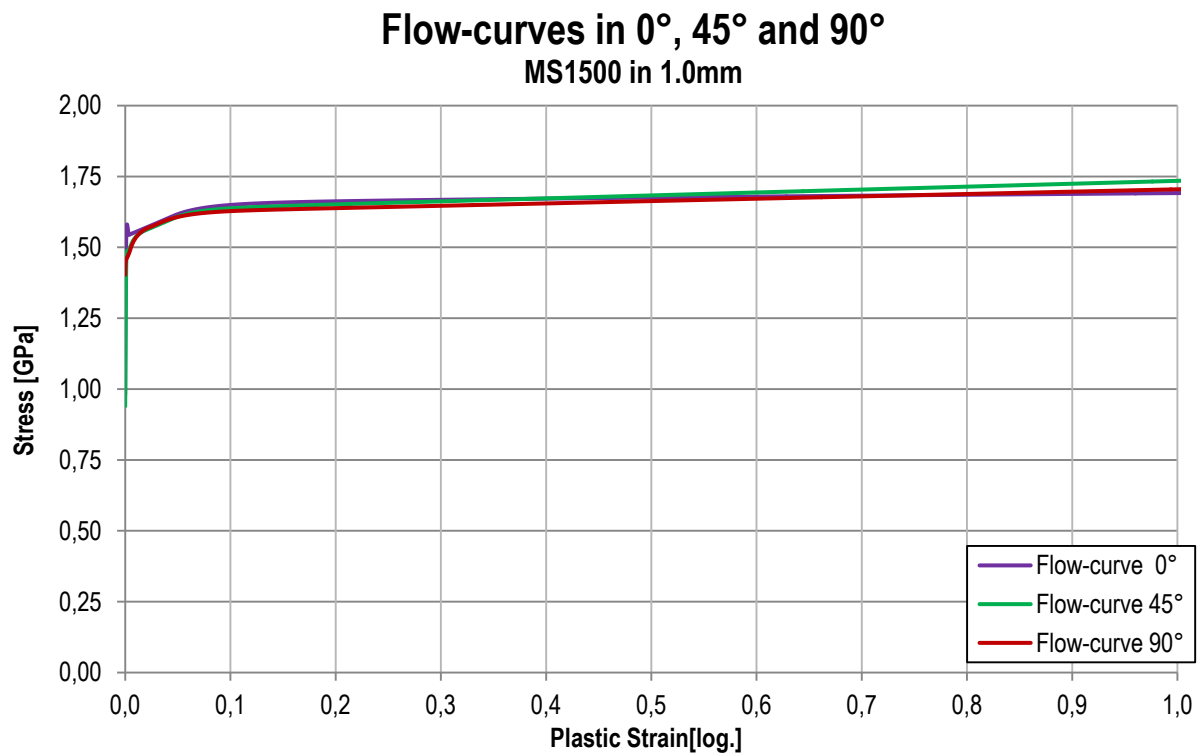


Figure 10-43: Characterised flow curves in 0°, 45° and 90° to RD of the investigated MS1500 with a sheet thickness of 1.0 mm

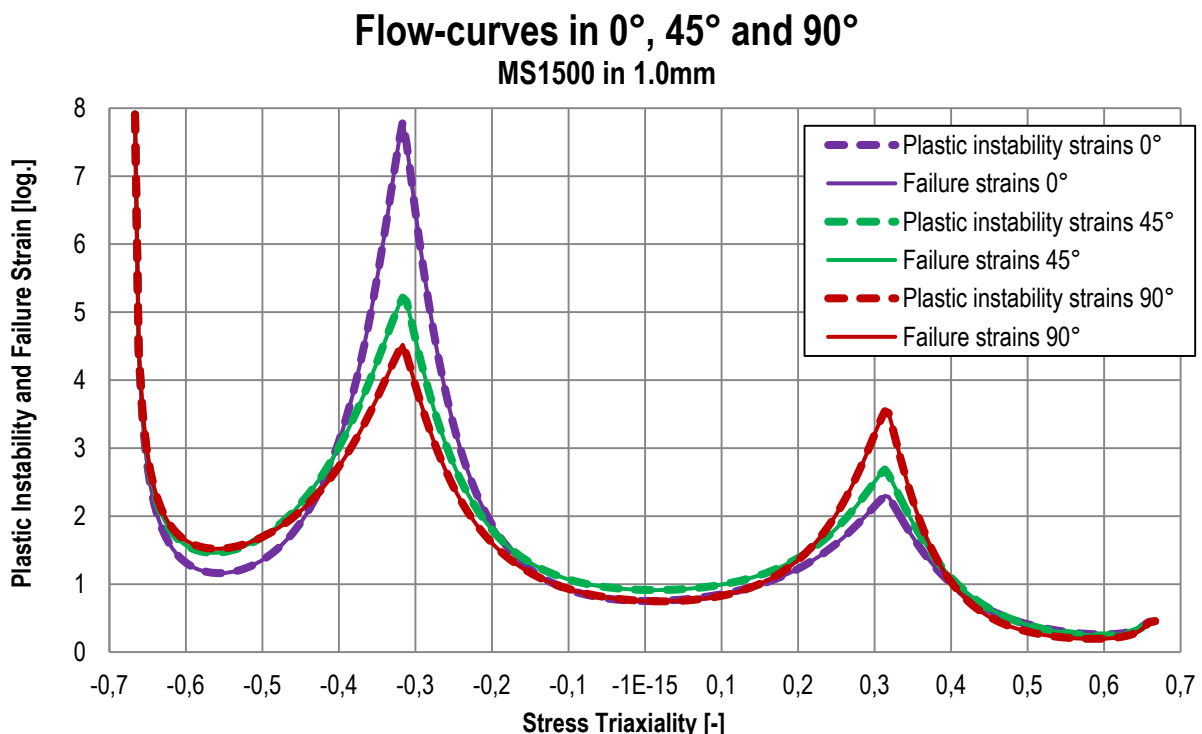


Figure 10-44: Characterised plastic instability as well as failure strain curves in 0°, 45° and 90° to RD of the CR340LA in 1.0 mm sheet thickness

Table 10-4: Applied Damage and Fading Exponents of the MS1500 in 1.0 mm thickness

Exponent	0°	45°	90°
Damage exponent	1.0	1.0	1.0
Fading exponent	3.3	3.3	3.3

10.6 Simulation Results CR340LA in 0.6 mm Sheet Thickness

10.6.1 CR340LA 0.6 mm: Force-Displacement & Local Strains

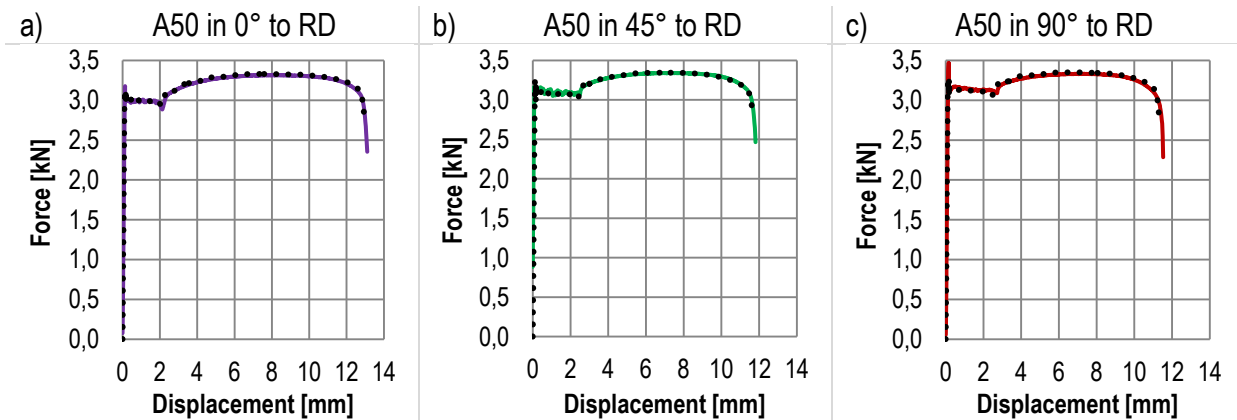


Figure 10-45: Comparison of experimental with numerical determined force-displacement behaviour of standard tensile tests of CR340LA with a sheet thickness of 0.6 mm in a) 0°, b) 45° and c) 90° to RD

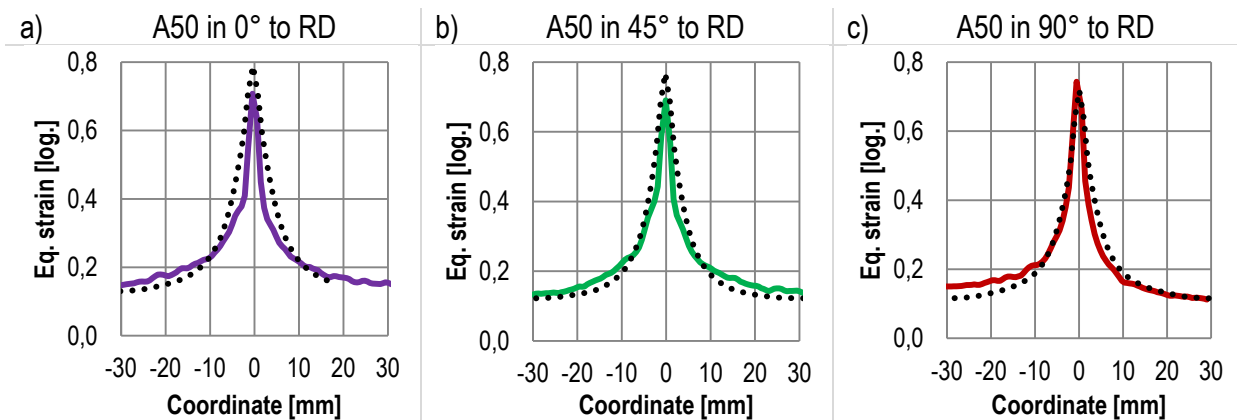


Figure 10-46: Comparison of experimental with numerical determined local strain behaviour of standard tensile specimens of CR340LA with a sheet thickness of 0.6 mm in a) 0°, b) 45° and c) 90° to RD

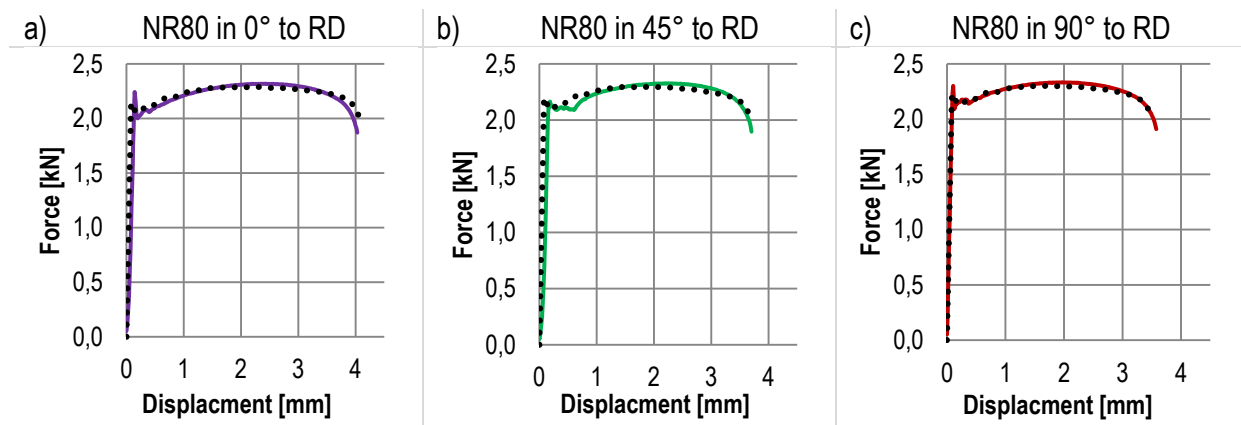


Figure 10-47: Comparison of experimental with numerical determined force-displacement behaviour of NR80 specimens of CR340LA with a sheet thickness of 0.6 mm in a) 0° , b) 45° and c) 90° to RD

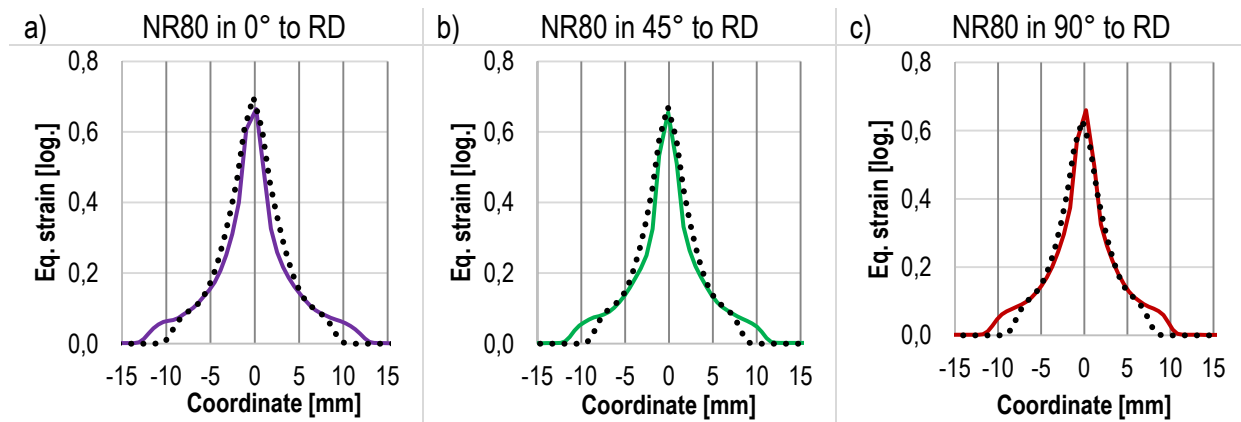


Figure 10-48: Comparison of experimental with numerical determined local strain behaviour of NR80 specimens of CR340LA with a sheet thickness of 0.6 mm in a) 0° , b) 45° and c) 90° to RD

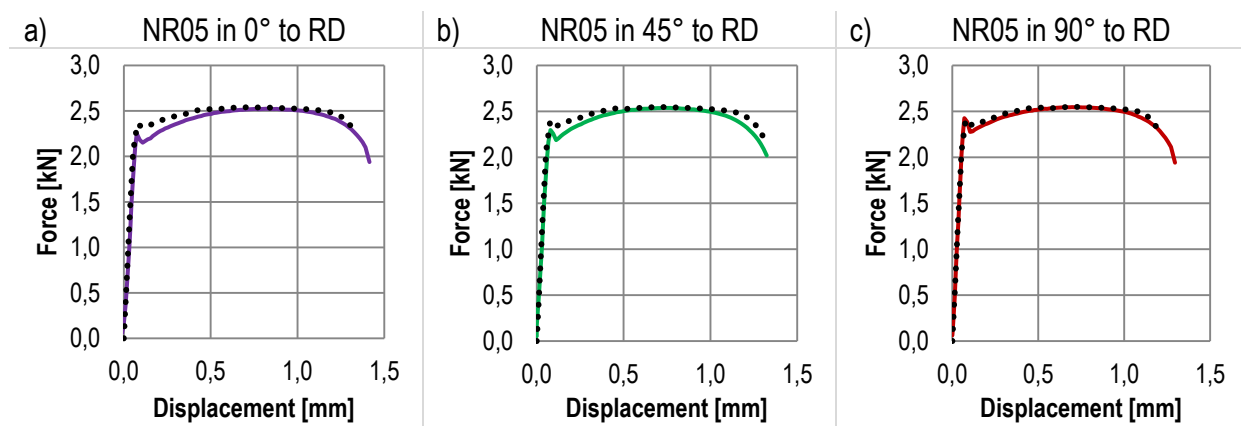


Figure 10-49: Comparison of experimental with numerical determined force-displacement behaviour of NR80 specimens of CR340LA with a sheet thickness of 0.6 mm in a) 0° , b) 45° and c) 90° to RD

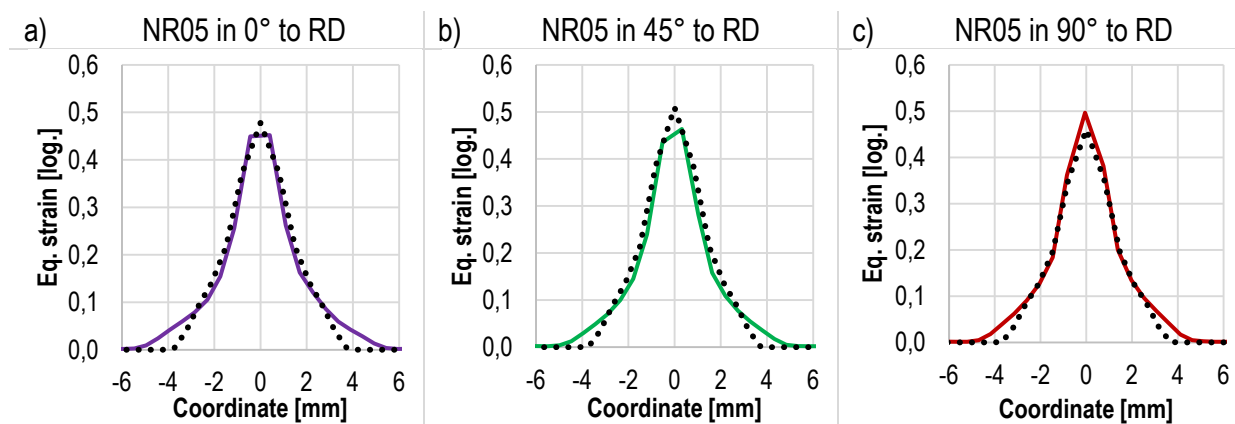


Figure 10-50: Comparison of experimental with numerical determined local strain behaviour of NR05 specimens of CR340LA with a sheet thickness of 0.6 mm in a) 0°, b) 45° and c) 90° to RD

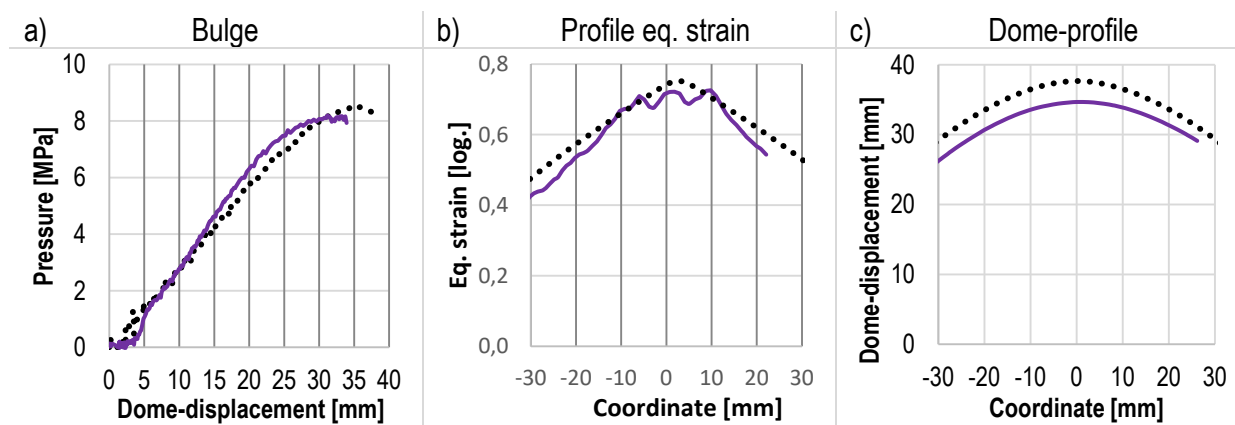


Figure 10-51: Comparison of experimental with numerical determined behaviour of CR340LA with a sheet thickness of 0.6 mm under biaxial loading, a) pressure-displacements at the dome, b) local strain profile, c) dome-displacement profile

10.6.2 CR340LA 0.6 mm: Validation

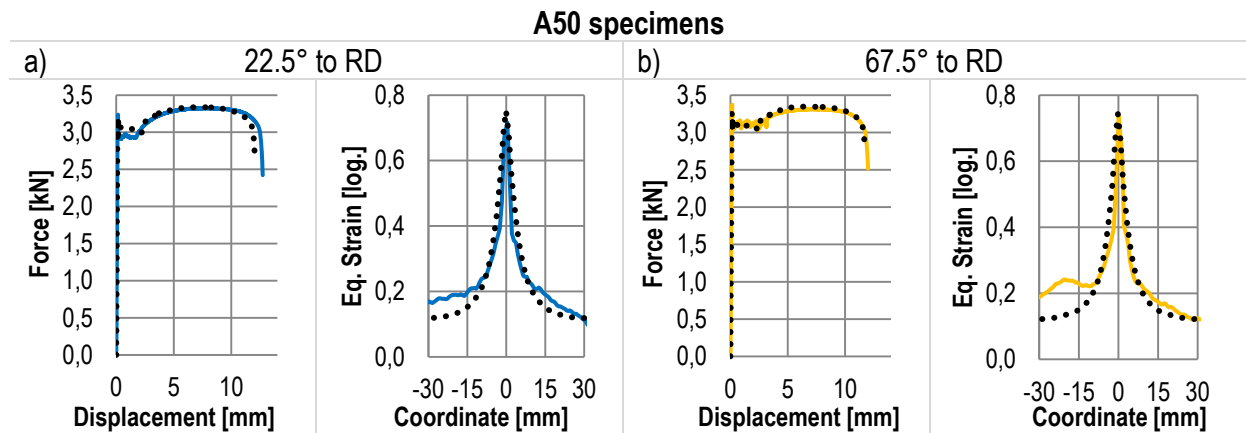


Figure 10-52: Validation of material model for CR340LA PB 0.6 mm at A50 specimens in 22.5° (a), left: force-displacements, right: local strain field) and 67.5° (b), left: force-displacements, right: local strain field)

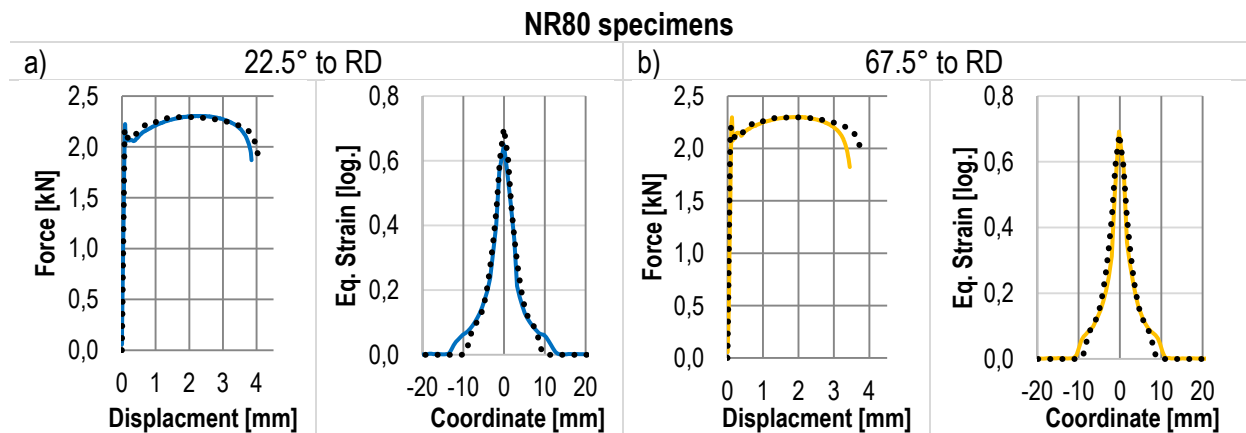


Figure 10-53: Validation of material model for CR340LA PB 0.6 mm at NR80 specimens in 22.5° (a), left: force-displacements, right: local strain field) and 67.5° (b), left: force-displacements, right: local strain field)

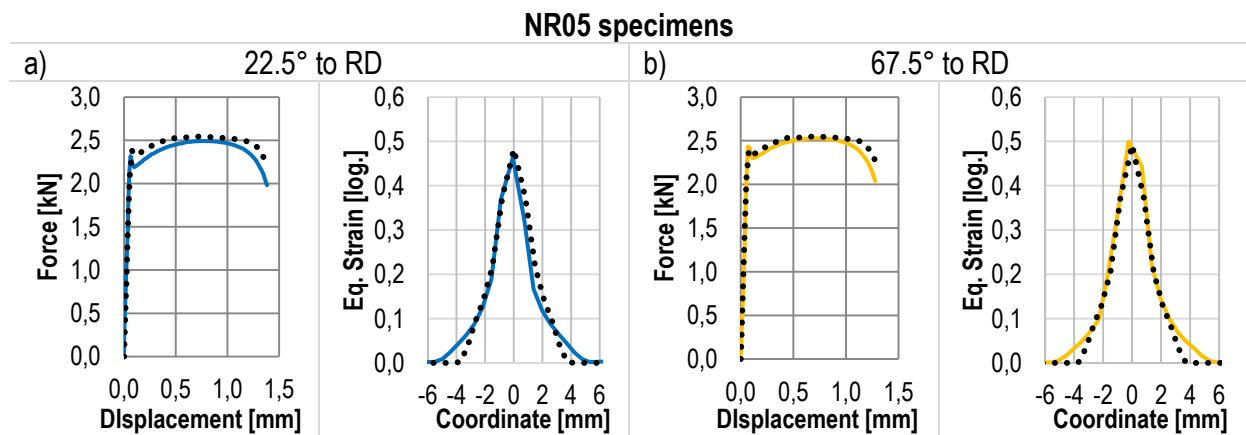


Figure 10-54: Validation of material model for CR340LA PB 0.6 mm at NR05 specimens in 22.5° (a), left: force-displacements, right: local strain field) and 67.5° (b), left: force-displacements, right: local strain field)

10.7 Simulation Results CR340LA in 1.8 mm Sheet Thickness

10.7.1 CR340LA 1.8 mm: Force-Displacement & Local Strains

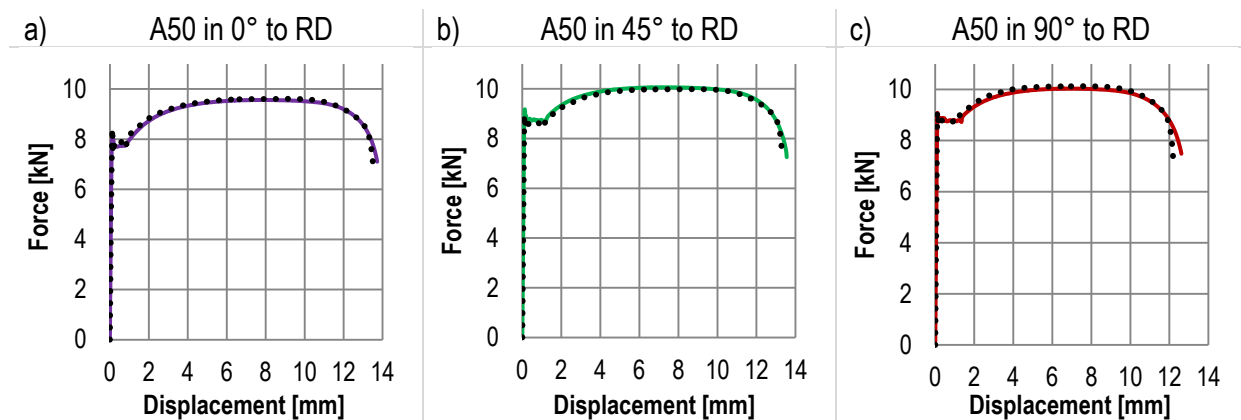


Figure 10-55: Comparison of experimental with numerical determined force-displacement behaviour of standard tensile tests of CR340LA with a sheet thickness of 1.8 mm in a) 0° , b) 45° and c) 90° to RD

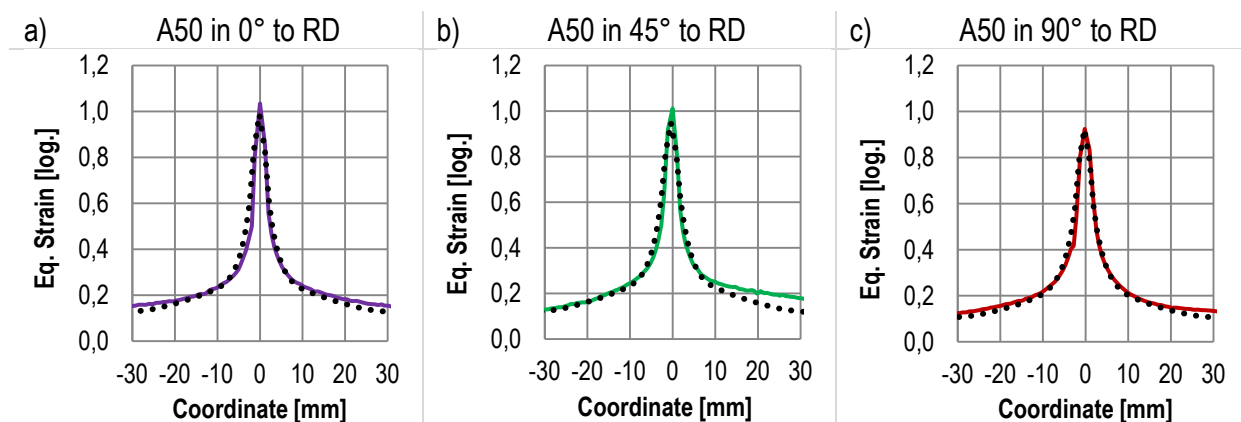


Figure 10-56: Comparison of experimental data and numerical simulation results in a) 0° , b) 45° and c) 90° to RD of standard tensile specimens of CR340LA in 1.8 mm sheet thickness. The upper picture shows the force displacement data, the lower the local strain profile just before fracture

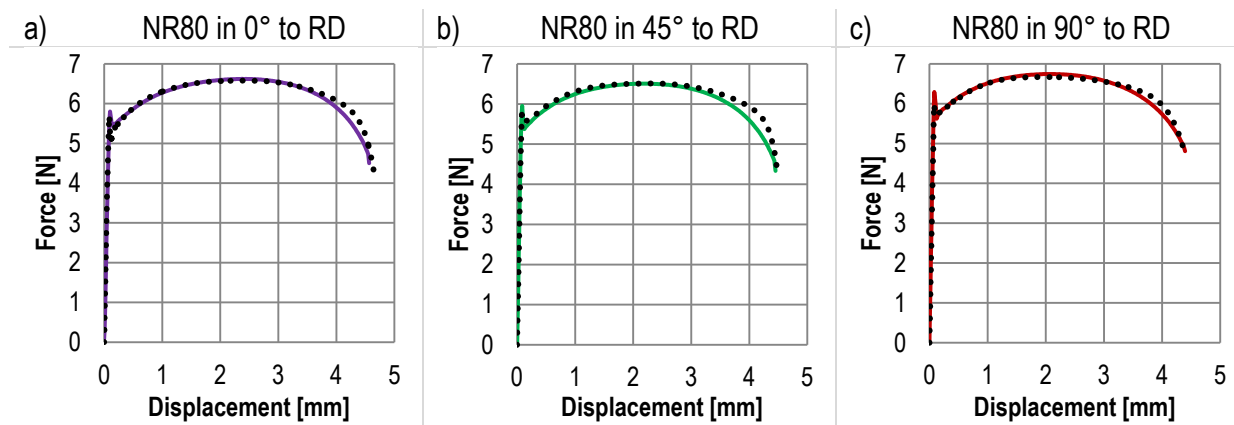


Figure 10-57: Comparison of experimental with numerical determined force-displacement behaviour of NR80 specimens of CR340LA with a sheet thickness of 1.8 mm in a) 0°, b) 45° and c) 90° to RD

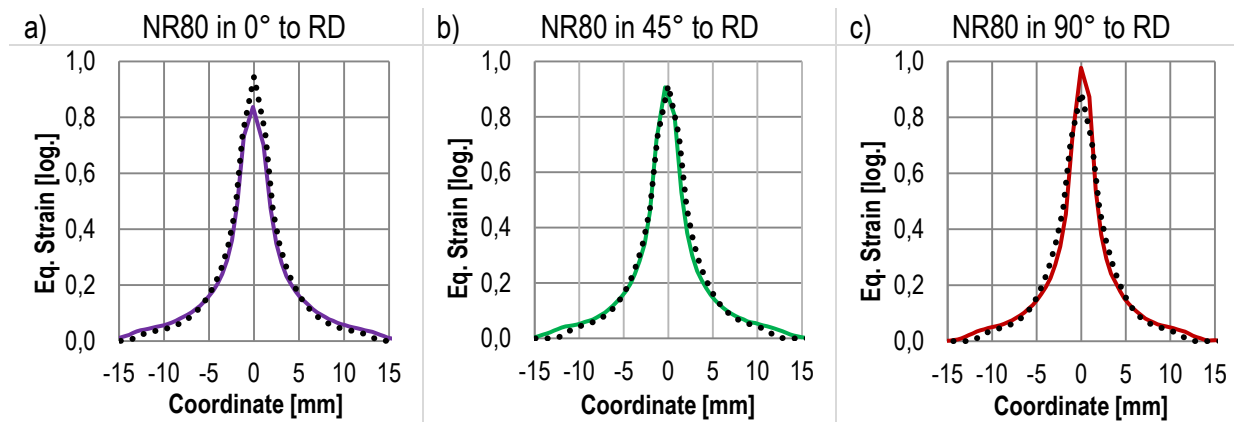


Figure 10-58: Comparison of experimental data and numerical simulation results in a) 0°, b) 45° and c) 90° to RD of NR80 specimens of CR340LA in 1.8 mm sheet thickness. The upper picture shows the force displacement data, the lower the local strain profile just before fracture

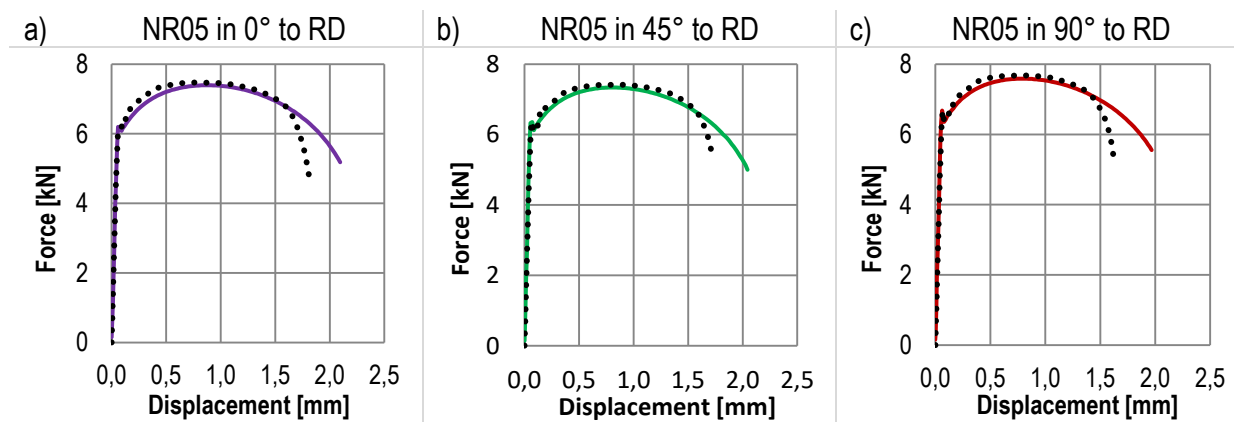


Figure 10-59: Comparison of experimental with numerical determined force-displacement behaviour of NR05 specimens of CR340LA with a sheet thickness of 1.8 mm in a) 0°, b) 45° and c) 90° to RD

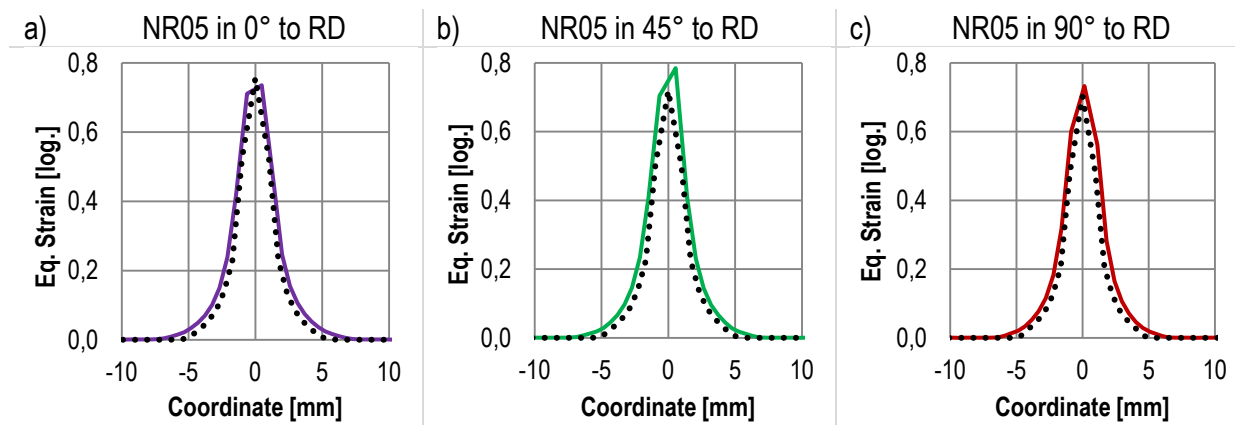


Figure 10-60: Comparison of experimental data and numerical simulation results in a) 0° , b) 45° and c) 90° to RD of NR05 specimens of CR340LA in 1.8 mm sheet thickness. The upper picture shows the force displacement data, the lower the local strain profile just before fracture

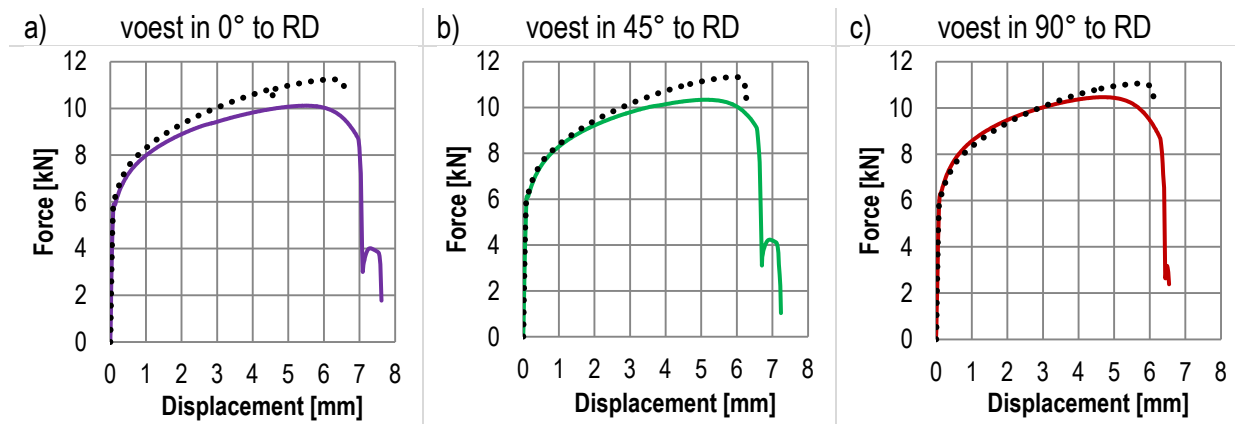


Figure 10-61: Comparison of experimental with numerical determined force-displacement behaviour of voest-shear specimens of CR340LA with a sheet thickness of 1.8 mm in a) 0° , b) 45° and c) 90°

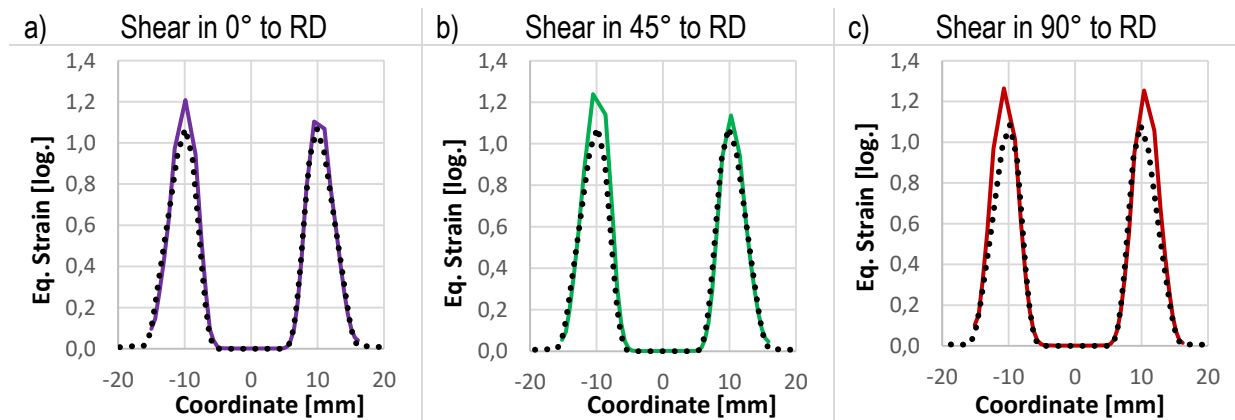


Figure 10-62: Comparison of experimental with numerical determined force-displacement behaviour of voest-shear specimens of CR340LA with a sheet thickness of 1.8 mm in a) 0° , b) 45° and c) 90° to RD

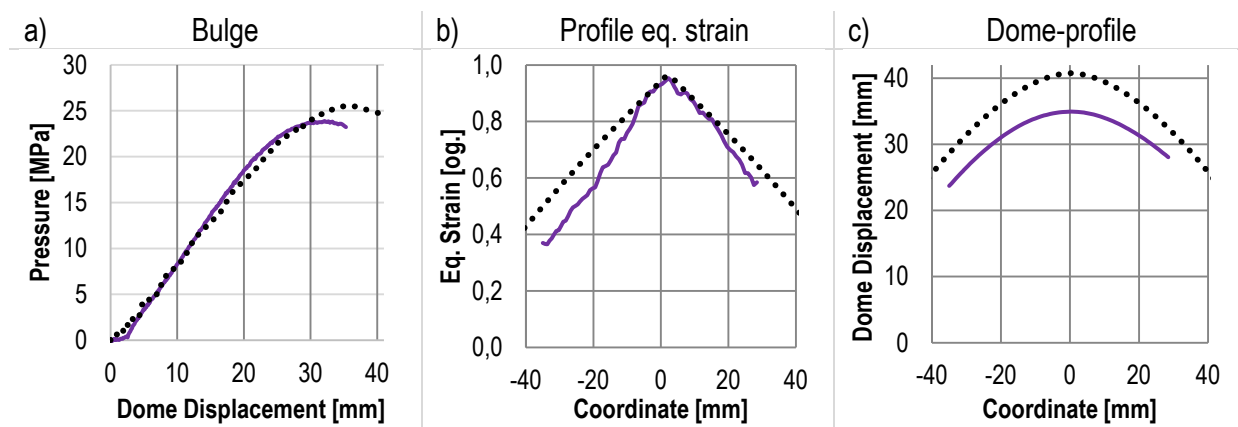


Figure 10-63: Comparison of experimental with numerical determined behaviour of CR340LA with a sheet thickness of 1.8 mm under biaxial loading, a) pressure-displacements at the dome, b) local strain profile, c) dome-displacement profile

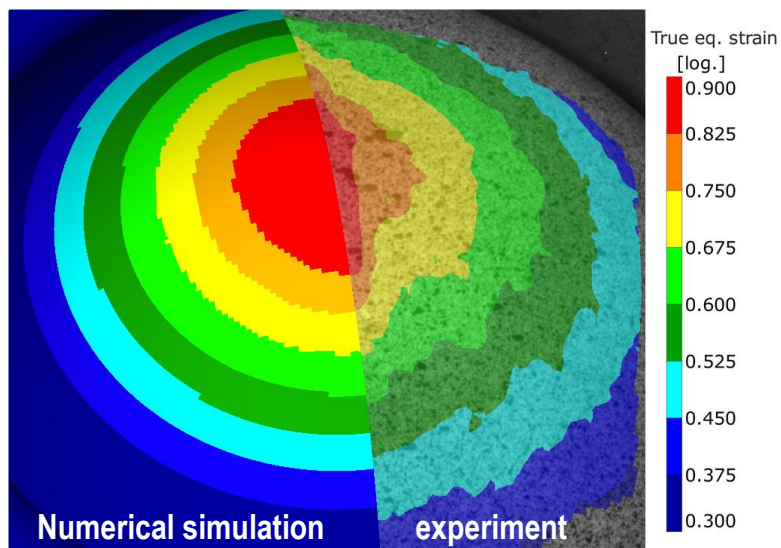


Figure 10-64: Opposition of surface equivalent strain fields, obtained from Bulge-tests at CR340LA with a sheet thickness of 1.8 mm

10.7.2 CR340LA 1.8 mm: Validation

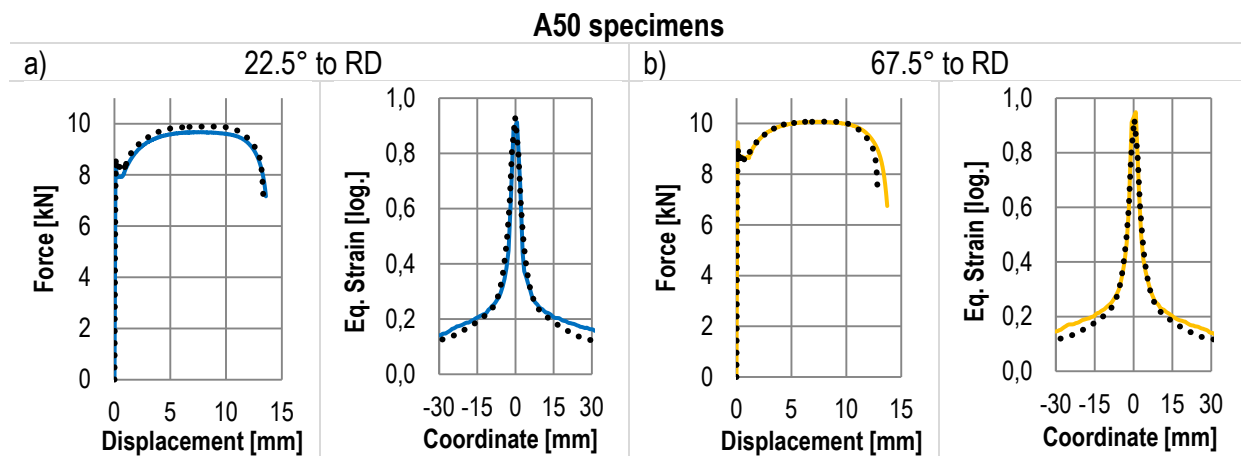


Figure 10-65: Validation of material model for CR340LA PB 1.8 mm at A50 specimens in 22.5° (a), left: force-displacements, right: local strain field) and 67.5° (b), left: force-displacements, right: local strain field)

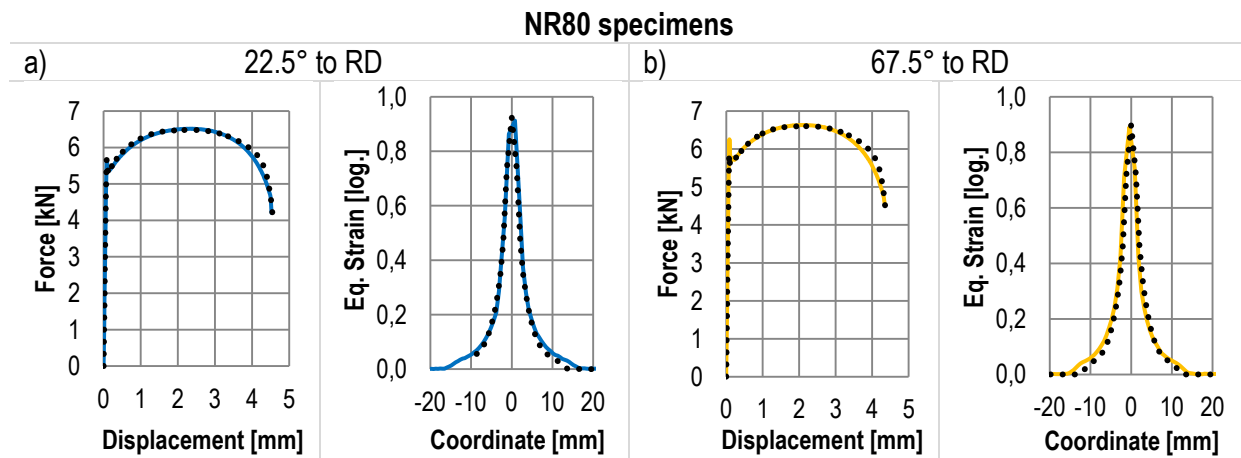


Figure 10-66: Validation of material model for CR340LA PB 1.8 mm at NR80 specimens in a) 22.5° to RD, left: force-displacements, right: local strain field) and b) 67.5° to RD, left: force-displacements, right: local strain field)

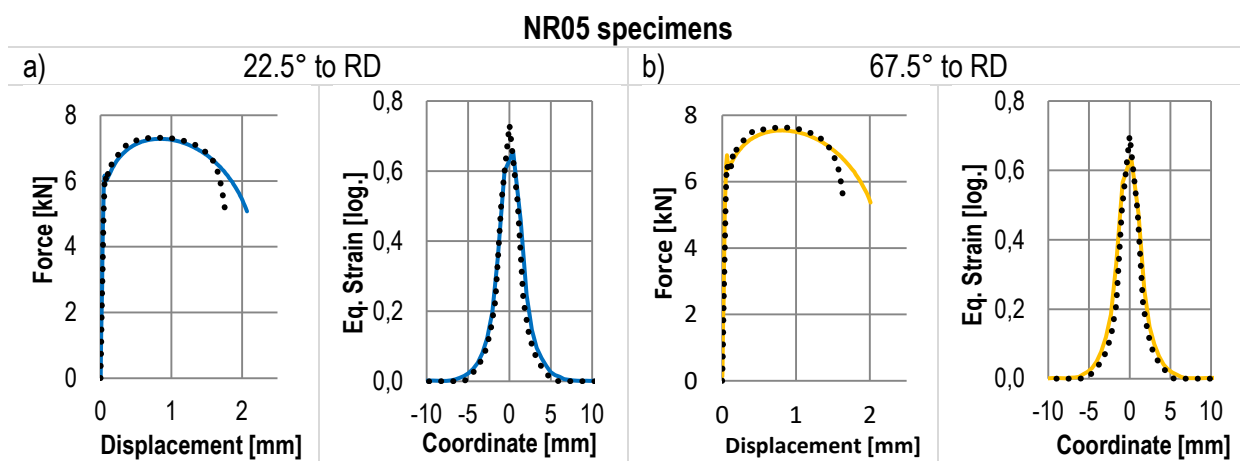


Figure 10-67: Validation of material model for CR340LA PB 1.8 mm at NR05 specimens in 22.5° (a), left: force-displacements, right: local strain field) and 67.5° (b), left: force-displacements, right: local strain field)

10.8 Virtual Component-Test Geometries

10.8.1 Geometry of Hole Expansion Test

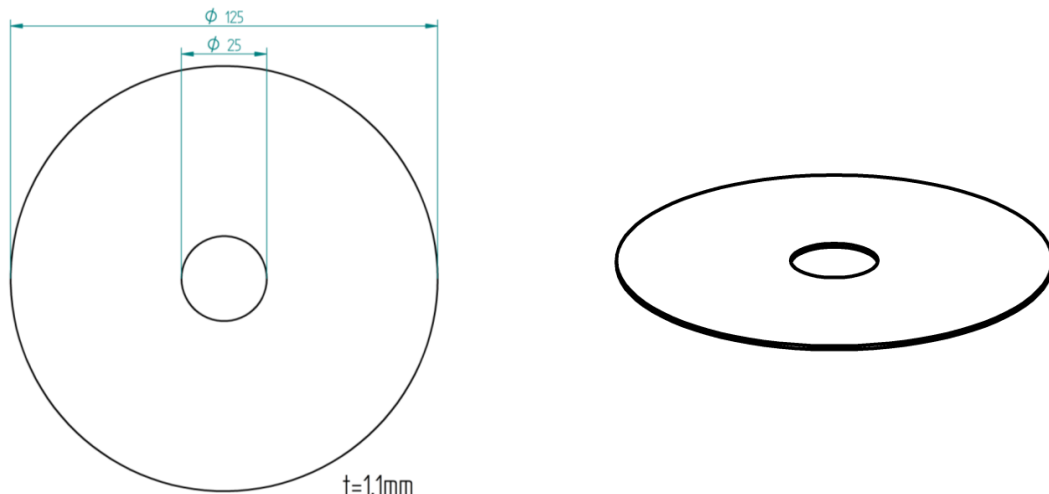


Figure 10-68: Utilised specimen geometry of virtual hole-expansion test

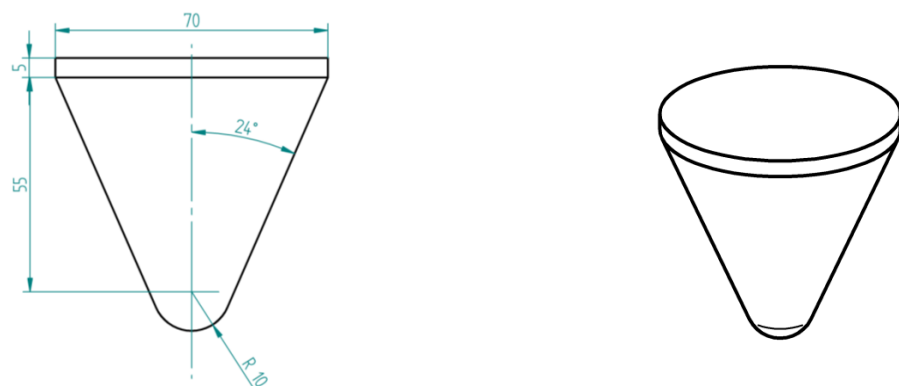


Figure 10-69: Utilised punch of virtual hole-expansion test

10.8.2 Geometry of Compression Test

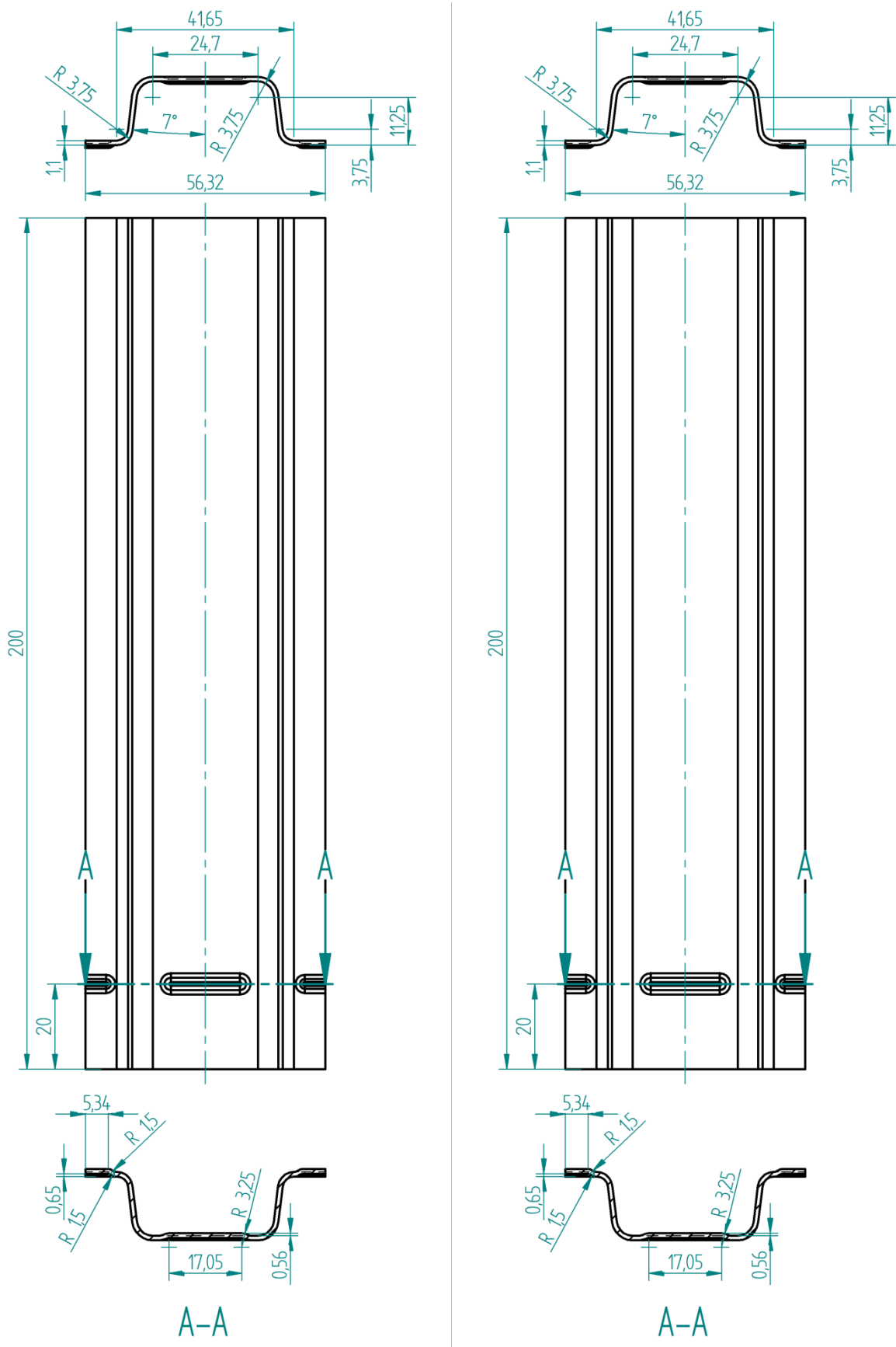


Figure 10-70: Utilised double-hat profile

11 Bibliography

[SEP06] 1240, S. (2006). Prüf- und Dokumentationsrichtlinie für die experimentelle Ermittlung mechanischer Kennwerte von Feinblechen aus Stahl für die CAE-Berechnung. Stahlinstitut VDEh.

[An13] An, Y., Vegte, H., Melzer, S., & Triguero, P. R. (2013). Evolution of the plastic anisotropy with straining and its implication on formability for sheet metals. *Journal of Materials Processing Technology* .

[And17] Andrade, F., & Feucht, M. (2017). A comparison of damage and failure models for the prediction of dual-phase steels. *Proceedings 11th European LS-DYNA Conference 2017* .

[Ant13] Antunes, R., & Eddine, M. (2013). Effect of Cold Rolling on the Earing Formation During Deep Drawing of the ASTM C22000 Copper Alloy. *Proceedings of the 22nd International Congress of Mechanical Engineering (COBEM 2013)* .

[Bai07] Bai, Y. (2007). *Effect of Loading History on Necking and Fracture*. Massachusetts Institute of Technology.

[Bal09] Ballarin, V., Soler, M., Perlade, A., Lemoine, X., & Forest, S. (2009). Mechanisms and Modeling of Bake-Hardening Steels: Part I. Uniaxial Tension. *Metallurgical and Materials Transactions A* (40), S. 1367-1374.

[Ban10] Banabic, D. (2010). *Sheet Metal Forming Processes - Constitutive Modelling and Numerical Simulation*. Berlin, Heidelberg: Springer.

[Ban05] Banabic, D., Aretz, H., Comsa, D., & Paraianu, L. (2005). An improved analytical description of orthotropy in metallic sheets. *International Journal of Plasticity* (21), S. 493-512.

[Ban00] Banabic, D., Balan, T., & Comsa, D. (2000). A New Yield Criterion for Orthotropic Sheet Metals Under Plane-Stress Conditions. *Proceedings of 7th COLD METAL FORMING Conference* , S. 217-224.

[Bar89] Barlat, F., & Lian, J. (1989). Plastic Behaviour and Stretchability of Sheet Metals. Part I: A Yield Function for Orthotropic Sheets under Plane Stress Conditions. *International Journal of Plasticity* , 5, S. 51-66.

[Bar03] Barlat, F., Brem, J., Yoon, J., Chung, K., Dick, R., Lege, D., et al. (2003). Plane stress yield function for aluminum alloy sheets - part 1: theory. *International Journal of Plasticity* , 19, S. 1297-1319.

[Bar91] Barlat, F., Lege, D., & Brem, J. (1991). A Six-Component Yield Function For Anisotropic Materials. *International Journal of Plasticity* , S. 693-712.

[Bar06a] Barsoum, I. (2006). *Ductile failure and rupture mechanisms combined tension and shear*. Stockholm, Sweden: Royal Institute of Technology.

[Bar07a] Barsoum, I., & Faleskog, J. (2007). Rupture mechanisms in combined tension and shear - Experiments. *International Journal of Solids and Structures* (44), S. 1768-1786.

[Bar07b] Barsoum, I., & Faleskog, J. (2007). Rupture mechanisms in combined tension and shear - Micromechanics. *International Journal of Solids and Structures* (44), S. 5481-5498.

[Bas11] Basaran, M. (2011). *Stress State Dependent Damage Modeling with a Focus on the Lode Angle Influence*. Darmstadt: Shaker Verlag.

[Bas10] Basaran, M., Wölkerling, S. D., Feucht, M., Neukamm, F., & Weichert, D. (2010). *An Extension of the GISSMO Damage Model Based on Lode Angle Dependence*. Bamberg: LS-Dyna-Anwenderkonferenz.

[Bau86] Bauschinger, J. (1886). Über die Veränderung der Elastizitätsgrenze und die Festigkeit des Eisens und Stahls durch Strecken und Quetschen, durch Erwärmen und Abkühlen und durch oftmals wiederholte Beanspruchungen. *Mittheilungen aus dem Mechanisch-technischen Laboratorium*, 13.

[Bec13] Becker, W. (2013). *Mechanik elastischer Körper und Strukturen*. Berlin, Heidelberg: Springer-Verlag.

[Bee10] Beese, A. M., Luo, M., Li, Y., Bai, Y., & Wierzbicki, T. (2010). Partially coupled anisotropic fracture model for aluminum sheets. *Engineering Fracture Mechanism* (77), S. 1128-1152.

[Beh16] Behrens, B.-A., & Pehsekodov, I. (2016). *Evaluation of different tests for fracture characterization of advanced high-strength sheet steels with the help of the finite element analysis*. Düsseldorf: Verlag und Vertriebsgesellschaft mbH.

[Ben06] Bennani, B., & Lauro, F. (2006). Damage models and identification procedures for crashworthiness of automotive light materials. *Latin American Journal of Solids and Structures* (3), S. 75-87.

[Ben02] Benzerga, A. (2002). Micromechanics of coalescence in ductile fracture. *Journal of the Mechanics and Physics of Solids*, 50, S. 1331-1362.

[Ben10] Benzerga, A., & Leblond, J.-B. (2010). *Ductile Fracture by Void Growth to Coalescence*.

[Ben04a] Benzerga, A., Besson, J., & Pineau, A. (2004). Anisotropic ductile fracture Part I: experiments. *Acta Materialia*, 52, S. 4623-4638.

[Ben04b] Benzerga, A., Besson, J., & Pineau, A. (2004). Anisotropic ductile fracture: Part II theory. *Acta Materialia* (52), S. 4639-4650.

[Ber04] Berdin, C., Besson, J., Bugat, S., Desmorat, R., Feyel, F., Forest, S., et al. (2004). *Local approach to fracture*. Mines: Presses de l'Ecole des Mines.

[Bie09] Bieler, T., Eisenlohr, P., Roter, F., Kumar, D., Mason, D., Crimp, M., et al. (2009). The role of heterogeneous deformation on damage nucleation at grain boundaries in single phase metals. *International Journal of Plasticity* (25), S. 1655-1683.

[Bor13] Borvall, T., Johansson, T., Schill, M., Jergeus, J., Mattiasson, K., & Bois, P. D. (2013). A General Damage Initiation and Evolution Model (DIEM) in LS-DYNA. *Proceedings of 9th European LS-DYNA Conference 2013* .

[Bri52] Bridgman, P. (1952). *Studies in large plastic flow and fracture, with special emphasis on the effects of hydrostatic pressure*. New York: McGraw Hill Inc.

[Bru14] Bruder, E., & Müller, C. (2014). *Physikalische Metallkunde*. Darmstadt: Technische Universität Darmstadt.

[Bun85] Bunge, H.-J. (1985). *An Introduction to Modern Texture Analysis in Preferred Orientation in Deformed Metal and Rocks*. London: Academic Press.

[Chu14] Chung, K., Kim, H., & Lee, C. (2014). Forming limit criterion for ductile anisotropic sheets as a material property and its deformation path insensitivity. Part I: Deformation path insensitive formula based on theoretical models. *International Journal of Plasticity* (58), S. 3-34.

[Coc68] Cockcroft, M. G., & Latham, D. J. (1968). Ductility and workability of metals. *Journal of the Institute of Metals* , S. 33-39.

[Com08] Comsa, D., & Banabic, D. (2008). Plane-Stress Yield Criterion for Highly-Anisotropic Sheet Metals. *Numisheet 2008* .

[Con85] Considere, A. (1885). *Annales des Ponts et Chaussees* , 9, 575-775.

[Cou76] Coulomb, C. (1776). Essai sur une application des règles des maximis et minimis à quelques problèmes de statique relatifs à la architecture. *Mem. Acad. Roy. Div. Sav.* (7), S. 343-387.

[Die16] Diez, C., Wieser, C., Harzheim, L., & Schumacher, A. (2016). Automated Generation of Robustness Knowledge for selected Crash Structures. *Proceedings of 14th LS-DYNA Forum 2016, Bamberg* .

[Dob10] Dobmann, G. (2010). Physical basics and industrial applications of 3MA - micromagnetic multiparameter microstructure and stress analysis. *Proceedings of 10th European Conference on Non-Destructive Testing* .

[Dub15] Dubisz, E. (2015). *Optimierung der Schubprobengeometrien für die experimentelle Materialkenngroßenermittlung zur Simulation von Versagen in höchstfesten Stählen*. Frankfurt: Frankfurt University of Applied Sciences.

[DuB16] DuBois, P., Erhart, P. T., Andrade, F., Haufe, A., Neukamm, F., Feucht, M., et al. (2016). A new versatile tool for simulation of failure in LS-DYNA and the application to aluminum extrusion.

[Dun14] Dunand, M., & Mohr, D. (2014). Effect of Lode parameter on plastic flow localization after proportional loading at low stress triaxialities. *Journal of the Mechanics and Physics of Solids* , 66.

[Dun10] Dunand, M., & Mohr, D. (2010). Hybrid experimental-numerical analysis of basic ductile fracture experiments for sheet metals. *INternational Journal of Solids and Structures* , 45, S. 1130-1143.

[Dun11] Dunand, M., & Mohr, D. (2011). On the predictive capabilities of the shear modified Gurson and the modified Mohr-Coulomb fracture models over a wide range of stress triaxialities and lode angles. *Journal of Mechanics and Physics of Solids* , 59, 1374-1394.

[Tub72] Duncombe, E. (1972). Tubes, Plastic Instability and Growth of Grooves and Patches in Plates or Tubes. *International Journal of Mechanical Sciences* (14), S. 325-337.

[ElB10] El Bartali, A., Evrard, P., Aubin, V., Herenu, S., Alvarez-Armas, I., Armas, A., et al. (2010). Strain heterogeneities between phases in a duplex stainless steel. Comparison between measures and simulation. *Procedia Engineering* , 2, S. 2229-2237.

[ElM94] El-Magd, E. (1994). Mechanical properties at high strain rates. *Journal De Physique III* , 4, S. 149-170.

[Erh17] Erhart, T., DuBois, P., & Andrade, F. (2017). Short Introduction of a New Generalized Damage Model. *Proceedings of 11th European LS-DYNA Conference* .

[DeF16] Faria, G. L., Godefroud, L. B., & Nery, F. V. (2016). Damage evolution in a tensile specimen of a ductile stainless steel. *Rem: Revista Escola de Minas* , 2 (69).

[Fes08] Fesich, T., Mohan, P., Marzougui, D., & Kan, C.-D. (2008). A Study of the Gruson Damage Model and Numerical Simulation of Ductile Failure in LS-DYNA. *Proceedings of 7. LS-DYNA Anwenderforum* .

[Feu08] Feucht, M. (2008). *Ein gradientenabhängiges Gursonmodell zur Beschreibung duktiler Schädigung mit Entfestigung*. Darmstadt: Technische Universität Darmstadt.

[Feu13] Feucht, M., & Haufe, A. (2013). *Damage and Failure Models in LS-DYNA*. Stuttgart: Dynamore GmbH.

[Fuj78] Fujita, H., & Miyazaki, S. (1978). Lüders Deformation in Polycrystalline Iron. *Acta Metallurgica* , S. 1273-1281.

[Gar05] Gardey, B., Bouvier, S., Richard, V., & Bacroix, B. (2005). Texture and dislocation structures observation in a dual-phase steel under strain-path changes at large deformation. *Materials Science and Engineering A* , 400-401, S. 136-141.

[Ger15] Gerstein, G., Klusemann, B., Bargmann, S., & Schaper, M. (2015). Characterization of the Microstructure Evolution in IF-Steel and AA6016 during Plane-Strain Tension and Simple Shear. *Materials* , 8.

[Gha10] Ghadbeigi, H., Pinna, C., & Yates, J. (2010). Local plastic strain evolution in a high strength dual-phase steel. *Materials Science and Engineering A* , 52, S. 5026-5032.

[Got13] Gottstein, G. (2013). *Materialwissenschaft und Werkstofftechnik: Physikalische Grundlagen*. Heidelberg: Springer Verlag.

[Gro07] Gross, D., & Seelig, T. (2007). *Bruchmechanik - Mit einer Einführung in die Mikromechanik*. Berlin, Heidelberg: Springer-Verlag.

[Gro14] Grote, K.-H. F. (2014). *Dubbel: Taschenbuch für den Maschinenbau* (24 Ausg.). Heidelberg: Springer Vieweg.

[Gu15] Gu, G., & Mohr, D. (2015). Anisotropic Hosford–Coulomb fracture initiation model: Theory and application. *Engineering Fracture Mechanics* (147).

[Gur77] Gurson, A. L. (1977). Continuum Theory of Ductile Rupture by Void Nucleation and Growth: Path I-Yield Function and Flow Rules of Porous Ductile Media. *ASME Transaction. J. Eng. Mat. Tech.* , S. 2-15.

[Han76] Hancock, J., & MacKenzie, A. (1976). On the Mechanisms of Ductile Failure in High-Strength Steels Subjected to Multi-Axial Stress-States. *Journal of the Mechanics and Physics of Solids* , 24, S. 147-169.

[Hao97] Hao, S., & Brocks, W. (1997). The Gurson-Tvergaard-Needleman-model for rate and temperature-dependent materials with isotropic and kinematic hardening. *Computational Mechanics* , 20, S. 34-40.

[Hen24] Hencky, H. (1924). On the theory of plastic deformations. *Zeitschrift für Angewandte Mathematik und Mechanik* (4), S. 323-334.

[Her54] Hershey, A. (1954). The plasticity of an isotropic aggregate of anisotropic face centred cubic crystals. *Journal of Applied Mechanics* (21), S. 241-249.

[Hil58] Hill, R. (1958). A General Theory of Uniqueness and Stability in Elastic-Plastic Solids. *Journal of the Mechanics and Physics of Solids* , 6, 236-249.

[Hil48] Hill, R. (1948). A Theory of the Yielding and Plastic Flow of Anisotropic Metals. *Proceedings of the Royal Society of London. Series A, Mathematical and Physical Sciences* , 193 (1033), S. 281-297.

[Hil92] Hill, R. (1992). A User-Friendly Theory of Orthotropic Plasticity in Sheet Metals. *International Journal of Mechanical Science* , 19-25.

[Hil90] Hill, R. (1990). Constitutive Modelling of Orthotropic Plasticity in Sheet Metals. *Journal of Mechanics and Physical Solids* (38), S. 405-417.

[Hol45] Hollomon, J. (1945). Tensile Deformation. *Trans. Metal Society AIME* , 112, S. 268.

[Hos72] Hosford, W. (1972). A generalised isotropic yield criterion. *Journal of Applied Mechanics* (39), S. 607-609.

[Hub04] Huber, M. (1904). Przyczynek do pdstaw wytormalosci. *Czasopismo Technicze* (22), S. 34-81.

[Huh05] Huh, M.-Y., Lee, J.-H., Park, S. H., Engler, O., & Raabe, D. (2005). Effect of Through-Thickness Macro and Micro-Texture Gradients on Ridging of 17%Cr Ferritic Stainless Steel Sheet. *Steel Research International* , 76 (11).

[Jai99] Jain, M., Allin, J., & Lloyd, D. (1999). Fracture limit prediction using ductile fracture criteria for forming of an automotive aluminum sheet. *International Journal of MEchanical Sciences* (41), S. 1273-1288.

[Jan14] Janbakhsh, M., Loghmanian, S., & Djavanroodi, F. (2014). Application of Different Hill's Yield Criteria to Predict Limit Strains for Aerospace Titanium and Aluminum Sheet Alloys. *International Journal of Advanced Design and Manufacturing Technology* .

[Kan87] Kanetake, N., & Tozawa, Y. (1987). Crystallographical Calculation of Earing in Deep Drawing under Various Conditions. (7), S. 131-147.

[Kan13] Kang, J., Mishra, R. K., & Wilkinson, D. S. (2013). Effect of Plastic Anisotropy on Shear Localization and Fracture in Automotive Sheets. *Proceedings of 13th International Conference on Fracture* .

[Kan07] Kang, J., Osokov, Y., Embury, J., & Wilkinson, D. (2007). Digital image correlation studies for microscopic strain distribution and damage in dual phase steels. *Scripta Materialia* , 56, S. 999-1002.

[Kan11] Kantereit, H. (2011). Bake Hardening Behaviour of Advanced High Strength Steels under Manufacturing Conditions. *SAE International* .

[Kar93] Karafillis, A., & Boyce, M. (1993). A General Anisotropic Yield Criterion Using Bounds and a Transformation Weighting Tensor. *Journal of the Mechanics and Physics of Solids* , 41, S. 1859-1886.

[Koc17] Koch, D., Haufe, A., & Feucht, M. (2017). Experimental Investigation and Numerical Characterization of the Bake-Hardening Effect of a Two-Phase Steel. *Proceedings 11th European LS-DYNA Conference* .

[Kre16] Kremer, A. (2016). *Korrelation von Mikrostruktur und anisotropen Materialkennwerten für die Crashberechnung*. Darmstadt: Technische Universität Darmstadt.

[Kul06] Kuleev, V., Tsar'kova, T., & Nichipuruk, A. (2006). Effect of Tensile Plastic Deformations on the Residual Magnetization and Initial Permeability of Low-Carbon Steels. *Russion Journal of Nondestructive Testing* (42), S. 261-271.

[Las07] Lassance, D., Fabregue, D., Delanny, F., & Pardoen, T. (2007). Micromechanics of room and high temperature fracture in 6xxx Al alloys. *Progress in Materials Science* , 52, S. 62-129.

[Lem05] Lemaitre, J., & Desmorat, R. (2005). *Engineering Damage Mechanics - Ductile, Creep, Fatigue and Brittle Failure*. Berlin - Heidelberg: Springer Verlag.

[Lin13] Lindqvist, K. (2013). *Bake hardening effect in advanced high-strength steels*. Gothenburg, Sweden: Chalmers University of Technology.

[Liv16a] Livermore Software Technology Corporation. (2016). *LS-Dyna Keyword User's Manual Volume I* (Livermore Software Technology Corporation Ausg.). Livermore, California: Livermore Software Technology Corporation.

[Liv16b] Livermore Software Technology Corporation. (2016). *LS-Dyna Keyword User's Manual Volume II - Material Models*. Livermore, California: Livermore Software Technology Corporation.

[Luo12] Luo, M. (2012). *Anisotropic Ductile Fracture of Metal Sheets: Experimental Investigation and Constitutive Modeling*. Cambridge: Massachusetts Institute of Technology.

[Luo09] Luo, M., & Wierzbicki, T. (2009). Ductile Fracture Calibration and Validation of Anisotropic Aluminum Sheets. *Proceedings of the SEM Annual Conference* .

[Mac92] Macherauch, E. (1992). *Praktikum in Werkstofflunde*. Braunschweig: Vieweg.

[Mar15b] Marcadet, S. (2015). *Ductile Fracture after Complex Loading Histories: Experimental Investigation and Constitutive Modeling*. Cambridge: Massachusetts Institute of Technology.

[Mar15a] Marcadet, S. J., Mohr, D., Roth, C. C., & Erice, B. (2015). A rate-dependent Hosford-Coulomb model for predicting ductile fracture at high strain rates. *EPJ Web of Conferences* (94).

[Mar67] Marciniaik, Z., & Kuczynski, K. (1967). Limit Strains in the Process of Stretch-Forming Sheet Metal. *International Journal of Mechanical Science* , S. 609-620.

[Maz07] Mazinani, M., & Poole, W. (2007). Effect of Martensite Plasticity on the Deformation Behavior of a Low-Carbon Dual-Phase Steel. *Metallurgical and Materials Transactions A* , 328 (38A), S. 328-339.

[McC68] McClintock, F. (1968). A criterion for ductile fracture by the growth of holes. *Journal of Applied Mechanics* , S. 363-371.

[McC71] McClintock, F., & Irwin, G. (1971). Plasticity aspects of fracture, in Fracture. *Academic Press* , 381 (III), S. 47-225.

[Moh09] Mohr, D., & Ebnoether, F. (2009). Plasticity and fracture of martensitic boron steel under plane stress conditions. *International Journal of Solids and Structures* , 46, S. 3535-3547.

[Moh06] Mohr, O. (1906). *Abhandlungen aus dem Gebiete der Technischen Mechanik*. Berlin: Verlag von Wilhelm Ernst & Sohn.

[Mon91] Montheillet, F., Jonas, J., & Benferrah, M. (1991). Development of Anisotropy During the Cold Rolling of Aluminum Sheet. *Int. Journal of Mechanical Sciences* (3), S. 197-209.

[Nee87] Needleman, A. (1987). A Numerical Study of Void Nucleation at Carbides. *Journal of the Mechanics and Physics of Solids* , 20, S. 981-998.

[Nee72] Needleman, A. (1972). Void Growth in an Elastic-Plastic Medium. *Journal of Applied Mechanics* , 39, S. 964-970.

[Nes01a] Nesterova, E., Bacroix, B., & Teodosiu, C. (2001). Experimental observation of microstructure evolution under strain-path changes in low-carbon IF steel. *Materials Science and Engineering A* , 309-310, S. 495-499.

[Nes01b] Nesterova, E., Bacroix, B., & Teodosiu, C. (2001). Microstructure and Texture Evolution under Strain-Path Changes in Low-Carbon Interstitial-Free Steel. *Metallurgical and Material Transactions A* , 32A.

[Nia12] Niazi, M. (2012). *Plasticity Induced Anisotropic Damage Modeling for Forming Processes*. Enschede: University of Twente.

[Ost14] Ostermann, F. (2014). *Anwendungstechnologie Aluminium*. Heidelberg, Berlin: Springer.

[Pat13] Patriarca, L., Abuzaid, W., Sehitoglu, H., & Maier, H. (2013). Slip transmission in bcc FeCr polycrystal. *Materials Science & Engineering A* , 588.

[Pee01b] Peeters, B., Bacroix, B., Teodosiu, C., Van Houtte, P., & Aernoudt, E. (2001). work-hardening/softening behaviour of b.c.c. polycrystals during changing strain paths: II. TEM observations of dislocation sheets in an if steel during two-stage strain paths and representation in terms of dislocation densities. *Acta Materialia* , 49, pp. 1621-1632.

[Pee01a] Peeters, B., Seefeldt, M., Teodosiu, C., Kalidindi, S., & Van Houtte, P. (2001). Work-Hardening/Softening behaviour of b.c.c. polycrystals during changing strain paths: I. an integrated model based on substructure and texture evolution and its prediction of the stress-strain behaviour of an if-steel during two-stage straining paths. *Acta Materialia* , 49, pp. 1607-1619.

[Ric69] Rice, J., & Tracey, D. (1969). On the Ductile Enlargement of Voids in Triaxial Stress Fields. *Journal of Mechanics and Physics of Solids* , 17, S. 201-217.

[Rie16] Riemensperger, D. (2016). Considering Bake Hardening for Deformed Sheet Steel - A phenomenological approach. *Proceedings 11th GERMAN LS-DYNA FORUM* .

[Ros08] Rossi, M., Broggiano, G., & S., P. (2008). Application of digital image correlation to the study of planar anisotropy of sheet metals at large strains. *Meccanica* (43), S. 185-199.

[Rou87] Rousselier, G. (1987). Ductile Fracture Models And Their Potential In Local Approach Of Frature. *Nuclear Engineering and Design* .

[Sav10] Savic, V., Hector, L., & Fekete, J. (2010). Digital Image Correlation Study of Plastic Deformation and Fracture in Fully Martensitic Steels. *Experimental Mechanics* , 50, S. 99-110.

[Sav95] Savoie, J., Jonas, J., MacEwen, S., & Perrin, P. (1995). Evolution of r-value during the tensile deformation of aluminium. *Textures and Microstructures* , 23, S. 149-171.

[Ste08] Steglich, D., Brocks, W., Heerens, J., & Pardoen, T. (2008). Anisotropic ductile fracture of Al 2024 alloys. *Engineering Fracture Mechanics* , 75, S. 3692-3706.

[Sto16] Stolzenburg, M., Tröster, T., Block, H., & Michler, T. R. (2016). Application of distortional hardening for numerical simulation of automotive sheet metals. *Proceedings of 35th International Deep Drawing Research Group (IDDRG) 2016* .

[Sto11] Stoughton, T., & Yoon, J. (2011). A new approach for failure criterion for sheet metals. *International Journal of Plasticity* , S. 440-459.

[Suw14] Suwas, S., & Ray, R. (2014). *Crystallographic Texture of Materials*. London: Springer-Verlag .

[Swi52] Swift, H. (1952). Plastic Instability Under Plane Stress. *Journal of the Mechanics and Physics of Solids* , 1, 1-18.

[Swi46] Swift, H. (1946). Plastic Strain in Isotropic-Hardening Material. *Engineering* , 1, S. 1.

[Tas09] Tasan, C., Hoefnagels, J., ten Horn, C., & Geers, M. (2009). Experimental analysis of strain path dependent ductile damage mechanics and forming limits. *Mechanics of Materials* (41), S. 1264-1276.

[Tho68] Thomason, P. (1968). Tensile plastic instability and ductile fracture criteria in uniaxial compression tests. *International Journal of Mechanical Sciences* (11).

[Til13] Till, E., & Hackl, B. (2013). Calibration of plasticity and failure models for AHSS sheets. *Proceedings of the International Deep Drawing Research Conference IDDRG 2013* .

[Tim08] Timokhina, I., Hodgson, P., Ringer, S., Zheng, R., & Pereloma, E. (2008). *Understanding Bake-Hardening in Modern High Strength Steels for the Automotive Industry Using Advanced Analytical Techniques*. Research Online.

[Tre64] Tresca, H. (1864). On the yield of solids at high pressures. . *Comptes Rendus Academie des Sciences* , S. 59-754.

[Tro15] Trondl, A., Klitschke, S., Böhme, W., & Sun, D.-Z. (2015). *Verformungs- und Versagensverhalten von Stählen für den Automobilbau unter crashartiger mehrachsiger Belastung*. Freiburg: Fraunhoferinstitut IWM.

[Tve81] Tvergaard, N. (1981). Influence of voids on shear band instabilities under plane strain conditions. *International Journal of Fracture* , S. 389-407.

[Tve82] Tvergaard, V. (1982). On localization in ductile materials containing spherical voids. *International Journal of Fracture* , 17, S. 389-407.

[Uth09] Uthaisangsuk, V., Prahl, U., & Bleck, W. (2009). Failure modeling of multiphase steels using representative volume elements based on real microstructures. *Procedia Engineering* , 1, S. 171-176.

[Voc45] Voce, E. (1945). Tensile deformation. *Transactions of AIME* .

[Vol11] Volk, W., & Hora, P. (2011). A new algorithm for a robust user-independent evaluation of beginning instability for experimental FLX determination. *International Journal of Material Forming* .

[vMi28] von Mises, R. (1928). Mechanik der plastischen Formänderung von Kristallen. *Zeitschrift für angewandte Mathematik und Mechanik* , 8, S. 582-592.

[Wei07] Weißbach, W. (2007). *Werkstoffkunde*. Wiesbaden: Vieweg.

[Wes30] Westphal, W. (1930). *Physik. Ein Lehrbuch für Studierende an den Universitäten und Technischen Hochschulen*, 2. Auflage. Berlin: Springer.

[Wie10] Wierzbicki, T., & Bai, Y. (2010). Application of extended Mohr–Coulomb criterion to ductile fracture. *International Journal of Fracture* (161), S. 1-20.

[Wil80] Wilkins, M., Streit, R., & Reaugh, J. (1980). *Cumulative-strain-damage model of ductile fracture: simulation and prediction of engineering fracture tests*. Livermore, California: Lawrence Livermore Laboratory.

[Wor17] WorldAutoSteel. (02.07.2017). http://www.worldautosteel.org/wp-content/uploads/2012/03/AHSSDiagram_WorldAutoSteel-copy.png.
<http://www.worldautosteel.org> .

[Xue07] Xue, L. (2007). *Ductile Fracture Modeling Theory, Experimental Investigation and Numerical Verification*. Cambridge: Massachusetts Institute of Technology.

[Yoo04] Yoon, J., Barlat, F., Dick, R., Chung, K., & Kang, T. (2004). Plane stress yield function for aluminum alloy sheets - part II: FE formulation and its implementation. *International Journal of Plasticity* , 20, S. 495-522.

[Zha00] Zhang, Z., Thaulow, C., & Odegard, J. (2000). A complete Gurson model approach for ductile fracture. *Engineering Fracture Mechanics* , 2, S. 155-168.

[Zha14] Zhao, Z., Tong, T., Liang, J., Yin, H., Zhao, A., & Tang, D. (2014). Microstructure, mechanical properties and fracture behaviour of ultra-high strength dual-phase steel. *Materials Science & Engineering A* .

Die Seite wurde aus datenschutzrechtlichen Gründen entfernt.